Dipl.-Ing. Mathias Mair

Nonlinear Structural Rotor Vibrations in Electrical Machines

DOCTORAL THESIS

to achieve the university degree of
Doktor der technischen Wissenschaften
submitted to

Graz University of Technology

Supervisor
Univ.-Prof. Dr.-Ing. habil. Katrin Ellermann
Institute for Mechanics

Graz, Mai 2016

AFFIDAVIT

I declare that I have authored this thesis independently, that I have not used other than the declared sources/resources, and that I have explicitly indicated all material which has been quoted either literally or by content from the sources used. The text document uploaded to TUGRAZonline is identical to the present doctoral thesis.

Date

Signature

Abstract

The predictability of rotor vibrations is gaining more and more in importance in an early stage of the development process of an electrical machine. Common methods in the simulation of rotor vibrations are mostly linear and not usable for arising nonlinear phenomena. Hence, methods for the computation of nonlinear effects are necessary.

In order to derive a suitable description of a rotor, thesis starts with the derivation of Timoshenko beam elements. Therefore, a variational formulation of the Timoshenko beam is done. The formulation of the beam is discretized using consistent shape functions. The necessary cross section parameters, e.g. shear center and shear correction factor, result from a two-dimensional finite element simulation of the shear stresses. A St. Venant torsion problem and a torsionless bending problem are solved.

The heterogeneous structure of the rotor is modeled by composite beam element. The formulation of these elements, which is based on the Timoshenko beam theory, is presented. The computation of the shear stresses is derived for orthotropic materials. Thus, the cross section parameters are determined. Using these element types, a mechanical model of an induction machine is prepared. The numerical model is validated by an experimental modal analysis. Furthermore, run up simulations of the rotor including nonlinear bearing stiffness are carried out in time domain.

A detailed investigation of the behavior of the nonlinear bearing stiffness is carried out with a simplified rotor model. The nonlinear rotor vibrations are classified and the influence of the stiffness coefficients is shown.

Finally, the unbalanced magnetic pull is computed for a model of a two-pole induction machine. An analytical model for the electromagnetic forces is coupled with the finite element model of the rotor. In this model, the static and dynamic eccentricities are considered in the computation of the unbalanced magnetic pull.

Acknowledgments

First of all, I want to express my sincere gratitude to my adviser Univ.-Prof. Dr.-Ing. habil. Katrin Ellermann for her supervision during the last years. Her enduring support has influenced my studies and academic development. I thank Katrin for offering me the great opportunity to work in this interesting scientific field and the freedom to opt for new and unplanned directions of research.

Besides my advisor, I would like to thank our cooperation partners Dipl.-Ing. Dr.techn. Hermann Lang and Dipl.-Ing. Dr.techn. Bernhard Weilharter from Elin Motoren GmbH for their important contribution and technical support.

Furthermore, many thanks are addressed to my colleagues at the Institute for Mechanics for the great time I have had working with them. In particular, I want to thank Dipl.-Ing. Stefan Haas. His technical know-how and his way to think about upcoming problems have been very inspiring.

Special thanks are address to my family, in particular to my parents Josef and Herta, for their support and help through my whole education and hence making all of this possible.

Finally, I want to thank my dear Sarah for continuous support, motivation and patience over so many years and for always believing in me. I am very grateful for the way we complement to each other.

Contents

List of Symbols

Notation	Description
A	area
α	derivative of torsion angle θ_x with respect to x
$\boldsymbol{B}$	derivative matrix of the shape function matrix $\boldsymbol{H}$
$\boldsymbol{\mathcal{B}}$	magnetic field
$\boldsymbol{b}$	left Cauchy-Green deformation tensor
$\boldsymbol{C}$	right Cauchy-Green deformation tensor
c	stiffness coefficient
C_M	warping constant
$\boldsymbol{\mathfrak{D}}$	differential operator matrix
$\boldsymbol{D}$	damping matrix
$\boldsymbol{\mathcal{D}}$	electrical displacement field
dA	infinitesimally small area
d_e	external damping coefficient
d_i	internal damping coefficient
dV	infinitesimally small volume in reference configuration
dv	infinitesimally small volume in general configuration
E	Young's modulus
$\boldsymbol{E}$	Green-Lagrangian strain tensor
$\boldsymbol{\mathcal{E}}$	electrical field
$\boldsymbol{e}$	eccentricity
$\boldsymbol{\varepsilon}$	linear strain tensor
ϵ	electric permittivity
$\boldsymbol{\mathcal{F}}$	deformation gradient

Notation	Description
$\boldsymbol{F}$	force vector
$\boldsymbol{f}^B$	body forces
G	shear modulus
$\boldsymbol{G}$	gyroscopic matrix
γ	material conductivity
$\boldsymbol{H}$	matrix of shape functions
$\mathcal{H}$	magnetic field intensity
h_{ij}	shape functions
I_T	St. Venant torsion stiffness
I_y, I_z and I_{yz}	second moment of area
J	Jacobian
$\mathcal{J}$	current density
$\boldsymbol{K}$	stiffness matrix
κ_y and κ_z	shear correction factor
$\mathcal{L}$	Lagrangian functional
$\boldsymbol{L}$	angular momentum
λ_i	i^{th} eigenvalue
$\boldsymbol{M}$	mass matrix
m	mass
μ	magnetic permeability
M_x	torsion moments
M_y and M_z	bending moments
N	normal force
$\boldsymbol{N}$	spin softening matrix
ν	Poisson's ratio

Notation	Description
Ω	rotational speed
ω	eigenfrequency
ω_d	damped eigenfrequency
Φ	Prandl's stress function
Π	strain energy
Ψ	stress function
ψ	warping function
Q_y and Q_z	shear forces
$\boldsymbol{R}$	transformation matrix
ρ	mass density
$\boldsymbol{r}_i$	i^{th} eigenvector
r, s and t	natural coordinates
$\boldsymbol{\sigma}$	stress tensor
σ_x	normal stress component
T	kinetic energy
t	time
$\boldsymbol{\tau}$	Cauchy stress tensor
τ_{xy} and τ_{xz}	shear stress components
θ_x, θ_y and θ_z	rotation angles about x-, y- and z-axis
Θ_a	axial mass moment of area
Θ_p	polar mass moment of area
$\boldsymbol{u}$	displacement field
u, v and w	displacements in x-, y- and z-direction
$\boldsymbol{V}$	matrix of frequency response functions
W	energy caused by external forces

Notation	Description
$\boldsymbol{X}$	coordinate vector in reference configuration
$\boldsymbol{x}$	coordinate vector in general configuration
x, y and z	cartesian coordinates
S_y and S_z	first moment of area
y_M and z_M	shear center coordinates
y_T and z_T	center of twist
ζ	modal damping

CHAPTER 1

Introduction

1.1 Motivation and contribution of this work

Electrical machines are a fundamental part of modern society. In a large variety of situations electrical machines facilitate daily life. Electrical machines are essential in industrial applications and are necessary for the operation of technical processes.

Additionally, a new public awareness for our environment has risen over the last years. People feel obliged to their descendants for a clean environment and a demand on sustainable and ecological friendly applications exist. For example, the market share of electrically powered cars and hybrid cars has significantly increased over the last years and more and more hybrid car as well purely electric powered cars are available. The energy producers are also striving for market growth and invest in new alternative energy plants, e.g. offshore wind farms or pump storage plants. These facts result in a highly request on efficient electrical machines.

The necessity of electrical power forces producers of electrical machines to push their developments for an increase in performance. In most cases, the frame size is limited by technical constraints. On the one hand, this discrepancy of boundary conditions has to be solved in the design process of electrical machines, which is one of the main challenges and inevitably leads to the achievement of technical borders. On the other hand, high power results in increased forces, which cause nonlinear effects in the vibrations. The standard linear techniques used in the design process cannot predict these effects. Thus, it raises a need for numerical methods in order to solve these challenges in structural vibrations.

The rotor is a main part in the electrical machine. The modeling of the rotor is usually carried out using one-dimensional finite elements or the transfer matrix approach. Rotordynamical problems with a long simulation time solved by three-dimensional finite element methods result in a high computational effort. A reduction of the degrees of freedom can be reached by using one-dimensional finite elements

for the rotor model. Timoshenko beam elements are generally accepted. The rotor of the electrical machine is a heterogeneous structure with different components made of different materials. Hence, the heterogeneous components are considered by a composite beam element in the rotor model. These elements are based on the Timoshenko beam theory.

For the formulation of beam elements shear coefficients are necessary. These coefficients are computed by a novel approach. Thereby, the St. Venant torsion problem and torsionless bending problem of a composite beam are solved using a two-dimensional finite element method. The formulation of these two problems is based on the general stress distribution in the multilayered cross section with different orthotropic material properties. The shear coefficients are computed with the resulting shear stresses based on the formulation of the internal strain energy. The introduced approach for the computation of the shear center and the shear correction factor is validated by an example. These results are compared to the solution of a three-dimensional model. This approach allows for the consideration of the material properties of the rotor core stack, the windings and the shaft in one beam element.

The rotor is modeled using Timoshenko beam elements and composite beam elements. A numerical modal analysis is carried out and eigenfrequencies and modes are calcuated. In order to validate the rotor model, a comparison between numerical and experimental results is drawn. For the experimental investigation the rotor is mounted on two steel racks for modal tests.

A run up simulation of the rotor is carried out using a roller bearing model. The roller bearing is included in the equation of motion as a nonlinear spring. The stiffness nonlinearities are given values of the roller bearing's producer. The Newton Raphson procedure and the Newmark algorithm are used to solve the nonlinear equation of motion. The nonlinearities are investigated using a simplified rotor model with a reduced set of degrees of freedom. This model is based on the same mass and bearing properties. Special effects of the rotating system, which are related to the bearing nonlinearities, are pointed out.

Additionally, the electromagnetical forces produce a nonlinear excitation of the rotor in the electrical machine. An analytical approach depending on the air gap width is used to compute the electromagnetical forces of a two-pole induction machine. In each time step the electromagnetical forces are updated and the Newton Raphson procedure is used to obtain the nonlinear transient solution. Finally, the results are discussed and details are worked out.

1.2 Review of literature

1.2.1 Beam modelling

Beams take an important part in modelling electrical machines. The beam theories are the foundation in describing the mechanical behavior in many rotor models.

1.2.1.1 Beam theories

First investigations on beams were carried out in the 18th century by Jacob Bernoulli. He derived a linear relation between the curvature of an elastic beam and the bending moment. Later, Daniel Bernoulli formulated a differential equation of a vibrating beam. Regarding the work of the Bernoullis, Leonhard Euler investigated beam displacements under various loads. The Euler-Bernoulli beam theory, also called the classical beam theory, includes the strain energy due to bending and the kinetic energy due to lateral displacement [177]. The Euler-Bernoulli theory allows for a prediction of vibrating beam's eigenfrequencies but the results tend to be too high.

John William Strutt (3. Baron Rayleigh) extended the Euler-Bernoulli beam theory by considering the rotational effect of the cross section [170] in 1877. The Rayleigh beam theory gives an improvement of the estimated eigenfrequencies.

Pochhammer (1876) [136] and independently Chree (1889) [28] investigated the problem of a vibrating solid cylinder in terms of general elastic equations. They introduced an exact formulation for the beam problem. A treatment of Pochhammer's work is noted in [105]. This exact formulation of the beam problem had not widely been used, since approximate solutions, considering transverse displacements, are sufficient for most applications [30].

Extending the Euler-Bernoulli beam theory by the effect of shear, the estimation of eigenfrequencies is improved remarkably. Timoshenko (1921,1922) introduced a beam theory which includes the effects of shear as well as the rotational effect of the cross section in the Euler-Bernoulli beam theory for non-slender beams [179]. Timoshenko extended the usual differential equation of a transverse vibrating beam in terms of rotatory inertia. Additionally, he assumed that the bending angle of the cross section depends on the angle of shear.

Following Timoshenko's work, the natural frequencies and mode shapes are investigated for beams with different boundary conditions in [98], [6], [183], [35], [78]. Kruszewski (1949) [98] gave a general solution for the differential equation introduced by Timoshenko in [179] together with the specific solutions of cantilevered beams and free-free beams. Kruszewski used a trial and error process for solving the frequency equations. Anderson (1953) [6] extended Timoshenko's approach with a second differential equation. The use of two differential equations allows for the description of the total deflection with two variables, the bending deflection and the shear deflection. Traill-Nash and Collar (1953) provided frequency equations

and mode shapes for the nine possible cases of boundary conditions of a beam for three usual types of end supports regarding a second spectrum of eigenfrequencies [183]. They used a matrix iteration process to calculate the natural frequencies of a test object. Dolph (1954) [35] investigated the boundary value problem of hinged-hinged and free-free Timoshenko beams with no external forces. He pointed out the orthogonality relations of the principle modes and briefly mentioned methods to solve the complete response function. Herrmann (1955) [71] noted the orthogonality properties of principle modes independently from Dolph, as he formulated forced motions of non-slender beams using Timoshenko's beam theory [71]. He introduced time-dependent boundary conditions of any admissible combination. Time-dependent loads and bending moments are considered. The solving approach is based on orthogonal properties of the principle modes of free vibration and the procedure of Mindlin and Goodman (1950) [116] for time-dependent boundary conditions. Huang (1961) [78] obtained frequency equations and mode shapes for all possible combinations of boundary conditions. He obtained a solution from two complete differential equations in total deflection and bending slope. A second spectrum was not taken into account. Abbas and Thomas (1977) found evidence of this second spectrum of frequencies of hinged-hinged beams [1].

Leckie and Lindberg (1963) published a beam finite element based on the Euler-Bernoulli beam[99]. The mass and stiffness matrix was determined from the exact differential equation of the infinitesimal element in static equilibrium by assuming a deflection form of a third order polynomial for the beam element. They evaluated the polynomial coefficients in terms of end deflections.

Kapur (1966) extended Leckie and Lindberg's work by including shear deformation and rotatory inertia in the analysis [89]. A cubic displacement function of the beam element was assumed for the bending deformation as well as for the shear deformation. Kapur split the bending and shear deformation into translation and rotation, respectively. This element has a total of eight degrees of freedom. Egle (1969) joined Kapur's work and introduced an approximate Timoshenko beam element with decoupled shear deformation and rotary inertia [40]. The assumed constraints for shear forces are consistent with the Euler-Bernoulli theory. Based on Leckie's and Lindberg's work, authors published further beam element formulations, e.g. [127], [40], [31], [174], [175], [32].

The shear locking phenomenon arises in a certain class of elements. Tessler and Dong (1981) published an approach for developing beam elements which are free of shear-locking [173]. They approximated the shear and bending field with interdependent polynomials in order to obtain a family of virgin elements. Shear constraint conditions were imposed on each element, therefrom a series of constrained elements was generated. Prathrap and Bashyam (1982) [138] derived that the shear locking occurs due to the elements inadvertently enforcing spurious constraints. These constraints appear from inconsistencies in the strains depending on the assumed displacement functions. Stolarski and Belytschko (1982) mentioned the locking phenomena in C^0 curved elements for hybrid-stress and mixed formulations [169]. They found that

hybrid-stress formulations avoid locking for beams. Further investigations of the shear locking phenomenon and locking-free elements are presented in [23], [46], [12] and [110].

Higher-order models are more complex models, because they consider greater expressions of the displacement coordinate's exponent in the cross section of beams. Lo et al. (1977) introduced a high-order model considering warping and striction for homogeneous cross sections [103] as well as for laminated cross sections [104] for thick plates.They have shown that the ratio of the load pattern's characteristic length to the plate thickness is of the corresponding unity's order. Low-order theories deliver inadequate results for this case. Reddy (1984) simplified the existing high-order models and took the warping into account in addition to displacements. He assumed a parabolic distribution of transverse shear strains through the thickness. Sheinman (2001) investigated analytical solutions of high-order models in a closed-form [153].

On the other hand, mixed models are used for beam modeling. Thereby, displacement and stress are considered as independent variables. The aim is to improve the stress description. A dimensional reduction method is imposed on the three-dimensional elastic body of a beam. Kantorovich and Krylov (1958) [86] mentioned a general mathematical procedure which uses geometry in order to reduce the problem's dimension of the three-dimensional partial differential equations of elasticity. Vogelius and Babuška (1981) introduced a mathematical procedure of an adaptive approximate approach for solving $(n + 1)$-dimensional boundary value problems by replacing it with systems of equations in n-dimensional space [188], [189] and [187]. Barta and Vidoli (2002) [11] used a three-dimensional Hellinger-Reissner mixed variational principle to derive a shear and normal deformable plate theory. Auricchio et al. (2010) and (2013) obtained a dimensional reduction procedure for beams using the three-dimensional Hellinger-Reissner variational principle [7], [8].

Some authors worked on the mechanical behavior of laminated beams. Anderson (1972) investigated free vibrations of a beam with parallel alternating layers of two homogeneous materials [5]. He assumed isotropic elasticity for both materials and treated each layer as a Timoshenko beam. Silverman (1980) used the Euler-Bernoulli theory to approach the flexure of a laminated beam [154]. Based on the minimization of the potential energy, forth order differential equations are derived for the deflection of a cantilevered beam. Giavotto et al. [56] studied on anisotropic beam sections applicable on rotor blades of helicopters or wind generators. They separated the three-dimensional warping field from the section' motion and yielded a linear system of second order differential equations. Following these works, further investigations are published in [161], [87] and [88].

Tsai et al. (1990) analyzed the torsional response of rectangular laminated composite plates based on the Mindlin-Reissner theory [185]. They incorporated shear properties of each layer separately and unidirectionally, as they used an experimental procedure in order to determine shear moduli. A theory for the torsion of laminated composite beams was introduced by Sankar (1993) [148]. This theory is based on the

shear deformable laminated plate theory. The displacement field of the laminated composite beam is achieved by retaining the first-order terms of the Tayler series expansion for the plate midplane deformations in the width coordinates. Sankar formulated a closed form-solution for the torsional problem of a special orthotropic beam. Kim and White (1997) investigated three-dimensional composite box beams using thin- and thick-walled composite beam theories [91]. They took the torsional warping and transverse shear effects into account and validated the method with experimental, analytical and numerical results.

The dynamical behavior of tapered composite beams with imposed harmonic excitation was presented by Ramalingeswara Rao and Ganesan (1997) [143]. They used the finite element method to solve the resulting differential equations for uniaxial bending. The Poisson effect is considered in a correction of the stress-stress relations. Further investigations of dynamic behaviour of laminated beam are presented in [158], [83] and [84].

1.2.1.2 Shear stresses in beam cross sections

Weber (1924) introduced an analytical approach based on Timoshenko's work to compute the deformation of beams for imposed shear forces [192]. He computed stress functions for different assumptions, e.g. beams with and without lateral contraction. The shear stresses were provided analytically. Additionally, the shear center of prismatic beams was determined in case of torsionless bending. Weber extended his investigations for the load case of a torque in 1926 [191]. He developed a general approach for calculation of torsion and adjusted this approach with experimental results introduced by Bach (1909) [9].

Schwalbe (1935) [151] calculated the shear center of an arbitrary cross section based on torsionless bending of a beam. He used the balance of momentum and compatibility equations of a continuum in order to formulate the equilibrium of moments. He divided the cross sections into cells with a triangular shape in order to carry out the necessary integration. Trefftz (1935) [184] showed that the solution of torsional problem also gives the shear center. Osgood (1943) [198] pointed out differences in the literature of the position of the shear center. Goodier (1944) [59] investigated the center of shear for multicellular sections based on the Saint-Venant theory. Weinstein (1947) [194] gave a proof that the center of shear and the center of twist are coincident. He used a formulation based on the Saint-Venant theory.

Herrmann (1965) [72] followed the finite element procedure and used the Ritz technique in combination with the approach of minimum potential energy to achieve an approximate solution of the torsional problem. It is possible to solve the torsional problem for any arbitrary cross section with this method, approximately. Manson and Herrmann (1968) [114] used the finite element method to obtain solutions for the shear stress distribution, the shear center and the shear deformation coefficients for arbitrary cross section shapes. Krahula and Lauterbach (1969) [97] solved the Saint-Venant problem for beams with anisotropic material behavior using the finite

element method. Haberl and Och (1974) [69] investigated the torsional stiffness and the shear center for arbitrary cross section in case of anisotropic material properties. They developed two types of elements, one based on Prandl's stress function the other one based on the warping function. Gruttmann et al. (1999) [62] investigated shear stresses in prismatic beam due to Saint-Venant torsion and torsionless bending. They used the finite element method to solve the weak form of the derived boundary value problems for both cases with respect to an arbitrary coordinate system. Gruttmann et al. introduced stress functions which fulfill the basic equilibrium equations.

Other authors used the boundary element method to solve the Saint-Venant torsion or torsionless bending of prismatic beams. Chou also (1993) [25] used the boundary element method to solve the shear center of arbitrary cross sections. Friedman and Kosmatka (2000) [47] presented an approach for solving the general flexure problem of isotropic beams with arbitrary cross sections of a single domain using the boundary element method. Sapountzakis and Protonotariou (2008) [150] extended this approach of Friedman and Kosmatka for arbitrary cross sections with multiple domains.

In his first paper [179], Timoshenko pointed out that the shear forces of transverse vibrating beams are overestimated and he correct his model's weak point with the shear coefficient for a rectangular cross section. In a second paper [180] Timoshenko (1922) introduced an improved coefficient, which allows for a closer match of his approach for beams supported on both ends to the two-dimensional theory. Different authors followed to improve the shear correction factors in a theoretical manner, e.g. Goens (1931) [58], Olsson (1934) [129], Pickett (1945) [134] or Mindlin and Deresiewicz (1954) [117]. Experimental investigations for achieving the shear correction factor were done by various authors, e.g. Hearmon (1958) [70], Spinner et al. (1960) [160] or Spence and Seldin (1970) [159]. Kaneko (1975) [85] gave a detailed review of works which deal with the shear correction factors theoretically and experimentally.

Stojek (1964) [168] derived the shear correction factor using an energy approach. The elastic shear strain energy of the Timoshenko beam was assumed to be equal to the elastic shear strain energy of the exact formulation of a general beam. The shear correction factor is obtained from this condition. Based on Stojek's work, Gruttmann and Wagner (2001) [61] introduced a method to solve the shear correction factor for arbitrary cross sections using the finite element method.

Cowper (1966) [29] obtained the equations of the Timoshenko beam theory by solving equations of the three-dimensional elasticity theory. The solution delivers a harmonic function which depends on the cross section and satisfies the boundary conditions. Cowper expressed the shear correction factor as solution of this harmonic function. He denoted numerical values for various shapes of cross sections.

Stephen (1980) [163] developed a formula for the shear correction factor which is structurally similar to Cowper's approach. Stephen achieved this expression by equating the Timoshenko beam's centerline curvature to the curvature of a general

beam subjected to uniform gravity loading. Hutchinson (2001) [79] derived the shear correction factor for symmetrical cross sections by formulating the Hellinger-Reissner principle. Stephen (2001) [162] noted the equivalence of Hutchinson's approach.

The stresses in a composite cantilevered beam were presented by Gerstner (1968) [55]. Gerstner introduced a closed-form solution of a three layer beam and investigated the interlaminar shear stresses. Rao and Ghosh (1979) [142] formulated a method which provides an exact static solution of a laminated beam. Therefore, a technique to find suitable Airy's stress functions was pointed out.

Nouri and Gay (1994) present the finite element procedure to compute shear stresses in a multilayered beam with orthotropic material layers under torsion [128]. The solution of two-dimensional partial differential equations yields the warping functions in the cross section domain. Further the torsion center is determined. Rand (1998) also investigated on shear stresses of unidirectional laminated composite beams under torsion [140]. His model includes the complete description of the warping from which the local interlaminar shear stresses can be determined. Klinkel and Govindjee (2003) extend this approch for anisotropic problem [95].

Mokos and Sapountzakis (2005) presented a method in order to determine the transverse and torsional shear stresses in a multilayered composite beam with arbitrary cross section [121]. They assumed linear elastic material properties. Boundary value problems of acting stress functions in the cross sections are solved by the boundary element method. Additionally, they obtained the shear center and the shear correction factors were directly calculated from these stress functions. Kourtis et al. (2009) presented a method for the computation of torsional and transverse shear stresses in arbitrary cross sections of prismatic beams [96]. They incorporated inhomogeneous material properties for isotropic elasticity and transversal isotropic elasticity in their method, respectively. Santoro (2011) [149] introduced a method for solving a Saint-Venant torsional and torsionless bending problem for orthotropic beams using the line element-less method (LEM).

1.2.2 Rotordynamics

Rankine was the first to publish a work concentrated on rotordynamics in 1869 [141]. He investigated the relation between centrifugal and restoring forces. Rankine figured out that a rotating flexible beam will get into a rotational speed at which the displacement amplitudes are increasing significantly. This speed is called the critical speed by other authors. However, he made a wrong conclusion with the statement that no stable running is possible for speeds higher than the critical speed. This was disproved later.

Further experimental and analytical investigations on the more complex shafts were done by Greenhill (1883) [60] and Dunkerley (1894) [38]. Dunkerley found natural eigenfrequencies of rotating shafts, he called them critical speeds. Further, he investigated continuous shafts with different geometries and boundary conditions.

Dunkerley introduced a rational numerical method for the computation of the lowest eigenfrequency of compound shafts.

At the end of the nineteenth century the development of steam turbines was pushed. These turbines operate with speeds which are far higher than common rotational speeds of mechanical applications at that time. Gustaf Patrick de Laval had to solve rotordynamical problems occurring in development of steam turbines. Föppl (1895) carried out fundamental investigations on the flexible one-mass rotor introduced by Laval [44]. He solved the whirling problem analytically and recognized the self-centering effect above the critical speed. Chree (1904) captured the numerical method of Dunkerley and took gyroscopic forces into account [27]. Morley (1909) computed critical speeds of compound rotors approximately and considered Rayleigh's correction for the rotatory inertia [122]. Stodola (1910) introduced a graphical procedure for the prediction of critical speeds [165]. In 1916, Stodola investigated the damping effect of an unbalanced rotor operating with critical speed in a fluid. He observed the decrease of the critical speed due to the damping [166]. Prandtl (1918) [137] transformed the equation of motion in a rotating coordinate system and obtained the critical speed due to the rotor's mass.

Jeffcott (1919) extended Föppl's investigations with damping and discussed the vibration amplitude at the critical speed [80]. The flexible one-mass rotor is widely known as the Jeffcott rotor. However, in German-speaking countries the Laval rotor became well known. The name was given by Föppl after its inventor. With the simple model of the Jeffcott rotor it is possible to explain the most important rotordynamical effects. The unstable behavior of a rotor in the subcritical speed range can be shown as well as the self-centering effect in the supercritical speed range. Further, the dependency of the rotor's eigenfrequencies on the rotational speed can be figured out and different damping effects can be investigated.

In 1924, Campbell investigated the vibrations of steam turbines [22]. He developed a diagram for the representation of critical speeds in relation to the cross points of the natural eigenfrequencies and straight lines proportional to the rotational speed. This diagram is known as the Campbell diagram.

In the same year, Newkirk (1924) investigated the shaft movements in unstable conditions due to different effects, e.g. friction, internal damping, bearings and flexible pedestals [125]. Kimball (1924, 1925) presented analytical and experimental results of internal and interface damped rotors [94] [93]. He observed that internal and interface damping cause instabilities for rotors with supercritical speeds. Both authors recognized that friction causes self-excited vibrations.

The influence of fluid bearings has been investigated by many authors. The first work regarding this topic was done by Stodola in 1916 [166]. Newkirk and Tayler (1925) presented the oil whip phenomena which is an instability due to the oil motion in the bearing clearance [126]. Robertson (1933) was the first to impose the Reynold's equation to the equation of motion of a rotating shaft [144]. Further works followed, e.g. Haag and Sankey (1958) [68] or Sternlicht (1959) [164].

In 1927, Stodola investigated the vibration of shafts with different stiffnesses in two perpendicular lateral directions [167]. Soderberg (1932) [157] identified unstable regions in subcritical speed range due to different stiffness in two perpendicular lateral directions for horizontal shafts loaded with gravity forces. The vibrations of asymmetric shafts become unstable at various rotational speeds. Taylor (1940) [172], Foote et al. (1943) [43], Brosens and Carndall (1961) [20] and Dimentberg (1959) [34] published further investigations on this problem.

The unbalance response and the balancing of continuous rotors were investigated in a series of papers by Bishop (1959) [15], Bishop and Gladwell (1959) [16] and Bishop and Parkinson (1965) [17]. Eshleman and Eubanks (1969) [41] developed a more detailed method for the investigation of unbalance response. They considered the effects of shear deformation, rotary inertia and gyroscopic moment.

Rotors with various cross sections along the shaft were first investigated by Frahm in 1902 [45]. Holzer (1907) picked up Frahm's method and created a tabular form for the calculation of the shaft vibrations [77]. Gümbel (1912) [63] and Tolle (1921)[182] revised Holzer's developed tabular form. An extension to the Holzer-Guembel-Tolle (HGT) method with lateral vibrations of lumped mass beams was introduced by van den Dungen (1928) [37]. Hohenemser and Prager (1933) [74] extended the HGT method for continuous but discretized beams.

The work of Myklestad (1944) and Prohl (1945) is essentially identical to the work of van den Dungen [124],[139]. Thomson (1950) wrote van den Dungen's method in a matrix form [176]. This approach is called the transfer matrix method.

Ruhl and Booker (1972) applied the finite element method on a rotor system [146]. Meirovitch (1974) [115] introduced an approach for the computation of the critical speed of discretized rotors. Nelson and McVaugh (1976) considered the rotary inertia, the gyroscopic moment and axial forces in their finite element approach.

1.2.3 Rotor vibrations in electrical machines

Walker et al. (1964) [190] investigated the relation between axial deflection and axial pressure of laminated structures in different tests. They took the mechanism of compression into account and included an example of a large hydroelectric generator. Garvey (1989) focused on the vibrational behavior of laminated components in an electrical machine [50]. He carried out vibrational experiments for different pressures on the laminated components and determined the moduli of shear and compression. In recent years material parameters for homogenized finite element models have been achieved by various optimization strategies. Mogenier et al. (2010) [119] set up a homogenized model of an electrical machine's rotor. For the optimization the modal error functions are used in a minimization functional. In a further paper [118] Mogenier et al. (2010) determined the minimization functional by a hybrid Rayleigh quotient in combination with the Guyan method. The optimization was carried out with the Levenberg-Marquardt algorithm. Van der Giet et al. (2012)

[57] compared different experimental methods for the determination of the material parameters of homogenized laminations. A test with static load on the laminated sheets, an ultrasonic measurement and a modal analysis was carried out. They pointed out the problem of the linearization of laminated components. Pirnat et al. [135] did modal tests on laminated sheets with different prestresses. In a static test, they determined contact stiffnesses. These results were validated by a model finite element simulation including nonlinear contact stiffnesses.

Modal properties are significant parameters for the design of a rotor in an electrical machine. Various papers have been presented on this topic. Ede et al. (2002) examined the rotor resonances of high-speed permanent-magnet brushless machines [39]. They numerically and experimentally investigated the influence of the geometrical length on the rotor's modal behavior. The stiffening effect of the laminated core on the flexible rotor shaft was investigated by Garvey et al. (2004) [51]. They contrasted the modal behavior of the rotor including the laminated core stiffness with the modal behavior of the rotor without laminated core stiffness. Garvey et al. performed numerical and experimental tests on a rotor in an electrical machine and showed a significant influence of the core stack's stiffness on the rotordynamics. The influence of the lamination pressure upon the rotor stiffness was investigated by Kim and Kim (2006) [92]. They analyzed the relation between lamination pressure and rotor eigenfrequencies. Singhal et al. (2011) [156] did numerical and experimental investigations on a large high speed induction motor. The core stiffness and its influence on the vibrations were studied. Mogenier et al. (2011) [120] investigated nonlinear centrifugal effects of tie rods in bores getting in contact. Werner (2011) [195] introduced a method of rigid balancing for large flexible induction rotors which run close below or above the first bending critical speed.

Bearings are important components in the electrical machine, as it has a significant influence on the rotor vibrations. Lim and Singh (1990) [101] introduced a mathematical model of roller bearings. They formulated a comprehensive nonlinear bearing stiffness matrix depending on the contact angle. In a further paper [102] the influence of the roller bearing on rotor vibrations was investigated. Further, the stability of the system was examined by the Liapunov's stability method. A validation with experimental results was done. Royston and Basdogan (1998) [145] introduced a model for the computation of direct and cross-coupling stiffness coefficients of spherical rolling element bearings. They focused on double row spherical ball bearings and pointed out the influence of the cross-coupling stiffness coefficients in axial and radial combined preloaded bearings. Lee and Lee (1999) [100] analyzed a misaligned rotor-ball bearing systems. The effect is considered by reaction loads and deformations at the bearings. The results agree well with experiments. Alfares and Elsharkawy (2003) [4] investigated the effect of axial preloaded ball bearings numerically. They used different materials and applied forces depended on the ware rate. The resulting vibrations were compared to each other. Čermelj and Boltežar (2004) [186] investigated the dynamical behavior of the ball bearing. The dynamics of three-dimensional finite element model were determined in frequency domain

and experiments were carried out. A perturbation method, including frequency response sensitivities, in combination with a correlation analysis updates the simulation model. Gunduz et al. (2012) [64] investigated preloaded ball bearings in a shaft-bearing assembly. A simulation model for the bearing vibrations was set up. Further experiments with various preloads on the investigated system were done. A stiffness matrix calculation for rolling bearing elements was carried out by Guo and Parker (2012) [66]. They set up a full three-dimensional finite element model and formulated a mechanical contact for the roller bearing. From the finite element solution a full bearing stiffness matrix was obtained.

Holmes (1960) [75] examined a stability of a rigid rotor in two journal bearings. Based on Reynold's equations linear stiffness and damping coefficients were achieved. Lund and Saibel (1967) [109] worked on the oil whip phenomena of sleeve bearings which causes self-excited vibrations of a rotor. They computed the whirl orbits using an averaging method and found that the oil whip phenomena occurs only near the unstable regions of the static equilibrium. In 1968 Lund introduced a method for the computation of linearized stiffness and damping coefficients for gas bearings [106]. These coefficients depend on the static load, the rotational speed and the whirling frequency. Lund (1974) [108] investigated the stability and damped critical speeds of a rotor supported by fluid-film bearings. He modeled a flexible rotor using the transfer matrix approach and considered the bearings by linearized stiffness and damping coefficients. Over the years papers have presented different methods for the computation of journal bearing's stiffness and damping properties. Further papers deal with this topic, e.g. [132], [107], [26], [2], [3] and [181].

Jordan et al. (1981) [81] investigated the influence of pole pairs on the unbalance magnetic pull. They used Maxwell's equations for the formulation of the electromagnetical forces. Früchtenicht et al. investigated the stability of rotors in induction machines [48]. Imposing the unbalance magnetic pull to the equation of motion of a rigid rotor, they achieved linear stiffness and damping coefficients. In these coefficients the effect of the unbalanced magnetic pull is included. In a second paper they imposed the theoretical model on an industrial application and validated their results by experiments [49]. Belmans (1987) [14] investigated the stability of a rotor loaded with unbalanced magnetic pull. The investigated rotor was considered as a Jeffcott rotor model. DeBortoli et al. (1993) presented a new model for the calculation of the unbalanced magnetic pull [33]. They considered the side effect of parallel windings in their formulation. Dorrell et al. (1997) [36] analysed the influence of the static and dynamic air gap eccentricity on the unbalanced magnetic pull. Ha and Hong (2001) [67] coupled the electromagnetics with a mechanical finite element model. They solved the problem by a time stepping procedure. In each time step, first the electromagnetical forces are calculated. Afterwards these forces are applied to the mechanical model. Ha and Hong analyzed the dynamic response of a switched reluctance rotor. Holopainen (2002) [76] examined the instability of a rotor system due to unbalanced magnetic pull on the Jeffcott rotor model. Guo et al. [65] followed Holopainen's approach and solved the system in the time domain. Werner

(2010) [196] used the same approach in order to investigate the shaft vibrations of a two-pole induction machine. Additionally, he considered a bearing model in the Jeffcott rotor model. Pennacchi (2009) [133] investigated nonlinear effects due to electromagnetical forces in generators with smooth poles. Pennacchi coupled the computation of the unbalanced magnetic pull and the electrodynamical solution iterative. Mair et al. (2015) [112] followed this approach including journal bearings in the structure mechanical model.

1.3 Outline of this work

After the current introduction, Chapter 2 treats the theoretical background of beam modeling, rotordynamics and the computation of electromagnetic forces from the theoretical formulation to the fundamental equation of each topic.

Chapter 3 is concerned with the formulation of the Timoshenko beam element. First, the fundamentals of the Timoshenko beam theory are described. Based on a variational formulation of the Timoshenko beam, the discretization of the displacement and strain field is carried out and the finite element formulation of the weak form is presented. The shape functions are determined based on the Timoshenko beam theory.

In Chapter 4, shear stresses in an arbitrary cross section of a prismatic beam are determined. First, the St. Venant torsion problem is solved. Afterwards, the solution of the torsionless bending problem is obtained, based on the solution of the St. Venant torsion. The resulting shear stresses are used to calculate the shear coefficients. These computations are based on linear elastic material with isotropic properties.

The formulation of composite beam elements is carried out in Chapter 5. A variational formulation of the composite beam is derived in order to discretize the displacement and strain field. A linear elastic material with orthotropic properties is assumed. Using the procedure in Chapter 4, shear stresses and shear coefficients are determined

In Chapter 6 the rotor of an induction machine is modeled using Timoshenko beam elements and composite beam elements. The mechanical model includes side effects like gyroscopic or spin softening. Further, structural damping is included. The modal results from experimental investigations are presented in this chapter. In order to validate the numeric model a numerical modal analysis is carried out and compared to the experimental data. Furthermore, a transient run up simulation of the rotor in the electrical machine is done. For this case, nonlinear bearing properties are considered and the unbalanced magnetic pull is neglected.

Chapter 7 presents the results of a detailed investigation of the bearing nonlinearities. A simple rotor model with less degrees of freedom and properties similar to those

in Chapter 6 is introduced. The model also uses the same bearing stiffnesses as in Chapter 6. A transient run up and run down simulation is presented and the rotor vibrations for different rotational speeds are investigated. These results are described in detail. The influence of different parameters on the rotor vibrations is studied.

The influence of the unbalanced magnetic pull is investigated in Chapter 8. A model of a two-pole induction machine is introduced and the analytical formulation of the unbalanced magnetic pull is presented. Therefore, the definition of the air gap rotor and stator is given. The formulation of permeance wave and the magnetic flux density follow and the determination of the force components is presented using Maxwell's stress tensor. Finally, results from a transient simulation of the rotor in an electromagnetic field are shown.

The final Chapter 9 summarizes the results. The outcome of this work is discussed.

CHAPTER 2

Fundamentals

The modeling and the simulation of nonlinear rotordynamical effects require fundamental mechanical and electrical knowledge. In this chapter, basics of the structural mechanics are elaborated. These include the kinematics and the kinetics of the structural problem. Further, the governing equations are formulated in the weak form and the equations of motion of a rotordynamical system are explained. Rotordynamical aspects, e.g. gyroscopic forces or spin softening, are examined. Finally, basics about electromagnetical forces are mentioned.

2.1 Structural mechanics

The analysis of most elastodynamical problems is based on the finite element method. A continuum mechanical formulation of the problem is necessary which includes the kinematics and kinetics of the problem.

2.1.1 Elastodynamic equilibrium

The kinematics in the field of continuum mechanics describes the motions, deformations and strains of a body and the corresponding time derivatives. Various kinematic quantities deliver the basis for the mechanical principles' formulation.

2.1.1.1 Deformation gradient and strains

The motion of a body B is noted in the euclidian space $\mathbb{E}^3$. The position of the body B is defined by the configuration $\varphi(B)$, where $\varphi(B) = \{\varphi(X) \| X \in B\}$. The position $\boldsymbol{X}$ of a particle P defines the reference configuration, compare Figure 2.1. A general configuration of the particle's position $\boldsymbol{x}$ is obtained from the transformation

$$\boldsymbol{x} = \varphi(\boldsymbol{X},t) \ , \tag{2.1}$$

where t is the time.

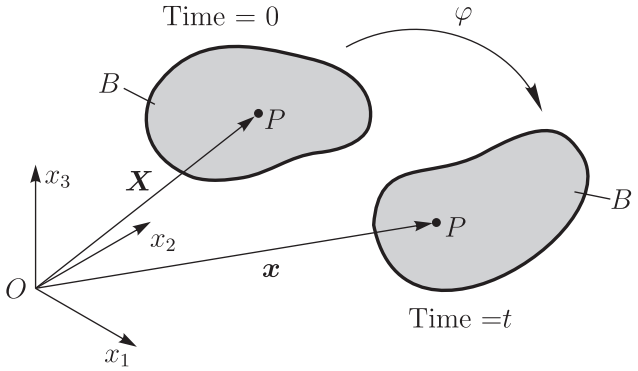

Figure 2.1: General motion of a deformable body

Mathematically, the deformation of the body B is described by the deformation gradient $\boldsymbol{\mathcal{F}}$. The deformation gradient is obtained from $\boldsymbol{\mathcal{F}} = {}^{\partial \boldsymbol{x}}/_{\partial \boldsymbol{X}}$ and

$$\boldsymbol{\mathcal{F}} = \frac{\partial \varphi(\boldsymbol{X},t)}{\partial \boldsymbol{X}} = \boldsymbol{\nabla}\varphi(\boldsymbol{X},t) = \mathcal{F}_{ij}\ \boldsymbol{e}_i \otimes \boldsymbol{E}_j = \frac{\partial x_i}{\partial X_j}\boldsymbol{e}_i \otimes \boldsymbol{E}_j\ , \tag{2.2}$$

follows in component notation with $i,j = 1,2,3$. In matrix notation the deformation gradient is written as

$$\boldsymbol{\mathcal{F}} = \begin{bmatrix} x_{1,1} & x_{1,2} & x_{1,3} \\ x_{2,1} & x_{2,2} & x_{2,3} \\ x_{3,1} & x_{3,2} & x_{3,3} \end{bmatrix}\ . \tag{2.3}$$

The inverse of the deformation gradient is denoted by

$$\boldsymbol{\mathcal{F}}^{-1} = \frac{\partial \boldsymbol{X}}{\partial \boldsymbol{x}} = \boldsymbol{\nabla}\varphi^{-1}(\boldsymbol{X},t) = (\mathcal{F}^{-1})_{ij}\ \boldsymbol{E}_j \otimes \boldsymbol{e}_i = \frac{\partial X_j}{\partial x_i}\boldsymbol{E}_j \otimes \boldsymbol{e}_i\ . \tag{2.4}$$

Noting that the displacement vector of a particle P is defined as $\boldsymbol{u}(\boldsymbol{X},t) = \varphi(\boldsymbol{X},t) - \boldsymbol{X}$ [18], [197]. Imposing this relation onto the equation (2.2) and introducing a displacement gradient $\boldsymbol{\Delta\mathcal{F}} = {}^{\partial \boldsymbol{u}}/_{\partial \boldsymbol{X}}$ the deformation gradient is rewritten as

$$\boldsymbol{\mathcal{F}} = \boldsymbol{\nabla}(\boldsymbol{X} + \boldsymbol{u}(\boldsymbol{X},t)) = \boldsymbol{1} + \boldsymbol{\nabla}\boldsymbol{u} = \boldsymbol{1} + \boldsymbol{\Delta\mathcal{F}}\ . \tag{2.5}$$

During the deformation process the deformation gradient must not become singular. Consequently, the Jacobian J has to be unequal zero

$$J = \det \boldsymbol{\mathcal{F}} \neq 0\ . \tag{2.6}$$

The deformation of the body B causes a volume change. This volume change is founded in terms of the Jacobian J as

$$dv = J\ dV\ , \tag{2.7}$$

where dv is the infinitesimally small volume of the deformed body and dV is the infinitesimally small volume of the undeformed body[18].

The scalar product of the vectors $d\boldsymbol{x}_1 \cdot d\boldsymbol{x}_2$ can be noted in terms of $d\boldsymbol{X}_1$ and $d\boldsymbol{X}_2$ by

$$d\boldsymbol{x}_1 d\boldsymbol{x}_2 = d\boldsymbol{X}_1 \, \boldsymbol{C} \, d\boldsymbol{X}_2 \ , \tag{2.8}$$

where $\boldsymbol{C} = \boldsymbol{\mathcal{F}}^T \boldsymbol{\mathcal{F}}$ is the right Cauchy-Green deformation tensor. The left Cauchy-Green deformation tensor $\boldsymbol{b} = \boldsymbol{\mathcal{F}} \boldsymbol{\mathcal{F}}^T$ is obtained from

$$d\boldsymbol{X}_1 \, d\boldsymbol{X}_2 = d\boldsymbol{x}_1 \, \boldsymbol{b}^{-1} \, d\boldsymbol{x}_2 \ . \tag{2.9}$$

Based on the reference configuration, the Green-Lagrangian strain tensor $\boldsymbol{E}$ is introduced by

$$\boldsymbol{E} = \frac{1}{2}(\boldsymbol{\mathcal{F}}^T \boldsymbol{\mathcal{F}} - 1) = \frac{1}{2}(\boldsymbol{C} - 1) \ . \tag{2.10}$$

Imposing equation (2.5) on the relation above, the Green-Lagrangian strain tensor $\boldsymbol{E}$ can be rewritten as

$$\boldsymbol{E} = \frac{1}{2}(\boldsymbol{\Delta\mathcal{F}} + \boldsymbol{\Delta\mathcal{F}}^T + \boldsymbol{\Delta\mathcal{F}}^T \boldsymbol{\Delta\mathcal{F}}) \ . \tag{2.11}$$

Assuming a small displacement gradient $\boldsymbol{\Delta\mathcal{F}} \ll 1$, a linear strain tensor $\boldsymbol{\varepsilon}$ is derived by

$$\boldsymbol{\varepsilon} = \frac{1}{2}(\boldsymbol{\Delta\mathcal{F}} + \boldsymbol{\Delta\mathcal{F}}^T) = \frac{1}{2} \left(u_{i,j} + u_{j,i}\right) \boldsymbol{E}_i \otimes \boldsymbol{E}_j \ . \tag{2.12}$$

2.1.1.2 Cauchy Stresses and equilibrium

Studying the translational equilibrium of an elemental tetrahedron, shown in Figure 2.2, the relation between the traction $\boldsymbol{\tau}$, referred to a general direction $\boldsymbol{n}$, and the reacting stresses $\boldsymbol{\tau}_i$ are determined. The formulation of the equilibrium on the

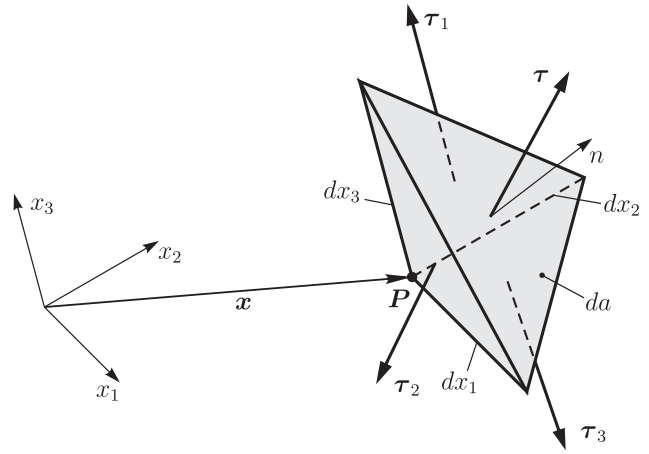

Figure 2.2: Elemental tetrahedron

elemental tetrahedron delivers

$$\boldsymbol{\tau} = \sum_{j=1}^{3} \boldsymbol{\tau}_j \frac{da_j}{da} = \sum_{j=1}^{3} \boldsymbol{\tau}_j (\boldsymbol{n} \cdot \boldsymbol{e}_j) \ . \tag{2.13}$$

The infinitesimally small area da is projected onto the orthogonal planes of the cartesian coordinate system with [171]

$$da_j = (\boldsymbol{n} \cdot \boldsymbol{e}_j) \ da \ . \tag{2.14}$$

A further mathematical simplification yields

$$\boldsymbol{\tau} = \sum_{i,j=1}^{3} \sigma_{ij} (\boldsymbol{e}_j \cdot \boldsymbol{n}) \boldsymbol{e}_i = \sum_{i,j=1}^{3} \sigma_{ij} (\boldsymbol{e}_j \otimes \boldsymbol{e}_i) \boldsymbol{n} \ , \tag{2.15}$$

where σ_{ij} are elements of the Cauchy stresses. These are summarized in the Cauchy stress tensor $\boldsymbol{\tau}$. The equation (2.15) can be formulated in the matrix notation as

$$\boldsymbol{\tau} = \boldsymbol{\sigma} \boldsymbol{n} \ . \tag{2.16}$$

An elemental hexahedron of a deformable body is depicted in Figure 2.3. In this figure the acting stress components σ_{ij}, the body force vectors $\boldsymbol{f}^B$ and the acceleration vectors $\ddot{\boldsymbol{u}}$ are shown. The translational equilibrium on the elemental hexahedron is noted by

$$\int_v \left(\boldsymbol{\nabla} \boldsymbol{\sigma} + \boldsymbol{f}^B - \varrho \ddot{\boldsymbol{u}} \right) \ dv = 0 \ , \tag{2.17}$$

where ρ is the density and $\boldsymbol{\sigma}$ is a stress tensor. Due to the fact that the equation

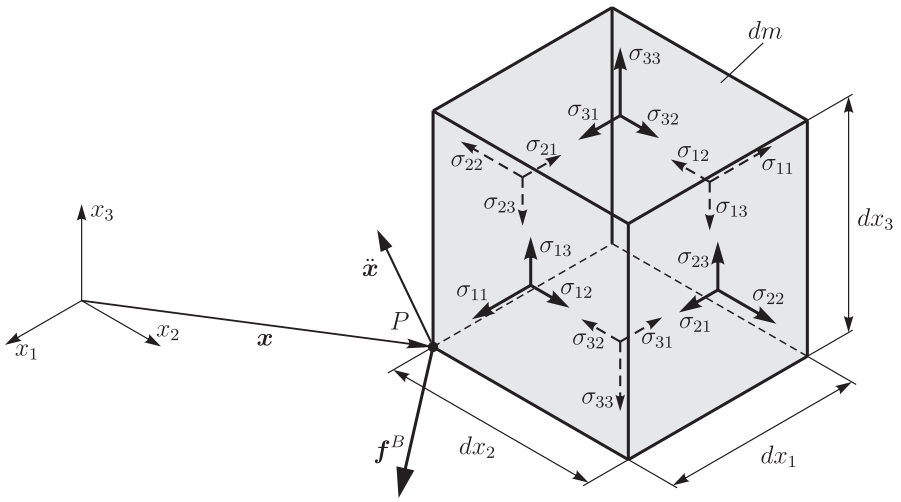

Figure 2.3: Elemental hexahedron

above can be applied to any enclosed region of a body, the integrals vanish and the equilibrium equation of a deformable body is obtained:

$$\boldsymbol{\nabla\sigma} + \boldsymbol{f}^B = \varrho\ddot{\boldsymbol{u}} \ . \tag{2.18}$$

2.1.2 Vibrations of a multi degree-of-freedom system

Based on the elastodynamical equilibrium of a body, a discretization of the weak form gives a general form of the n-dimensional equation of motion

$$\boldsymbol{M}(\boldsymbol{u},t)\ \ddot{\boldsymbol{u}} = \boldsymbol{F}(\boldsymbol{u},\dot{\boldsymbol{u}},t) \ , \tag{2.19}$$

where $\boldsymbol{M}(\boldsymbol{u},t)$ is the symmetric mass matrix with the size of $[n \times n]$. The general $[n \times 1]$ displacement vector is denoted by $\boldsymbol{u}$. The general $[n \times 1]$ force vector $\boldsymbol{F}(\boldsymbol{u},\dot{\boldsymbol{u}},t)$ contains all active forces acting in the system. Different methods are available for the discretization of continuum mechanical equations. A frequently used discretization method in the finite element analysis is the Ritz method.

Neglecting gyroscopic effects and assuming constant system matrices, the linearized equation of motion becomes

$$\boldsymbol{M}\ \ddot{\boldsymbol{u}} + \boldsymbol{D}\ \dot{\boldsymbol{u}} + \boldsymbol{K}\ \boldsymbol{u} = \boldsymbol{F} \ . \tag{2.20}$$

The symmetric $[n \times n]$ damping matrix is denoted by $\boldsymbol{D}$ and the symmetric $[n \times n]$ stiffness matrix by $\boldsymbol{K}$. The first term on the left side of the equation determines the inertia of the system. The second term considers the dissipation, which, in most cases of structural mechanics, takes the system's damping into account. The stiffness term obtains the potential forces of the system. The rest of the conservative and non-conservative forces are summarized in the force vector $\boldsymbol{F}$. [10]

The displacement vector is assumed to be harmonic

$$\boldsymbol{u} = \hat{\boldsymbol{u}}\, \mathrm{e}^{j\omega t} \ . \tag{2.21}$$

The vector $\hat{\boldsymbol{u}}$ labels the amplitude of the harmonic displacement wave which oscillates with a frequency ω. With the assumption of harmonic waves and a linear mechanical system, the force also has to confirm a harmonic oscillation [53],

$$\boldsymbol{F} = \hat{\boldsymbol{F}}\, \mathrm{e}^{j\omega t} \ . \tag{2.22}$$

Requiring an asymptotical stability of this problem's solution, the harmonic approach in equations (2.21) and (2.22) can be inserted in the linear equation of motion (2.20):

$$\left(-\Omega^2\boldsymbol{M} + j\omega\boldsymbol{D} + \boldsymbol{K}\right)\ \hat{\boldsymbol{u}} = \hat{\boldsymbol{F}} \tag{2.23}$$

The transient components vanish and the steady-state vibration results in

$$\hat{\boldsymbol{u}} = \left(-\omega^2 \boldsymbol{M} + j\omega \boldsymbol{D} + \boldsymbol{K}\right)^{-1} \hat{\boldsymbol{F}} \ . \tag{2.24}$$

The frequency response functions (FRFs) define the relation between the input and the output signals of mechanical structures. These are defined as

$$\boldsymbol{V}(\omega) = \frac{\hat{\boldsymbol{x}}}{\hat{\boldsymbol{F}}} = \left(-\omega^2 \boldsymbol{M} + j\omega \boldsymbol{D} + \boldsymbol{K}\right)^{-1} \ . \tag{2.25}$$

The matrix $\boldsymbol{V}$ contains all frequency response functions. The number of the column is equal to the node number of the excitation point and the number of the row is equal to the node number of the response point. [42]

Neglecting the damping properties, a general eigenvalue problem is formulated:

$$\boldsymbol{K}\boldsymbol{r}_i = \lambda_i \, \boldsymbol{M} \, \boldsymbol{r}_i \quad \ldots \quad \forall i = \{i \in \mathbb{Z} | 1 \leq i \leq p\}. \tag{2.26}$$

The solution of this eigenvalue problem delivers p eigenvalues λ_i with p corresponding eigenvectors $\boldsymbol{r}_i$. The number of extract eigenvalues p depends on the investigated frequency range of the used numerical solver. For a damped system, the equation of motion (2.20) must be transformed into a differential equation of first order

$$\begin{bmatrix} \boldsymbol{M} & \boldsymbol{0} \\ \boldsymbol{0} & -\boldsymbol{I} \end{bmatrix} \begin{bmatrix} \ddot{\boldsymbol{x}} \\ \dot{\boldsymbol{x}} \end{bmatrix} + \begin{bmatrix} \boldsymbol{D} & \boldsymbol{K} \\ \boldsymbol{I} & \boldsymbol{0} \end{bmatrix} \begin{bmatrix} \dot{\boldsymbol{u}} \\ \boldsymbol{u} \end{bmatrix} = \begin{bmatrix} \boldsymbol{F} \\ \boldsymbol{0} \end{bmatrix} \ . \tag{2.27}$$

The eigenvalue problem of the system

$$\left(\begin{bmatrix} \boldsymbol{D} & \boldsymbol{K} \\ \boldsymbol{I} & \boldsymbol{0} \end{bmatrix} + \lambda \begin{bmatrix} \boldsymbol{M} & \boldsymbol{0} \\ \boldsymbol{0} & -\boldsymbol{I} \end{bmatrix} \right) \boldsymbol{r} = \boldsymbol{0} \tag{2.28}$$

delivers complex eigenvectors and eigenvalues. [10]

2.2 Rotordynamics

The rotordynamics reveals many different phenomena. Several effects can be explained by the spin of the rotor. The classical Jeffcott rotor [44], [80] is a simple model to explain most of these effects.

2.2.1 The Jeffcott rotor

The Jeffcott rotor model consists of an elastic massless shaft. The shaft is connected to a disc of mass m. The bearings are assumed to be rigid and the damping is neglected. These assumptions are acceptable for rotors with roller bearings. Figure 2.4 depicts the Jeffcott rotor model.

The rotor shaft axis coincides with the x-axis of the introduced cartesian coordinate system. The origin O of the cartesian coordinate system is in the disc's midplane. In the undeformed case, the position of the origin O and the disc's midpoint M are identical. The center of gravity C is defined by an eccentricity $\boldsymbol{e}$. The eccentricity of the rotor is defined by the unbalance quality. The motion of the disc in the yz-plane has three degrees of freedom, two translational deflections, u_y and u_z, and one rotational deflection φ_x. The angle φ_x is rotating about the x-axis. Figure

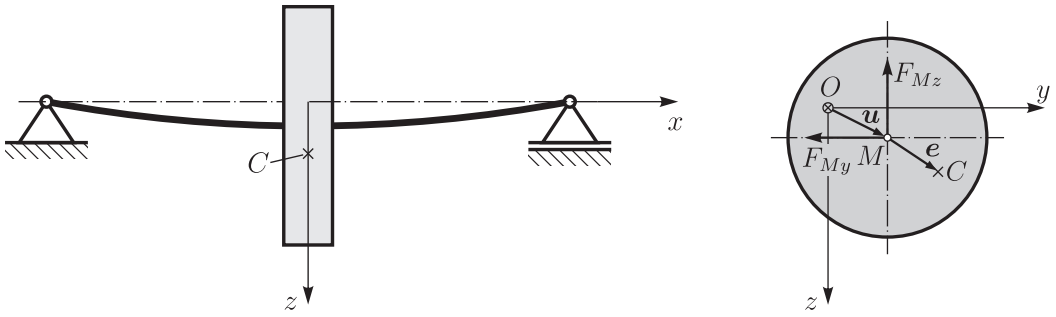

(a) Jeffcott rotor model in xz-plane

(b) Free body diagram of disc in yz-plane

Figure 2.4: Jeffcott rotor model

2.4b shows a free body diagram of the disc. Restoring forces $F_{My} = c\ u_y$ and $F_{Mz} = c\ u_z$ act in the midpoint M. For a steady-state operation ($\dot{\varphi}_x = \Omega = const.$ and $\varphi_x = \Omega t + \gamma$), the equation of motion for the Jeffcott rotor is given by

$$\ddot{\boldsymbol{u}} + \omega^2 \boldsymbol{u} = |\boldsymbol{e}|\Omega^2 \begin{bmatrix} \cos(\Omega t + \gamma) \\ \sin(\Omega t + \gamma) \end{bmatrix} , \tag{2.29}$$

where γ is an integration constant [52]. The rotor eigenfrequency ω is defined by

$$\omega = \sqrt{\frac{c}{m}} . \tag{2.30}$$

The shaft stiffness is denoted by c and the rotor mass by m.

In case of rotor balance ($|\boldsymbol{e}| = 0$), the homogeneous part of the differential equation (2.29) determines the solution

$$u_{hy}(t) = u_{y0} \cos(\omega t + \zeta_y) \qquad \text{and} \qquad u_{hz}(t) = u_{z0} \cos(\omega t + \zeta_z) . \tag{2.31}$$

The initial deflections u_{y0} and u_{z0} determine the amplitude, and the angles ζ_y and ζ_z the phase of the rotor bending vibration.

The unbalance excited rotor vibrations are influenced by the inhomogeneous part of the differential equation (2.29),

$$u_{iy}(t) = |\boldsymbol{e}|\frac{\Omega^2}{\omega^2 - \Omega^2}\cos(\Omega t + \gamma) \qquad \text{and} \qquad u_{iz}(t) = |\boldsymbol{e}|\frac{\Omega^2}{\omega^2 - \Omega^2}\sin(\Omega t + \gamma)\ . \tag{2.32}$$

The homogeneous part vanishes for steady-state vibrations and the inhomogeneous part determines the rotor vibrations. The midpoint M of the disc rotates harmonically in a circle with a constant radius r_M about the origin O. The amplitude depends on the eccentricity ϵ and the rotational speed Ω. A rotational speed Ω, which is equal to the rotor eigenfrequency ω, results in a singularity. The speed range lower than the eigenfrequency is called subcritical and the higher is called supercritical.

The motion of the center of gravity results in

$$u_{cy} = |\boldsymbol{e}|\frac{\omega^2}{\omega^2 - \Omega^2}\cos(\Omega t + \gamma) \qquad \text{and} \qquad u_{cz} = |\boldsymbol{e}|\frac{\omega^2}{\omega^2 - \Omega^2}\sin(\Omega t + \gamma)\ . \tag{2.33}$$

The center of gravity oscillates also on a circle with the radius r_C. For subcritical speed $\Omega < \omega$ the term $\omega^2/(\omega^2 - \Omega^2)$ becomes a positive value and the center of gravity is located outside the orbit ($r_C > r_M$), shown in Figure 2.5a. The center of gravity abruptly folds inside ($r_C < r_M$) when increasing the rotational speed above the critical speed ($\Omega > \omega$), compare Figure 2.5c. The denominator of the term $\omega^2/(\omega^2 - \Omega^2)$ becomes negative. If the rotational speed is increased further, a self-centering effect on the rotor occurs. In the special case of critical speed ($\Omega = \omega$), the center of gravity is folded forward 90°, compare Figure 2.5b. The orbit of the center of gravity C and the orbit of the midpoint M are identical for the critical speed. [54]

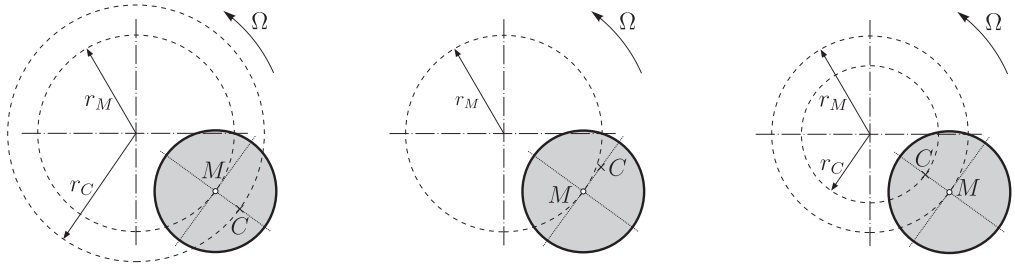

(a) Orbit of subcritical speed $\Omega < \omega$

(b) Orbit of critical speed $\Omega = \omega$

(c) Orbit of supercritical speed $\Omega > \omega$

Figure 2.5: Orientation of center of gravity depending on rotor speed for undamped Jeffcott rotors

2.2.2 Internal and external damping

In the previous section, damping effects were neglected. Generally, two types of damping exist, the internal and external damping. The internal damping reduces the rotor vibrations in the subcritical and excites the rotor vibrations in the supercritical speed range. The external damping acts in the entire speed range. [52]

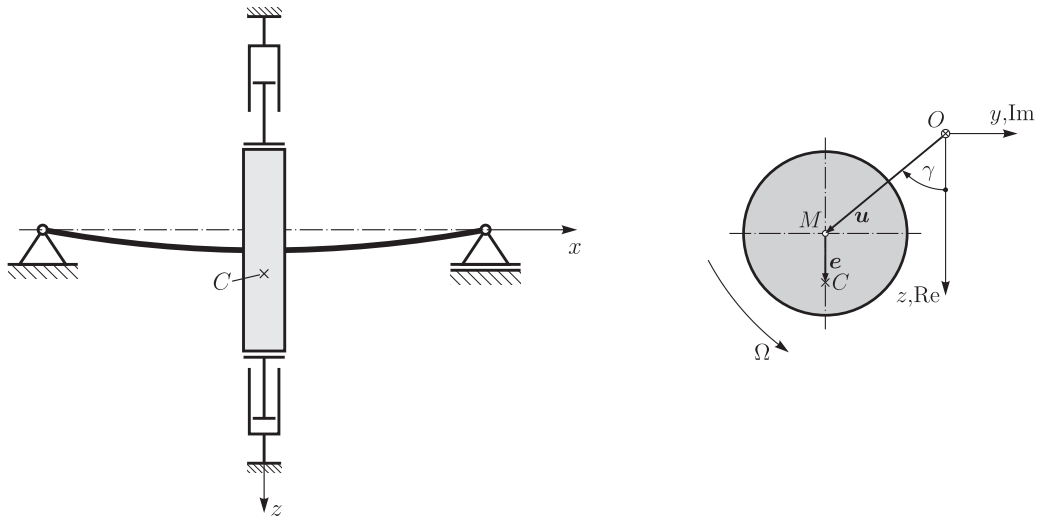

(a) External damped Jeffcott rotor model in xz-plane

(b) Rotor position in yz-plane of external damped Jeffcott rotor

Figure 2.6: External damped Jeffcott rotor model

Figure 2.6 shows an externally damped Jeffcott rotor. Introducing complex coordinates $u = u_z + ju_y$, the corresponding equation of motion is

$$\ddot{u} + \frac{d_e}{m}\dot{u} + \omega^2 u = |\boldsymbol{e}|\Omega^2 \, \mathrm{e}^{j(\Omega t+\beta)} \ , \tag{2.34}$$

where d_e is the external damping coefficient. The solution for the homogeneous part of this differential equation is given by

$$u_h(t) = \hat{u}_{ha} \, \mathrm{e}^{(\alpha+j\omega_d)t} + \hat{u}_{hb} \, \mathrm{e}^{(\alpha-j\omega_d)t} \ . \tag{2.35}$$

The coefficient α is equal to $-{}^{d_e}/_{(2m)}$ and determines the decay of the homogeneous solution. The coefficient ω_d labels the damped eigenfrequency of the homogeneous system and is defined by $\omega_d = \omega\sqrt{1 - ({}^{d_e}/_{2m\omega})^2}$. The solution of the inhomogeneous part is given by

$$u_i(t) = |\boldsymbol{e}| \frac{\Omega^2}{(\omega^2 - \Omega^2) + j\Omega\frac{d_e}{m}} \, \mathrm{e}^{j(\Omega t+\beta)} \ . \tag{2.36}$$

The steady-state system has a negative imaginary part of the solution

$$u_i(t) = |\boldsymbol{e}| \frac{\Omega^2 \left((\omega^2 - \Omega^2) - j\Omega \frac{d_e}{m} \right)}{(\omega^2 - \Omega^2)^2 + \Omega^2 \frac{d_e^2}{m^2}} \, \mathrm{e}^{j(\Omega t + \beta)} \ , \tag{2.37}$$

which results in a phase delay of the rotor's motion, shown in Figure 2.6b.

The external damping is proportional to velocities which are related to an external fixed coordinate system. In contrast, the internal damping occurs due to damping effects of the structure. Thus, the internal damping coefficients are proportional to velocities which are related to a body-fixed coordinate system, which rotates like the rotor with a rotational speed Ω.

The equation of motion for the internal damped Jeffcott rotor is given by

$$\ddot{\eta} + \left(2j\Omega + \frac{d_i}{m} \right) \dot{\eta} + \left(\omega^2 - \Omega^2 \right) \eta = |\boldsymbol{\epsilon}| \Omega^2 \, \mathrm{e}^{\beta} \ , \tag{2.38}$$

where d_i is a internal damping coefficient. The body-fixed coordinates are summarized in the complex coordinate $\eta = u'_z + j u'_y$. The homogeneous part of the solution follows:

$$\eta_h(t) = \hat{\eta}_{ha} \, \mathrm{e}^{\lambda_a t} + \hat{\eta}_{hb} \, \mathrm{e}^{\lambda_b t} \ . \tag{2.39}$$

The eigenvalues result in

$$\lambda_{a,b} = - \left(j\Omega + \frac{d_i}{2m} \right) \pm \sqrt{\left(j\Omega + \frac{d_i}{m} \right)^2 - (\omega^2 - \Omega^2)} \ . \tag{2.40}$$

Figure 2.7 depicts the stability diagram of the internally damped Jeffcott rotor. In this diagram the eigenvalues are plotted as a function of the rotational speed Ω. It can be seen that the eigenvalue λ_a of the system becomes unstable for supercritical rotational speeds. An increase of the external damping coefficient reduces the unstable operation range of the rotor. [52]

2.2.3 Gyroscopic effect

For the model of the Jeffcott rotor, the mass is assumed to be concentrated in a point. However, a pitch of the rotor affects bending moments during the rotation of the system. These effects are due to the mass moment of inertia of the rotor. If these mass moments are small, the Jeffcott rotor model can be applied. In order to explain the gyroscopic effect, a four degree-of-freedom model of a cantilevered rotor is introduced, shown in Figure 2.8.

The displacements of the disc are summarized in the vector

$$\boldsymbol{u} = [\ u_z \quad \varphi_y \quad u_y \quad \varphi_z \ ]^T \tag{2.41}$$

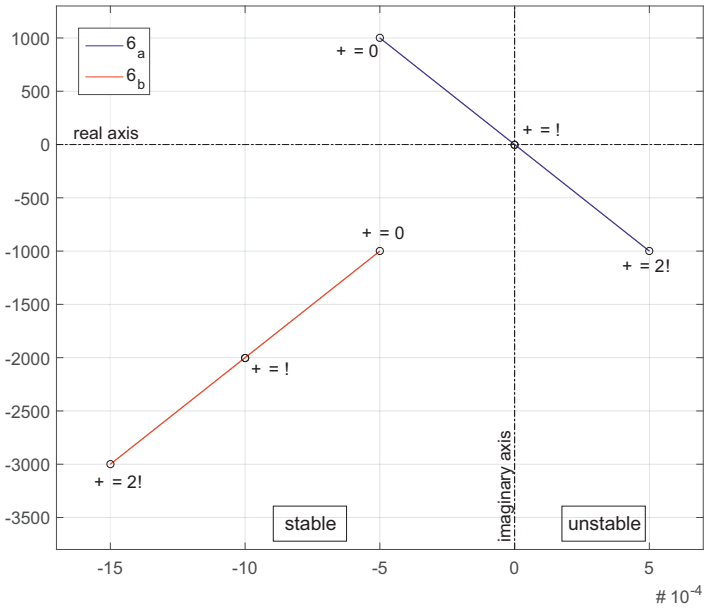

Figure 2.7: Stability diagram for internal damped Jeffcott rotor ($m = 1\,\mathrm{kg}$, $d = 0.001\,\mathrm{Ns/m}$, $c = 1 \times 10^6\,\mathrm{N/m}$)

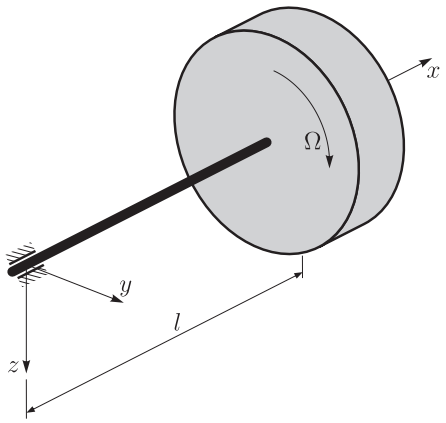

Figure 2.8: Model of a cantilevered rotor

and the stiffness matrix is given by

$$\boldsymbol{K} = \begin{bmatrix} s_{11} & s_{12} & 0 & 0 \\ s_{21} & s_{22} & 0 & 0 \\ 0 & 0 & s_{11} & -s_{12} \\ 0 & 0 & -s_{21} & s_{22} \end{bmatrix} . \tag{2.42}$$

The displacements of the xy- and xz-plane are decoupled from one another. Hence, the deviation parts of the stiffness matrix are zero.

The angular momentum of the rotor in a body-fixed cartesian coordinate system $\boldsymbol{L}$ is defined as

$$\boldsymbol{L} = \begin{bmatrix} \Theta_p & 0 & 0 \\ 0 & \Theta_a & 0 \\ 0 & 0 & \Theta_a \end{bmatrix} \begin{bmatrix} \dot{\varphi}_{xs} \\ \dot{\varphi}_{ys} \\ \dot{\varphi}_{zs} \end{bmatrix} , \tag{2.43}$$

where Θ_p is the polar mass moment of inertia about the x-axis and Θ_a is the axial mass moment of inertia. The axes of the body-fixed coordinate system are mass centroid axes. Thus, the deviation mass moments are zero. Using the assumption of small angles, the angular momentum can be transformed into the inertial coordinate system, shown in Figure 2.8,

$$L_y = \Theta_a \, \dot{\varphi}_{ys} + \Omega \, \Theta_p \, \varphi_{zs} \qquad \text{and} \qquad L_z = \Theta_a \, \dot{\varphi}_{zs} - \Omega \, \Theta_p \, \varphi_{ys} \; . \tag{2.44}$$

Using the Newton-Euler principle [131], the equation of motion

$$\begin{bmatrix} m & 0 & 0 & 0 \\ 0 & \Theta_a & 0 & 0 \\ 0 & 0 & m & 0 \\ 0 & 0 & 0 & \Theta_a \end{bmatrix} \begin{bmatrix} \ddot{u}_{zs} \\ \ddot{\varphi}_{ys} \\ \ddot{u}_{ys} \\ \ddot{\varphi}_{zs} \end{bmatrix} + \begin{bmatrix} 0 & 0 & 0 & 0 \\ 0 & 0 & 0 & \Omega\Theta_p \\ 0 & 0 & 0 & 0 \\ 0 & -\Omega\Theta_p & 0 & 0 \end{bmatrix} \begin{bmatrix} \dot{u}_{zs} \\ \dot{\varphi}_{ys} \\ \dot{u}_{ys} \\ \dot{\varphi}_{zs} \end{bmatrix} + \ldots$$
$$\ldots + \begin{bmatrix} s_{11} & s_{12} & 0 & 0 \\ s_{21} & s_{22} & 0 & 0 \\ 0 & 0 & s_{11} & -s_{12} \\ 0 & 0 & -s_{21} & s_{22} \end{bmatrix} \begin{bmatrix} u_{zs} \\ \varphi_{ys} \\ u_{ys} \\ \varphi_{zs} \end{bmatrix} = \begin{bmatrix} 0 \\ 0 \\ 0 \\ 0 \end{bmatrix} \tag{2.45}$$

is formulated. The equation of motion is rewritten as

$$\boldsymbol{M}\ddot{\boldsymbol{u}}_s + \boldsymbol{G}\dot{\boldsymbol{u}}_s + \boldsymbol{K}\boldsymbol{u}_s = \boldsymbol{0} \; , \tag{2.46}$$

in matrix notation. The mass matrix is denoted by $\boldsymbol{M}$ and has symmetric and positive definite properties. The gyroscopic matrix $\boldsymbol{G}$ is proportional to the velocity. The term $-\boldsymbol{G}\boldsymbol{u}_s$ results in conservative forces which do not contribute work. The gyroscopic matrix has skew symmetric properties, $\boldsymbol{G} = -\boldsymbol{G}^T$ [123]. The eigenvalues of this system change with the rotational speed due to the dependency of the gyroscopic matrix.

Introducing the complex coordinates

$$\eta = u_{zs} + j u_{ys} \qquad \text{and} \qquad \varphi_s = \varphi_{zs} - j\varphi_{ys} \tag{2.47}$$

in the equation of motion (2.46), the transformed system

$$\boldsymbol{M}'\ddot{\boldsymbol{u}}'_s + \boldsymbol{G}'\dot{\boldsymbol{u}}'_s + \boldsymbol{K}'\boldsymbol{u}'_s = \boldsymbol{0} \tag{2.48}$$

results. The displacement vector is now reduced to $\boldsymbol{u}' = [\ \eta \quad \varphi_s\ ]^T$ and system matrices are rewritten as

$$\boldsymbol{M}' = \begin{bmatrix} m & 0 \\ 0 & \Theta_a \end{bmatrix}, \quad \boldsymbol{G}' = \begin{bmatrix} 0 & 0 \\ 0 & -j\Omega\Theta_p \end{bmatrix} \quad \text{and} \quad \boldsymbol{K}' = \begin{bmatrix} s_{11} & s_{12} \\ s_{21} & s_{22} \end{bmatrix}. \tag{2.49}$$

The eigenvalues of this free vibrating system are determined by introducing the approach $\boldsymbol{u}_s' = \hat{\boldsymbol{u}}_s' \, \mathrm{e}^{j\omega t}$ into the equation of motion and formulating the nontrivial solution. The equation

$$\begin{aligned} &m\,\Theta_a\,\omega^4 - m\,\Theta_p\,\Omega\,\omega^3 - (s_{22}\,m + s_{11}\,\Theta_a)\,\omega^2 + \ldots \\ &s_{11}\Theta_p\,\Omega\,\omega + \left(s_{11}\,s_{22} - s_{12}^2\right) = 0 \end{aligned} \tag{2.50}$$

then yields four eigenvalues.

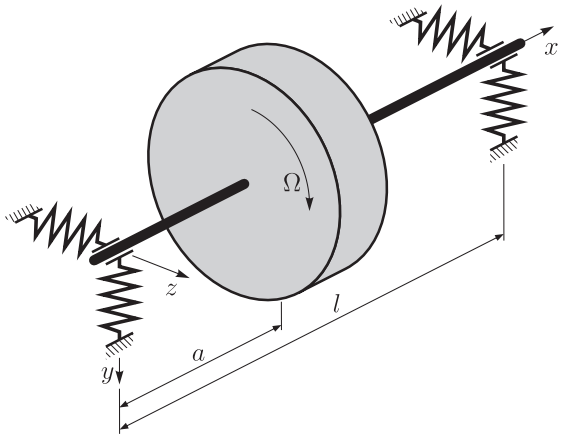

Figure 2.9: Asymmetric rigid rotor on two equal elastic supports

The four eigenfrequencies of an asymmetric rigid rotor on two elastic supports are shown in Figure 2.9. The eigenfrequencies related to the rotational speed are computed for different values of the distance a, i.e. $a = l/2$, $a = l/5$ and $a = l/10$. These results are summarized in Figure 2.10. The blue lines mark the four eigenfrequencies of the symmetric rotor, the green and red lines the four eigenfrequencies of the two asymmetric models.

First the symmetric model will be discussed, where $a = l/2$. Due to the symmetry the system is uncoupled ($s_{12} = 0$). Figure 2.10 shows that for each rotational speed, two positive and two negative eigenfrequencies exist. As already mentioned, the eigenfrequencies depend on the rotational speed of the rotor. In the special case of the symmetric rotor, only two eigenfrequencies are independent from the rotational speed. These modes are conical whirling and depicted as the two horizontal lines in Figure 2.10. The two other modes, which depend on the rotational speed, are cylindrical [54]. For high positive rotational speeds Ω the corresponding eigenfrequencies of

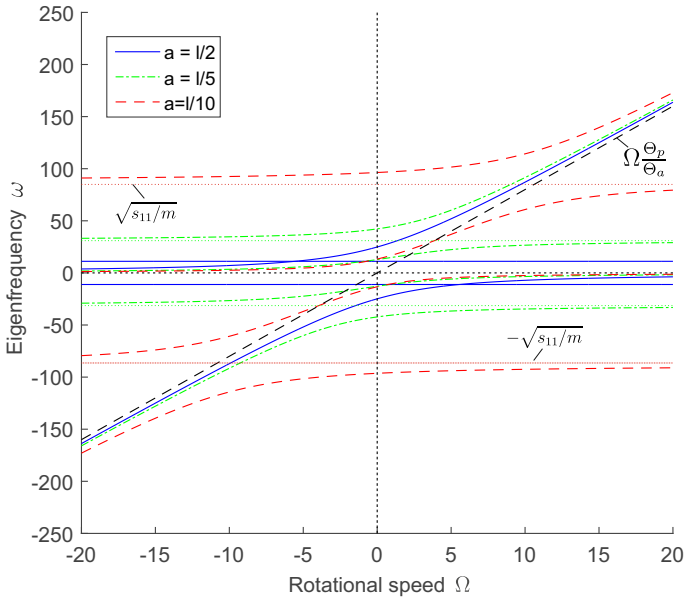

Figure 2.10: Campbell diagram of an asymmetric rigid rotor on two equal elastic supports ($m = 10\,\mathrm{kg}$, $\Theta_p = 4\,\mathrm{kgm}^2$, $\Theta_a = 0.5\,\mathrm{kgm}^2$, $EI = 25.77\,\mathrm{Nm}^2$, $l = 1\,\mathrm{m}$)

the cylindrical modes tend to $\Omega\Theta_p/\Theta_a$ and zero, for high negative rotational speeds $-\Omega$ the eigenfrequencies tend to zero and $-\Omega\Theta_p/\Theta_a$, compare Figure 2.10.

Asymmetric rotor models result in a coupling ($s_{12} \neq 0$), for example $a = l/5$ or $a = l/10$. The two cylindrical modes show similar behavior as the symmetric model. One of the two modes also approximates $\Omega\,\Theta_p/\Theta_a$ for a rotational speed Ω and the other mode $-\Omega\,\Theta_p/\Theta_a$ for a rotational speed $-\Omega$. However, they do not tend to zero. Two further horizontal asymptotes at $\sqrt{s_{11}/m}$ and $-\sqrt{s_{11}/m}$ arise. The conical modes dependent on the rotational speed. The positive conical modes tend to a horizontal asymptotic at $\sqrt{s_{11}/m}$ for high positive rotational speeds Ω and to zeros for high negative rotational speeds $-\Omega$, see Figure 2.10. The negative conical mode have an inverse behavior.

2.3 Electromagnetics

The effect of electromagnetic fields can be described by Maxwell's equations [24]. These equations are a system of linear differential equations of first order and formulate the interaction of electric and magnetic fields in consideration of boundary effects. The Maxwell equations comprise the Gauss' laws for electricity and magnetism in differential form, Faraday's law of induction and Ampere's law.

The Ampere's law

$$\boldsymbol{\nabla} \times \boldsymbol{\mathcal{H}} = \boldsymbol{\mathcal{J}} + \frac{\partial \boldsymbol{\mathcal{D}}}{\partial t} \tag{2.51}$$

is extended by Maxwell's term $\frac{\partial \mathfrak{D}}{\partial t}$ to include a time dependency, where the electrical displacement field is denoted by $\mathfrak{D}$. Further, the magnetic field intensity $\mathfrak{H}$ and the current density $\mathfrak{J}$ are taken into account. Faraday's law of induction

$$\boldsymbol{\nabla} \times \mathfrak{E} = -\frac{\partial \mathfrak{B}}{\partial t} \tag{2.52}$$

considers the circulating electrical field $\mathfrak{E}$ resulting from the time-dependent change of the magnetic field $\mathfrak{B}$. The Gauss' law of magnetism

$$\boldsymbol{\nabla} \cdot \mathfrak{B} = 0 \tag{2.53}$$

describes that the magnetic flux density $\mathfrak{B}$ through a closed surface is zero. The Gauss' law of electricity is given by

$$\boldsymbol{\nabla} \cdot \mathfrak{D} = \rho \ . \tag{2.54}$$

The electrical displacement $\mathfrak{D}$ resulting from the electric charges density ρ, and means a divergence from positive charges and converges to negative charges.

In order to apply Maxwell's equations, it is necessary to formulate constitute relations. In case of linear material properties the constitutive relations

$$\mathfrak{D} = \epsilon \mathfrak{E} \qquad \mathfrak{B} = \mu \mathfrak{H} \qquad \text{and} \qquad \mathfrak{J} = \gamma \left(\mathfrak{E} + \mathfrak{E}_e \right) \tag{2.55}$$

are valid. The electric displacement is related to the electric field by the electric permittivity ϵ. The permittivity ϵ is generally determined by $\epsilon = \epsilon_0 \epsilon_r$, where the permittivity in vacuum is $\epsilon_0 = 8.8543 \times 10^{-12}\,\mathrm{F/m}$ and ϵ_r is a dimensionless constant of the material. The magnetic permeability μ is also defined by $\mu = \mu_0 \mu_r$, with $\mu_0 = 4\pi 10^{-7}\,\mathrm{H/m}$ and μ_r as a dimensionless material constant. The conductivity of the material is denoted by γ. An imposed electric field is denoted with $\mathfrak{E}_e$. [24]

2.3.1 Quasi-static fields in electrical machines

The application of Maxwell's equations in the field of electrical machines allow the simplification of the equations in case of quasi-static fields. Therefore, the time dependent terms are negligible,

$$|\mathfrak{J}| \gg \left| \frac{\partial \mathfrak{D}}{\partial t} \right| \ . \tag{2.56}$$

For electrical machines Maxwell's equations are formulated for two regions, the conducting domain Ω_c and the non-conducting domain Ω_n. The following set of differential equations is used for the computation of the electric and magnetic fields:

$$\begin{aligned}
\boldsymbol{\nabla} \times \boldsymbol{\mathcal{H}} &= \boldsymbol{\mathcal{J}} && \text{in } \Omega_c \ , \\
\boldsymbol{\nabla} \times \boldsymbol{\mathcal{H}} &= \boldsymbol{\mathcal{J}}_0 && \text{in } \Omega_n \ , \\
\boldsymbol{\nabla} \times \boldsymbol{\mathcal{E}} &= -\frac{\partial \boldsymbol{\mathcal{B}}}{\partial t} && \text{in } \Omega_c \ , \\
\boldsymbol{\nabla} \cdot \boldsymbol{\mathcal{B}} &= 0 && \text{in } \Omega_c \ , \\
\boldsymbol{\nabla} \cdot \boldsymbol{\mathcal{B}} &= 0 && \text{in } \Omega_n \ , \\
\boldsymbol{\mathcal{J}} &= \gamma \boldsymbol{\mathcal{E}} && \text{in } \Omega_c \ .
\end{aligned} \tag{2.57}$$

The current density $\boldsymbol{\mathcal{J}}$ in the domain Ω_c is unknown, whereas the current density is given with $\boldsymbol{\mathcal{J}}_0$ in the domain Ω_n. The boundary conditions on $\partial\Omega_c$ and $\partial\Omega_n$ are assumed to be continuous. Subjected to symmetric boundary planes and artificial far boundaries, the boundary equations are formulated by

$$\boldsymbol{\mathcal{H}} \times \boldsymbol{n} = \boldsymbol{0} \quad \text{on } \partial\Omega_c \qquad \text{and} \qquad \boldsymbol{\mathcal{H}} \times \boldsymbol{n} = \boldsymbol{0} \quad \text{on } \partial\Omega_n \ . \tag{2.58}$$

On symmetry planes the tangential component of $\boldsymbol{\mathcal{H}}$ is zero and on the far boundary of the nonconducting region $\partial\Omega_n$ the tangential component of $\boldsymbol{\mathcal{H}}$ vanishes. For simple geometries, analytical solutions exist for the formulated problem above.

2.3.2 Electromagnetic forces

In case of electrical machines it is acceptable to neglect forces acting on charges q in an electric field $\boldsymbol{\mathcal{E}}$. The electromagnetic forces are significant for vibrations in electrical machines. The derivation of these forces follow the approach presented in [19].

For a linear magnetic material the magnetic energy density U_m is determined by

$$U_m = \int_0^{\boldsymbol{\mathcal{B}}} \boldsymbol{\mathcal{H}} \, d\boldsymbol{\mathcal{B}} = \frac{1}{2} \, \boldsymbol{\mathcal{H}} \cdot \boldsymbol{\mathcal{B}} \ , \tag{2.59}$$

where the magnetic flux density $\boldsymbol{\mathcal{B}}$ and the magnetic field intensity $\boldsymbol{\mathcal{H}}$ are formulated at a defined position $\boldsymbol{r}$. Hence, the identity

$$\boldsymbol{\nabla} \cdot (\boldsymbol{\mathcal{B}}(\boldsymbol{\mathcal{H}} \cdot \boldsymbol{v}) - U_m \boldsymbol{v}) \equiv \boldsymbol{v} \cdot (\boldsymbol{\nabla} \times \boldsymbol{\mathcal{H}} \times \boldsymbol{\mathcal{B}} + \boldsymbol{\mathcal{H}} \, \boldsymbol{\nabla} \cdot \boldsymbol{\mathcal{B}} - U_m \boldsymbol{v}) \tag{2.60}$$

is obtained by introducing an uniform vector field $\boldsymbol{v}$ [19]. Imposing the Maxwell

equations for quasi static fields (2.57) derived in the subsection above, an equation for the total force $\boldsymbol{F}$ acting in a domain Ω follows:

$$\boldsymbol{F} = \int_{\Omega} \boldsymbol{\nabla} \cdot (\boldsymbol{\mathcal{B}} \otimes \boldsymbol{\mathcal{H}} - U_m \boldsymbol{I})\, d\Omega = \int_{\Omega} (\boldsymbol{\mathcal{J}} \times \boldsymbol{\mathcal{B}} - \boldsymbol{\nabla} U_m)\, d\Omega \ . \tag{2.61}$$

The acting force consists of two parts. The first part describes the Lorenz force which occurs due to a current density in a magnetic field. The second part denotes the force considering the magnetic energy density. These terms have a significant influence on the boundary of highly permeable materials surrounded by air [193]. Magnetostrictive effects, which are introduced in [19], do not influence the vibrations in electrical machines significantly [13]. The magnetostriction is not taken into account in the computation of electromagnetic forces.

The terms in brackets are summarized in the tensor

$$\boldsymbol{T} = \boldsymbol{\mathcal{B}} \otimes \boldsymbol{\mathcal{H}} - \frac{1}{2}(\boldsymbol{\mathcal{H}} \cdot \boldsymbol{\mathcal{B}})\boldsymbol{I} \ , \tag{2.62}$$

which is called the Maxwell stress tensor. Applying Gauss' law, the total force $\boldsymbol{F}$ of the magnetic field is computed by

$$\boldsymbol{F} = \int_{\Omega} \boldsymbol{\nabla} \cdot \boldsymbol{T} d\Omega = \oint_{\partial\Omega} \boldsymbol{T}\, \boldsymbol{n}\, ds \ . \tag{2.63}$$

The Maxwell stress tensor allows for the computation of electromagnetical forces acting on the rotor during operation.

CHAPTER 3

Three-dimensional Timoshenko beam model

Generally, it has to be differentiated between different methods for modeling flexible prismatic beams. The simplest model is the Euler-Bernoulli beam theory [177]. It is also called the classical beam theory, because it is the most commonly used beam theory. The Euler-Bernoulli beam theory takes the bending into account and assumes that the cross section of the beam is in any case orthogonal to the beam axis. As a fact of this assumption, the natural eigenfrequencies of the Euler-Bernoulli model are slightly overestimated. However, the rotating inertia is neglected in this beam theory. The Rayleigh beam theory [170] is an extension of the Euler-Bernoulli beam theory and includes this rotating inertia. The deformation of the Euler-Bernoulli beam and the Rayleigh beam is only resulting from bending moments. Timoshenko [179] adds the effect of the shear deformation to the Rayleigh model in his beam theory. This is a major improvement for short thick beams.

In the following, the Timoshenko beam element is presented. It comprises the derivation of the Timoshenko beam in the three-dimensional space based on a three-dimensional continuum. The derived kinematics, internal forces and stresses as well as inertia forces, are used for the weak formulation of the dynamic equilibrium. Consistent shape functions for the three-dimensional two-node beam element are constructed from the general solution. The system matrices are obtained by discretizing the dynamic equilibrium with this consistent shape functions. The validation of this beam element is carried out on a cantilevered beam with a constant load on its free end. Thereby, different methods are compared with the introduced beam elements.

3.1 Timoshenko beam theory

The Timoshenko beam theory [179] gives a correction of the rotary inertia and the shear deformation to the classical Euler-Bernoulli beam for bending vibrations. This allows for an adequate estimation of higher mode vibrations of elastic beams.

Some assumptions are made for this beam model as follows. The direction of the beam axis is considerable larger than the other two directions so that the in-plane strains are neglected. Small displacements and rotation angles are adopted. The beam material is linear elastic and the Poisson effect is neglected.

3.1.1 Kinematics of the Timoshenko beam

The position of an arbitrary point P in a cross section of a flexible three-dimensional beam is depicted in Figure 3.1. The grey shadowed beam shows an undeformed configuration of the beam and the transparent beam the deformed one. The measures in the deformed configuration are marked by $()'$. The displacement of this point P

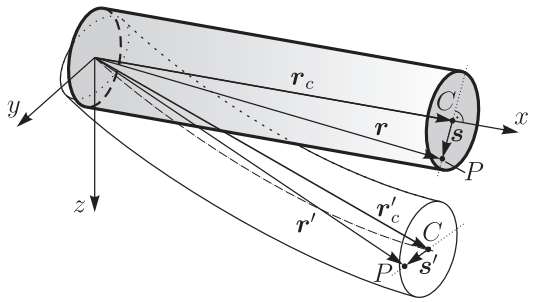

Figure 3.1: Kinematics of an arbitrary point P in a three-dimensional Timoshenko beam

is described by six degrees of freedom, which are three degrees of freedom for the translation of the point C in the cross section and on the beam axis as well as three degrees of freedom for the rotation the cross section plane.

Generally, the displacement vector $\overline{\boldsymbol{u}}$ of the point P is defined by

$$\overline{\boldsymbol{u}} = \boldsymbol{r}' - \boldsymbol{r} \ . \tag{3.1}$$

The vector $\boldsymbol{r}'$ describes the position of the point P in the deformed configuration, $\boldsymbol{r}$ gives the position of the point P in the undeformed configuration. This vector $\boldsymbol{r}$ is split into the position vector $\boldsymbol{r}_c$ defined by point C and the relative position of P with respect to C is marked by vector $\vec{s}$,

$$\boldsymbol{r}' = \boldsymbol{r}'_c + \boldsymbol{s}' \qquad \text{and} \qquad \boldsymbol{r} = \boldsymbol{r}_c + \boldsymbol{s} \ . \tag{3.2}$$

The vector $\boldsymbol{s} = [\, 0 \ \ y \ \ z \,]^T$ is situated in the plane of the cross section. Defining a transformation matrix $\boldsymbol{R}$, the vector $\boldsymbol{s}$ is transformed into the deformed configuration by the operation

$$\boldsymbol{s}' = \boldsymbol{R}\, \boldsymbol{s} \ . \tag{3.3}$$

According to the Euler-Chalses' theorem [130], the transformation matrix $\boldsymbol{R}$ is defined by a Taylor series

$$\boldsymbol{R} = \boldsymbol{I} + \tilde{\boldsymbol{\phi}} + \frac{1}{2}\tilde{\boldsymbol{\phi}}^2 + \dots \ , \tag{3.4}$$

where $\boldsymbol{I}$ is a 3×3 identity matrix. The skew symmetric matrix $\tilde{\boldsymbol{\phi}}$ illustrates the rotational degrees of freedom [155]

$$\tilde{\boldsymbol{\phi}} = \begin{bmatrix} 0 & -\theta_z & \theta_y \\ \theta_z & 0 & -\theta_x \\ -\theta_y & \theta_x & 0 \end{bmatrix} , \tag{3.5}$$

where θ_x, θ_y and θ_z are the rotation angles about the axis x, y and z. Using the equations (3.1), (3.3) and (3.2), the displacement of the point P is written as

$$\overline{\boldsymbol{u}} = \boldsymbol{u}_c' + (\boldsymbol{R} - \boldsymbol{I})\boldsymbol{s} \ = \boldsymbol{u}_c' + \tilde{\boldsymbol{\phi}}\ \boldsymbol{s}. \tag{3.6}$$

The displacement is now split into a translational part given by the vector $\boldsymbol{u}_{\underline{c}}' = [u_c \ \ v_c \ \ w_c]^T$, which is the translation of the point C and the rotational part $\tilde{\boldsymbol{\phi}}\ \boldsymbol{s}$, which considers the displacement of the point P according to the rotation of the cross section. Considering the assumption of small displacements and rotations, it is possible to neglect the higher order terms of the rotation matrix $\boldsymbol{R}$ in Equation (3.4). The linearized displacement becomes

$$\overline{\boldsymbol{u}} = \begin{bmatrix} u(x,y,z) \\ v(x,y,z) \\ w(x,y,z) \end{bmatrix} = \begin{bmatrix} u_c - y\ \theta_z + z\ \theta_y \\ v_c - z\ \theta_x \\ w_c + y\ \theta_x \end{bmatrix} , \tag{3.7}$$

where u, v and w are the displacements in x-, y- and z-direction. The coordinates of the particle P are denoted by y and z. The strain-displacement relation is given by

$$\boldsymbol{\varepsilon} = \mathfrak{D}\ \overline{\boldsymbol{u}} \ , \tag{3.8}$$

where $\mathfrak{D}$ is a differential operator matrix. In case of the Timoshenko beam, no in-plane displacements exist and a small strain-displacement relation is assumed. Thus, the differential operator matrix is defined as

$$\mathfrak{D} = \begin{bmatrix} \frac{\partial}{\partial x} & 0 & 0 \\ \frac{\partial}{\partial y} & \frac{\partial}{\partial x} & 0 \\ \frac{\partial}{\partial z} & 0 & \frac{\partial}{\partial x} \end{bmatrix} . \tag{3.9}$$

According to Equation (3.8), the strains in the Timoshenko beam element are obtained from

$$\boldsymbol{\varepsilon} = \begin{bmatrix} \varepsilon_x \\ \gamma_{xy} \\ \gamma_{xz} \end{bmatrix} = \begin{bmatrix} u_{c,x} - y\ \theta_{z,x} + z\ \theta_{y,x} \\ v_{c,x} - z\ \theta_{x,x} - \theta_z \\ w_{c,x} + y\ \theta_{x,x} + \theta_y \end{bmatrix} . \tag{3.10}$$

The expression $()_{,x}$ denotes the derivative of a measure with respect to the coordinate x.

3.1.2 Stresses and internal forces

The stress components acting in the cross section are σ_x, τ_{xy} and τ_{xz}. Considering the assumptions for the kinematics of the Timoshenko beam, the stress components σ_y, σ_z and τ_{yz} are neglected:

$$\sigma_y = 0 \ , \qquad \sigma_z = 0 \ , \qquad \tau_{yz} = 0 \ . \tag{3.11}$$

The acting stress components in the cross section σ_x, τ_{xy} and τ_{yz} are defined as

$$\sigma_x = E_x \, \epsilon_x \ , \qquad \tau_{xy} = G_{xy} \, \gamma_{xy} \quad \text{and} \quad \tau_{xz} = G_{xz} \, \gamma_{xz} \tag{3.12}$$

for the linear elastic material, where E_x is the Young's modulus in the direction of the beam axis, G_{xy} and G_{xz} are shear moduli acting in the xy-plane and xz-plane.

Figure 3.2 depicts the free punch of the beam with an arbitrary cross section and the acting internal forces and moments.

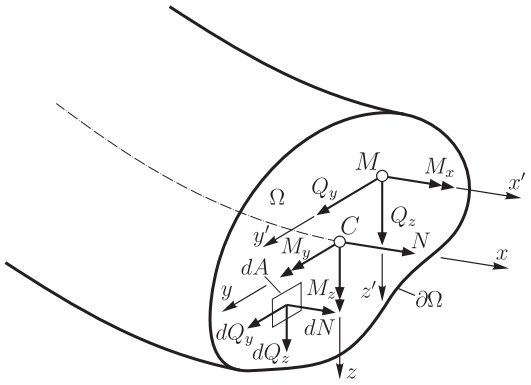

Figure 3.2: Internal forces in a beam with arbitrary cross section

The infinitesimal small internal forces,

$$dN = \sigma_x \, dA \ , \qquad dQ_y = \tau_{xy} \, dA \quad \text{and} \quad dQ_z = \tau_{xz} \, dA \ , \tag{3.13}$$

are defined on a infinitesimal small area dA of the cross section. The internal forces and moments of the total area are obtained from

$$\begin{aligned} N &= \int_\Omega \sigma_x \, dA \ , & Q_y &= \int_\Omega \tau_{xy} \, dA \ , & Q_z &= \int_\Omega \tau_{xz} \, dA \ , \\ M_y &= \int_\Omega z\sigma_x \, dA \ , & M_z &= -\int_\Omega y\sigma_x \, dA \ , & M_x &= \int_\Omega (-\bar{z}\tau_{xy} + \bar{y}\tau_{xz}) \, dA \ . \end{aligned} \tag{3.14}$$

$N$is the normal force, which is defined as a force in normal x-direction to the cross

section. Q_y and Q_z are the shear forces and operate in lateral y- and z-directions. M_y and M_z are the bending moments with respect to the y- and z-axis. y and z mark the distances of the infinitesimal small area dA to the origin C, which is equal to the center of area. M_x is the torsion moment and $\bar{y}$ and $\bar{z}$ are the distances of the infinitesimally area dA to the shear center M:

$$\bar{y} = y - y_M \qquad \text{and} \qquad \bar{z} = z - z_M \ . \tag{3.15}$$

The shear center is defined as y_M and z_M.

Using the equations for the internal forces and moments in (3.14), the linear elastic material behavior in Equation (3.12) and and the strain expressions in Equation (3.10), the normal force is obtained as

$$N = \int_\Omega E_x \ \epsilon_x \ dA = \int_\Omega E_x \ (u_{c,x} - y \ \theta_{z,x} + z \ \theta_{y,x}) \ dA \ . \tag{3.16}$$

The shear forces result in

$$Q_y = \int_\Omega G_{xy} \ \gamma_{xy} \ dA = \int_\Omega G_{xy} \ (v_{c,x} - z \ \theta_{x,x} - \theta_z) \ dA \tag{3.17}$$

and

$$Q_z = \int_\Omega G_{xz} \ \gamma_{xz} \ dA = \int_\Omega G_{xz} \ (w_{c,x} + y \ \theta_{x,x} + \theta_y) \ dA \ . \tag{3.18}$$

The torsional moment is expressed as

$$\begin{aligned} M_x &= \int_\Omega (-\bar{z} G_{xy} \gamma_{xy} + \bar{y} G_{xz} \gamma_{xz}) \ dA \\ &= \int_\Omega (-\bar{z} G_{xy} (v_{c,x} - z \ \theta_{x,x} - \theta_z) + \bar{y} G_{xz} (w_{c,x} + y \ \theta_{x,x} + \theta_y)) \ dA \end{aligned} \tag{3.19}$$

and the bending moments are

$$M_y = \int_\Omega z \ E_x \ \epsilon_x \ dA = \int_\Omega z \ E_x \ (u_{c,x} - y \ \theta_{z,x} + z \ \theta_{y,x}) \ dA \tag{3.20}$$

and

$$M_z = -\int_\Omega y \ E_x \ \epsilon_x \ dA = -\int_\Omega y \ E_x \ (u_{c,x} - y \ \theta_{z,x} + z \ \theta_{y,x}) \ dA \ . \tag{3.21}$$

The evaluation of the internal forces and moments leads to the cross section parameters of the Timoshenko beam. These parameters are summarized:

$$\begin{aligned} A &= \int_\Omega dA \ , & S_y &= \int_\Omega z \ dA \ , & S_z &= \int_\Omega y \ dA \\ I_y &= \int_\Omega z^2 \ dA \ , & I_z &= \int_\Omega y^2 \ dA \ , & I_{yz} &= \int_\Omega yz \ dA \ . \end{aligned} \tag{3.22}$$

A is the area of the cross section. S_y and S_z are the first moments of area. I_y, I_z and I_{yz} are the second moments of area.

Symmetric shapes of cross sections are assumed with the properties that the center of area coincides with the center of shear [113], $y = \bar{y}$ and $z = \bar{z}$. The internal forces and moments are determined using the cross section parameters of Equation (3.22):

$$N = E_x \ A \ u_{c,x} - E_x \ S_z \ \theta_{z,x} + E_x \ S_y \ \theta_{y,x} \tag{3.23}$$

$$Q_y = \kappa_y \ G_{xy} \ A \ (v_{c,x} - \theta_z) - \kappa_y \ G_{xy} \ S_y \ \theta_{x,x} \tag{3.24}$$

$$Q_z = \kappa_z \ G_{xz} \ A \ (w_{c,x} + \theta_y) + \kappa_z \ G_{xz} \ S_z \ \theta_{x,x} \tag{3.25}$$

$$M_x = -\kappa_y \ G_{xy} \ S_y(v_{c,x} - \theta_z) + \kappa_y \ I_y \ G_{xy} \ \theta_{x,x} + \kappa_z \ G_{xz} \ S_z(w_{c,x} + \theta_y) + \kappa_z \ I_z \ G_{xz} \ \theta_{x,x} \tag{3.26}$$

$$M_y = E_x \ S_z \ u_{c,x} - E_x \ I_{yz} \ \theta_{z,x} + E_x \ I_y \ \theta_{y,x} \tag{3.27}$$

$$M_z = -E_x \ S_y \ u_{c,x} + E_x \ I_z \ \theta_{z,x} - E_x \ I_{yz} \ \theta_{y,x} \ . \tag{3.28}$$

Additionally, the shear correction factors κ_y and κ_z are introduced [179]. The assumption of a plane cross section leads to wrong values of the shear stress distributions. The shear correction factor gives a correction of these wrong stress values, see Section 4.2.

According to the equations (3.7) and (3.10), a relation between bending and shear,

$$\frac{\partial v}{\partial x} = \theta_z + \gamma_{xy} \qquad \text{and} \qquad \frac{\partial w}{\partial x} = -\theta_y + \gamma_{xz} \ , \tag{3.29}$$

exists for the Timoshenko beam. Using the Voigt notation, which is a method to reduce the order of symmetric tensors, the strain is rewritten as

$$\boldsymbol{\varepsilon} = \begin{bmatrix} u_{c,x} & (v_{c,x} - \theta_z) & (w_{c,x} + \theta_y) & \theta_{x,x} & \theta_{y,x} & \theta_{z,x} \end{bmatrix}^T \ . \tag{3.30}$$

The equations (3.23)-(3.28) are summarized in a tensor notation by

$$\boldsymbol{p} = \boldsymbol{K}_t \ \boldsymbol{\varepsilon} \ , \tag{3.31}$$

where $\boldsymbol{p}$ contains the internal forces and moments

$$\boldsymbol{p} = \begin{bmatrix} N & Q_y & Q_z & M_x & M_y & M_z \end{bmatrix}^T \tag{3.32}$$

and $\boldsymbol{K}_t$ is a stiffness tensor of the Timoshenko beam. The stiffness tensor is given by

$$\boldsymbol{K}_t = \begin{bmatrix} E_x A & 0 & 0 & 0 & E_x S_y & -E_x S_z \\ 0 & \kappa_y G_{xy} A & 0 & -\kappa_y G_{xy} S_y & 0 & 0 \\ 0 & 0 & \kappa_z G_{xz} A & \kappa_z G_{xz} S_z & 0 & 0 \\ 0 & -\kappa_y G_{xy} S_y & \kappa_z G_{xz} S_z & \kappa_y I_y G_{xy} + \kappa_z I_z G_{xz} & 0 & 0 \\ E_x S_y & 0 & 0 & 0 & E_x I_y & -E_x I_{yz} \\ -E_x S_z & 0 & 0 & 0 & -E_x I_{yz} & E_x I_z \end{bmatrix} . \quad (3.33)$$

3.1.3 Variational formulation for the Timoshenko beam

The local form of the momentum balance is given by

$$\nabla \boldsymbol{\sigma} + \boldsymbol{f} = \varrho \ddot{\boldsymbol{u}} \ , \quad (3.34)$$

where $\boldsymbol{\sigma}$ is the Cauchy stress tensor, $\boldsymbol{f}$ is the external force, ϱ is the density and $\ddot{\boldsymbol{u}}$ is the acceleration. The term $\varrho \ddot{\boldsymbol{u}}$ describes the inertia force, which is taken into account for the formulation of an elastodynamic problem. The approximated solution of this system of equations is obtained by setting up a variational formulation.

In order to formulate the equations of motion of the Timoshenko beam, Hamilton's principle is used [171]. It generalises the principle of the minimum of potential energy from elastostatics to elastodynamics. Hamilton's principle states, that of all possible paths on which a dynamical system may move from one point to another within a specified time interval, the actual path followed is the one which minimizes the time integral of the difference between the kinetic and potential energies [21].

Mathematically, the Hamilton's principle requires the stationarity of the functional $\mathfrak{S}$ and the first variation of this functional has to be zero:

$$\delta \mathfrak{S} = \delta \int_{t_0}^{t_1} \mathcal{L}(\overline{\boldsymbol{u}}, \overline{\ddot{\boldsymbol{u}}}, t) \, dt = 0 \ , \quad (3.35)$$

where $\mathcal{L}$ is the Lagrangian functional, defined as $\mathcal{L} = T - \Pi + W$. T is the kinetic energy, Π is the strain energy and W is the energy caused by external forces. Using this definition, the variation of the functional $\delta\mathfrak{S}$ is rewritten as

$$\delta \mathfrak{S} = \int_{t_0}^{t_1} (\delta T - \delta \Pi + \delta W) \, dt = 0 \ . \quad (3.36)$$

The kinetic energy T of the Timoshenko beam is given by

$$T = \frac{1}{2} \int_{\Omega} \overline{\boldsymbol{v}}^T \, \varrho \, \overline{\boldsymbol{v}} \, dV \ , \quad (3.37)$$

where $\overline{\boldsymbol{v}}$ is the velocity. The variation of the kinetic energy leads to

$$\delta T = \int_{\Omega} \delta\overline{\boldsymbol{v}}^T \, \varrho \, \overline{\boldsymbol{v}} \, dV \ . \tag{3.38}$$

The strain energy $\mathit{\Pi}$ of the elastic beam is expressed as

$$\mathit{\Pi} = \frac{1}{2} \int_{\Omega} \boldsymbol{\epsilon}^T \boldsymbol{\sigma} \, dV \ . \tag{3.39}$$

$\boldsymbol{\epsilon}$ is the strain received from the kinematics of the Timoshenko beam element and $\boldsymbol{\sigma}$ is the stress tensor. The variation of of the strain energy yields

$$\delta\mathit{\Pi} = \int_{\Omega} \delta\boldsymbol{\epsilon}^T \boldsymbol{\sigma} \, dV \ . \tag{3.40}$$

The energy caused by external forces is given by

$$W = \int_{\Omega} \overline{\boldsymbol{u}}^T \, \boldsymbol{f}^B \, dV + \int_{\mathit{\Gamma}_\sigma} \overline{\boldsymbol{u}}_\sigma^T \, \boldsymbol{t}_\sigma \, dS_\sigma + \int_{\mathit{\Gamma}_u} \overline{\boldsymbol{u}}_u^T \, \boldsymbol{t}_u \, dS_u + \sum_i \overline{\boldsymbol{u}}_i^T \, F_{Ni} \ . \tag{3.41}$$

The term $\int_\Omega \overline{\boldsymbol{u}}^T \, \boldsymbol{f}^B \, dV$ considers the energy of body forces $\boldsymbol{f}^B$. The Neumann boundary conditions are regarded by $\int_{\mathit{\Gamma}_\sigma} \overline{\boldsymbol{u}}_\sigma^T \, \boldsymbol{t}_\sigma \, dS_\sigma$, where $\forall \overline{\boldsymbol{u}}_\sigma^T \in \mathit{\Gamma}_\sigma$. $\boldsymbol{t}_\sigma$ is a predefined surface force and $\overline{\boldsymbol{u}}_\sigma$ is the resulting displacement of the domain $\mathit{\Gamma}_\sigma$. The Dirichlet boundary conditions are included by $\int_{\mathit{\Gamma}_u} \overline{\boldsymbol{u}}_u^T \, \boldsymbol{t}_u \, dS_u$, where $\overline{\boldsymbol{u}}_u^T \in \mathit{\Gamma}_u$. $\overline{\boldsymbol{u}}_u$ is a predefined displacement and $\boldsymbol{t}_u$ is the resulting stress in the corresponding domain $\mathit{\Gamma}_u$. $\sum_i \overline{\boldsymbol{u}}_i^T \, F_{Ni}$ is the energy term caused by single external forces F_{Ni}. The variation of the energy caused by external forces results from

$$\delta W = \int_{\Omega} \delta\overline{\boldsymbol{u}}^T \, \boldsymbol{f}^B \, dV + \int_{\mathit{\Gamma}_\sigma} \delta\overline{\boldsymbol{u}}_\sigma^T \, \boldsymbol{t}_\sigma \, dS_\sigma + \sum_i \delta\overline{\boldsymbol{u}}_i^T \, \boldsymbol{F}_{Ni} \tag{3.42}$$

The energy term of the Dirichlet boundary conditions vanishes due to the variation. Time-integration by parts and the fact that the virtual displacement at the time t_0 as well as at the time t_1 is zero, $\delta\boldsymbol{u}(t_0) = \delta\boldsymbol{u}(t_1) = \boldsymbol{0}$, the part of the kinetic energy in the Lagrangian functional is substituted by $-\frac{1}{2} \int_{t_0}^{t_1} \int_\Omega \delta\overline{\boldsymbol{u}}^T \, \varrho \, \ddot{\overline{\boldsymbol{u}}} \, dV \, dt$.

The notation is changed now form the tensor notation in the Voigt notation. Therefore, the displacement vector is defined as

$$\boldsymbol{u} = \begin{bmatrix} u_c & v_c & w_c & \theta_x & \theta_y & \theta_z \end{bmatrix}^T \ . \tag{3.43}$$

For the Timoshenko beam element the first variation of the functional $\mathfrak{S}$ is written as

$$\delta\mathfrak{S} = \int_{t_0}^{t_1} \left(-\int_l \delta\boldsymbol{u}^T \, \boldsymbol{M}_t \, \ddot{\boldsymbol{u}} \, dx - \int_l \delta\boldsymbol{\varepsilon}^T \boldsymbol{D} \, \boldsymbol{\varepsilon} \, dx + \int_l \delta\boldsymbol{u}^T \, \boldsymbol{f}_L \, dx + \ \ldots \right.$$
$$\left. \int_l \delta\boldsymbol{u}_\sigma^T \, \boldsymbol{t}_{l_\sigma} \, dx + \sum_i \delta\boldsymbol{u}_i^T \, \hat{\boldsymbol{F}}_{Ni} \right) \, dt = 0 \ , \tag{3.44}$$

with the tensor

$$\boldsymbol{M}_t = \begin{bmatrix} \varrho A & 0 & 0 & 0 & \varrho S_y & -\varrho S_z \\ 0 & \varrho A & 0 & -\varrho S_y & 0 & 0 \\ 0 & 0 & \varrho A & \varrho S_z & 0 & 0 \\ 0 & -\varrho S_y & \varrho S_z & \varrho(I_y + I_z) & 0 & 0 \\ \varrho S_y & 0 & 0 & 0 & \varrho I_y & -\varrho I_{yz} \\ -\varrho S_z & 0 & 0 & 0 & -\varrho I_{yz} & \varrho I_z \end{bmatrix} \ , \tag{3.45}$$

which contains the inertia terms of the Timoshenko beam.

3.2 Shape functions for the three-dimensional Timoshenko beam element

In order to set up the equation of motion, the continuum has to be discretized. This requires a subdivision of the continuum in finite elements. In case of the Timoshenko beams the used elements are beam elements with two nodes. Each node has six degrees of freedom. The axial and torsional deflection is uncoupled and the bending and shear deflection is coupled to each other, compare Subsection 3.1.1.

According to the standard finite element method, the deformation of an arbitrary point in the displacement field $\boldsymbol{u}_P$ is approximated by

$$\boldsymbol{u}_P \approx \boldsymbol{H}(x_P,y_P,z_P) \, \hat{\boldsymbol{u}} \ , \tag{3.46}$$

where x_P,y_P and z_P are coordinates of an arbitrary point P and $\hat{\boldsymbol{u}}$ are the nodal displacement values. $\boldsymbol{H}(x_P,y_P,z_P)$ is the matrix, which contains the shape functions h_{ij} for the three-dimensional domain. In case of the beam formulation the displacement field becomes

$$\boldsymbol{u}_P \approx \boldsymbol{H}(x) \, \hat{\boldsymbol{u}} \ . \tag{3.47}$$

The order of the interpolation domain for the beam is reduced to the order one. The shape functions h_{ij} of an displacement field depend on the coordinate x of the

beam axis. The interpolation fields of the Timoshenko beam are approximated by the matrix of shape functions $\boldsymbol{H}(x)$, which is defined as

$$\boldsymbol{H}(x) = \begin{bmatrix} h_{11} & h_{12} & \cdots & h_{1j} & \cdots & h_{1n} \\ h_{21} & h_{22} & & & & h_{2n} \\ \vdots & & \ddots & & & \vdots \\ h_{i1} & & & h_{ij} & & h_{in} \\ \vdots & & & & \ddots & \vdots \\ h_{m1} & h_{m2} & \cdots & h_{mj} & \cdots & h_{mn} \end{bmatrix} . \tag{3.48}$$

The matrix of shape functions $\boldsymbol{H}(x)$ has a size of $m \times n$, where m is the number of degrees of freedom of an interpolation field and n is the number of nodal degrees of freedom. The matrix contains the shape functions h_{ij}. For the Timoshenko beam element, each node and the interpolation fields have six degrees of freedom. Thereby results a size for the shape function matrix of 6×12.

3.2.1 Shear and bending displacement field

The shear displacement field $v(x)$ and $w(x)$ in the directions y and z are given by

$$v(x) = a_0 + a_1 x + a_2 x^2 + a_3 x^3 \tag{3.49}$$

and

$$w(x) = b_0 + b_1 x + b_2 x^2 + b_3 x^3 \ . \tag{3.50}$$

the constants a_0, a_1, a_2, a_3, b_0, b_1, b_2 and b_3 are unknown coefficients for the shear displacements $v(x)$ and $w(x)$, respectively. The shear displacement field is written in matrix form as

$$\mathfrak{u} = \boldsymbol{A}_{coeff}\ \mathfrak{v} \ , \tag{3.51}$$

where $\mathfrak{u}$ is a vector, which contains the shear displacement fields $v(x)$ and $w(x)$,

$$\mathfrak{u} = \begin{bmatrix} v(x) & w(x) \end{bmatrix}^T \ . \tag{3.52}$$

The matrix $\boldsymbol{A}_{coeff}$ summarizes the unknown coefficients, expressed by

$$\boldsymbol{A}_{coeff} = \begin{bmatrix} a_0 & a_1 & a_2 & a_3 \\ b_0 & b_1 & b_2 & b_3 \end{bmatrix} . \tag{3.53}$$

The vector $\mathfrak{v}$ is given by

$$\mathfrak{v} = \begin{bmatrix} 1 & x & x^2 & x^3 \end{bmatrix}^T \ . \tag{3.54}$$

According to Equation (3.29), the shear strains γ_{xy} and γ_{xz} are assumed to be constant in Timoshenko's beam theory,

$$\gamma_{xy} = \text{const.} \qquad \text{and} \qquad \gamma_{xz} = \text{const.} \ , \tag{3.55}$$

along the beam axis x. The relation between the bending moments and shear forces is given by

$$\frac{dM_y}{dx} = Q_z \qquad \text{and} \qquad \frac{dM_z}{dx} = -Q_y \ . \tag{3.56}$$

Bending moments and shear displacements are related by

$$M_y = E_x I_y \frac{\partial^2 w}{\partial x^2} \qquad \text{and} \qquad M_z = -E_x I_z \frac{\partial^2 v}{\partial x^2} \ , \tag{3.57}$$

depending on the Young's modulus E_x and the second moments of area I_y and I_z. The shear forces depend on the transverse shear strains:

$$Q_y = \kappa_y G_{xy} A \ \gamma_{xy} \qquad \text{and} \qquad Q_z = \kappa_z G_{xz} A \ \gamma_{xz} \ . \tag{3.58}$$

Taking the Equation (3.29) and substituting it into the equations (3.49) and (3.50), the bending displacement fields are obtained by

$$\theta_y = -b_1 - 2b_2 x - 3b_3 x^2 + \gamma_{xz} \tag{3.59}$$

and

$$\theta_z = a_1 + 2a_2 x + 3a_3 x^2 - \gamma_{xy} \ . \tag{3.60}$$

Using the relation between bending moments and shear displacements in Equation (3.57) as well as deriving the shear displacements $v(x)$ and $w(x)$ with respect to x two times yields

$$M_y = E_x I_y (2b_2 + 6b_3 x) \tag{3.61}$$

and

$$M_z = -E_x I_z (2a_2 + 6a_3 x) \ . \tag{3.62}$$

The derivatives of the equations (3.61) and (3.62) with respect to the coordinate x and the relation between bending moments and shear forces in Equation (3.56) leads to the equations

$$6E_x I_y b_3 + \kappa_z G_{xz} A \gamma_{xz} = 0 \tag{3.63}$$

and

$$-6E_x I_z a_3 - \kappa_y G_{xy} A \gamma_{xy} = 0 \tag{3.64}$$

for the determination of the shear strains. The shear strains γ_{xy} and γ_{xz} follows with

$$\gamma_{xy} = -6\frac{E_x I_z}{\kappa_y G_{xy} A} a_3 \qquad \text{as well as} \qquad \gamma_{xz} = -6\frac{E_x I_y}{\kappa_z G_{xz} A} b_3 \tag{3.65}$$

and the bending displacement fields are rewritten as

$$\theta_y = -b_1 - 2b_2 x - (3x^2 + 6\frac{E_x I_y}{\kappa_z G_{xz} A})b_3 \tag{3.66}$$

and

$$\theta_z = a_1 + 2a_2 x + (3x^2 + 6\frac{E_x I_z}{\kappa_y G_{xy} A})a_3 \ . \tag{3.67}$$

In order to determine the coefficients of the bending and shear displacement fields the following boundary conditions have to be satisfied:

$$\begin{aligned} &v(x=0) = v_1 \ , \quad v(x=l) = v_2 \ , \quad w(x=0) = w_1 \ , \quad w(x=l) = w_2, \\ &\theta_y(x=0) = \theta_{y1} \ , \quad \theta_y(x=l) = \theta_{y2} \ , \quad \theta_z(x=0) = \theta_{z1} \ , \quad \theta_z(x=l) = \theta_{z2} \ . \end{aligned} \tag{3.68}$$

The shear displacement fields $v(x)$ and $w(x)$ at the positions $x = 0$ and $x = l$ have to be equal to the nodal values v_1, v_2, w_1 and w_2. The same applies to the bending displacement field $\theta_y(x)$ and $\theta_z(x)$. The bending displacement field at the positions $x = 0$ and $x = l$ has to be equal to the nodal values θ_{y1}, θ_{y2}, θ_{z1} and θ_{z2}. Considering this boundary conditions, a system of equation is set up for the xy-plane

$$\begin{aligned} v(x=0) \quad &= a_0 &&= v_1 \ , \\ \theta_z(x=0) \quad &= a_1 + 6\frac{E_x I_z}{\kappa_y G_{xy} A} a_3 &&= \theta_{z1} \ , \\ v(x=l) \quad &= a_0 + a_1 l + a_2 l^2 + a_3 l^3 &&= v_2 \ , \\ \theta_z(x=l) \quad &= a_1 + 2a_2 l + (3l^2 + 6\frac{E_x I_z}{\kappa_y G_{xy} A})a_3 &&= \theta_{z2} \end{aligned} \tag{3.69}$$

and the xz-plane

$$\begin{aligned} w(x=0) \quad &= b_0 &&= w_1 \ , \\ \theta_y(x=0) \quad &= -b_1 - 6\frac{E_x I_y}{\kappa_z G_{xz} A} b_3 &&= \theta_{y1} \ , \\ w(x=l) \quad &= b_0 + b_1 l + b_2 l^2 + b_3 l^3 &&= w_2 \ , \\ \theta_y(x=l) \quad &= -b_1 - 2b_2 l - (3l^2 + 6\frac{E_x I_y}{\kappa_z G_{xz} A})b_3 &&= \theta_{y2} \ . \end{aligned} \tag{3.70}$$

This system of equations is rewritten in matrix form

$$\hat{\boldsymbol{u}}_v = \mathfrak{C}_1 \ \boldsymbol{a}_{coeff} \qquad \text{and} \qquad \hat{\boldsymbol{u}}_w = \mathfrak{C}_2 \ \boldsymbol{b}_{coeff} \ , \tag{3.71}$$

where $\boldsymbol{a}_{coeff}$ and $\boldsymbol{b}_{coeff}$ are a coefficient vectors and contains the unknown coefficients of the shear displacement fields

$$\boldsymbol{a}_{coeff} = \begin{bmatrix} a_0 \\ a_1 \\ a_2 \\ a_3 \end{bmatrix} \qquad \text{and} \qquad \boldsymbol{b}_{coeff} = \begin{bmatrix} b_0 \\ b_1 \\ b_2 \\ b_3 \end{bmatrix} . \tag{3.72}$$

The matrices $\mathfrak{C}_1$ and $\mathfrak{C}_2$ are system matrices, which contain the beam properties for the displacement fields. These matrices depend on geometrical properties of the Timoshenko beam like the length of the beam l, the area of the cross section A, the second moments of the area I_y and I_z and the shear correction factors κ_y and κ_z as well as on material parameters like the Young's modulus E_x and the shear moduli G_{xy} and G_{xz}. The system matrix $\mathfrak{C}_1$ is given by

$$\mathfrak{C}_1 = \begin{bmatrix} 1 & 0 & 0 & 0 \\ 0 & 1 & 0 & 6\frac{E_x I_z}{\kappa_y G_{xy} A} \\ 1 & l & l^2 & l^3 \\ 0 & 1 & 2l & \left(3l^2 + 6\frac{E_x I_z}{\kappa_y G_{xy} A}\right) \end{bmatrix} \tag{3.73}$$

and the system matrix $\mathfrak{C}_2$ is expressed as

$$\mathfrak{C}_2 = \begin{bmatrix} 1 & 0 & 0 & 0 \\ 0 & -1 & 0 & -6\frac{E_x I_z}{\kappa_y G_{xy} A} \\ 1 & l & l^2 & l^3 \\ 0 & -1 & -2l & \left(-3l^2 - 6\frac{E_x I_y}{\kappa_z G_{xz} A}\right) \end{bmatrix} . \tag{3.74}$$

The nodal values are summarized in the vectors $\hat{\boldsymbol{u}}_v$ and $\hat{\boldsymbol{u}}_w$:

$$\hat{\boldsymbol{u}}_v = \begin{bmatrix} v_1 \\ \theta_{z1} \\ v_2 \\ \theta_{z2} \end{bmatrix} \qquad \text{and} \qquad \hat{\boldsymbol{u}}_w = \begin{bmatrix} w_1 \\ \theta_{y1} \\ w_2 \\ \theta_{y2} \end{bmatrix} . \tag{3.75}$$

The unknown coefficients of the shear displacement field are computed by solving the inverse problem of Equation (3.71)

$$\boldsymbol{a}_{coeff} = \mathfrak{C}_1^{-1}\, \hat{\boldsymbol{u}}_v \qquad \text{and} \qquad \boldsymbol{b}_{coeff} = \mathfrak{C}_2^{-1}\, \hat{\boldsymbol{u}}_w . \tag{3.76}$$

Further the parameters

$$\Phi_y = \frac{12 E_x I_y}{\kappa_z G_{xz} A l^2} \qquad \text{and} \qquad \Phi_z = \frac{12 E_x I_z}{\kappa_y G_{xy} A l^2} \tag{3.77}$$

are introduced. With determination of the coefficients the displacement fields for shear and bending are obtained. The shear displacement field $v(x)$ is rewritten in the form

$$v(x) = h_{22}\, v_1 + h_{26}\, \theta_{z1} + h_{28}\, v_2 + h_{212}\, \theta_{z2} \ , \tag{3.78}$$

where the shape functions are:

$$\begin{aligned} h_{22} &= \frac{(l-x)\left(l^2 + lx - 2x^2 + l^2\Phi_z\right)}{l^3(1+\Phi_z)} \ , \\ h_{26} &= \frac{(l-x)x(2l - 2x + l\Phi_z)}{2l^2(1+\Phi_z)} \ , \\ h_{28} &= \frac{x\left(3lx - 2x^2 + l^2\Phi_z\right)}{l^3(1+\Phi_z)} \ , \\ h_{212} &= -\frac{(l-x)x(2x + l\Phi_z)}{2l^2(1+\Phi_z)} \ . \end{aligned} \tag{3.79}$$

The indices i and j denotes the row and column location of the shape functions h_{ij} in the element shape function matrix $\boldsymbol{H}$. The shear displacement field $w(x)$ is expressed by

$$w(x) = h_{33}\, w_1 + h_{35}\, \theta_{y1} + h_{39}\, w_2 + h_{311}\, \theta_{y2} \ . \tag{3.80}$$

The corresponding shape functions are

$$\begin{aligned} h_{33} &= \frac{(l-x)\left(l^2 + lx - 2x^2 + l^2\Phi_y\right)}{l^3(1+\Phi_y)} \ , \\ h_{35} &= -\frac{x(-l+x)(-2l + 2x - l\Phi_y)}{2l^2(1+\Phi_y)} \ , \\ h_{39} &= \frac{x\left(3lx - 2x^2 + l^2\Phi_y\right)}{l^3(1+\Phi_y)} \ , \\ h_{311} &= \frac{(l-x)x(2x + l\Phi_y)}{2l^2(1\Phi_y)} \ . \end{aligned} \tag{3.81}$$

According to Equation (3.59), the bending displacement field $\theta_y(x)$ is approximated by

$$\theta_y(x) = h_{53}\, w_1 + h_{55}\, \theta_{y1} + h_{59}\, w_2 + h_{511}\, \theta_{y2} \ , \tag{3.82}$$

where

$$\begin{aligned} h_{53} &= \frac{6(l-x)x}{l^3(1+\Phi_y)} \ , \\ h_{55} &= \frac{(l-x)(l-3x+l\Phi_y)}{l^2(1+\Phi_y)} \ , \\ h_{59} &= -\frac{6(l-x)x}{l^3(1+\Phi_y)} \ , \\ h_{511} &= \frac{x(-2l+3x+l\Phi_y)}{l^2(1+\Phi_y)} \ . \end{aligned} \tag{3.83}$$

The interpolation of bending displacement field $\theta_z(x)$ with respect to x is given by

$$\theta_z(x) = h_{62}\, w_1 + h_{66}\, \theta_{z1} + h_{68}\, w_2 + h_{612}\, \theta_{z2} \ . \tag{3.84}$$

The corresponding shape functions are

$$\begin{aligned} h_{62} &= -\frac{6(l-x)x}{l^3(1+\Phi_z)} \ , \\ h_{66} &= \frac{(l-x)(l-3x+l\Phi_z)}{l^2(1+\Phi_z)} \ , \\ h_{68} &= \frac{6(l-x)x}{l^3(1+\Phi_z)} \ , \\ h_{612} &= \frac{x(-2l+3x+l\Phi_z)}{l^2(1+\Phi_z)} \ . \end{aligned} \tag{3.85}$$

3.2.2 Axial and torsional displacement field

The axial displacement field $u(x)$ is expressed linearly as

$$u(x) = c_0 + c_1 x \ , \tag{3.86}$$

where c_0 and c_1 are unknown coefficients and x is the axial coordinate of the beam element, referred to the coordinate system in Figure 3.3. Analogically, the torsional displacement field

$$\theta_x(x) = d_0 + d_1 x \tag{3.87}$$

is a linear combination of the unknown coefficients d_0 and d_1 and the axial coordinate x. The axial displacement field $u(x)$ has to satisfy the boundary conditions

$$u(x=0) = u_1 \qquad \text{and} \qquad u(x=l) = u_2 \ . \tag{3.88}$$

The axial beam displacement at the position $x = 0$ has to be equal the nodal axial displacement u_1 and at the position $x = l$ the axial displacement has to match

the nodal axial displacement u_2, where l is the length of the beam element. The torsional displacement field had to satisfy the boundary conditions

$$\theta_x(x = 0) = \theta_{x1} \qquad \text{and} \qquad \theta_x(x = l) = \theta_{x2} \ . \tag{3.89}$$

At the axial positions $x = 0$ and $x = l$ the torsional displacement field has to match the nodal torsional displacements θ_{x1} and θ_{x2}.

Determining the unknown coefficients c_0 and c_1 the axial displacement field $u(x)$ is rewritten as

$$u(x) = h_{11}\, u_1 + h_{17}\, u_2 \ , \tag{3.90}$$

where

$$h_{11} = 1 - \frac{x}{l} \qquad \text{and} \qquad h_{17} = \frac{x}{l} \ . \tag{3.91}$$

h_{11} and h_{17} are the linear shape functions of the axial displacement field, depending on the axial coordinate x and the length of the Timoshenko beam element l. The same procedure applies to the torsional displacement field, after determining the unknown coefficients d_0 and d_1 the torsional displacement field $\theta_x(x)$ is obtained by

$$\theta_x(x) = h_{44}\, \theta_{x1} + h_{410}\, \theta_{x2} \ . \tag{3.92}$$

The linear shape functions

$$h_{44} = 1 - \frac{x}{l} \qquad \text{and} \qquad h_{410} = \frac{x}{l} \tag{3.93}$$

also depending on the axial coordinate x and the length of the Timoshenko beam element l.

3.2.3 Transformation into local coordinates

Using the global cartesian coordinate system (x,y,z), the numerical integration, which is carried out in order to derive the element matrices, is rather computationally costly. The usage of natural coordinates r, s and t reduces the numerical effort significant. Figure 3.3 depicts a two-node beam element with a local coordinate (x,y,z) and a natural coordinate (r,s,t). The origin of the local coordinate is equal

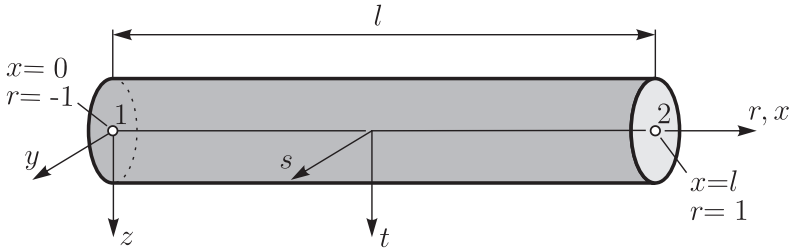

Figure 3.3: Node coordinates of a beam element in Cartesian coordinates (x,y,z) and natural coordinates (r,s,t)

to the position of the node 1. The origin of the natural coordinate is in the middle of the beam, or rather at the position $x = \frac{l}{2}$ with respect to the local coordinate system. The natural coordinate r varies in a range of -1 to 1, $\forall r = \{r \in \mathbb{R} | -1 \leq r \leq 1\}$. The local coordinates are mapped to a natural coordinate system by the transformation

$$x = \frac{l}{2}(r+1) \quad . \tag{3.94}$$

Independent from the length of the beam element the shape functions are always mapped onto the interval $r \in [-1,1]$.

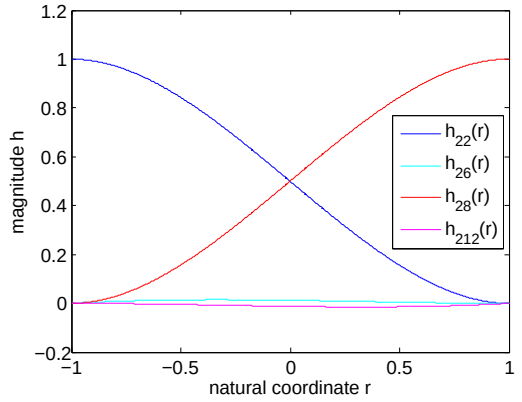

(a) Shape functions of the shear displacement field $v(r)$

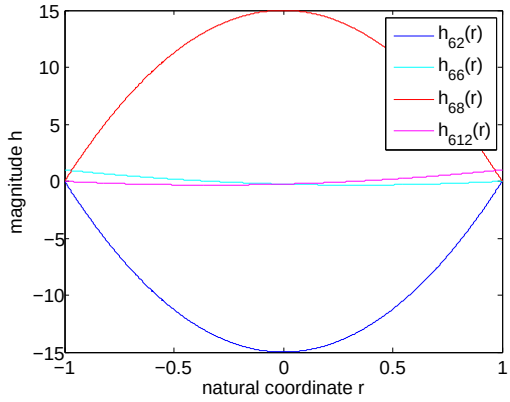

(b) Shape functions of the bending displacement field $\theta_z(r)$

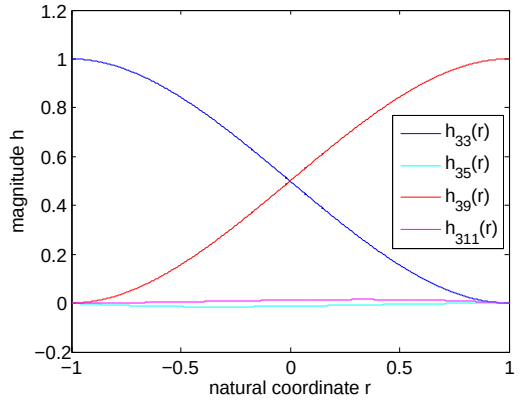

(c) Shape functions of the shear displacement field $w(r)$

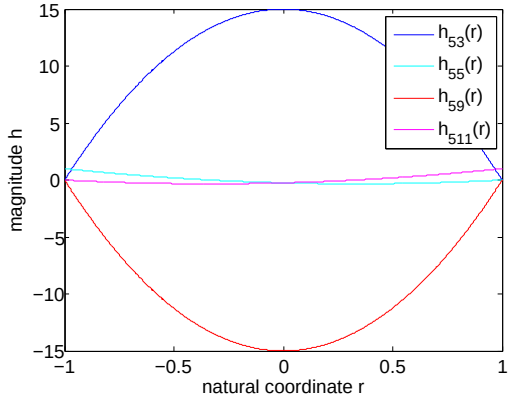

(d) Shape functions of the bending displacement field $\theta_y(r)$

Figure 3.4: Consistent shape functions of Timoshenko beam element (length $l = 100\,\text{mm}$) with a rectangular square ($b = 1\,\text{mm}$ and $h = 1\,\text{mm}$) and isotropic material properties ($E = 1 \times 10^5\,\text{N/mm}^2$ and $\nu = 0.3$)

Figure 3.4 shows the shape functions derived in Subsection 3.2.1. The shape functions are mapped onto the natural coordinate system and depend on the natural

coordinate r. The approximated beam has a rectangular cross section with a width of $b = 1\,\text{mm}$ and a height of $h = 1\,\text{mm}$ and the length of the beam element is given with $l = 100\,\text{mm}$. The material properties are isotropic and linear elastic with a Young's modulus of $E = 1 \times 10^5\,\text{N/mm}^2$ and a Poisson's ratio of $\nu = 0.3$. Figures 3.4a and 3.4c show the shape functions of the shear displacement fields $v(r)$ and $w(r)$. Figures 3.4b and 3.4d show the shape functions of the bending displacement fields $\theta_z(r)$ and $\theta_y(r)$.

3.3 Discretization of the continuum mechanical equation

The continuum of the beam is divided in a finite number of elements. Each element has a node at each end. The nodes of neighboring elements are merged. The displacement field in the beam is approximated using the shape functions derived in Section 3.2.

3.3.1 The Jacobian matrix

The computation of local element matrices, compare Subsection 3.3.3, requires the derivatives of the displacement fields in the local coordinate systems (x,y,z). Since the interpolation field of the displacements is defined in natural coordinates (r,s,t), the relation between these (r,s,t) derivatives with respect to the (x,y,z) derivatives has to determined. This relation is defined by the Jacobian matrix $\boldsymbol{J}(r,s,t)$. In case of beam elements the Jacobian matrix reduces to a scalar.

The derivative $\frac{\partial()}{\partial X}$ is written in the form

$$\frac{\partial()}{\partial X} = \frac{\partial()}{\partial r}\frac{\partial r}{\partial X} \ . \tag{3.95}$$

The relation between the derivatives $\frac{\partial()}{\partial X}$ and $\frac{\partial()}{\partial r}$ is given by the term $\frac{\partial r}{\partial X}$, which has to be determined. It follows

$$\frac{\partial r}{\partial X} = \left(\frac{\partial X}{\partial r}\right)^{-1} = \left(\sum_{i=1}^{n} \frac{\partial H_{1i}(r)}{\partial r} X_i\right)^{-1} = J(r)^{-1} \ , \tag{3.96}$$

whereby the inverse of the Jacobian results. X_i is the i-th coordinate of a beam element with n degrees of freedom in the reference configuration and $H_{1i}(r)$ is a corresponding shape function. For the Timoshenko beam element with twelve degrees of freedom the Jacobian yields

$$J(r) = \sum_{i=1}^{12} \frac{\partial H_{1i}(r)}{\partial r} X_i \ . \tag{3.97}$$

3.3.2 Discretization of the displacement and strain field

The nodal displacement vector of the Timoshenko beam element is defined by

$$\hat{\boldsymbol{u}} = \begin{bmatrix} \hat{u}_1 & \hat{v}_1 & \hat{w}_1 & \hat{\theta}_{x1} & \hat{\theta}_{y1} & \hat{\theta}_{z1} & \hat{u}_2 & \hat{v}_2 & \hat{w}_2 & \hat{\theta}_{x2} & \hat{\theta}_{y2} & \hat{\theta}_{z2} \end{bmatrix}^T . \tag{3.98}$$

Using the shape functions derived in Section 3.2, the displacement field $\boldsymbol{u}$ is approximated by

$$\boldsymbol{u} = \boldsymbol{H}(r)\hat{\boldsymbol{u}} . \tag{3.99}$$

Based on the derived Equation (3.10), the interpolation of the strain field $\boldsymbol{\varepsilon}$ of the Timoshenko beam element follows with

$$\boldsymbol{\varepsilon} = J(r)^{-1}\, \boldsymbol{B}(r)\, \hat{\boldsymbol{u}} + \boldsymbol{H}_\theta(r)\, \hat{\boldsymbol{u}} , \tag{3.100}$$

where $\boldsymbol{B}(r)$ is the derivative with respect to r of the shape function matrix $\boldsymbol{H}(r)$,

$$\boldsymbol{B}(r) = \frac{\partial}{\partial r}\left(\boldsymbol{H}(r)\right) . \tag{3.101}$$

According to the Equation (3.10), the strain field depends on the rotations about the y- and z-axis. Hence, the term $\boldsymbol{H}_\theta(r)\, \hat{\boldsymbol{u}}$ has to considered in the strain field. The rotation field $\boldsymbol{H}_\theta(r)$ is defined as

$$\begin{aligned} &H_{\theta_{2j}}(r) = -H_{6j}(r) \quad \forall \quad \{j \in \mathbb{Z} | 1 \leq j \leq 12\} , \\ &H_{\theta_{3j}}(r) = H_{5j}(r) \quad \forall \quad \{j \in \mathbb{Z} | 1 \leq j \leq 12\} , \\ &H_{\theta_{ij}}(r) = 0 \quad \forall \quad \{i \in \mathbb{Z} | i = 1 \wedge 4 \leq i \leq 6\} \ \wedge \ \{j \in \mathbb{Z} | 1 \leq j \leq 12\} . \end{aligned} \tag{3.102}$$

3.3.3 Finite Element formulation of the weak form

Based on the variational formulation (3.44), the dynamic equilibrium of each finite element is derived. Thereby the integral terms are assembled to the global system. The beam is divided into a finite number of of elements n_e. The variational part of the kinetic energy is rewritten as

$$\int_l \delta \boldsymbol{u}^T\, \boldsymbol{M}_t\, \ddot{\boldsymbol{u}}\, dx = \bigcup_{e=1}^{n_e} \int_l \delta \boldsymbol{u}_e^T\, \boldsymbol{M}_t\, \ddot{\boldsymbol{u}}_e\, dx , \tag{3.103}$$

where $e = 1 \ \ldots \ n_e$ is the element number. $\boldsymbol{u}_e$ is the nodal displacement of the element e and $\ddot{\boldsymbol{u}}_e$ is the nodal acceleration of the element e. The variational part of the stain energy is assembled by

$$\int_l \delta \boldsymbol{\varepsilon}^T \boldsymbol{K}_t \boldsymbol{\varepsilon}\, dx = \bigcup_{e=1}^{n_e} \int_l \delta \boldsymbol{\varepsilon}_e^T \boldsymbol{K}_t \boldsymbol{\varepsilon}_e\, dx . \tag{3.104}$$

The nodal strains are noted as $\boldsymbol{\varepsilon}_e$. The variation of the virtual work related to the external forces consists of different parts. These parts depend on external forces, which are composed of body forces $\boldsymbol{f}_L$, forces due to the Neumann boundary conditions $\boldsymbol{t}_{l_\sigma}$ and nodal forces $\hat{\boldsymbol{F}}_{Ni}$. Assembling the integral parts of the body forces of all volume elements e, the forces of all surface elements m applied with a Neumann boundary condition and the nodal forces of all nodes k, the virtual work is noted as

$$\begin{aligned} &\int_l \delta\boldsymbol{u}^T\ \boldsymbol{f}_L\ dx\ + \int_l \delta\boldsymbol{u}_\sigma^T\ \boldsymbol{t}_{l_\sigma}\ dx + \sum_i \delta\boldsymbol{u}_i^T\ \hat{\boldsymbol{F}}_{Ni} = \ \ldots \\ &\bigcup_{e=1}^{n_e} \int_l \delta\boldsymbol{u}_e^T\ \boldsymbol{f}_{Le}\ dx + \bigcup_{m=1}^{n_m} \int_l \delta\boldsymbol{u}_m^T\ \boldsymbol{t}_{l_\sigma m}\ dx + \bigcup_{k=1}^{n_k} \delta\hat{\boldsymbol{u}}_k^T\ \hat{\boldsymbol{F}}_{Nk}\ . \end{aligned} \tag{3.105}$$

The first variation of the functional $\mathfrak{S}$ for the Timoshenko beam noted in Equation (3.44) has to be discretized in order to achieve a system of equations for the dynamic equilibrium. Therefore, the discretization of the displacement field in Equation (3.99) and of the strain field in Equation (3.101) are applied to the variational formulation. For the variational part of the kinetic energy follows

$$\begin{aligned} &\int_l \delta\boldsymbol{u}^T\ \boldsymbol{M}_t\ \ddot{\boldsymbol{u}}\ dx = \bigcup_{e=1}^{n_e} \int_l \hat{\boldsymbol{u}}_e^T\ \boldsymbol{H}(r)^T\ \boldsymbol{M}_t\ \boldsymbol{H}(r)\ \ddot{\hat{\boldsymbol{u}}}_e\ dx = \ldots \\ &\bigcup_{e=1}^{n_e} \delta\hat{\boldsymbol{u}}_e^T \underbrace{\int_{-1}^{1} \boldsymbol{H}(r)^T\ \boldsymbol{M}_t\ \boldsymbol{H}(r)\ \det J(r)\ dr}_{\boldsymbol{M_e}}\ \ddot{\hat{\boldsymbol{u}}}_e\ . \end{aligned} \tag{3.106}$$

The shape functions are derived in a natural coordinate system, compare Section 3.2, thus it is necessary to evaluate the integral in an interval of -1 to 1 and the determinate of the Jacobian matrix has to be considered. The evaluated integral yields the element mass matrix

$$\boldsymbol{M_e} = \int_{-1}^{1} \boldsymbol{H}(r)^T\ \boldsymbol{M}_t\ \boldsymbol{H}(r)\ \det J(r)\ dr\ . \tag{3.107}$$

The discretization of the variational part of the strain energy gives

$$\begin{aligned}
&\int_l \delta\boldsymbol{\varepsilon}^T \boldsymbol{K}_t \boldsymbol{\varepsilon}\, dx = \bigcup_{e=1}^{n_e} \int_l \delta\boldsymbol{\varepsilon}_e^T \boldsymbol{K}_t \boldsymbol{\varepsilon}_e\, dx = \dots \\
&\bigcup_{e=1}^{n_e} \int_l \delta\hat{\boldsymbol{u}}_e^T \left(\boldsymbol{H}_\theta(r)^T + J(r)^{-1}\boldsymbol{B}(r)^T\right) \boldsymbol{K}_t \left(J(r)^{-1}\boldsymbol{B}(r) + \boldsymbol{H}_\theta(r)\right) \hat{\boldsymbol{u}}_e\, dx = \dots \\
&\bigcup_{e=1}^{n_e} \delta\hat{\boldsymbol{u}}_e^T \underbrace{\int_{-1}^{1} \left(\boldsymbol{H}_\theta(r)^T + J(r)^{-1}\boldsymbol{B}(r)^T\right) \boldsymbol{K}_t \left(J(r)^{-1}\boldsymbol{B}(r) + \boldsymbol{H}_\theta(r)\right) \det J(r)\, dr\, \hat{\boldsymbol{u}}_e}_{\boldsymbol{K_e}} .
\end{aligned} \tag{3.108}$$

The element stiffness matrix is obtained by the evaluation of the integral,

$$\boldsymbol{K_e} = \int_{-1}^{1} \left(\boldsymbol{H}_\theta(r)^T + J(r)^{-1}\boldsymbol{B}(r)^T\right) \boldsymbol{K}_t \left(J(r)^{-1}\boldsymbol{B}(r) + \boldsymbol{H}_\theta(r)\right) \det J(r)\, dr\ . \tag{3.109}$$

According to the isoparametric concept, the interpolation of the forces uses the same shape functions $\boldsymbol{H}(r)$ as the displacement field. The variation of the virtual work related to the body forces is discretized by

$$\begin{aligned}
&\int_l \delta\boldsymbol{u}^T\, \boldsymbol{f}_L\, dx = \bigcup_{e=1}^{n_e} \int_l \delta\boldsymbol{u}_e^T\, \boldsymbol{f}_{Le}\, dx = \bigcup_{e=1}^{n_e} \int_l \delta\hat{\boldsymbol{u}}_e^T\, \boldsymbol{H}(r)\, \boldsymbol{f}_{Le}\, dx = \dots \\
&\bigcup_{e=1}^{n_e} \delta\hat{\boldsymbol{u}}_e^T \underbrace{\int_{-1}^{1} \boldsymbol{H}(r)\, \boldsymbol{f}_{Le}\, \det J(r)\, dr}_{\hat{\boldsymbol{F}}_{Be}} ,
\end{aligned} \tag{3.110}$$

where the element body force is given by

$$\hat{\boldsymbol{F}}_{Be} = \int_{-1}^{1} \boldsymbol{H}(r)\, \boldsymbol{f}_{Le}\, \det J(r)\, dr\ . \tag{3.111}$$

Analogously to the variation of the virtual work related to body forces, the discretization of the variation of the virtual work related to Neumann boundary conditions is given by

$$\begin{aligned}
&\int_l \delta\boldsymbol{u}_\sigma^T\, \boldsymbol{t}_{l_\sigma}\, dx = \bigcup_{m=1}^{n_m} \int_l \delta\boldsymbol{u}_m^T\, \boldsymbol{t}_{l_\sigma m}\, dx = \bigcup_{m=1}^{n_m} \int_l \delta\hat{\boldsymbol{u}}_m^T\, \boldsymbol{H}(r)\, \boldsymbol{t}_{l_\sigma m}\, dx = \dots \\
&\bigcup_{m=1}^{n_m} \delta\hat{\boldsymbol{u}}_m^T \underbrace{\int_{-1}^{1} \boldsymbol{H}(r)\, \boldsymbol{t}_{l_\sigma m}\, \det J(r)\, dr}_{\hat{\boldsymbol{F}}_{Se}} ,
\end{aligned} \tag{3.112}$$

where the surface forces of the Neumann boundary condition

$$\hat{\boldsymbol{F}}_{Se} = \int_{-1}^{1} \boldsymbol{H}(r)\ \boldsymbol{t}_{l_\sigma m}\ \det J(r)\ dr \tag{3.113}$$

is obtained. The variational formulation of the functional $\mathfrak{S}$ is rewritten as

$$\begin{aligned}\delta\mathfrak{S} = \int_{t_0}^{t_1} \Bigg(&- \bigcup_{e=1}^{n_e} \delta\hat{\boldsymbol{u}}_e^T \boldsymbol{M_e}\ \ddot{\boldsymbol{u}}_e - \bigcup_{e=1}^{n_e} \delta\hat{\boldsymbol{u}}_e^T \boldsymbol{K_e}\ \hat{\boldsymbol{u}}_e + \bigcup_{e=1}^{n_e} \delta\hat{\boldsymbol{u}}_e^T \hat{\boldsymbol{F}_{Be}} + \ \ldots \\ &\bigcup_{m=1}^{n_m} \delta\hat{\boldsymbol{u}}_m^T \hat{\boldsymbol{F}_{Se}} + \bigcup_{k=1}^{n_k} \delta\hat{\boldsymbol{u}}_k^T\ \hat{\boldsymbol{F}}_{Nk} \Bigg)\ dt = 0\end{aligned} \tag{3.114}$$

and after assembling the expression of the functional noted as

$$\delta\mathfrak{S} = \int_{t_0}^{t_1} \delta\hat{\boldsymbol{u}}^T \left(-\boldsymbol{M}\ \ddot{\hat{\boldsymbol{u}}} - \boldsymbol{K}\ \hat{\boldsymbol{u}} + \hat{\boldsymbol{F}} \right)\ dt = 0\ . \tag{3.115}$$

The stationarity of this functional is only satisfied if the expression in the brackets getting zero. The equation of motion is obtained:

$$\boldsymbol{M}\ \ddot{\hat{\boldsymbol{u}}} + \boldsymbol{K}\ \hat{\boldsymbol{u}} = \boldsymbol{F}\ . \tag{3.116}$$

3.4 Example: Isotropic cantilevered beam with load on the free end

Based on the above introduced beam element, the capability of these elements are illustrated on an example of an isotropic cantilevered beam with a load on the free end. Figure 3.5 shows a sketch of the three-dimensional cantilever beam. The beam

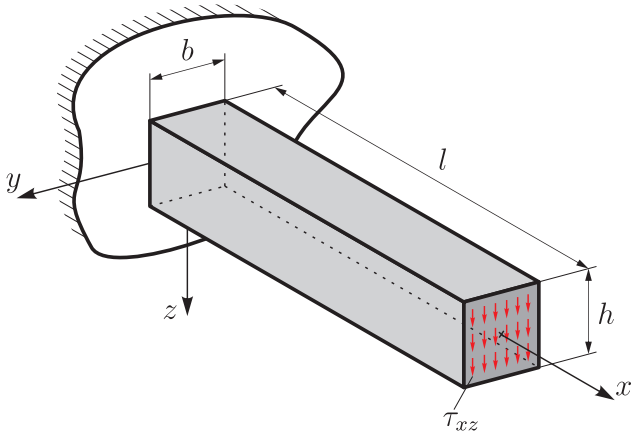

Figure 3.5: Cantilever beam with constant load on the free end

has a length of l, a width of b and a hight of h. In the initial configuration the cross

section of the beam at the position $x = 0$ is clamped. The volume load is neglected and a distributed surface load τ_{xz} is applied on the cross section of the free end. Table 3.1 summarizes the used parameters for the static simulation of the cantilever beam. The finite element solution using Timoshenko beam elements (FE1DTB) is

Table 3.1: Parameters of isotropic cantileverd beam

parameter	value
length l	10 mm
width b	1 mm
height h	1 mm
shear correction factor κ_y	0.8307
shear correction factor κ_z	0.8307
Young's modulus E	1×10^5 N/mm^2
Poisson's ratio ν	0.2
surface load τ_{xz}	1 MPa

compared with the solution of analytical and numerical methods. The analytical methods are the classical Euler-Bernoulli beam theory (EBT) and the Timoshenko beam theory (TBT). For the numerical methods the finite element solutions of three-dimensional models with different mesh sizes are computed. Therefore, the beam is modeled using three-dimensional 8 node brick elements with a uniform mesh of $5 \times 5 \times 50$ elements (FE3D02), a uniform mesh of $10 \times 10 \times 100$ elements (FE3D01) and a uniform mesh of $50 \times 50 \times 500$ elements (FE3Dref). The solution of this very fine meshed model is used as the reference solution.

In order to be able to consider the nodal displacements of the analytical beam models, the model of the one-dimensional Timoshenko beam and the three-dimensional finite element models, the mean values of cross section displacements are determined

$$\overline{w}(x) = \frac{\int_\Omega \boldsymbol{H}_w^T \, \boldsymbol{w}(x) \, dA}{\int_\Omega dA} \, , \tag{3.117}$$

where A is the area cross section, $\boldsymbol{H}_w$ are the shape function according to the displacement field $\boldsymbol{w}$ evaluated at the longitudinal position x of the beam. Additionally, the relative errors

$$e_{wrel} = \frac{|w - w_{ref}|}{|w_{ref}|} \tag{3.118}$$

of the shear displacements w are determined, where w_{ref} is the shear displacement of the reference solution.

The comparison of the shear displacements $w(l)$ of the cross section of the free end is carried out for all beam models and summarized in Table 3.1. The two analytical models give a relative error under 5 ‰. As expected the Timoshenko beam theory and the one-dimensional finite element solution using Timoshenko beam element

Table 3.2: Comparison of shear displacements $w(l)$ of different beam models

Beam model	$w(10)$ in mm	e_{wrel}
Euler-Bernoulli (EBT)	4.0000×10^{-2}	4.554×10^{-3}
Timoshenko (TBT)	4.0289×10^{-2}	2.636×10^{-3}
FE 1D Timoshenko beam elements ($^h/_l = 1$) (FE1DTB)	4.0289×10^{-2}	2.636×10^{-3}
FE 3D model (mesh $5 \times 5 \times 50$) (FE3D02)	4.1814×10^{-2}	40.589×10^{-3}
FE 3D model (mesh $10 \times 10 \times 100$) (FE3D01)	4.0566×10^{-2}	9.531×10^{-3}
FE 3D model (mesh $50 \times 50 \times 500$) (FE3Dref)	4.1814×10^{-2}	-

delivers identical results. This is due to the fact that the shape functions are derived from the Timoshenko beam. The element size of the beam elements is chosen with $^h/_l = 1$. The resulting error of the shear displacement for these two models is 2.636 ‰. The error of the three-dimensional solution increases significantly with a coarser mesh.

Figure 3.6a depicts the bending line of the isotropic cantilevered beam solved with different methods. With the exception of the coarse three-dimensional finite element model (FE3D02), all solutions are very close together. The corresponding errors are plotted in Figure 3.6b. The error of the model with Timoshenko beam elements and the Timoshenko beam theory match exactly. Further, the error decreases for larger x values. This effect is stronger for the analytical solutions than for the three-dimensional finite element solution of FE3D01. Even the solution of the FE3D02 has a small increase in the error.

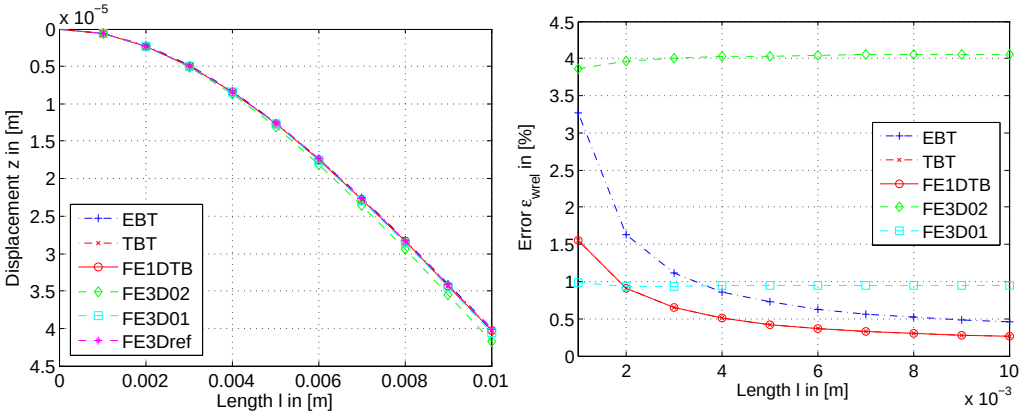

(a) Displacements of the isotropic cantilevered beam

(b) Relative errors of different beam models

Figure 3.6: Bending of the isotropic cantilevered beam using Timoshenko beam elements in comparison with different beam models

Figure 3.7 depicts the error of the Timoshenko beam element with respect to the

ratio of the beam height to the beam length h/l. A monotonic convergence behavior of the shear displacement error is shown.

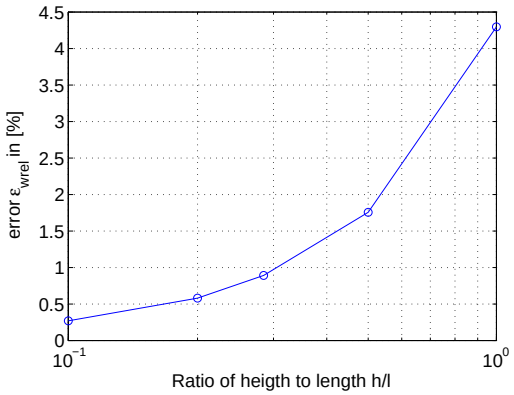

Figure 3.7: Relative error ε_{wrel} as a function of the ratio of height to length h/l

CHAPTER 4

Cross section parameters for beam elements of arbitrary shapes

The problem of shear stresses due to torsional and flexural shearing in prismatic beams has been pointed out by various authors in a number of publications [192],[191], [184] and [59] based on the Saint-Venant theory of torsion and torsionless bending. There is no formulation for the twist center or the shear center in the theories of the Saint-Venant torsion and the torsionless bending for a uniform cross section, respectively. The problem of the shear center and twist center has also been discussed in several works [151], [198].

In this chapter, the shear stresses in prismatic beams are computed. The linear elastic material of the investigated beams has isotropic properties. Two separate causes resulting in shear stresses are considered: on the one hand the Saint-Venant torsion problem and on the other hand the torsionless bending problem. The shear stresses are determined for both problems using stress functions. In order to determine these stress functions, the weak form of a boundary value problem is formulated [62]. Using the finite element method, the shear stresses are computed for completely arbitrary shapes of cross sections with arbitrary coordinate systems. Furthermore, the known stress functions allow for the determination of the shear center and the shear correction factor. A proof is given that the shear center and the center of twist are identical. Finally, the shear stresses are computed for a defined cross section for an example.

4.1 Shear stresses in arbitrary cross sections

The Saint-Venant torsion problem and the torsionless bending problem of prismatic beams with arbitrary cross sections are formulated. The weak form of the resulting boundary value problem is derived. Using the finite element method, the shear stresses are computed approximately.

4.1.1 Basic assumptions for prismatic beams with arbitrary cross sections

The arbitrary cross section Ω of a prismatic beam is depicted in Figure 4.1. The beam axis is denoted by x and positions on the cross sections are marked by the y- and z-coordinates. An additional coordinate system is defined parallel in the centroid of the cross section C by the position vector $\boldsymbol{r}_C = [\ 0 \quad y_C \quad z_C\ ]^T$. The outward normal vector $\boldsymbol{n}_o = [\ 0 \quad n_{oy} \quad n_{oz}\ ]^T$ and the tangent vector $\boldsymbol{t}_o = [\ 0 \quad t_{oy} \quad t_{oz}\ ]^T$ of a right-hand-sided coordinate system are placed on the outer boundary of the cross section $\partial\Omega_o$. The inward normal vector $\boldsymbol{n}_i = [\ 0 \quad n_{iy} \quad n_{iz}\ ]^T$ is placed on an inner boundary $\partial\Omega_i$ and shows in the opposite direction as compared to the outward normal vector $\boldsymbol{n}_o$. The orientation of the inward tangent vector is opposite $\boldsymbol{t}_i = [\ 0 \quad t_{iy} \quad t_{iz}\ ]^T$. The boundaries $\partial\Omega_i$ and $\partial\Omega_o$ are summarized in $\partial\Omega = \partial\Omega_o \bigcup \partial\Omega_i$.

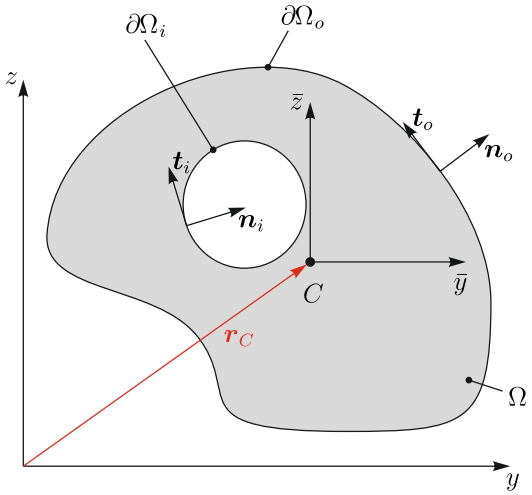

Figure 4.1: Arbitrary cross section Ω of a prismatic beam

Neglecting the volume and inertia forces, the momentum of balance in Equation (3.34) becomes

$$\nabla\boldsymbol{\sigma} = 0\ , \tag{4.1}$$

and can be written differently in scalar equations as

$$\begin{aligned} \sigma_{x,x} + \tau_{xy,y} + \tau_{xz,z} &= 0 \\ \sigma_{y,y} + \tau_{yz,z} + \tau_{xy,x} &= 0 \\ \sigma_{z,z} + \tau_{xz,x} + \tau_{yz,y} &= 0\ . \end{aligned} \tag{4.2}$$

Assuming a prismatic beam the components σ_y, σ_z and τ_{yz} vanish in Equation (4.2). Thus, the boundary condition of cross section

$$\tau_{xy}dz - \tau_{xz}dy = 0 \qquad \text{on } \partial\Omega \tag{4.3}$$

has to be complied with $dz = n_y d\vartheta$ and $dy = -n_z d\vartheta$, where the coordinate ϑ :

$\partial\Omega \rightarrow \mathbb{R}$ defines the arc length of the boundary. Furthermore, the shear stresses τ_{xy} and τ_{xz} are independent from the coordinate x.

4.1.2 Saint-Venant torsion

A cantilevered beam is loaded with a constant torque imposed on the free end of the beam, which is defined as

$$M_T = \int_{\Omega} (-z\tau_{xy} + y\tau_{xz})\, dA \ . \tag{4.4}$$

The beam can be deformed unimpeded and a pure torque is acting in any cross section of the beam. The displacement field for a cantilevered beam under torsion, considering Equation (3.7), is given by

$$\overline{\boldsymbol{u}} = \begin{bmatrix} u(x,y,z) \\ v(x,y,z) \\ w(x,y,z) \end{bmatrix} = \begin{bmatrix} \alpha\, \psi(y,z) \\ -z\, \theta_x \\ +y\, \theta_x \end{bmatrix} \ . \tag{4.5}$$

$\psi(y,z)$ is the warping function. The expression α denotes the derivative of the torsion angle with respect to the beam axis $\alpha = \theta_{x,x}$.

4.1.2.1 Shear stresses

The strains related to torsion are computed by using the displacement vector in Equation (4.5) and the strain-displacement relation in Equation (3.8). The resulting strains are summarized in the vector

$$\boldsymbol{\epsilon} = \begin{bmatrix} \gamma_{xy} \\ \gamma_{xz} \end{bmatrix} = \alpha \begin{bmatrix} \psi(y,z)_{,y} - z \\ \psi(y,z)_{,z} + y \end{bmatrix} \ . \tag{4.6}$$

All the remaining components of the strains ϵ_x, ϵ_y, ϵ_z and γ_{yz} are equal zero.

According to the material law of Equation (3.12) with $G_{xy} = G_{xz}$ and imposing the strains γ_{xy} and γ_{xz} of Equation (4.6), the shear stresses for the cantilevered beam under torque are obtained as

$$\boldsymbol{\tau} = \begin{bmatrix} \tau_{xy} \\ \tau_{xz} \end{bmatrix} = \alpha\, G \begin{bmatrix} \psi(y,z)_{,y} - z \\ \psi(y,z)_{,z} + y \end{bmatrix} \ . \tag{4.7}$$

The boundary condition in Equation (4.3) is satisfied by writing the shear stresses in terms of Prandl's stress function Φ [113], where

$$\tau_{xy} = \phi_{,z} \qquad \text{and} \qquad \tau_{xz} = -\phi_{,y} \ . \tag{4.8}$$

Imposing Prandl's stress function to Equation (4.7), a relation between Prandl's stress function and the warping function

$$\begin{bmatrix} \phi_{,z} \\ \phi_{,y} \end{bmatrix} = \alpha\, G \begin{bmatrix} \psi(y,z)_{,y} - z \\ -\psi(y,z)_{,z} - y \end{bmatrix} , \tag{4.9}$$

is obtained. After a second partial derivative of Prandl's stress function, the Poisson's equation

$$\Delta\phi = -2\, G\, \alpha \tag{4.10}$$

is found. [178]

Rewriting the boundary condition in Equation (4.3) with Equation (4.8) one obtains

$$-\tau_{xz}\, dy + \tau_{xy}\, dz = \phi_{,y}\, dy + \phi_{,z}\, dz = d\phi = 0 . \tag{4.11}$$

Hence, the Prandl's stress function is constant on the boundary and does not influence the stresses. The stress function ϕ may set to be zero on the outer boundary $\partial\Omega_o$. For cross sections with cavities, only the outer boundary may be set to zero. ϕ takes different values along each inner boundary. These values are determined by the condition that the displacement u along the inner boundary must be continuous [62].

The relation for Prandl's stress function in Equation (4.8) is imposed on Equation (4.4). Applying the product rule to the derivatives, the torque becomes

$$M_x = -\int_\Omega (y\phi_{,y} + z\phi_{,z})\; dA = -\int_\Omega ((y\phi)_{,y} + (z\phi)_{,z})\; dA + 2\int_\Omega \phi\, dA . \tag{4.12}$$

Gauss's theorem applied to the last expression of the torque leads to

$$M_x = -\oint_{\partial\Omega} \phi\; (y\, n_y + z\, n_z)\; d\vartheta + 2\int_\Omega \phi\, dA . \tag{4.13}$$

The first part of this equation describes the integration over the boundary $\partial\Omega$ and the second part the integration over the surface Ω. Due to the fact that ϕ is zero on the boundary $\partial\Omega$ for full cross sections, the torque is simply determined by

$$M_x = 2\int_\Omega \phi\, dA \tag{4.14}$$

for this case.

Imposing the coordinate transformation $y' = y - y_M$ and $z' = z - z_M$ in Equation

(3.14) and assuming that the beam is free of shear forces $Q_y = Q_z = 0$, the torque is expressed by

$$M_x = \int_\Omega \left(\tau_{xz}\ y - \tau_{xy}\ z\right)\ dA = G\ \alpha \int_\Omega \left(y^2 + z^2 + y\ \psi(y,z)_{,z} - z\ \psi(y,z)_{,y}\right)\ dA\ . \tag{4.15}$$

The integral part

$$I_T = \int_\Omega \left(y^2 + z^2 + y\ \psi(y,z)_{,z} - z\ \psi(y,z)_{,y}\right)\ dA \tag{4.16}$$

yields the Saint-Venant torsion stiffness I_T, which is a parameter of the cross section. The relation between the torsion and torque is given by

$$\alpha = \frac{M_x}{G\ I_T}\ . \tag{4.17}$$

4.1.2.2 Warping function

Using the shear stresses in Equation (4.7) and assuming isotropic material behavior, the equation of the momentum of balance (4.2) yields the strong form of the Neumann boundary value problem [10]

$$\psi_{,yy} + \psi_{,zz} = \Delta\psi = 0 \quad \text{in } \Omega\ , \tag{4.18}$$

with the boundary condition

$$n_y\ \psi_{,y} + n_z\ \psi_{,z} = n_y\ z - n_z\ y \quad \text{in } \partial\Omega\ . \tag{4.19}$$

If the boundary condition is formulated in the special form $f(y,z) = 0$ with Δf =const., a closed-form solution exists.

It is required that the warping function has to fulfill the constraint

$$\int_\Omega \psi(y,z)\ dA = 0\ . \tag{4.20}$$

The warping function is normalized by

$$\bar{\psi} = \psi - \frac{1}{A}\int_\Omega \psi\ dA, \tag{4.21}$$

where $\bar{\psi}$ is the unit warping function. The normalized unit warping also fulfills the constraint of Equation (4.20) and

$$\int_\Omega \bar{\psi}(y,z)\ dA = 0 \tag{4.22}$$

holds. Defining the coordinates of the center of twist with y_T and z_T, the unit warping function is transformed in relation to the center of twist by

$$\tilde{\psi} = \bar{\psi} + y_T \bar{z} - z_T \bar{y} \ . \tag{4.23}$$

The center of twist is the point of rest in pure torsion of a beam. In this case, the beam is free of normal forces and bending moments. According to Equation (3.14), N, M_y and M_z have to be zero, which yields orthogonal conditions

$$\int_\Omega \tilde{\psi} \, dA = 0 \ , \tag{4.24}$$

$$\int_\Omega \tilde{\psi} \, y \, dA = 0 \tag{4.25}$$

and

$$\int_\Omega \tilde{\psi} \, z \, dA = 0 \ . \tag{4.26}$$

In order to determine the coordinates of the center of twist y_T and z_T, a linear system of equation is formulated with equations (4.25) and (4.26),

$$\int_\Omega \tilde{\psi} \, y \, dA = \int_\Omega \tilde{\psi} \, \bar{y} \, dA = \int_\Omega \left(\bar{\psi}\bar{y} + y_T \bar{y}\bar{z} - z_T \bar{y}^2 \right) \, dA = 0 \tag{4.27}$$

and

$$\int_\Omega \tilde{\psi} \, z \, dA = \int_\Omega \tilde{\psi} \, \bar{z} \, dA = \int_\Omega \left(\bar{\psi}\bar{z} + y_T \bar{z}^2 - z_T \bar{y}\bar{z} \right) \, dA = 0 \ . \tag{4.28}$$

The notation $I_{\zeta\xi} = \int_\Omega \zeta\xi \, dA$ is now introduced. Hence, the center of twist is given by

$$y_T = -\frac{I_{\bar{\psi}\bar{z}} \, I_{\bar{y}\bar{y}} - I_{\bar{\psi}\bar{y}} \, I_{\bar{y}\bar{z}}}{I_{\bar{y}\bar{y}} \, I_{\bar{z}\bar{z}} - I_{\bar{y}\bar{z}}^2} \ , \qquad z_T = \frac{I_{\bar{\psi}\bar{y}} \, I_{\bar{z}\bar{z}} - I_{\bar{\psi}\bar{z}} \, I_{\bar{y}\bar{z}}}{I_{\bar{y}\bar{y}} \, I_{\bar{z}\bar{z}} - I_{\bar{y}\bar{z}}^2} \ . \tag{4.29}$$

The expressions $I_{\bar{y}\bar{y}}$ and $I_{\bar{z}\bar{z}}$ confirm the second moments of area $I_{\bar{z}}$ and $I_{\bar{y}}$, respectively.

The warping constant C_M related to the center of shear is determined by

$$C_M = \int_\Omega \tilde{\psi} \, \tilde{\psi} \, dA \ . \tag{4.30}$$

4.1.3 Torsionless bending

Following the linear beam theory, the normal stress σ_x is defined by a linear combination of two constant expressions with respect to $\bar{y}$ and $\bar{z}$ [90]. The normal stress is defined as

$$\sigma_x = \frac{M_y\, I_{\bar{z}} + M_z\, I_{\bar{y}\bar{z}}}{I_{\bar{y}}\, I_{\bar{z}} - I_{\bar{y}\bar{z}}^2}\bar{z} - \frac{M_z\, I_{\bar{y}} + M_y\, I_{\bar{y}\bar{z}}}{I_{\bar{y}}\, I_{\bar{z}} - I_{\bar{y}\bar{z}}^2}\bar{y}\ . \tag{4.31}$$

A derivation of the normal stress σ_x with respect to the coordinate x of the beam axis leads to

$$\sigma_{x,x} = \frac{Q_y\, I_{\bar{y}} - Q_z\, I_{\bar{y}\bar{z}}}{I_{\bar{y}}\, I_{\bar{z}} - I_{\bar{y}\bar{z}}^2}\bar{y} + \frac{Q_z\, I_{\bar{z}} - Q_y\, I_{\bar{y}\bar{z}}}{I_{\bar{y}}\, I_{\bar{z}} - I_{\bar{y}\bar{z}}^2}\bar{z}\ , \tag{4.32}$$

while taking $M_{y,x} = Q_z$ and $M_{z,x} = -Q_y$ into account [114]. The linear coefficients are summarized in

$$a_1 = \frac{Q_y\, I_{\bar{y}} - Q_z\, I_{\bar{y}\bar{z}}}{I_{\bar{y}}\, I_{\bar{z}} - I_{\bar{y}\bar{z}}^2} \quad \text{and} \quad a_2 = \frac{Q_z\, I_{\bar{z}} - Q_y\, I_{\bar{y}\bar{z}}}{I_{\bar{y}}\, I_{\bar{z}} - I_{\bar{y}\bar{z}}^2} \tag{4.33}$$

and the linear combination is written by a function

$$f_1(\bar{y},\bar{z}) = a_1\ \bar{y} + a_2\ \bar{z}\ . \tag{4.34}$$

The derivative is now expressed by terms of this function $f_1(\bar{y},\bar{z})$ with

$$\sigma_{x,x} = f_1(\bar{y},\bar{z})\ . \tag{4.35}$$

The shear stresses are assumed to be

$$\tau_{xy} = \Psi_{,z} - \frac{1}{2}\, a_1\, \bar{y}^2 \quad \text{and} \quad \tau_{xz} = -\Psi_{,y} - \frac{1}{2}\, a_2\, \bar{z}^2\ , \tag{4.36}$$

where Ψ is an unknown stress function. This stress function has to be selected such that the equilibrium of Equation (4.2) is satisfied [62]. According to this momentum of balance in Equation (4.2), the rest of the stress components σ_y, σ_z and τ_{xy} are zero:

$$\sigma_y = \sigma_z = \tau_{xy} = 0\ . \tag{4.37}$$

Assuming isotropic linear elasticity, the stress function Ψ has to observe the Beltrami-Michell compatibility conditions [147]. In case of the beam theory one has to use the two equations

$$(1+\nu)\ \Delta\tau_{xy} + (\sigma_x + \sigma_y + \sigma_z)_{,xy} = 0 \tag{4.38}$$

and

$$(1+\nu)\ \Delta\tau_{xz} + (\sigma_x + \sigma_y + \sigma_z)_{,xz} = 0 \tag{4.39}$$

of the Beltrami-Michell compatibility conditions, where ν denotes the Poisson ratio.

The other four equations of these compatibility conditions are satisfied. Using the equations (4.38) and (4.39), derivatives of the stress function

$$\Delta\Psi_{,y} = \frac{\nu}{1+\nu} a_2 \quad \text{and} \quad \Delta\Psi_{,z} = \frac{\nu}{1+\nu} a_1 \tag{4.40}$$

are found. These terms are integrated with respect to $\bar{y}$ and $\bar{z}$ which gives the function $f_2(y,z)$ in form of

$$f_2(y,z) = \frac{\nu}{1+\nu} \left(a_1 \left(z - z_0 \right) - a_2 \left(y - y_0 \right) \right) \ . \tag{4.41}$$

y_0 and z_0 are integration constants. According to Figure 4.1, the differences of the cross section coordinates $\bar{y} - \bar{y}_0$ and $\bar{z} - \bar{z}_0$ are equal to $y - y_0$ and $z - z_0$, respectively. One determines the boundary conditions of the stress function by substituting the shear stresses determined in Equation (4.36) into Equation (4.3). This leads to the conditions

$$\left(\Psi_{,z} - \frac{1}{2} \, a_1 \, \bar{y}^2 \right) dz - \left(-\Psi_{,y} - \frac{1}{2} \, a_2 \, \bar{z}^2 \right) dy = 0 \ . \tag{4.42}$$

This expression is integrated with respect to $\bar{y}$ and $\bar{z}$ and yields $\Psi(\bar{y},\bar{z})$ for the boundary. Now, the Dirichlet problem

$$\Delta\Psi = f_2(y,z) \qquad \text{in } \Omega \tag{4.43}$$

with

$$\Psi(\vartheta) = \Psi_0 + \frac{1}{2} \left(a_1 \, \bar{y}^2 \bar{z} - a_2 \, \bar{z}^2 \bar{y} \right) \qquad \text{on } \partial\Omega \tag{4.44}$$

is formulated. As in the discussion of Prandl's stress function, the constant Ψ_0 may set to be zero for outer boundaries $\partial\Omega_o$. For cross sections with cavities, the constant Ψ_0 may also set to be zero on the outer boundary. Ψ_0 takes different values along each inner boundary.

Introducing a conjugate stress function $\bar{\Psi}$ [62], the shear stresses of the Dirichlet problem are transformed into

$$\tau_{xy} = \Psi_{,z} - \frac{1}{2} \, a_1 \, \bar{y}^2 = \bar{\Psi}_{,y} - g_1(z) \tag{4.45}$$

and

$$\tau_{xz} = -\Psi_{,y} - \frac{1}{2} \, a_2 \, \bar{z}^2 = \bar{\Psi}_{,z} + g_2(y) \ . \tag{4.46}$$

The functions $g_1(z)$ and $g_2(y)$ take the form

$$g_1(z) = -\frac{1}{2} \frac{\nu}{1+\nu} \, a_1 \, (z - z_0)^2 \tag{4.47}$$

and

$$g_2(y) = \frac{1}{2} \frac{\nu}{1+\nu} \, a_2 \, (y - y_0)^2 \ . \tag{4.48}$$

This transformation holds the Poisson Equation (4.43). The differential equation is expressed in terms of $\bar{\Psi}$ and a Neumann problem

$$\Delta\bar{\Psi} = -f_1(y,z) \qquad \text{in } \Omega \tag{4.49}$$

is found. The boundary condition

$$n_y\ \bar{\Psi}_{,y} + n_z\ \bar{\Psi}_{,z} = n_y\ g_1(z) - n_z\ g_2(y) \qquad \text{on } \partial\Omega \tag{4.50}$$

results by substituting the equations (4.45) and (4.46) into Equation (4.3).

In order to solve for the stress function Ψ the integration constants y_0 and z_0 have to be determined. The procedure for the determination of these constants follows. The beam is loaded by torsionless bending, which claims that the torque in Equation (3.14) has to be zero. The condition for torsionless bending

$$\int_\Omega (\tau_{xz}\ y - \tau_{xy}\ z)\ dA = 0 \tag{4.51}$$

must hold. Based on Equation (4.9), one introduces a relation of the torsion function Φ and the cross section coordinates y and z with

$$y = -\Phi_{,y} - \bar{\psi}_{,z} \quad \text{and} \quad z = -\Phi_{,z} + \bar{\psi}_{,y}\ , \tag{4.52}$$

where the torsional function Φ is defined as

$$\Phi_{,y} = \frac{\phi_{,y}}{\alpha G} \qquad \text{and} \qquad \Phi_{,z} = \frac{\phi_{,z}}{\alpha G}\ . \tag{4.53}$$

This relation is employed on the condition of torsionless bending. Therefore, the Equation (4.51) may be rewritten as

$$\int_\Omega \left(\tau_{xz}\left(-\Phi_{,y} - \bar{\psi}_{,z}\right) - \tau_{xy}\left(-\Phi_{,z} + \bar{\psi}_{,y}\right)\right)\ dA = 0\ . \tag{4.54}$$

The shear stresses of equations (4.45) and (4.46) are introduced in the condition for torsionless bending. Applying the Gauss's theorem on the condition above, the relation

$$\begin{aligned}
&\int_\Omega \left(\bar{\Psi}_{,y}\Phi_{,z} - \bar{\Psi}_{,z}\Phi_{,y}\right) dA - \oint_{\partial\Omega} \left(n_y\Phi_{,z} - n_z\Phi_{,y}\right)\ \bar{\Psi}\ d\vartheta - \dots \\
&\int_\Omega \left(\left(\bar{\Psi}_{,y} - g_1\right)\bar{\psi}_{,y} + \left(\bar{\Psi}_{,z} + g_2\right)\bar{\psi}_{,z}\right) dA + \dots \\
&\oint_{\partial\Omega} \left(n_y\left(\Phi_{,y} - g_1\right) + n_z\left(\Phi_{,z} + g_2\right)\right)\bar{\psi}\ d\vartheta - \int_\Omega \left(g_1\ \Phi_{,z} + g_2\ \Phi_{,y}\ \right)\ dA = 0
\end{aligned} \tag{4.55}$$

follows. Applying the equations (4.19), (4.49) and (4.50), the boundary integrals vanish. Taking Green's theorem into account, the relation

$$\int_\Omega (\Phi_{,yz} - \Phi_{,yz})\,\bar{\Psi}\; dA - \int_\Omega \Delta\bar{\Psi}\;\bar{\psi}\; dA - \int_\Omega (g_1\;\Phi_{,z} + g_2\;\Phi_{,y}\;)\; dA = 0\;. \tag{4.56}$$

is determined. The first integral vanishes because the expression in the brackets is zero. The second integral is also zero, considering the orthogonal conditions of equations (4.24), (4.25) and (4.26). Thus, the third integral remains

$$\frac{\nu}{2(1+\nu)} \int_\Omega \left(\Phi_{,z}\; a_1\;(z-z_0)^2 - \Phi_{,y}\; a_2\;(y-y_0)^2\right)\; dA = 0\;, \tag{4.57}$$

where the functions g_1 and g_2 are given in the equations (4.47) and (4.48). Furthermore, the expressions

$$\begin{aligned}
K_y &= -\int_\Omega \Phi_{,y}\; y\; dA = \int_\Omega \left(\bar{\psi}_{,z} + y\right)\; y\; dA \\
K_{yy} &= -\int_\Omega \Phi_{,y}\; y^2\; dA = \int_\Omega \left(\bar{\psi}_{,z} + y\right)\; y^2\; dA \\
K_z &= \int_\Omega \Phi_{,z}\; z\; dA = \int_\Omega \left(\bar{\psi}_{,y} - z\right)\; z\; dA \\
K_{zz} &= \int_\Omega \Phi_{,z}\; z^2\; dA = \int_\Omega \left(\bar{\psi}_{,y} - z\right)\; z^2\; dA
\end{aligned} \tag{4.58}$$

are introduced. The integration of the derivatives of the torsional function Φ with respect to y and z over the cross section Ω disappears [62]

$$\int_\Omega \Phi_{,y}\; dA = 0 \quad \text{and} \quad \int_\Omega \Phi_{,z}\; dA = 0\;. \tag{4.59}$$

Considering these conditions and the introduced constants of Equation (4.58), the relation in Equation (4.57) is rewritten as

$$\frac{\nu}{2(1+\nu)}\,(a1(K_{zz} - 2\;z_0\;K_z) + a_2(K_{yy} - 2\;y_0\;K_y)) = 0\;. \tag{4.60}$$

Due to the fact that the constants a_1 and a_2 are not zero, the condition is only fulfilled if both terms in brackets are zero. This gives the integral constants

$$y_0 = \frac{K_{yy}}{2K_y} \quad \text{and} \quad z_0 = \frac{K_{zz}}{2K_z}\;. \tag{4.61}$$

4.1.4 Finite element formulation

The formulated boundary value problem of the shear stresses is solved approximately with the finite element method, see Section 2.1. The solution of the resulting linear system of equation is used to determine the shear stresses and other cross section parameters.

4.1.4.1 Finite element formulation for the Saint-Venant torsion problem

The nodal displacement vector $\boldsymbol{x} = [\ y \ \ z\ ]^T$ uses the same shape function $h_i(r,s)$ as the warping function ψ and the test function η, corresponding to the isoparametric concept. The interpolation field is defined as

$$\boldsymbol{x} = \sum_{i=1}^{n_e} h_i(r,s)\ \boldsymbol{x}_i\ , \qquad \psi = \sum_{i=1}^{n_e} h_i(r,s)\ \psi_i \qquad \text{and} \qquad \eta = \sum_{i=1}^{n_e} h_i(r,s)\ \eta_i\ . \quad (4.62)$$

The index i denotes the nodal number of an element and n_e defines the number of nodes of an element. The shape functions $h_i(r,s)$ are defined in a local natural coordinate system by the coordinates r and s. The weak form of the boundary value problem in Equation (4.18) and (4.19) is given by the functional

$$\mathfrak{S} = \int_{\Omega} (\psi_{,y}\ \eta_{,y} + \psi_{,z}\ \eta_{,z})\ dA - \oint_{\partial\Omega} (n_y\ z - n_z\ y)\ \eta\ d\vartheta = 0\ . \quad (4.63)$$

Using the interpolation field in Equation (4.62), the weak form of the boundary value problem is discretized and a linear system of equations follows with

$$S = \bigcup_{e=1}^{el} \sum_{i=1}^{n_e} \sum_{j=1}^{n_e} \eta_i \left(K_{ij}^e\ \psi_j - f_i^e\right) = 0\ . \quad (4.64)$$

The index e denotes the element number. el is the number of all element in the domain and $\bigcup$ is the assembling operator. The stiffness matrix is determined by

$$K_{ij}^e = \int_{\Omega_e} \left(h_{i,y}\ h_{j,y} + h_{i,z}\ h_{j,z}\right) dA_e\ . \quad (4.65)$$

The corresponding force vector is computed by the line integral

$$f_i^e = \int_{\partial\Omega} (n_y\ z - n_z\ y)\ h_i\ d\vartheta\ . \quad (4.66)$$

The normal vector is oriented outwards for the outer boundary and vice versa for inner boundaries. The direction of the boundary coordinate ϑ on the inner

boundaries $\partial\Omega_i$ has to be in the opposite direction as compared to the outer boundary $\partial\Omega_o$, compare Figure 4.1. The differential of the boundary coordinate is defined as

$$d\vartheta = |\boldsymbol{x}|\, dr \quad \text{with } \{r \in \mathbb{R} | -1 \leq r \leq 1\} \ , \tag{4.67}$$

where r is the natural coordinate of the boundary element. The derivative of the shape function with respect to ϑ is calculated by $h_{i,\vartheta} = {}^{h_{i,r}}/_{|\boldsymbol{x}|}$. Hence, one obtains the tangent vector

$$\boldsymbol{t} = \begin{bmatrix} t_y \\ t_z \end{bmatrix} = \sum_{i}^{n_e} h_{i,\vartheta}\ \boldsymbol{x}_i \ . \tag{4.68}$$

Considering the orthogonality condition $\boldsymbol{n}^T\boldsymbol{t} = 0$, the normal vector

$$\boldsymbol{n} = \begin{bmatrix} -t_z \\ t_y \end{bmatrix} \tag{4.69}$$

is derived.

4.1.4.2 Finite element formulation for the torsionless bending problem

The computation of the shear stress function Ψ is almost equal to the computation of the warping function above. The interpolation field of the coordinates of the cross section $\boldsymbol{x}$, the stress function Ψ and the test function η

$$\boldsymbol{x} = \sum_{i=1}^{n_e} h_i(r,s)\ \boldsymbol{x}_i \ , \qquad \bar{\Psi} = \sum_{i=1}^{n_e} h_i(r,s)\ \bar{\Psi}_i \qquad \text{and} \qquad \eta = \sum_{i=1}^{n_e} h_i(r,s)\ \eta_i \tag{4.70}$$

follow the isoparameteric concept. The weak form is derived from the Neumann problem in Equation (4.49) and (4.50) and formulated as the functional

$$\begin{aligned} \mathfrak{S} = &\int_{\Omega} \left(\bar{\Psi}_{,y}\ \eta_{,y} + \bar{\Psi}_{,z}\ \eta_{,z}\right)\ dA - \ldots \\ &\int_{\Omega} f_0(y,z)\ \eta\ dA - \oint_{\partial\Omega} \left(n_y\ g_1(z) - n_z\ g_2(y)\right)\ \eta\ d\vartheta = 0 \ . \end{aligned} \tag{4.71}$$

A linear system of equation

$$S = \bigcup_{e=1}^{el} \sum_{i=1}^{n_e} \sum_{j=1}^{n_e} \eta_i \left(K_{ij}^e\ \bar{\Psi}_j - f_i^e\right) = 0 \tag{4.72}$$

is obtained from the weak form by discretizing the displacement and stress field with Equation (4.70). The resulting stiffness matrix

$$K_{ij}^e = \int_{\Omega_e} \left(h_{i,y}\ h_{j,y} + h_{i,z}\ h_{j,z}\right) dA_e \tag{4.73}$$

is identical with the stiffness matrix from the Saint-Venant torsion problem, compare Equation (4.65). The force vector is computed by

$$f_i^e = \int_{\Omega_e} f_1(y,z)\ h_i\ dA_e + \int_{\partial\Omega} (n_y\ g_1(z) - n_z\ g_2(y))\ h_i\ d\vartheta\ , \tag{4.74}$$

where the functions $f_1(y,z)$, $g_1(z)$ and $g_2(y)$ are defined in Subsection 4.1.3. The definition of normal vectors of the cross section boundaries is identical to the torsion problem and given in Equation (4.69).

4.2 Cross section parameters of arbitrary cross sections

In the following, the shear center and the shear correction factor are derived. Based on the stress function achieved in the section above and the assumption of torsionless bending, the shear center is determined. The approach for deriving the shear correction factor for an arbitrary cross section is referred to the balance of energy.

4.2.1 Shear center

The shear center is denoted as point M. Shear forces acting at this point do not evoke torsion. In general, the shear center is not equal to the centroid of a cross section unless the cross section has two axes of symmetry. [191]

The coordinates of the shear center have to satisfy the condition [151]

$$Q_z\ y_M - Q_y\ z_M = \int_{\Omega} (\tau_{xz}\ y - \tau_{xy}\ z)\ dA\ . \tag{4.75}$$

Replacing the coordinates y and z by Equation (4.52), one obtains

$$Q_z\ y_M - Q_y\ z_M = \int_{\Omega} \left(\tau_{xz}\left(-\Phi_{,y} - \bar{\psi}_{,z}\right) - \tau_{xy}\left(-\Phi_{,z} + \bar{\psi}_{,y}\right)\right)\ dA\ . \tag{4.76}$$

The shear stresses τ_{xy} and τ_{xz} are derived from equations (4.45) and (4.46) for torsionless bending. One applies these shear stresses and imposes the relations of equations (4.19), (4.49) and (4.50) to the condition above. Using the Green's theorem,

$$\begin{aligned} Q_z\ y_M - Q_y\ z_M = &\int_{\Omega} (\Phi_{,yz} - \Phi_{,yz})\,\bar{\Psi}\ dA - \ldots \\ &\int_{\Omega} \Delta\bar{\Psi}\ \bar{\psi}\ dA - \int_{\Omega} (g_1\ \Phi_{,z} + g_2\ \Phi_{,y}\ )\ dA \end{aligned} \tag{4.77}$$

is received and the first integral vanishes. For torsionless bending, the condition in Equation (4.57) is applied and the third integral becomes zero. The Equation (4.75) is rewritten as

$$Q_z\ y_M - Q_y\ z_M = \int_\Omega \Delta\bar{\Psi}\ \bar{\psi}\ dA\ . \tag{4.78}$$

The Laplacian of the stress function is given by $\Delta\bar{\Psi} = -f_1(\bar{y},\bar{z})$ and one obtains the conditional equation for the center of shear becomes

$$Q_z\ y_M - Q_y\ z_M = -\int_\Omega (a_1\ \bar{y} + a_2\ \bar{z})\ \bar{\psi}\ dA\ , \tag{4.79}$$

where the constants a_1 and a_2 are defined in Equation (4.33). The coordinates of the shear center y_M and z_M are received by setting the shear forces Q_y and Q_z to zero respectively,

$$y_M = -\frac{I_{\bar{\psi}\bar{z}}\ I_{\bar{y}\bar{y}} - I_{\bar{\psi}\bar{y}}\ I_{\bar{y}\bar{z}}}{I_{\bar{y}\bar{y}}\ I_{\bar{z}\bar{z}} - I_{\bar{y}\bar{z}}^2} \qquad \text{and} \qquad z_M = \frac{I_{\bar{\psi}\bar{y}}\ I_{\bar{z}\bar{z}} - I_{\bar{\psi}\bar{z}}\ I_{\bar{y}\bar{z}}}{I_{\bar{y}\bar{y}}\ I_{\bar{z}\bar{z}} - I_{\bar{y}\bar{z}}^2}\ . \tag{4.80}$$

Comparing these coordinates to the center of twist in Equation (4.29), it has to be noted that the center of shear is identical with the center of twist.

4.2.2 Shear correction factor

The Timoshenko beam theory assumes a constant shear stress distribution in the beam cross section. In general, the shear deformation is not linear and the maximum of the shear stress is lcated in the beam axis. The shear correction factor is introduced for the Timoshenko beam theory. The corrected shear stress confirms the real shear stress distribution. [180]

Timoshenko introduced a correction factor which is a ratio of the averaged shear strain on a cross section to the shear strain on the centroid [177]. In [29] it is pointed out that the Timoshenko beam theory in combination with a shear correction factor defined by Timoshenko yields unsatisfactory results for higher frequencies of vibrating beams. An approach based on the strain energy is introduced for the determination of the shear correction factor in [168]. This approach delivers a significant improvement for the shear correction factor. This approach is enhanced for arbitrary cross sections by [61], which is used in the following.

The balance of energy of a Timoshenko beam has to be satisfied for linear elasticity, referring to [168]. The internal strain energy Π exists in equilibrium with the external work W, written as

$$\Pi = W\ . \tag{4.81}$$

The internal strain energy $\mathit{\Pi}$ [131] is defined as

$$\mathit{\Pi} = \frac{1}{2} \int_x \int_\Omega \left(\frac{\sigma_x^2}{E} + \frac{\tau_{xy}^2 + \tau_{xz}^2}{G} \right) \, dA \, dx \; . \tag{4.82}$$

In order to determine a shear correction factor, one focusses on the part of shear stresses of the internal strain energy. First, averaged shear stresses $\bar{\tau}_{xy}$ and $\bar{\tau}_{xz}$ are introduced

$$\int_\Omega \left(\tau_{xy}^2 + \tau_{xz}^2 \right) \, dA = \int_{\Omega_{sy}} \bar{\tau}_{xy}^2 \, dA_{sy} + \int_{\Omega_{sz}} \bar{\tau}_{xz}^2 \, dA_{sz} \; , \tag{4.83}$$

which are defined as

$$\bar{\tau}_{xy} = \frac{Q_y}{A_{sy}} \quad \text{and} \quad \bar{\tau}_{xz} = \frac{Q_z}{A_{sz}} \; . \tag{4.84}$$

The shear areas are denoted as A_{sy} and A_{sz}. These are defined as

$$A_{sy} = \kappa_y \, A \quad \text{and} \quad A_{sz} = \kappa_z \, A \tag{4.85}$$

and are not equal to the area of the beam cross section A. These shear areas are introduced due to the requirement that the averaged shear stresses $\bar{\tau}_{xy}$ and $\bar{\tau}_{xz}$ have to represent the shear stress distributions τ_{xy} and τ_{xz}. The size of these shear areas are determined by the shear correction factors κ_y and κ_z. Employing equations (4.84) and (4.85) in Equation (4.83), one obtains the condition

$$\int_\Omega \left(\tau_{xy}^2 + \tau_{xz}^2 \right) \, dA = \frac{Q_y^2}{\kappa_y \, A} + \frac{Q_z^2}{\kappa_z \, A} \; . \tag{4.86}$$

The left-hand side of this condition combined with equations (4.45) and (4.46) yields

$$\begin{aligned} \int_\Omega \left(\tau_{xy}^2 + \tau_{xz}^2 \right) \, dA = & \int_\Omega \left(\tau_{xy} \, \bar{\Psi}_{,y} + \tau_{xz} \bar{\Psi}_{,z} \right) \, dA - \ldots \\ & \int_\Omega \left(\tau_{xy} \, g_1(z) - \tau_{xz} \, g_2(y) \right) \, dA \; . \end{aligned} \tag{4.87}$$

Applying an integration by parts and the Gauss's theorem, the left-hand side becomes

$$\begin{aligned} \int_\Omega \left(\tau_{xy}^2 + \tau_{xz}^2 \right) \, dA = & - \int_\Omega \left(\tau_{xy_{,y}} + \tau_{xz_{,z}} \right) \, \bar{\Psi} \, dA + \ldots \\ & \oint_{\partial\Omega} \left(\tau_{xy} \, n_y + \tau_{xz} \, n_z \right) \, \bar{\Psi} \, d\vartheta - \ldots \\ & \int_\Omega \left(\tau_{xy} \, g_1(z) - \tau_{xz} \, g_2(y) \right) \, dA \end{aligned} \tag{4.88}$$

Considering Equation (4.50), the boundary integral vanishes. Employing the equations (4.45) and (4.46) a second time in the above condition, one obtains

$$\int_\Omega \left(\tau_{xy}^2 + \tau_{xz}^2\right)\, dA = \int_\Omega \left(\bar{\Psi}_{,yy} + \bar{\Psi}_{,zz}\right)\, \bar{\Psi}\, dA - \int_\Omega \left(\tau_{xy}\, g_1(z) - \tau_{xz}\, g_2(y)\right)\, dA\ . \quad (4.89)$$

Using equations (4.49), (4.34), (4.47) and (4.48), the part of the shear stresses of the strain energy is rewritten as

$$\begin{aligned}\int_\Omega \left(\tau_{xy}^2 + \tau_{xz}^2\right)\, dA = &\int_\Omega \left(a_1\, \bar{y} + a_2\, \bar{z}\right)\, \bar{\Psi}\, dA + \dots \\ &\frac{\nu}{2(1+\nu)} \int_\Omega \left(\tau_{xy}\, a_1\, (\bar{z} - \bar{z}_0)^2 + \tau_{xz}\, a_2\, (\bar{y} - \bar{y}_0)^2\right)\, dA\ .\end{aligned} \quad (4.90)$$

Terms are summarized to the constants $J_{\bar{y}\bar{y}}$ and $J_{\bar{z}\bar{z}}$ with

$$J_{\bar{y}\bar{y}} = \int_\Omega \tau_{xz}\, (\bar{y} - \bar{y}_0)^2\, dA \qquad \text{and} \qquad J_{\bar{z}\bar{z}} = \int_\Omega \tau_{xy}\, (\bar{z} - \bar{z}_0)^2\, dA\ . \quad (4.91)$$

Applying equations (4.90) and (4.86) and the notation $I_{\zeta\xi} = \int_\Omega \zeta\xi\, dA$, the conditional equation for the shear correction factors κ_y and κ_z is derived

$$\begin{aligned} Q_y &\left(\frac{I_{\bar{\Psi}\bar{y}}\, I_{\bar{z}\bar{z}} - I_{\bar{\Psi}\bar{z}}\, I_{\bar{y}\bar{z}}}{I_{\bar{y}\bar{y}}\, I_{\bar{z}\bar{z}} - I_{\bar{y}\bar{z}}^2} + \frac{\nu}{2(1+\nu)} \frac{J_{\bar{z}\bar{z}}\, I_{\bar{z}\bar{z}} - J_{\bar{y}\bar{y}}\, I_{\bar{y}\bar{z}}}{I_{\bar{y}\bar{y}}\, I_{\bar{z}\bar{z}} - I_{\bar{y}\bar{z}}^2} - \frac{Q_y}{\kappa_y\, A}\right) + \dots \\ Q_z &\left(\frac{I_{\bar{\Psi}\bar{z}}\, I_{\bar{y}\bar{y}} - I_{\bar{\Psi}\bar{y}}\, I_{\bar{y}\bar{z}}}{I_{\bar{y}\bar{y}}\, I_{\bar{z}\bar{z}} - I_{\bar{y}\bar{z}}^2} + \frac{\nu}{2(1+\nu)} \frac{J_{\bar{y}\bar{y}}\, I_{\bar{y}\bar{y}} - J_{\bar{z}\bar{z}}\, I_{\bar{y}\bar{z}}}{I_{\bar{y}\bar{y}}\, I_{\bar{z}\bar{z}} - I_{\bar{y}\bar{z}}^2} - \frac{Q_z}{\kappa_z\, A}\right) = 0\ . \end{aligned} \quad (4.92)$$

Assuming that the shear force Q_z is zero, the shear correction factor for shear loads in y-direction κ_y results in

$$\frac{1}{\kappa_y} = \frac{A}{Q_y} \left(\frac{I_{\bar{\Psi}\bar{y}}\, I_{\bar{z}\bar{z}} - I_{\bar{\Psi}\bar{z}}\, I_{\bar{y}\bar{z}}}{I_{\bar{y}\bar{y}}\, I_{\bar{z}\bar{z}} - I_{\bar{y}\bar{z}}^2} + \frac{\nu}{2(1+\nu)} \frac{J_{\bar{z}\bar{z}}\, I_{\bar{z}\bar{z}} - J_{\bar{y}\bar{y}}\, I_{\bar{y}\bar{z}}}{I_{\bar{y}\bar{y}}\, I_{\bar{z}\bar{z}} - I_{\bar{y}\bar{z}}^2}\right)\ . \quad (4.93)$$

Analogously, setting the shear force $Q_y = 0$, the shear correction factor κ_z is obtained from

$$\frac{1}{\kappa_z} = \frac{A}{Q_z} \left(\frac{I_{\bar{\Psi}\bar{z}}\, I_{\bar{y}\bar{y}} - I_{\bar{\Psi}\bar{y}}\, I_{\bar{y}\bar{z}}}{I_{\bar{y}\bar{y}}\, I_{\bar{z}\bar{z}} - I_{\bar{y}\bar{z}}^2} + \frac{\nu}{2(1+\nu)} \frac{J_{\bar{y}\bar{y}}\, I_{\bar{y}\bar{y}} - J_{\bar{z}\bar{z}}\, I_{\bar{y}\bar{z}}}{I_{\bar{y}\bar{y}}\, I_{\bar{z}\bar{z}} - I_{\bar{y}\bar{z}}^2}\right)\ . \quad (4.94)$$

4.3 Example: Shear stresses of a rectangular cross section with off-centered hole

A cantilevered beam and the corresponding cross section with quadratic shape and an off-center hole are depicted in Figure 4.2. The side length of the quadrat is given

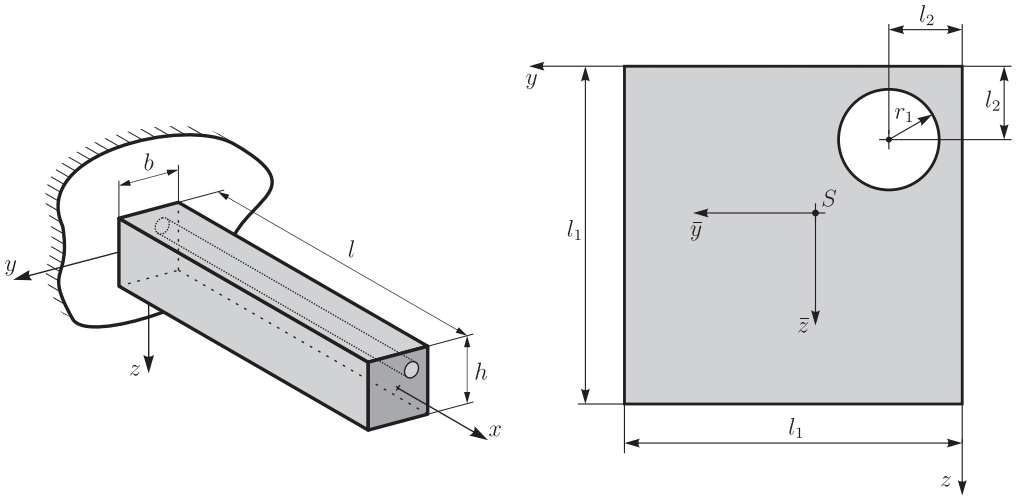

(a) Cantilevered beam with an off-center hole

(b) Geometry of a test cross section

Figure 4.2: Cantilevered beam and corresponding cross section defined as a test shape

by l_1. The hole with the radius r_1 has a distance of l_2 to the outer edges in both directions. The numerical values of these geometric parameters and the resulting values of the area, the center of area and the first and second moments of area are summarized in Table 4.1. The length of the investigated beam is given with 10 mm. The material properties are isotropic. A Young's modulus of $E = 2 \times 10^5\,\mathrm{N/mm^2}$ and a Poisson ratio of $\nu = 0.3$ are assumed. In this example the body forces are neglected. The cantilevered beam is loaded with transversal shear forces and a torque on the free end, respectively. The shear forces are evenly distributed on the surface of the free beam end.

The derived boundary value problems of the warping function for the Saint-Venant torsion and of the introduced stress function for the torsionless bending case in Section 4.1 are determined by the finite element method. The cross section is meshed with two-dimensional 4-node elements using linear shape functions. Shear stresses and cross section parameters are evaluated for the test cross section in case of Saint-Venant torsion and torsionless bending. The numerical solution is computed with different mesh sizes. These results are compared to the solution of a three-dimensional finite element simulation of the cantilevered beam. Therefore, a very fine mesh is generated with 20-node brick elements and a total number of

Table 4.1: Geometric parameters of test cross section

Parameter	Value
Length l_1	4 mm
Length l_2	1 mm
Radius r_1	0.5 mm
Area A	15.2136 mm^2
Center of area y_C	2.0517 mm
Center of area z_C	2.0517 mm
First moment of area $S_{\bar{y}}$	0.7864 mm^3
First moment of area $S_{\bar{z}}$	0.7864 mm^3
Second moment of area $I_{\bar{y}\bar{y}}$	20.4978 mm^4
Second moment of area $I_{\bar{z}\bar{z}}$	20.4978 mm^4
Second moment of area $I_{\bar{y}\bar{z}}$	-0.7864 mm^4

983484 elements. The resulting stresses in the cross section of the beam at $\bar{x} = 5\,\text{mm}$ are defined as the reference solution.

4.3.1 Saint-Venant torsion

The beam is loaded with a constant torque $M_x = 1000\,\text{N/mm}^2$ on the free end. The computation of the Saint-Venant torsion stiffness I_T is defined in Equation (4.16). The resulting values are summarized in Table 4.2 for different numbers of elements. The warping constant $C_{\bar{\psi}\bar{\psi}}$ is calculated from Equation (4.30) and the center of twist is given by Equation (4.29). Increasing the number of elements el, the numerical error of these parameters is reduced.

Figures 4.3a and 4.3b show the resulting shear stress distributions τ_{xy} and τ_{xz} in the cross section. It is seen, that the shear stresses are zero at the coordinates of the center of twist. On the outer boundary the shear stresses take the largest values. A vector plot of the shear stress distribution is depicted in Figure 4.4.

Tables 4.3 and 4.4 summarize error values of the shear stress distribution computed with different mesh sizes. The absolute error of the shear stress is defined as

$$\varepsilon_{\tau_{xy}} = |\tau_{xy} - \tau_{xy_{ref}}| \qquad \text{and} \qquad \varepsilon_{\tau_{xz}} = |\tau_{xz} - \tau_{xz_{ref}}| \,. \tag{4.95}$$

Table 4.2: Saint-Venant torsion stiffness I_T, warping constant $C_{\bar{\psi}\bar{\psi}}$ and center of twist y_T and z_T of the test cross section in relation to the center of area for different mesh sizes with computed an element number el

el	I_T in mm^4	$C_{\bar{\psi}\bar{\psi}}$ in mm^4	y_T in mm	z_T in mm
80	35.937226	179.059421	2.047009	2.047009
212	34.420515	184.838517	2.079994	2.079994
272	34.173621	185.663470	2.084631	2.084631
500	33.880681	186.796207	2.090999	2.090999
948	33.710134	187.428342	2.094538	2.094538
1648	33.619605	187.753648	2.096357	2.096357
6536	33.535201	188.068272	2.098114	2.098114

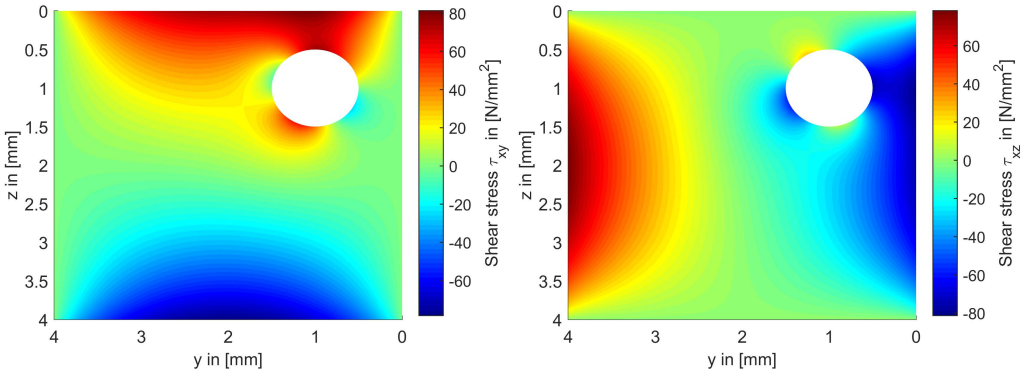

(a) Shear stress τ_{xy} **(b)** Shear stress τ_{xz}

Figure 4.3: Shear stresses τ_{xy} and τ_{xz} of a cantilevered beam, loaded on the free end with a torque $M_x = 1000\,\mathrm{N/mm^2}$

The mean absolute error is obtained from

$$\bar{\varepsilon}_{\tau_{xy}} = \frac{\int_\psi \varepsilon_{\tau_{xy}} dA}{\int_\psi dA} \qquad \text{and} \qquad \bar{\varepsilon}_{\tau_{xz}} = \frac{\int_\psi \varepsilon_{\tau_{xz}} dA}{\int_\psi dA} \,. \tag{4.96}$$

The mean absolute errors decrease with greater mesh sizes. For a mesh with 6536 elements the mean errors $\bar{\varepsilon}_{\tau_{xy}}$ and $\bar{\varepsilon}_{\tau_{xz}}$ reach a value which is about $0.5\,\mathrm{N/mm^2}$. This decrease of the error values takes effect for the maximum of the absolute errors $\varepsilon_{max,\tau_{xy}}$ and $\varepsilon_{max,\tau_{xz}}$, but both maximum values are approximately $8\,\mathrm{N/mm^2}$. This indicates the existence of some numerical peaks in the error distribution. The minimum of the absolute errors $\varepsilon_{min,\tau_{xy}}$ and $\varepsilon_{min,\tau_{xz}}$ is close to zero for each mesh size. For the minimum absolute error, a decrease of the numerical value for a larger mesh size is not detected.

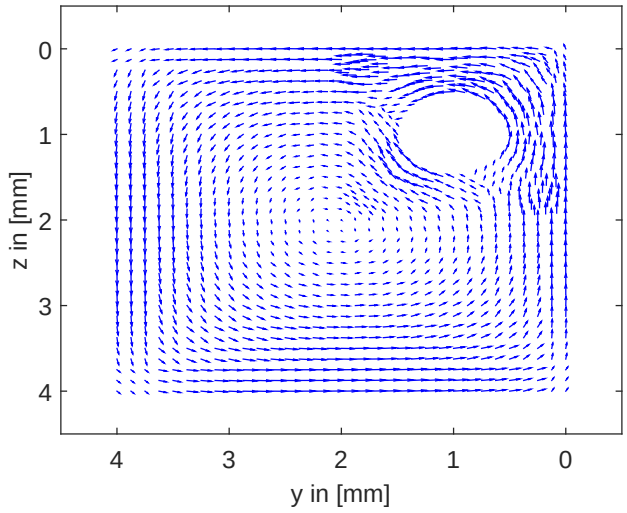

Figure 4.4: Resulting shear stresses $\boldsymbol{\tau}$ in the test cross section of a cantilevered beam, loaded on the free end with a torque $M_x = 1000\,\mathrm{N/mm^2}$

Table 4.3: Mean absolute error $\bar{\varepsilon}_{\tau_{xy}}$, maximum error $\varepsilon_{max,\tau_{xy}}$ and minimum error $\varepsilon_{min,\tau_{xy}}$ in $\mathrm{N/mm^2}$ of the stress distribution τ_{xy} of a cantilevered beam for different mesh sizes computed with an element number el, loaded on the free end with a torque $M_x = 1000\,\mathrm{Nmm}$

el	$\bar{\varepsilon}_{\tau_{xy}}$ in $\mathrm{N/mm^2}$	$\varepsilon_{max,\tau_{xy}}$ in $\mathrm{N/mm^2}$	$\varepsilon_{min,\tau_{xy}}$ in $\mathrm{N/mm^2}$
80	0.543682	8.223019	6.683399×10^{-6}
212	0.227556	4.987881	0.349911×10^{-6}
272	0.182041	4.988122	2.523897×10^{-6}
500	0.098916	4.686244	0.548172×10^{-6}
948	0.053189	1.810877	0.451259×10^{-6}
1648	0.032371	1.668087	0.007893×10^{-6}
6536	0.015718	0.546703	0.117395×10^{-6}

Figures 4.5a and 4.5b show the distribution of the absolute error of the shear stresses $\varepsilon_{\tau_{xy}}$ and $\varepsilon_{\tau_{xz}}$ for a mesh with 6536 elements. At the first look, the shear stresses have a nearly constant error distribution with local maxima. These are mainly located at the inner boundary of the hole. In order to compute the error values, the nodal stress values of the boundary value problem are interpolated to the mesh of the reference solution. This transfer of the mesh data leads to a numerical error.

4.3.2 Torsionless bending

Transversal shear forces $Q_y = 100\,\mathrm{N}$ and $Q_z = 100\,\mathrm{N}$ are loaded on the free end of the beam. These shear forces are imposed on the free end as surface forces. The

Table 4.4: Mean absolute error $\bar{\varepsilon}_{\tau_{xz}}$, maximum error $\varepsilon_{max,\tau_{xz}}$ and minimum error $\varepsilon_{min,\tau_{xz}}$ in $^{\mathrm{N}}/_{\mathrm{mm}^2}$ of the stress distribution τ_{xz} of a cantilevered beam for different mesh sizes computed with an element number el, loaded on the free end with a torque $M_x = 1000\,\mathrm{Nmm}$

el	$\bar{\varepsilon}_{\tau_{xz}}$ in $^{\mathrm{N}}/_{\mathrm{mm}^2}$	$\varepsilon_{max,\tau_{xz}}$ in $^{\mathrm{N}}/_{\mathrm{mm}^2}$	$\varepsilon_{min,\tau_{xz}}$ in $^{\mathrm{N}}/_{\mathrm{mm}^2}$
80	0.545607	8.321315	6.483559×10^{-6}
212	0.229863	5.092621	0.649470×10^{-6}
272	0.184374	5.092877	0.648795×10^{-6}
500	0.101269	4.780779	0.496860×10^{-6}
948	0.055527	1.819919	0.684199×10^{-6}
1648	0.034000	1.587001	0.384101×10^{-6}
6536	0.015274	0.561123	0.172634×10^{-6}

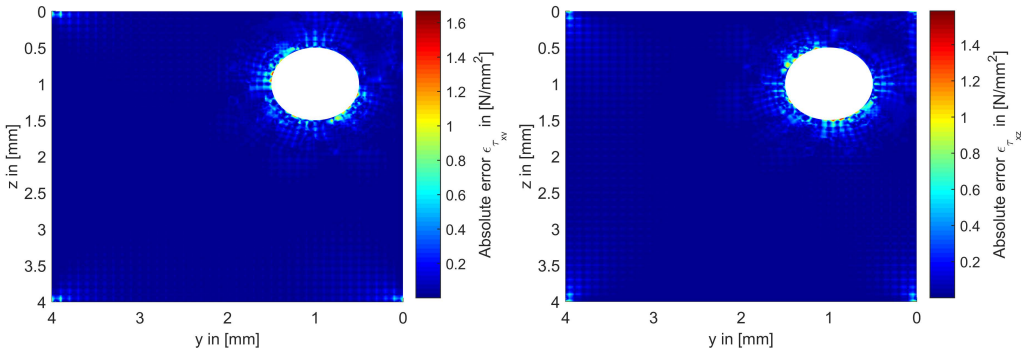

(a) Absolute error of the shear stress τ_{xy} **(b)** Absolute error of the shear stress τ_{xz}

Figure 4.5: Absolute errors $\varepsilon_{\tau_{xy}}$ and $\varepsilon_{\tau_{xz}}$ of the shear stresses of a cantilevered beam, loaded on the free end with a torque $M_x = 1000\,^{\mathrm{N}}/_{\mathrm{mm}^2}$

shear center y_M and z_M and the shear correction factors κ_y and κ_z are determined according to Equation (4.80) and equations (4.93) and (4.94), respectively.

Table 4.5 contains the shear center and the shear correction factors for different mesh sizes. The numerical values of the shear center and the shear correction factor approximate the correct values increasing the number of elements el of the meshed cross section. A change of the number of elements from 1648 to 6536 elements causes an increase in third decimal place of the shear center of two digits. The shear correction factors are constant for these mesh sizes.

Figures 4.6a and 4.6b depicts the shear stresses τ_{xy} and τ_{xz} due to torsionless bending. The computation of the shear stresses is carried out with a mesh size with 6536 elements. In contrast to the Saint-Venant torsion, the shear stress on the boundary tends to zero for the edges which are normal to the load direction. The shear stress distribution of the boundary edge in load direction is parabolic.

Table 4.5: Shear center y_M and z_M and shear correction factors κ_y and κ_z of the test cross section in relation to the center of area for different mesh sizes computed with an element number el

el	y_M in mm	z_M in mm	κ_y	κ_z
80	2.047009	2.047009	0.797479	0.797479
212	2.079994	2.079994	0.797391	0.797391
272	2.084631	2.084631	0.797389	0.797389
500	2.090999	2.090999	0.797370	0.797370
948	2.094538	2.094538	0.797366	0.797366
1648	2.096357	2.096357	0.797364	0.797364
6536	2.098114	2.098114	0.797364	0.797364

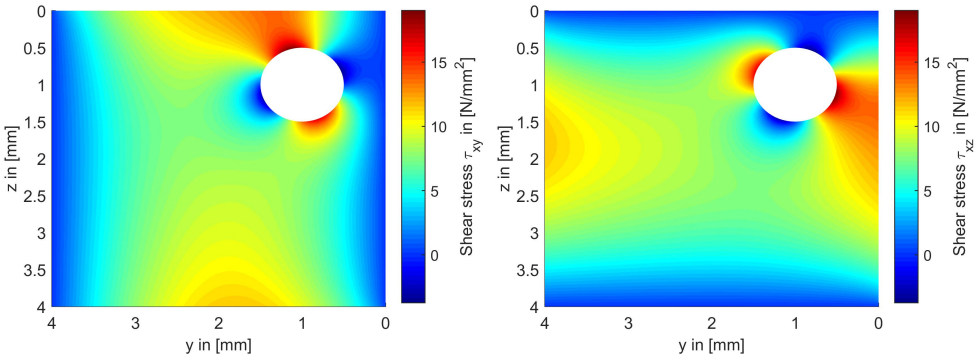

(a) Shear stress τ_{xy} **(b)** Shear stress τ_{xz}

Figure 4.6: Shear stresses τ_{xy} and τ_{xz} of a cantilevered beam, loaded on the free end with transversal forces $F_y = 100\,\mathrm{N}$ and $F_z = 100\,\mathrm{N}$

Due to the geometric symmetry about the diagonal, the stress distribution τ_{xy} is symmetric to τ_{xz} about the diagonal. A vector plot of the shear stress distribution with respect to torsionless bending is shown in Figure 4.7.

Tables 4.6 and 4.7 summarize the error values of the shear stress distribution due to torsionless bending for different mesh sizes. The mean absolute error is computed from Equation (4.96), equal to the Saint-Venant problem. An increase of the element number results in a reduction of the mean errors $\bar{\varepsilon}_{\tau_{xy}}$ and $\bar{\varepsilon}_{\tau_{xz}}$ and the maximum absolute errors $\varepsilon_{max,\tau_{xy}}$ and $\varepsilon_{max,\tau_{xz}}$. For a mesh with 6536 elements the mean errors $\bar{\varepsilon}_{\tau_{xy}}$ and $\bar{\varepsilon}_{\tau_{xz}}$ are about $0.42\,\mathrm{N/mm^2}$. This is about a tenth of the maximum errors $\varepsilon_{max,\tau_{xy}}$ and $\varepsilon_{max,\tau_{xz}}$. The maximum of the absolute error is about $1.6\,\mathrm{N/mm^2}$ in this case. This large distance between mean value and maximum value signifies that some outliers exist in the error distribution. The minimum of the error distributions $\varepsilon_{\tau_{xy}}$ and $\varepsilon_{\tau_{xz}}$ is close to zero.

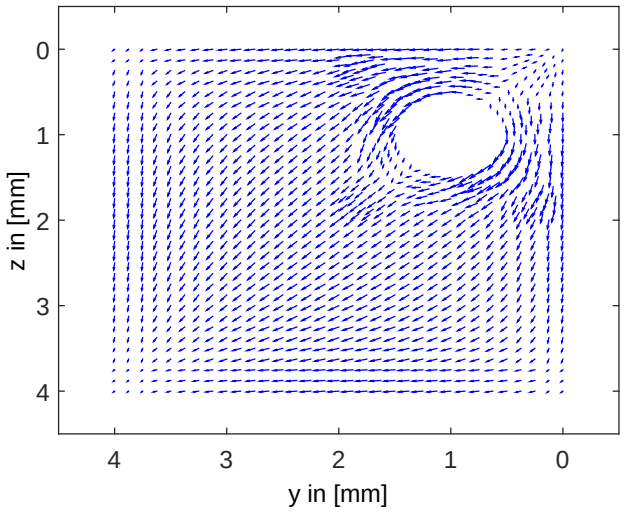

Figure 4.7: Resulting shear stresses $\boldsymbol{\tau}$ in the test cross section of a cantilevered beam, loaded on the free end with transversal forces $F_y = 100\,\mathrm{N}$ and $F_z = 100\,\mathrm{N}$

Table 4.6: Mean absolute error $\bar{\varepsilon}_{\tau_{xy}}$, maximum error $\varepsilon_{max,\tau_{xy}}$ and minimum error $\varepsilon_{min,\tau_{xy}}$ in $^{\mathrm{N}}/_{\mathrm{mm}^2}$ of the stress distribution τ_{xy} of a cantilevered beam for different mesh sizes computed with an element number el, loaded on the free end with $F_y = 100\,\mathrm{N}$ and $F_z = 100\,\mathrm{N}$

el	$\bar{\varepsilon}_{\tau_{xy}}$ in $^{\mathrm{N}}/_{\mathrm{mm}^2}$	$\varepsilon_{max,\tau_{xy}}$ in $^{\mathrm{N}}/_{\mathrm{mm}^2}$	$\varepsilon_{min,\tau_{xy}}$ in $^{\mathrm{N}}/_{\mathrm{mm}^2}$
80	0.107458	2.052266	1.133535×10^{-6}
212	0.066199	1.208040	1.100146×10^{-6}
272	0.062875	1.208061	1.215432×10^{-6}
500	0.051209	0.988043	0.507969×10^{-6}
948	0.046536	0.499208	0.458474×10^{-6}
1648	0.044545	0.459709	0.934158×10^{-6}
6536	0.042662	0.299883	1.855173×10^{-6}

Figures 4.8a and 4.8b show the distribution of the absolute errors $\varepsilon_{\tau_{xy}}$ and $\varepsilon_{\tau_{xz}}$ for a mesh with 6536 elements. A similar error behavior as for the Saint-Venant torsion is seen. The largest errors occur at the boundary of the off-centered hole. The error distribution contains also numerical outliers equal to the Saint-Venant torsion problem. These errors are effected numerically in postprocessing by transferring the mesh data from the mesh of the computed boundary value problem to the mesh of the reference simulation.

The shear correction factors are computed by equations (4.93) and (4.94). In these equations, the dependency of the shear correction factor is given by the term $\nu/2(1+\nu)$. Increasing the Poisson ratio, this term increases and the shear correction factors decrease.

Table 4.7: Mean absolute error $\bar{\varepsilon}_{\tau_{xz}}$, maximum error $\varepsilon_{max,\tau_{xz}}$ and minimum error $\varepsilon_{min,\tau_{xz}}$ in $^{\mathrm{N}}/_{\mathrm{mm}^2}$ of the stress distribution τ_{xz} of a cantilevered beam for different mesh sizes computed with an element number el, loaded on the free end with $F_y = 100\,\mathrm{N}$ and $F_z = 100\,\mathrm{N}$

el	$\bar{\varepsilon}_{\tau_{xz}}$ in $^{\mathrm{N}}/_{\mathrm{mm}^2}$	$\varepsilon_{max,\tau_{xz}}$ in $^{\mathrm{N}}/_{\mathrm{mm}^2}$	$\varepsilon_{min,\tau_{xz}}$ in $^{\mathrm{N}}/_{\mathrm{mm}^2}$
80	0.107331	2.024919	0.470652×10^{-6}
212	0.066274	1.330008	0.532938×10^{-6}
272	0.062939	1.329903	0.228878×10^{-6}
500	0.051154	1.001714	0.695802×10^{-6}
948	0.046478	0.448745	0.209375×10^{-6}
1648	0.044464	0.402385	1.985698×10^{-6}
6536	0.042608	0.330768	0.320580×10^{-6}

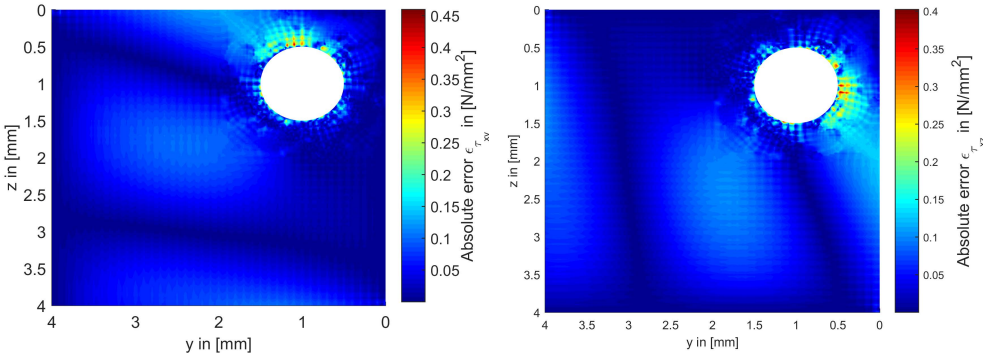

(a) Absolute error of the shear stress τ_{xy} **(b)** Absolute error of the shear stress τ_{xz}

Figure 4.8: Absolute errors $\varepsilon_{\tau_{xy}}$ and $\varepsilon_{\tau_{xz}}$ of the shear stresses of a cantilevered beam, loaded on the free end with transversal forces $F_y = 100\,\mathrm{N}$ and $F_z = 100\,\mathrm{N}$

Table 4.8: Shear correction factors κ_y and κ_z with varied Poisson ratio ν

ν	κ_y	κ_z	ν	κ_y	κ_z
0	0.802461	0.802461	0.3	0.797364	0.797364
0.05	0.802243	0.802243	0.35	0.796038	0.796038
0.1	0.801666	0.801666	0.4	0.794674	0.794674
0.15	0.800825	0.800825	0.45	0.793289	0.793289
0.2	0.799794	0.799794	0.5	0.791898	0.791898
0.25	0.798626	0.798626			

Table 4.8 contains the shear correction factors κ_y and κ_z for different Poisson ratios. As already mentioned, the shear correction factors decrease for larger values of the Poisson ratio.

Figures 4.9a and 4.9b depict the shear stress distribution τ_{xz} for Poisson ratios of

$\nu = 0$ and $\nu = 0.5$. For a Poisson ratio of 0.5 the shear stresses increase on the outer boundary.

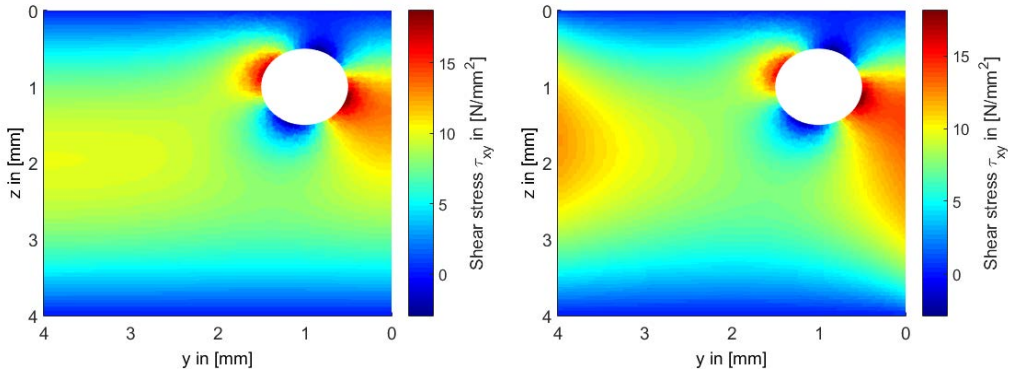

(a) Shear stress τ_{xz} computed with a Poisson ratio of 0

(b) Shear stress τ_{xz} computed with a Poisson ratio of 0.5

Figure 4.9: Comparison of shear stress distribution τ_{yz} for a Poisson ratio of 0 and 0.5

CHAPTER 5

Formulation of composite beam structures using Timoshenko beam theory

Many researches have addressed problems of composite structures in the past years. Most of them investigated the behavior of laminated structures [5] or [185] and the behavior of thin-walled structures [82]. Mokos and Sapountzakis [121] examined the transverse shear loading of composite beams with isotropic material behavior. They used the boundary element method for solving the derived partial differential equations.

In this chapter, a prismatic beam element for a composite structure is discussed. The variational formulation of a composite beam element based on the Timoshenko beam theory is introduced. Further, the shear stresses of general composite beams with arbitrary cross sections are investigated. First, the shear stresses due to torsion are computed. The warping function of an arbitrary cross section is introduced and a partial differential equation for orthotropic material with respect to the warping function is formulated. Second, the shear stresses occurring due to transverse loads are determined. A stress function is introduced and the corresponding Dirichlet and Neumann problems are formulated. The necessary shear center and shear correction factor for the composite Timoshenko beam are obtained. Finally, an example of a cantilevered composite beam with a defined cross section is carried out.

5.1 Timoshenko beam element for composite structures

A beam with arbitrarily shaped cross section and heterogeneous material distribution is formulated using a composite beam theory. The cross section consists of a finite number of regions Ω_k with $\{k \in \mathbb{Z} | 1 \leq j \leq m\}$, where each region consists of a different material, see Figure 5.1. Each material region is firmly bounded to the adjacent regions. Additionally, the assumptions of the Timoshenko beam are also valid for this multilayered beam, compare Section 3.1.1. The in-plane strains are

neglected and the displacements and rotation angles have to be small. The different materials are assumed to be homogeneous and linear elastic with orthotropic behavior. The strains are defined by

$$\begin{bmatrix} \varepsilon_x \\ \varepsilon_y \\ \varepsilon_z \\ \gamma_{xy} \\ \gamma_{yz} \\ \gamma_{zx} \end{bmatrix} = \begin{bmatrix} 1/E_x & -\nu_{xy}/E_y & -\nu_{xz}/E_z & 0 & 0 & 0 \\ -\nu_{yx}/E_x & 1/E_y & -\nu_{yz}/E_z & 0 & 0 & 0 \\ -\nu_{zx}/E_x & -\nu_{zy}/E_y & 1/E_z & 0 & 0 & 0 \\ 0 & 0 & 0 & 1/G_{xy} & 0 & 0 \\ 0 & 0 & 0 & 0 & 1/G_{yz} & 0 \\ 0 & 0 & 0 & 0 & 0 & 1/G_{zx} \end{bmatrix} \begin{bmatrix} \sigma_x \\ \sigma_y \\ \sigma_z \\ \tau_{xy} \\ \tau_{yz} \\ \tau_{zx} \end{bmatrix} . \quad (5.1)$$

Due to symmetry properties of the compliance matrix, the conditions

$$\frac{\nu_{xy}}{E_y} = \frac{\nu_{yx}}{E_x} , \quad \frac{\nu_{xz}}{E_z} = \frac{\nu_{zx}}{E_x} \quad \text{and} \quad \frac{\nu_{yz}}{E_z} = \frac{\nu_{zy}}{E_y} \quad (5.2)$$

must hold.

5.1.1 Shear stresses and internal forces of the composite Timoshenko beam

The stresses in each region Ω_k in the cross section of the beam are determined from

$$\sigma_x^k = E_x^k \, \epsilon_x^k , \qquad \tau_{xy}^k = G_{xy}^k \, \gamma_{xy}^k \quad \text{and} \quad \tau_{xz}^k = G_{xz}^k \, \gamma_{xz}^k . \quad (5.3)$$

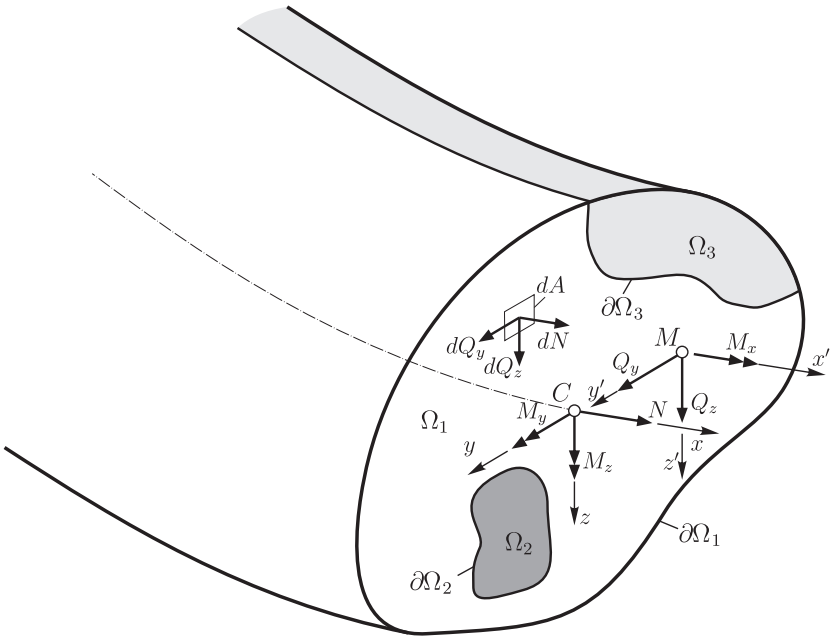

Figure 5.1: Internal forces in a composite beam with arbitrary cross section

The index k stands for the corresponding region Ω_k of the parameters. Compared to the Timoshenko beam theory, no in-plane displacements are available for the composite beam. The stress components σ_y, σ_z and τ_{yz} are neglectable and the strains in each region Ω_k are equal,

$$\epsilon_x^1 = \epsilon_x^k \ = \epsilon_x, \qquad \gamma_{xy}^1 = \gamma_{xy}^k = \gamma_{xy} \quad \text{and} \quad \gamma_{xz}^1 = \gamma_{xz}^k = \gamma_{xz} \ . \tag{5.4}$$

Using the equality of the strains, the stresses of the composite beam become

$$\sigma_x^k = E_x^k \ \epsilon_x \ , \qquad \tau_{xy}^k = G_{xy}^k \ \gamma_{xy} \quad \text{and} \quad \tau_{xz}^k = G_{xz}^k \ \gamma_{xz} \ . \tag{5.5}$$

Figure 5.1 depicts the internal forces acting in the cross section of a composite beam. The centroid of the composite cross section is denoted by C and the shear center by M. The acting forces and moments in each region Ω_k are defined by

$$\begin{aligned} N^k &= \int_{\Omega_k} \sigma_x^k \ dA \ , \quad & Q_y^k &= \int_{\Omega_k} \tau_{xy}^k \ dA \ , \quad & Q_z^k &= \int_{\Omega_k} \tau_{xz}^k \ dA \ , \\ M_y^k &= \int_{\Omega_k} z\sigma_x^k \ dA \ , \quad & M_z^k &= -\int_{\Omega_k} y\sigma_x^k \ dA \ , \quad & M_x^k &= \int_{\Omega_k} (-z'\tau_{xy}^k + y'\tau_{xz}^k) \ dA \ . \end{aligned} \tag{5.6}$$

The normal force in the region Ω_k is denoted by N^k. The shear forces in Ω_k are Q_y^k and Q_z^k and the acting internal moments are M_x^k, M_y^k and M_z^k. Summing up the internal forces and moments in all regions of the composite cross section, the total internal forces and moments are obtained:

$$\begin{aligned} N &= \sum_k^m \int_{\Omega_k} \sigma_x^k \ dA \ , \quad & Q_y &= \sum_k^m \int_{\Omega_k} \tau_{xy}^k \ dA \ , \\ Q_z &= \sum_k^m \int_{\Omega_k} \tau_{xz}^k \ dA \ , \quad & M_y &= \sum_k^m \int_{\Omega_k} z\sigma_x^k \ dA \ , \\ M_z &= \sum_k^m \int_{\Omega_k} (-y\sigma_x^k) \ dA \ , \quad & M_x &= \sum_k^m \int_{\Omega_k} (-z'\tau_{xy}^k + y'\tau_{xz}^k) \ dA \ . \end{aligned} \tag{5.7}$$

Using the strain displacement relation of the Timoshenko beam in Equation (3.10), the normal force

$$N = \sum_k^m \int_{\Omega_k} E_x^k \ \epsilon_x \ dA = \sum_k^m \int_{\Omega_k} E_x^k \ (u_{c,x} - y \ \theta_{z,x} + z \ \theta_{y,x}) \ dA \ . \tag{5.8}$$

is obtained. The shear forces are obtained from

$$Q_y = \sum_k^m \int_{\Omega_k} G_{xy}^k \ \gamma_{xy} \ dA = \sum_k^m \int_{\Omega_k} G_{xy}^k \ (v_{c,x} - z \ \theta_{x,x} - \theta_z) \ dA \tag{5.9}$$

and

$$Q_z = \sum_k^m \int_{\Omega_k} G_{xz}^k \, \gamma_{xz} \, dA = \sum_k^m \int_{\Omega_k} G_{xz}^k \, (w_{c,x} + y \, \theta_{x,x} + \theta_y) \, dA \; . \tag{5.10}$$

The torsional moment results in

$$\begin{aligned} M_x &= \sum_k^m \int_{\Omega_k} (-z' G_{xy}^k \gamma_{xy} + y' G_{xz}^k \gamma_{xz}) \, dA \\ &= \sum_k^m \int_{\Omega_k} (-z' G_{xy}^k (v_{c,x} - z \, \theta_{x,x} - \theta_z) + y' G_{xz}^k (w_{c,x} + y \, \theta_{x,x} + \theta_y)) \, dA \end{aligned} \tag{5.11}$$

and the bending moments become

$$M_y = \sum_k^m \int_{\Omega_k} z \, E_x^k \, \epsilon_x \, dA = \sum_k^m \int_{\Omega_k} z \, E_x^k \, (u_{c,x} - y \, \theta_{z,x} + z \, \theta_{y,x}) \, dA \tag{5.12}$$

and

$$M_z = - \sum_k^m \int_{\Omega_k} y \, E_x^k \, \epsilon_x \, dA = - \sum_k^m \int_{\Omega_k} y \, E_x^k \, (u_{c,x} - y \, \theta_{z,x} + z \, \theta_{y,x}) \, dA \; . \tag{5.13}$$

Evaluating the integrals of internal forces and moments of the composite cross section, the parameters of Equation (3.22) are achieved for each region Ω_k. These parameters are the area A^k, the first moments of area S_y^k and S_z^k and the second moments of area I_y^k, I_z^k and I_{yz}^k. Using these cross section parameters the internal forces and moments are written as

$$N = \sum_k^m \left(E_x^k \, A^k \right) \, u_{c,x} - \sum_k^m \left(E_x^k \, S_z^k \right) \, \theta_{z,x} + \sum_k^m \left(E_x^k \, S_y^k \right) \, \theta_{y,x} \; , \tag{5.14}$$

$$Q_y = \kappa_y \, \sum_k^m \left(G_{xy}^k \, A^k \right) \, (v_{c,x} - \theta_z) - \kappa_y \, \sum_k^m \left(G_{xy}^k \, S_y^k \right) \, \theta_{x,x} \; , \tag{5.15}$$

$$Q_z = \kappa_z \, \sum_k^m \left(G_{xz}^k \, A^k \right) \, (w_{c,x} + \theta_y) + \kappa_z \, \sum_k^m \left(G_{xz}^k \, S_z^k \right) \, \theta_{x,x} \; , \tag{5.16}$$

$$\begin{aligned} M_x = &- \kappa_y \, \sum_k^m \left(G_{xy}^k \, S_y^k \right) \, (v_{c,x} - \theta_z) + \kappa_y \, \sum_k^m \left(I_y^k \, G_{xy}^k \right) \, \theta_{x,x} \ldots \\ &+ \kappa_z \, \sum_k^m \left(G_{xz}^k \, S_z^k \right) \, (w_{c,x} + \theta_y) + \kappa_z \, \sum_k^m \left(I_z^k \, G_{xz}^k \right) \, \theta_{x,x} \; , \end{aligned} \tag{5.17}$$

$$M_y = \sum_k^m \left(E_x^k \; S_y^k\right) \; u_{c,x} - \sum_k^m \left(E_x^k \; I_{yz}^k\right) \; \theta_{z,x} + \sum_k^m \left(E_x^k \; I_y^k\right) \; \theta_{y,x} \tag{5.18}$$

and

$$M_z = -\sum_k^m \left(E_x^k \; S_z^k\right) \; u_{c,x} + \sum_k^m \left(E_x^k \; I_z^k\right) \; \theta_{z,x} - \sum_k^m \left(E_x^k \; I_{yz}^k\right) \; \theta_{y,x} \; . \tag{5.19}$$

The internal forces and moments are summarized in the vector $\boldsymbol{p}$, compare Equation (3.32). In tensor notation, these forces and moments are defined by

$$\boldsymbol{p} = \sum_k^m \boldsymbol{K}_t^k \; \boldsymbol{\varepsilon} \; , \tag{5.20}$$

where the strain vector $\boldsymbol{\varepsilon}$ is denoted in Equation (3.30). The stiffness tensor of each region in the composite cross section $\boldsymbol{D}^k$ is given by

$$\boldsymbol{K}_t^k = \begin{bmatrix} E_x^k A^k & 0 & 0 & 0 & E_x^k S_y^k & -E_x^k S_z^k \\ 0 & \kappa_y G_{xy}^k A^k & 0 & -\kappa_y G_{xy}^k S_y^k & 0 & 0 \\ 0 & 0 & \kappa_z G_{xz}^k A^k & \kappa_z G_{xz}^k S_z^k & 0 & 0 \\ 0 & -\kappa_y G_{xy}^k S_y^k & \kappa_z G_{xz}^k S_z^k & \kappa_y I_y^k G_{xy}^k + \kappa_z I_z^k G_{xz}^k & 0 & 0 \\ E_x^k S_y^k & 0 & 0 & 0 & E_x^k I_y^k & -E_x^k I_{yz}^k \\ -E_x^k S_z^k & 0 & 0 & 0 & -E_x^k I_{yz}^k & E_x^k I_z^k \end{bmatrix} \; . \tag{5.21}$$

5.1.2 Variational formulation of the composite Timoshenko beam

The equation of motion of a composite Timoshenko beam is formulated, using Hamilton's principle. A detailed derivation of the equation of motion formulated for the Timoshenko beam is given in Subsection 3.1.3.

The variation of the functional $\delta\mathfrak{S}$ has to be zero. In case of the composite beam, the variation of the functional is written as

$$\begin{aligned} \delta\mathfrak{S} = \int_{t_0}^{t_1} \Bigg(& - \int_l \delta \boldsymbol{u}^T \; \sum_k^m \boldsymbol{M}_t^k \; \ddot{\boldsymbol{u}} \; dx - \int_l \delta \boldsymbol{\varepsilon}^T \sum_k^m \boldsymbol{K}_t^k \; \boldsymbol{\varepsilon} \; dx + \; \ldots \\ & \int_l \delta \boldsymbol{u}^T \; \boldsymbol{f}_L \; dx \; + \int_l \delta \boldsymbol{u}_\sigma^T \; \boldsymbol{t}_{l_\sigma} \; dx + \sum_i \delta \boldsymbol{u}_i^T \; \hat{\boldsymbol{F}}_{Ni} \Bigg) \; dt = 0 \; , \end{aligned} \tag{5.22}$$

with the tensor

$$\boldsymbol{M}_t^k = \begin{bmatrix} \varrho^k A^k & 0 & 0 & 0 & \varrho^k S_y^k & -\varrho^k S_z^k \\ 0 & \varrho^k A^k & 0 & -\varrho^k S_y^k & 0 & 0 \\ 0 & 0 & \varrho^k A^k & \varrho^k S_z^k & 0 & 0 \\ 0 & -\varrho^k S_y^k & \varrho^k S_z^k & \varrho^k (I_y^k + I_z^k) & 0 & 0 \\ \varrho^k S_y^k & 0 & 0 & 0 & \varrho^k I_y^k & -\varrho^k I_{yz}^k \\ -\varrho^k S_z^k & 0 & 0 & 0 & -\varrho^k I_{yz}^k & \varrho^k I_z^k \end{bmatrix} . \tag{5.23}$$

The discretization of this continuum equation uses the same shape functions as the standard Timoshenko beam element, derived in Section 3.2.

5.2 Shear loading of composite beams

The problems of torsion and torsionless bending of a prismatic composite beam with different regions of material in arbitrary cross sections are formulated. These investigations include orthotropic material behavior. The formulation of these two problems lead to weak forms of partial differential equations. The finite element method is used to obtain a solution of acting shear stresses in the cross section.

Figure 5.2 depicts an arbitrary cross section with different regions Ω_k, where $k \in \mathbb{Z}$. These regions are outlined by the boundary $\partial\Omega_k$. Point C marks the centroid of the composite cross section. The boundary shapes $\partial\Omega_k$ define the normal vector $\boldsymbol{n} = [\ 0 \quad n_y \quad n_z\ ]^T$ and the tangent vector $\boldsymbol{t} = [\ 0 \quad t_y \quad t_z\ ]^T$. The direction of the tangent vector of outer boundary lines $\partial\Omega_{ko}$ is defined anticlockwise and the direction of inner boundary lines $\partial\Omega_{ki}$, e.g. holes, have to be clockwise. The boundaries $\partial\Omega_{ki}$ and $\partial\Omega_{ko}$ are summarized in $\partial\Omega_k = \partial\Omega_{ko} \bigcup \partial\Omega_{ki}$.

The momentum of balance in Equation (3.34) for different composite layers becomes

$$\begin{aligned} \sigma_{x,x}^k + \tau_{xy,y}^k + \tau_{xz,z}^k &= 0 \\ \sigma_{y,y}^k + \tau_{yz,z}^k + \tau_{xy,x}^k &= 0 \\ \sigma_{z,z}^k + \tau_{xz,x}^k + \tau_{yz,y}^k &= 0 \ . \end{aligned} \tag{5.24}$$

The volume and inertia forces are neglected. For a prismatic beam, the components σ_y^k, σ_z^k and τ_{yz}^k vanish. The stresses on the outer boundary and on the boundary of holes vanish in normal direction,

$$\tau_{xy}^k dz - \tau_{xz}^k dy = 0 \qquad \text{on } \partial\Omega_k \ . \tag{5.25}$$

The stresses in normal direction on the interfaces separating two regions k and l are equal and in opposite direction, denoted as

$$\tau_{xy}^k dz - \tau_{xz}^k dy = \tau_{xy}^l dz - \tau_{xz}^l dy \qquad \text{on } \partial\Omega_k \bigcap \partial\Omega_l \ . \tag{5.26}$$

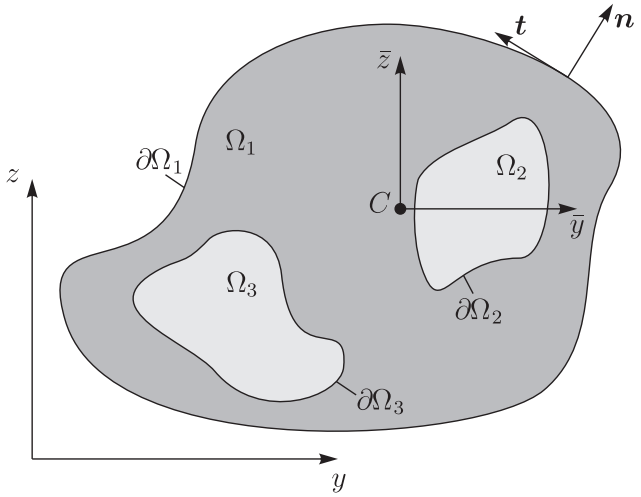

Figure 5.2: Arbitrary cross section of a composite beam

5.2.1 Torsion of a composite Timoshenko beam with orthotropic material properties

A cantilevered prismatic composite beam is loaded with a constant torque on the free end. The beam is free from body forces and other external forces. The displacement field for a cantilevered beam under torsion is introduced in Equation (4.5). Using the strain-displacement relation in Equation (3.8), the shear stresses of a composite region with orthotropic material behavior under torsion are given by

$$\boldsymbol{\tau}^k = \begin{bmatrix} \tau^k_{xy} \\ \tau^k_{xz} \end{bmatrix} = \alpha \begin{bmatrix} G^k_{xy} \ (\psi(y,z)_{,y} - z) \\ G^k_{xz} \ (\psi(y,z)_{,z} + y) \end{bmatrix} . \tag{5.27}$$

Using the momentum of balance of a composite prismatic beam in Equation (5.24) and the relation of shear stresses for orthotropic materials in Equation (5.27), the strong form of a partial differential equation

$$G^k_{xy}\ \psi_{,yy} + G^k_{xz}\ \psi_{,zz} = 0 \quad \text{in } \Omega_k \ , \tag{5.28}$$

with the boundary condition

$$n_y\ \psi_{,y}\ G^k_{xy} + n_z\ \psi_{,z}\ G^k_{xz} = n_y\ z\ G^k_{xy} - n_z\ y\ G^k_{xz} \quad \text{on } \partial\Omega_k \ . \tag{5.29}$$

is derived.

The shear stresses can be expressed by the Prandl's stress function ψ. The relation between the shear stresses and Prandl's stress function

$$\tau^k_{xy} = \alpha\ G^k_{xy}\ \phi^k_{,z} \qquad \text{and} \qquad \tau^k_{xy} = -\alpha\ G^k_{xz}\ \phi^k_{,y} \tag{5.30}$$

have to satisfy the boundary condition of Equation (5.25). Introducing Prandl's stress function in Equation (5.27) and carrying out a second partial derivative, the Poisson equation

$$\Delta\phi^k = -\alpha \left(G^k_{xy} + G^k_{xz} \right) + \alpha \, \psi_{,yz} \, \left(G^k_{xy} - G^k_{xz} \right) \tag{5.31}$$

results.

The torque is given by

$$M_T = \sum_k^m \int_{\Omega_k} \left(y\tau^k_{xz} - z\tau^k_{xy} \right) dA \ , \tag{5.32}$$

where the reference axis can be chosen arbitrarily. Imposing the relation of shear stresses and Prandl's stress function in Equation (5.30) to the equation of the torque and applying the product rule of differential calculus, the torque is rewritten as

$$M_T = 2 \sum_k^m \int_{\Omega_k} \phi^k \, dA - \sum_k^m \int_{\Omega_k} \left((y\phi^k)_{,y} + (z\phi^k)_{,z} \right) \, dA \ . \tag{5.33}$$

The Gauss theorem applied to the last expression yields the torque in terms of Prandl's stress function ϕ,

$$M_T = 2 \sum_k^m \int_{\Omega_k} \phi^k \, dA - \sum_k^m \oint_{\partial\Omega_k} \phi^k \, (y \, n_y + z \, n_z) \, ds \ . \tag{5.34}$$

The torque can also be expressed in terms of the warping function $\psi(y,z)$. The shear stresses in Equation (5.27) are used and the torque leads in case of orthotropic material behavior to

$$M_T = \alpha \, \sum_k^m \int_{\Omega_k} \left(G^k_{xz}(y^2 + \psi_{,z}y) + G^k_{xy}(z^2 - \psi_{,y}z) \right) \, dA \tag{5.35}$$

The torsional stiffness is divided into two parts, the torsional stiffness $I_{T_{xy}}$ corresponding to the xy-plane and the torsional stiffness $I_{T_{xz}}$ to the xz-plane. These torsional stiffnesses for orthotropic materials are computed from

$$I^k_{T_{xy}} = \int_{\Omega_k} (z^2 - \psi_{,y}z) \, dA \qquad \text{and} \qquad I^k_{T_{xz}} = \int_{\Omega_k} (y^2 + \psi_{,z}y) \, dA \ , \tag{5.36}$$

respectively. The relation between torque and torsion is derived from

$$\alpha = \frac{M_T}{\sum_k^m \left(G^k_{xy} \, I^k_{T_{xy}} + G^k_{xz} \, I^k_{T_{xz}} \right)} \ . \tag{5.37}$$

5.2.2 Torsionless bending of a composite Timoshenko beam with orthotropic material properties

Equal to Subsection 4.1.3, the strain field $\epsilon_x(\bar{y},\bar{z})$ of the cross section is defined by a linear combination of two constants $\tilde{a}_1$ and $\tilde{a}_2$ multiplied with the coordinates $\bar{y}$ and $\bar{z}$. The coordinates are related to the centroid of the cross section. The constants are written as

$$\epsilon_x = \tilde{a}_1 \bar{y} + \tilde{a}_2 \bar{z} \ . \tag{5.38}$$

Using the strain stress relation in normal direction, noted in Equation (5.3), imposed on the internal moments in Equation (5.7) one obtains

$$M_y = \sum_k^m E_x^k \int\limits_{\Omega_k} \left(\tilde{a}_1 \bar{y}\bar{z} + \tilde{a}_2 \bar{z}^2 \right) \, dA \tag{5.39}$$

and

$$M_z = -\sum_k^m E_x^k \int\limits_{\Omega_k} \left(\tilde{a}_1 \bar{y}^2 + \tilde{a}_2 \bar{y}\bar{z} \right) \, dA \tag{5.40}$$

Introducing the second moments of area $I_{\bar{y}}^k$, $I_{\bar{z}}^k$ and $I_{\bar{y}\bar{z}}^k$, the constants $\tilde{a}_1$ and $\tilde{a}_2$ are

$$\tilde{a}_1 = -\frac{M_z \sum\limits_k^m E_x^k \, I_{\bar{y}}^k + M_y \sum\limits_k^m E_x^k \, I_{\bar{y}\bar{z}}^k}{\sum\limits_k^m E_x^k \, I_{\bar{y}}^k \sum\limits_k^m E_x^k \, I_{\bar{z}}^k - \left(\sum\limits_k^m E_x^k \, I_{\bar{y}\bar{z}}^k \right)^2} \tag{5.41}$$

and

$$\tilde{a}_2 = \frac{M_y \sum\limits_k^m E_x^k \, I_{\bar{z}}^k + M_z \sum\limits_k^m E_x^k \, I_{\bar{y}\bar{z}}^k}{\sum\limits_k^m E_x^k \, I_{\bar{y}}^k \sum\limits_k^m E_x^k \, I_{\bar{z}}^k - \left(\sum\limits_k^m E_x^k \, I_{\bar{y}\bar{z}}^k \right)^2} \ . \tag{5.42}$$

The normal stress results in

$$\begin{aligned} \sigma_x = &-\frac{M_z \sum\limits_k^m E_x^k \, I_{\bar{y}}^k + M_y \sum\limits_k^m E_x^k \, I_{\bar{y}\bar{z}}^k}{\sum\limits_k^m E_x^k \, I_{\bar{y}}^k \sum\limits_k^m E_x^k \, I_{\bar{z}}^k - \left(\sum\limits_k^m E_x^k \, I_{\bar{y}\bar{z}}^k \right)^2} \, \bar{y} + \dots \\ &\frac{M_y \sum\limits_k^m E_x^k \, I_{\bar{z}}^k + M_z \sum\limits_k^m E_x^k \, I_{\bar{y}\bar{z}}^k}{\sum\limits_k^m E_x^k \, I_{\bar{y}}^k \sum\limits_k^m E_x^k \, I_{\bar{z}}^k - \left(\sum\limits_k^m E_x^k \, I_{\bar{y}\bar{z}}^k \right)^2} \, \bar{z} \ . \end{aligned} \tag{5.43}$$

The derivative of the normal stress σ_x^k with respect to x yields

$$\begin{aligned}\sigma_{x,x} =& \frac{Q_y \sum_k^m E_x^{k^2}\ I_{\bar{y}}^k - Q_z \sum_k^m E_x^{k^2}\ I_{\bar{y}\bar{z}}^k}{\sum_k^m E_x^k\ I_{\bar{y}}^k \sum_k^m E_x^k\ I_{\bar{z}}^k - \left(\sum_k^m E_x^k\ I_{\bar{y}\bar{z}}^k\right)^2}\ \bar{y} + \dots \\ & \frac{Q_z \sum_k^m E_x^{k^2}\ I_{\bar{z}}^k - Q_y \sum_k^m E_x^{k^2}\ I_{\bar{y}\bar{z}}^k}{\sum_k^m E_x^k\ I_{\bar{y}}^k \sum_k^m E_x^k\ I_{\bar{z}}^k - \left(\sum_k^m E_x^k\ I_{\bar{y}\bar{z}}^k\right)^2}\ \bar{z}\ .\end{aligned} \tag{5.44}$$

The constant expressions are summarized to the constants a_1 and a_2 noted by

$$a_1 = \frac{Q_y \sum_k^m E_x^{k^2}\ I_{\bar{y}}^k - Q_z \sum_k^m E_x^{k^2}\ I_{\bar{y}\bar{z}}^k}{\sum_k^m E_x^k\ I_{\bar{y}}^k \sum_k^m E_x^k\ I_{\bar{z}}^k - \left(\sum_k^m E_x^k\ I_{\bar{y}\bar{z}}^k\right)^2} \tag{5.45}$$

and

$$a_2 = \frac{Q_z \sum_k^m E_x^{k^2}\ I_{\bar{z}}^k - Q_y \sum_k^m E_x^{k^2}\ I_{\bar{y}\bar{z}}^k}{\sum_k^m E_x^k\ I_{\bar{y}}^k \sum_k^m E_x^k\ I_{\bar{z}}^k - \left(\sum_k^m E_x^k\ I_{\bar{y}\bar{z}}^k\right)^2}\ . \tag{5.46}$$

The shear stresses τ_{xy} and τ_{yz} are formulated using a stress function Ψ. In case of the composite beam, the shear stresses are written as

$$\tau_{xy}^k = \Psi_{,z}^k - \frac{1}{2} a_1 \bar{y}^2 \qquad \text{and} \qquad \tau_{yz}^k = -\Psi_{,y}^k - \frac{1}{2} a_2 \bar{z}^2\ . \tag{5.47}$$

The stress function Ψ^k has to fulfill the compatibility equations $\varepsilon_{yz,yx} + \varepsilon_{yx,yz} - \varepsilon_{zx,yy} - \varepsilon_{yy,zx} = 0$ and $\varepsilon_{zx,zy} + \varepsilon_{zy,zx} - \varepsilon_{xy,zz} - \varepsilon_{zz,xy} = 0$ [147]. For an orthotropic material the strain-stress relation of Equation (5.1) is used. Considering the assumptions for a Timoshenko beam

$$\sigma_y^k = \sigma_z^k = \tau_{yz}^k = 0 \tag{5.48}$$

the compatibility equations

$$\frac{1}{G_{yz}^k}\tau_{xz,xx}^k + \frac{1}{G_{xz}^k}\tau_{xz,yy}^k + \frac{1}{G_{xy}^k}\tau_{xz,zz}^k + \left(\frac{1}{G_{xy}^k} - \frac{2\nu_{xy}^k}{E_y^k}\right)\sigma_{x,xz}^k = 0 \tag{5.49}$$

and

$$\frac{1}{G_{yz}^k}\tau_{xy,xx}^k + \frac{1}{G_{xz}^k}\tau_{xy,yy}^k + \frac{1}{G_{xy}^k}\tau_{xy,zz}^k + \left(\frac{1}{G_{xz}^k} - \frac{2\nu_{xz}^k}{E_z^k}\right)\sigma_{x,xy}^k = 0 \tag{5.50}$$

for a layer of a composite beam with orthotropic material are derived. The compatibility equations yield the two partial differential equations

$$G_{xy}^k \Psi_{yyz}^k + G_{xz}^k \Psi_{zzz}^k = 2 G_{xy}^k G_{xz}^k \frac{\nu_{xz}^k}{E_z^k} a_1 \tag{5.51}$$

and

$$G_{xy}^k \Psi_{yyy}^k + G_{xz}^k \Psi_{zzy}^k = -2 G_{xy}^k G_{xz}^k \frac{\nu_{xy}^k}{E_y^k} a_2 \ . \tag{5.52}$$

Furthermore, the boundary condition for the shear stress given in Equation (5.25) has to be complied. The integration of the partial differential equations above and the boundary condition with respect to $\bar{y}$ and $\bar{z}$ lead to the Dirichlet problem:

$$\begin{aligned} G_{xy}^k \, \Psi_{yy}^k + & G_{xz}^k \, \Psi_{zz}^k = \dots \\ & 2 \, G_{xy}^k \, G_{xz}^k \left(\frac{\nu_{xz}^k}{E_z^k} \, a_1 \, (\bar{z} - \bar{z}_0) - \frac{\nu_{xy}^k}{E_y^k} \, a_2 \, (\bar{y} - \bar{y}_0) \right) \quad \text{in } \Omega_k \end{aligned} \tag{5.53}$$

$$\Psi^k(s) = \Psi_0^k + \frac{1}{2} \left(a_1 \, \bar{y}^2 \bar{z} - a_2 \, \bar{z}^2 \bar{y} \right) \qquad \text{on } \partial\Omega_k \ . \tag{5.54}$$

The boundary value problem can also be formulated by introducing a conjugate stress function $\bar{\Psi}$. In this case, the shear stresses are given by

$$\tau_{xy}^k = \Psi_{,z}^k - \frac{1}{2} a_1 \bar{y}^2 = G_{xy}^k \bar{\Psi}_{,y}^k - g_1^k(z) \tag{5.55}$$

and

$$\tau_{xz}^k = -\Psi_{,y}^k - \frac{1}{2} a_2 \bar{z}^2 = G_{xz}^k \bar{\Psi}_{,z}^k + g_2^k(y) \ . \tag{5.56}$$

Note that the relations $y - y_0 = \bar{y} - \bar{y}_0$ and $z - z_0 = \bar{z} - \bar{z}_0$ are valid. Imposing the above relations between the stress function Ψ and the conjugate stress function $\bar{\Psi}$ on Equation (5.53), an integration with respect to $\bar{y}$ and $\bar{z}$ gives the unknown functions

$$g_1^k(z) = -G_{xy}^k \frac{\nu_{xz}^k}{E_z^k} a_1 (z - z_0)^2 \tag{5.57}$$

and

$$g_2^k(y) = G_{xz}^k \frac{\nu_{xy}^k}{E_y^k} a_2 (y - y_0)^2 \ . \tag{5.58}$$

The boundary value problem is transferred into a Neumann problem using the conjugate stress function $\bar{\Psi}$. Based on the condition $\Psi_{,zy} - \Psi_{,yz} = 0$ and Equation (5.25), the Neumann problem is written as

$$G_{xy}^k \, \bar{\Psi}_{,yy}^k + G_{xz}^k \, \bar{\Psi}_{,zz}^k = -a_1 \bar{y} - a_2 \bar{z} \qquad \text{in } \Omega \tag{5.59}$$

$$n_y \, G_{xy}^k \, \bar{\Psi}_{,y}^k + n_z \, G_{xz}^k \, \bar{\Psi}_{,z}^k = n_y \, g_1^k(z) - n_z \, g_2^k(y) \qquad \text{on } \partial\Omega \ . \tag{5.60}$$

The condition for torsionless bending

$$\sum_k^m \int_{\Omega_k} \left(\tau_{xz}^k \; y - \tau_{xy}^k \; z \right) dA = 0 \tag{5.61}$$

must hold for the orthotropic composite beam. The torsion vanishes for a beam loaded with shear forces. The relations between the Prandl's stress function and warping function

$$y = -\Phi_{,y} - \bar{\psi}_{,z} \qquad \text{and} \qquad z = -\Phi_{,z} + \bar{\psi}_{,y} \tag{5.62}$$

are introduced in the condition of torsionless bending. The condition of torsionless bending becomes

$$\sum_k^m \int_{\Omega_k} \left[\left(G_{xz}^k \bar{\Psi}_{,z}^k + g_2^k(y) \right) \; \left(-\Phi_{,y} - \bar{\psi}_{,z} \right) - \left(G_{xy}^k \bar{\Psi}_{,y}^k - g_1^k(z) \right) \; \left(-\Phi_{,z} + \bar{\psi}_{,y} \right) \right] dA = 0 \tag{5.63}$$

including the stress formulation with the conjugate stress function $\bar{\Psi}$. Integration by parts yields

$$\begin{aligned}
&\sum_k^m \int_{\Omega_k} \left[\left(G_{xz}^k \Phi_{,z} \bar{\Psi} \right)_{,y} - \left(G_{xy}^k \Phi_{,y} \bar{\Psi} \right)_{,z} \right] dA - \sum_k^m \int_{\Omega_k} \left[G_{xz}^k \Phi_{,zy} - G_{xy}^k \Phi_{,yz} \right] \bar{\Psi} \; dA - \dots \\
&\sum_k^m \int_{\Omega_k} \left[\left(\left(G_{xy}^k \bar{\Psi}_{,y}^k - g_1^k(z) \right) \bar{\psi} \right)_{,y} - \left(\left(G_{xz}^k \bar{\Psi}_{,z}^k + g_2^k(y) \right) \bar{\psi} \right)_{,z} \right] dA + \dots \\
&\sum_k^m \int_{\Omega_k} \left[G_{xy}^k \bar{\Psi}_{,yy} + G_{xz}^k \bar{\Psi}_{,zz} \right] \bar{\psi} \; dA - \sum_k^m \int_{\Omega_k} \left(g_1^k(z) \; \Phi_{,z} + g_2^k(y) \; \Phi_{,y} \right) \bar{\psi} \; dA = 0 \; .
\end{aligned} \tag{5.64}$$

Applying Green's theorem the condition is rewritten as

$$\begin{aligned}
&\sum_k^m \oint_{\partial\Omega_k} \left(G_{xz}^k \Phi_{,z} \; n_y - G_{xy}^k \Phi_{,y} \, n_z \right) \bar{\Psi} \; ds - \dots \\
&\sum_k^m \oint_{\partial\Omega_k} \left[\left(G_{xy}^k \bar{\Psi}_{,y}^k - g_1^k(z) \right) \; n_y - \left(G_{xz}^k \bar{\Psi}_{,z}^k + g_2^k(y) \right) \; n_z \right] \bar{\psi} \; ds + \dots \\
&\sum_k^m \int_{\Omega_k} \left[G_{xy}^k \bar{\Psi}_{,yy} + G_{xz}^k \bar{\Psi}_{,zz} \right] \bar{\psi} \; dA - \sum_k^m \int_{\Omega_k} \left(g_1^k(z) \; \Phi_{,z} + g_2^k(y) \; \Phi_{,y} \right) \bar{\psi} \; dA = 0 \; .
\end{aligned} \tag{5.65}$$

Considering the boundary condition of the torsional problem in Equation (5.29) and

the boundary condition of the Neumann problem in torsionless case in Equation (5.60), the boundary integrals vanish. The equation above becomes

$$\sum_{k}^{m} \int_{\Omega_k} \Bigg[G_{xy}^{k} \frac{\nu_{xz}^{k}}{E_{z}^{k}} \, a_1 \, (z - z_0)^2 (\bar{\psi}_{,y} - z) + \ldots \\ G_{xz}^{k} \frac{\nu_{xy}^{k}}{E_{y}^{k}} \, a_2 \, (y - y_0)^2 (\bar{\psi}_{,z} + y) \Bigg] \, dA = 0 \tag{5.66}$$

for torsionless conditions. Additionally, the resultants of the torsion shear stresses

$$\sum_{k}^{m} \int_{\Omega_k} \tau_{xy}^{k} \, dA = \alpha \sum_{k}^{m} \int_{\Omega_k} G_{xy}^{k} \, (\bar{\psi}_{,y} - z) \, dA = 0 \tag{5.67}$$

and

$$\sum_{k}^{m} \int_{\Omega_k} \tau_{xz}^{k} \, dA = \alpha \sum_{k}^{m} \int_{\Omega_k} G_{xz}^{k} \, (\bar{\psi}_{,z} + y) \, dA = 0 \tag{5.68}$$

vanish. Based on Equation (5.66) the following definitions are introduced:

$$K_{y}^{k} = \int_{\Omega_k} (\bar{\psi}_{,z} + y) y \, dA \tag{5.69}$$

$$K_{yy}^{k} = \int_{\Omega_k} (\bar{\psi}_{,z} + y) y^2 \, dA \tag{5.70}$$

$$K_{z}^{k} = \int_{\Omega_k} (\bar{\psi}_{,y} - z) z \, dA \tag{5.71}$$

$$K_{zz}^{k} = \int_{\Omega_k} (\bar{\psi}_{,y} - z) z^2 \, dA \tag{5.72}$$

Imposing these definitions on Equation (5.66) one obtains

$$\sum_{k}^{m} \left[G_{xy}^{k} \frac{\nu_{xz}^{k}}{E_{z}^{k}} \, a_1 \, (K_{zz}^{k} - 2 \, z_0 \, K_{z}^{k}) + G_{xz}^{k} \frac{\nu_{xy}^{k}}{E_{y}^{k}} \, a_2 \, (K_{yy}^{k} - 2 \, y_0 \, K_{y}^{k}) \right] = 0 \, . \tag{5.73}$$

The Young's moduli E_{y}^{k} and E_{z}^{k}, shear moduli G_{xy}^{k} and G_{xz}^{k}, Poisson ratios ν_{xy}^{k} and ν_{xz}^{k} and constants a_1 and a_2 are unequal zero. The equation above is only fulfilled, if both parenthetical expressions become zero, which gives the integration constants

$$y_0 = \frac{\sum_{k}^{m} K_{yy}^{k}}{2 \sum_{k}^{m} K_{y}^{k}} \quad \text{and} \quad z_0 = \frac{\sum_{k}^{m} K_{zz}^{k}}{2 \sum_{k}^{m} K_{z}^{k}} \, . \tag{5.74}$$

5.2.3 Shear center of composite beams

The shear center for composite beams with orthotropic material is determined by the condition

$$Q_z\ y_M - Q_y\ z_M = \sum_k^m \int_{\Omega_k} \left(\tau_{xz}^k\ y - \tau_{xy}^k\ z \right) dA\ . \tag{5.75}$$

The coordinates of the shear center are defined, so that the resulting torsional moments due to the shear forces are equal to the resulting torsional moments caused by the shear stresses.

The shear forces of the composite beam are given by

$$Q_y = \sum_k^m \int_{\Omega_k} \tau_{xy}^k\ dA \qquad \text{and} \qquad Q_z = \sum_k^m \int_{\Omega_k} \tau_{xz}^k\ dA. \tag{5.76}$$

The shear stresses are replaced with the expressions in equations (5.55) and (5.56). Additionally, the shear forces are extended by a term of the Neumann problem in Equation (5.59), which is identical to zero. The shear forces are rewritten as

$$Q_y = \sum_k^m \int_{\Omega_k} \left[G_{xy}^k \bar{\Psi}_{,y}^k - g_1^k(\bar{z}) + \bar{y} \left(G_{xy}^k \bar{\Psi}_{,yy}^k + G_{xz}^k \bar{\Psi}_{,zz}^k + a_1\ \bar{y} + a_2\ \bar{z} \right) \right]\ dA \tag{5.77}$$

and

$$Q_z = \sum_k^m \int_{\Omega_k} \left[G_{xz}^k \bar{\Psi}_{,z}^k + g_2^k(\bar{y}) + \bar{z} \left(G_{xy}^k \bar{\Psi}_{,yy}^k + G_{xz}^k \bar{\Psi}_{,zz}^k + a_1\ \bar{y} + a_2\ \bar{z} \right) \right]\ dA\ . \tag{5.78}$$

Integrating by parts and applying Green's theorem, the shear forces are

$$\begin{aligned} Q_y = & \sum_k^m \oint_{\partial\Omega_k} \left(G_{xy}^k \bar{\Psi}_{,y}^k\ n_y + G_{xz}^k \bar{\Psi}_{,z}^k\ n_z \right)\ \bar{y}\ ds + \dots \\ & \sum_k^m \int_{\Omega_k} \left(a_1\ \bar{y}^2 + a_2\ \bar{y}\bar{z} - g_1^k(\bar{z}) \right) dA \end{aligned} \tag{5.79}$$

and

$$\begin{aligned} Q_z = & \sum_k^m \oint_{\partial\Omega_k} \left(G_{xy}^k \bar{\Psi}_{,y}^k\ n_y + G_{xz}^k \bar{\Psi}_{,z}^k\ n_z \right)\ \bar{z}\ ds + \dots \\ & \sum_k^m \int_{\Omega_k} \left(a_1\ \bar{y}\bar{z} + a_2\ \bar{z}^2 + g_2^k(\bar{y}) \right) dA\ . \end{aligned} \tag{5.80}$$

The boundary condition in Equation (5.60) and Green's theorem are imposed on the shear forces, which become

$$\begin{aligned} Q_y = &\sum_k^m \int_{\Omega_k} \left[\left(\bar{y}\; g_1^k(\bar{z}) \right)_{,y} - \left(\bar{y}\; g_2^k(\bar{y}) \right)_{,z} \right] dA + \dots \\ &\sum_k^m \int_{\Omega_k} \left(a_1\; \bar{y}^2 + a_2\; \bar{y}\bar{z} - g_1^k(\bar{z}) \right) dA \end{aligned} \tag{5.81}$$

and

$$\begin{aligned} Q_z = &\sum_k^m \int_{\Omega_k} \left[\left(\bar{z}\; g_1^k(\bar{z}) \right)_{,y} - \left(\bar{z}\; g_2^k(\bar{y}) \right)_{,z} \right] dA + \dots \\ &\sum_k^m \int_{\Omega_k} \left(a_1\; \bar{y}\bar{z} + a_2\; \bar{z}^2 + g_2^k(\bar{y}) \right) dA \; . \end{aligned} \tag{5.82}$$

It is shown that the computation shear forces are independent from the functions $g_1^k(\bar{z})$ and $g_2^k(\bar{y})$ and therefore, they are set to zero in further formulations,

$$g_1^k(\bar{z}) = g_2^k(\bar{y}) = 0 \; . \tag{5.83}$$

The shear forces are derived as

$$Q_y = \sum_k^m \int_{\Omega_k} \tilde{\tau}_{xy}^k dA = \sum_k^m \int_{\Omega_k} \left(a_1\; \bar{y}^2 + a_2\; \bar{y}\bar{z} \right) dA \tag{5.84}$$

and

$$Q_z = \sum_k^m \int_{\Omega_k} \tilde{\tau}_{xz}^k dA = \sum_k^m \int_{\Omega_k} \left(a_1\; \bar{y}\bar{z} + a_2\; \bar{z}^2 \right) dA \; , \tag{5.85}$$

where

$$\tilde{\tau}_{xy}^k = G_{xy}^k \bar{\Psi}_{,y}^k \qquad \text{and} \qquad \tilde{\tau}_{xz}^k = G_{xz}^k \bar{\Psi}_{,z}^k \; . \tag{5.86}$$

The introduced condition for the shear center is now formulated as

$$\begin{aligned} &Q_z\; y_M - Q_y\; z_M = \dots \\ &\qquad \sum_k^m \int_{\Omega_k} \left[G_{xz}^k \bar{\Psi}_{,z}^k\; \left(-\Phi_{,y} - \bar{\psi}_{,z} \right) - G_{xy}^k \bar{\Psi}_{,y}^k\; \left(-\Phi_{,z} + \bar{\psi}_{,y} \right) \right] dA \; . \end{aligned} \tag{5.87}$$

Applying the Green's theorem and the Neumann problem noted in Equation (5.59), the condition is rewritten as

$$\begin{aligned} Q_z\ y_M - Q_y\ z_M = \sum_k^m \oint_{\partial\Omega_k} \left[G^k_{xy} \Phi_{,z}\ n_y - G^k_{xz} \Phi_{,y}\ n_z \right]\ \bar{\Psi}^k\ ds - \dots \\ \sum_k^m \oint_{\partial\Omega_k} \left[G^k_{xy} \bar{\Psi}^k_{,y}\ n_y + G^k_{xz} \bar{\Psi}^k_{,z}\ n_z \right]\ \bar{\psi}\ ds - \sum_k^m \int_{\Omega_k} (a_1\ \bar{y} + a_2\ \bar{z})\ \bar{\psi}\ dA\ . \end{aligned} \tag{5.88}$$

The boundary integrals vanish using equations (5.29), (5.60) and (5.83) and

$$Q_z\ y_M - Q_y\ z_M = -\sum_k^m \left(a_1\ I^k_{\bar{\psi}\bar{y}} + a_2\ I^k_{\bar{\psi}\bar{z}} \right) \tag{5.89}$$

follows. The shear center is obtained from this condition as

$$y_M = -\frac{\sum_k^m \left(I^k_{\bar{\psi}\bar{z}}\ I^k_{\bar{y}\bar{y}} - I^k_{\bar{\psi}\bar{y}}\ I^k_{\bar{y}\bar{z}} \right)}{\sum_k^m \left(I^k_{\bar{y}\bar{y}}\ I^k_{\bar{z}\bar{z}} - I^{k^2}_{\bar{y}\bar{z}} \right)} \qquad \text{and} \qquad z_M = \frac{\sum_k^m \left(I^k_{\bar{\psi}\bar{y}}\ I^k_{\bar{z}\bar{z}} - I^k_{\bar{\psi}\bar{z}}\ I^k_{\bar{y}\bar{z}} \right)}{\sum_k^m \left(I^k_{\bar{y}\bar{y}}\ I^k_{\bar{z}\bar{z}} - I^{k^2}_{\bar{y}\bar{z}} \right)} \tag{5.90}$$

by setting the shear forces Q_y and Q_z to zero, respectively. As already mentioned in Section 4.2 for isotropic beams, the shear center is identical to the center of twist.

5.2.4 Shear correction factors of composite beams

The composite beam is based on the Timoshenko beam theory. The computation of the shear correction factor depends on the material properties and gives different values for orthotropic materials and for isotropic materials with equal cross sectional shapes.

Based on the work of Stojek [168], the balance of energy has to by satisfied for composite beams. The internal strain energy of a composite beam with orthotropic material has to be equal to the external energy,

$$W_{int} = W_{ext}\ . \tag{5.91}$$

The internal energy of a composite beam with orthotropic material is given by

$$W_{int} = \frac{1}{2} \int_x \sum_k^m \int_{\Omega_k} \left(\frac{\sigma_x^{k^2}}{E_x^k} + \frac{\tau_{xy}^{k^2}}{G_{xy}^k} + \frac{\tau_{xz}^{k^2}}{G_{xz}^k} \right)\ dA\ dx\ . \tag{5.92}$$

The assumptions of the Timoshenko beam theory claim a constant strain distribution

in the cross section. The shear stresses τ_{xy}^k and τ_{xz}^k are replaced by the constant shear stresses $\bar{\tau}_{xy}^k$ and $\bar{\tau}_{xz}^k$ in the integral terms

$$\sum_k^m \int_{\Omega_k} \frac{\tau_{xy}^{k^2}}{G_{xy}^k} dA + \sum_k^m \int_{\Omega_k} \frac{\tau_{xz}^{k^2}}{G_{xz}^k} dA = \sum_k^m \int_{\Omega_{k_{sy}}} \frac{\bar{\tau}_{xy}^{k^2}}{G_{xy}^k} dA_{sy} + \sum_k^m \int_{\Omega_{k_{sz}}} \frac{\bar{\tau}_{xz}^{k^2}}{G_{xz}^k} dA_{sz} \ . \quad (5.93)$$

The constant shear stresses are defined as

$$\bar{\tau}_{xy}^k = \frac{Q_y^k}{A_{sy}^k} \quad \text{and} \quad \bar{\tau}_{xz}^k = \frac{Q_z^k}{A_{sz}^k} \ , \quad (5.94)$$

where the shear areas A_{sy}^k and A_{sz}^k are assumed as

$$A_{sy}^k = \kappa_y \ A^k \qquad \text{and} \qquad A_{sz}^k = \kappa_z \ A^k. \quad (5.95)$$

The inaccuracy of the strain energy resulting from the assumption of a constant stress distribution is compensated by introducing these shear areas. Equation (5.93) is rewritten as

$$\sum_k^m \int_{\Omega_k} \frac{\tau_{xy}^{k^2}}{G_{xy}^k} dA + \sum_k^m \int_{\Omega_k} \frac{\tau_{xz}^{k^2}}{G_{xz}^k} dA = \sum_k^m \frac{Q_y^{k^2}}{\kappa_y \ A^k \ G_{xy}^k} + \sum_k^m \frac{Q_z^{k^2}}{\kappa_z \ A^k \ G_{xz}^k} \ . \quad (5.96)$$

Introducing the inverse stress function $\bar{\Psi}$ defined in equations (5.55) and (5.56),

$$\begin{aligned} \sum_k^m \frac{Q_y^{k^2}}{\kappa_y \ G_{xy}^k \ A^k} + \sum_k^m \frac{Q_z^{k^2}}{\kappa_z \ G_{xz}^k \ A^k} = \ldots \\ \sum_k^m \int_{\Omega_k} \left(\frac{\tau_{xy}^k}{G_{xy}^k} \ G_{xy}^k \bar{\Psi}_{,y}^k + \frac{\tau_{xz}^k}{G_{xz}^k} \ G_{xz}^k \bar{\Psi}_{,z}^k \right) dA - \ldots \\ \sum_k^m \int_{\Omega_k} \left(\frac{\tau_{xy}^k}{G_{xy}^k} \ g_1^k(\bar{z}) - \frac{\tau_{xz}^k}{G_{xz}^k} \ g_2^k(\bar{y}) \right) dA \end{aligned} \quad (5.97)$$

follows. Applying integration by parts and the Green's theorem, the equation above leads to

$$\begin{aligned} &\sum_k^m \frac{Q_y^{k^2}}{\kappa_y \ G_{xy}^k \ A^k} + \sum_k^m \frac{Q_z^{k^2}}{\kappa_z \ G_{xz}^k \ A^k} = \sum_k^m \oint_{\partial\Omega_k} \left(\tau_{xy}^k \ n_y + \tau_{xz}^k \ n_z \right) \bar{\Psi}^k ds - \ldots \\ &\sum_k^m \int_{\Omega_k} \left[\left(G_{xy}^k \bar{\Psi}_{,y}^k - g_1^k(\bar{z}) \right)_{,y} + \left(G_{xz}^k \bar{\Psi}_{,z}^k + g_2^k(\bar{y}) \right)_{,z} \right] \bar{\Psi}^k dA - \ldots \\ &\sum_k^m \int_{\Omega_k} \left(\frac{\tau_{xy}^k}{G_{xy}^k} \ g_1^k(\bar{z}) - \frac{\tau_{xz}^k}{G_{xz}^k} \ g_2^k(\bar{y}) \right) dA \ . \end{aligned} \quad (5.98)$$

Considering (5.25) the boundary integral vanishes. Introducing the partial differential equation of the Neumann problem in Equation (5.59), one obtains

$$\begin{aligned}\sum_k^m \frac{Q_y^{k^2}}{\kappa_y\, G_{xy}^k\, A^k} + \sum_k^m \frac{Q_z^{k^2}}{\kappa_z\, G_{xz}^k\, A^k} &= \sum_k^m \int_{\Omega_k} (a_1\, \bar{y} + a_2\, \bar{z})\, \bar{\Psi}^k dA + \dots \\ a_1 \sum_k^m \int_{\Omega_k} \tau_{xy}^k\, \frac{\nu_{xz}^k}{E_z^k} (\bar{z} - \bar{z}_0)^2 dA &+ a_2 \sum_k^m \int_{\Omega_k} \tau_{xz}^k\, \frac{\nu_{xy}^k}{E_y^k} (\bar{y} - \bar{y}_0)^2 dA\end{aligned} \tag{5.99}$$

The terms

$$J_{\bar{y}\bar{y}}^k = \int_{\Omega_k} \tau_{xz}^k \frac{\nu_{xy}^k}{E_y^k} (\bar{y} - \bar{y}_0)^2 dA \qquad \text{and} \qquad J_{\bar{z}\bar{z}}^k = \int_{\Omega_k} \tau_{xy}^k \frac{\nu_{xz}^k}{E_z^k} (\bar{z} - \bar{z}_0)^2 dA \tag{5.100}$$

are summarized and an equation, which determines the unknown shear correction factors, is given by

$$\begin{aligned}\sum_k^m \frac{Q_y^{k^2}}{\kappa_y\, G_{xy}^k\, A^k} + \sum_k^m \frac{Q_z^{k^2}}{\kappa_z\, G_{xz}^k\, A^k} &= \dots \\ Q_y \Bigg(&\frac{\sum_k^m E_x^{k^2} I_{\bar{\Psi}\bar{y}}^k \sum_k^m E_x^{k^2} I_{\bar{y}}^k - \sum_k^m E_x^{k^2} I_{\bar{\Psi}\bar{z}}^k \sum_k^m E_x^{k^2} I_{\bar{y}z}^k}{\sum_k^m E_x^k\, I_{\bar{y}}^k \sum_k^m E_x^k\, I_{\bar{z}}^k - \left(\sum_k^m E_x^k\, I_{\bar{y}z}^k\right)^2} + \dots \\ &\frac{\sum_k^m E_x^{k^2} J_{\bar{z}\bar{z}}^k \sum_k^m E_x^{k^2} I_{\bar{y}}^k - \sum_k^m E_x^{k^2} J_{\bar{y}\bar{y}}^k \sum_k^m E_x^{k^2} I_{\bar{y}z}^k}{\sum_k^m E_x^k\, I_{\bar{y}}^k \sum_k^m E_x^k\, I_{\bar{z}}^k - \left(\sum_k^m E_x^k\, I_{\bar{y}z}^k\right)^2} \Bigg) + \dots \\ Q_z \Bigg(&\frac{\sum_k^m E_x^{k^2} I_{\bar{\Psi}\bar{z}}^k \sum_k^m E_x^{k^2} I_{\bar{z}}^k - \sum_k^m E_x^{k^2} I_{\bar{\Psi}\bar{y}}^k \sum_k^m E_x^{k^2} I_{\bar{y}z}^k}{\sum_k^m E_x^k\, I_{\bar{y}}^k \sum_k^m E_x^k\, I_{\bar{z}}^k - \left(\sum_k^m E_x^k\, I_{\bar{y}z}^k\right)^2} + \dots \\ &\frac{\sum_k^m E_x^{k^2} J_{\bar{y}\bar{y}}^k \sum_k^m E_x^{k^2} I_{\bar{z}}^k - \sum_k^m E_x^{k^2} J_{\bar{z}\bar{z}}^k \sum_k^m E_x^{k^2} I_{\bar{y}z}^k}{\sum_k^m E_x^k\, I_{\bar{y}}^k \sum_k^m E_x^k\, I_{\bar{z}}^k - \left(\sum_k^m E_x^k\, I_{\bar{y}z}^k\right)^2} \Bigg)\end{aligned} \tag{5.101}$$

The shear correction factors κ_y and κ_z are determined by setting $Q_z = 0$ and $Q_y = 0$, respectively:

$$\frac{1}{\kappa_y} = \sum_k^m \frac{G_{xy}^k A^k}{Q_y^{k^2}} Q_y \left(\frac{\sum_k^m E_x^{k^2} I_{\bar{\Psi}\bar{y}}^k \sum_k^m E_x^{k^2} I_{\bar{y}}^k - \sum_k^m E_x^{k^2} I_{\bar{\Psi}\bar{z}}^k \sum_k^m E_x^{k^2} I_{\bar{y}z}^k}{\sum_k^m E_x^k I_{\bar{y}}^k \sum_k^m E_x^k I_{\bar{z}}^k - \left(\sum_k^m E_x^k I_{\bar{y}z}^k\right)^2} + \dots \right.$$
$$\left. \frac{\sum_k^m E_x^{k^2} J_{\bar{z}\bar{z}}^k \sum_k^m E_x^{k^2} I_{\bar{y}}^k - \sum_k^m E_x^{k^2} J_{\bar{y}\bar{y}}^k \sum_k^m E_x^{k^2} I_{\bar{y}z}^k}{\sum_k^m E_x^k I_{\bar{y}}^k \sum_k^m E_x^k I_{\bar{z}}^k - \left(\sum_k^m E_x^k I_{\bar{y}z}^k\right)^2} \right) \tag{5.102}$$

$$\frac{1}{\kappa_z} = \sum_k^m \frac{G_{xz}^k A^k}{Q_z^{k^2}} Q_z \left(\frac{\sum_k^m E_x^{k^2} I_{\bar{\Psi}\bar{z}}^k \sum_k^m E_x^{k^2} I_{\bar{z}}^k - \sum_k^m E_x^{k^2} I_{\bar{\Psi}\bar{y}}^k \sum_k^m E_x^{k^2} I_{\bar{y}z}^k}{\sum_k^m E_x^k I_{\bar{y}}^k \sum_k^m E_x^k I_{\bar{z}}^k - \left(\sum_k^m E_x^k I_{\bar{y}z}^k\right)^2} + \dots \right.$$
$$\left. \frac{\sum_k^m E_x^{k^2} J_{\bar{y}\bar{y}}^k \sum_k^m E_x^{k^2} I_{\bar{z}}^k - \sum_k^m E_x^{k^2} J_{\bar{z}\bar{z}}^k \sum_k^m E_x^{k^2} I_{\bar{y}z}^k}{\sum_k^m E_x^k I_{\bar{y}}^k \sum_k^m E_x^k I_{\bar{z}}^k - \left(\sum_k^m E_x^k I_{\bar{y}z}^k\right)^2} \right) . \tag{5.103}$$

5.3 Example: Cantilevered composite beam loaded on the free end

The beam bending and the shear stresses are computed for a cantilevered composite beam shown in Figure 5.3a. The composite beam consists of two material layers, region Ω_1 and region Ω_2. It has a length of l. The cross section of this beam is depicted in Figure 5.3b. The outer boundary has of a quadratic shape with an edge length of l_1. A circle separates the two material layers. This circle has a radius r_1. The position of this circle is defined by the length l_2. These geometric quantities are summarized in Table 5.1.

Table 5.1: Geometric quantities of the composite cross section

Parameter	value
Length l	10 mm
Length l_1	4 mm
Length l_2	1 mm
Radius r_1	0.5 mm

The geometric parameters of the multilayered cross section which are necessary for further computations are calculated. These parameters are the area, the center of

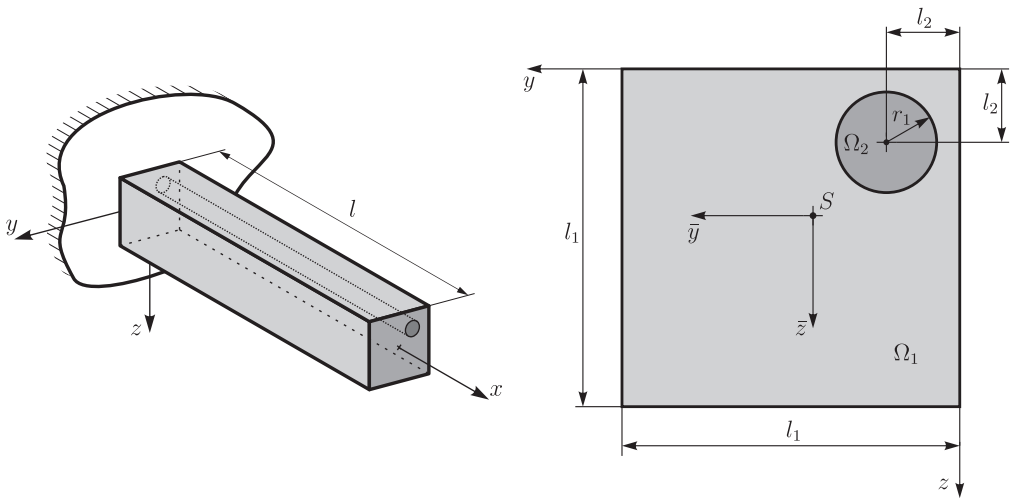

(a) Cantilevered composite beam

(b) Geometry of a test cross section with two material layers

Figure 5.3: Cantilevered beam and corresponding cross section with two material layers defined as a test shape

area and the first and second moments of area. Table 5.2 contains the numerical values.

Table 5.2: Geometric parameters of test cross section

Parameter	All regions $\sum_k \Omega_k$	Region Ω_1	Region Ω_2
Area A	16 mm^2	15.2136 mm^2	0.7864 mm^2
Center of area y_C	2 mm	2.0517 mm	1 mm
Center of area z_C	2 mm	2.0517 mm	1 mm
First moment of area $S_{\bar{y}}$	0 mm^3	0.7864 mm^3	-0.7864 mm^3
First moment of area $S_{\bar{z}}$	0 mm^3	0.7864 mm^3	-0.7864 mm^3
Second moment of area $I_{\bar{y}\bar{y}}$	21.3333 mm^4	20.4978 mm^4	0.8356 mm^4
Second moment of area $I_{\bar{z}\bar{z}}$	21.3333 mm^4	20.4978 mm^4	0.8356 mm^4
Second moment of area $I_{\bar{y}\bar{z}}$	0 mm^4	-0.7864 mm^4	0.7864 mm^4

5.3.1 Beam bending of the cantilevered composite beam

In order to investigate the bending of the composite beam, the beam is clamped on $x = 0$ and a surface force of $f_z^s = 100\,\mathrm{N}$ is applied on the cross section of the free end of the beam at $x = l$. This force is acting in z-direction. The beam consists of two material layers with different material properties. The material of the layer Ω_1 is supposed to have orthotropic properties. The second layer Ω_2 is defined by a material with isotropic properties. The material data for both layers is noted in Table 5.3.

Table 5.3: Material parameters of the composite beam

Parameter	Region Ω_1	Region Ω_2
Young's Modulus E_x	$150 \times 10^9\ \frac{\mathrm{N}}{\mathrm{m}^2}$	$200 \times 10^9\ \frac{\mathrm{N}}{\mathrm{m}^2}$
Young's Modulus E_y	$100 \times 10^9\ \frac{\mathrm{N}}{\mathrm{m}^2}$	-
Young's Modulus E_z	$200 \times 10^9\ \frac{\mathrm{N}}{\mathrm{m}^2}$	-
Poisson ration ν_{xy}	0.1	0.3
Poisson ration ν_{yz}	0.2	-
Poisson ration ν_{xz}	0.3	-
Shear modulus G_{xy}	$20\ \frac{\mathrm{N}}{\mathrm{m}^2}$	-
Shear modulus G_{yz}	$15\ \frac{\mathrm{N}}{\mathrm{m}^2}$	-
Shear modulus G_{xz}	$10\ \frac{\mathrm{N}}{\mathrm{m}^2}$	-

The beam bending is computed by the finite element analyses using composite Timoshenko beam elements (F1CTB). The solution is compared to analytical approaches using the Euler-Bernoulli beam theory (EBT) and the Timoshenko beam theory (TBT). Additionally, a three-dimensional finite element model of the composite beam is created with 21573 elements. For this model 20-node brick elements are used. The numerical solution of this three-dimensional model is used as a reference solution (FE3Dref). In order to compare the solution of the three-dimensional reference model to the one-dimensional solutions, equations (3.117) and (3.118) are used.

Table 5.4: Comparison of shear displacements $w(l)$ of different beam models

Beam model	$w(10)$ in mm	e_{wrel}
Euler-Bernoulli (EBT)	1.0282×10^{-2}	3.9096×10^{-1}
Timoshenko (TBT)	1.6960×10^{-2}	4.5356×10^{-3}
FE 1D composite Timoshenko beam (FE1CTB)	1.6867×10^{-2}	9.5818×10^{-4}
FE 3D model (FE3Dref)	1.6883×10^{-2}	-

The shear displacements $w(l)$ of the cross section's free end is computed for all beam models and summarized in Table 3.1. The analytical Euler-Bernoulli model (EBT) creates an enormous error of $e_{wrel} = 39.1\,\%$ for the displacement of the composite beam's free end. The analytical solution of the Timoshenko beam theory (TBT) produces a significantly better result. The error of the displacement $w(l)$ is below $5\,‰$. The best result is obtained using the finite element method with one-dimensional composite Timoshenko beam elements. In this case, the error of the displacement $w(l)$ is below $1\,‰$.

Figure 5.4a depicts the beam bending of the cantilevered composite beam computed with different beam models. The corresponding errors are shown in Figure 5.4b. The Euler-Bernoulli beam theory (EBT) does not show accurate results. The Timoshenko beam theory (TBT) and the solution of the one-dimensional finite element model F1CTB fit the reference system in a better way. Using larger values of x, the errors of the different models decrease.

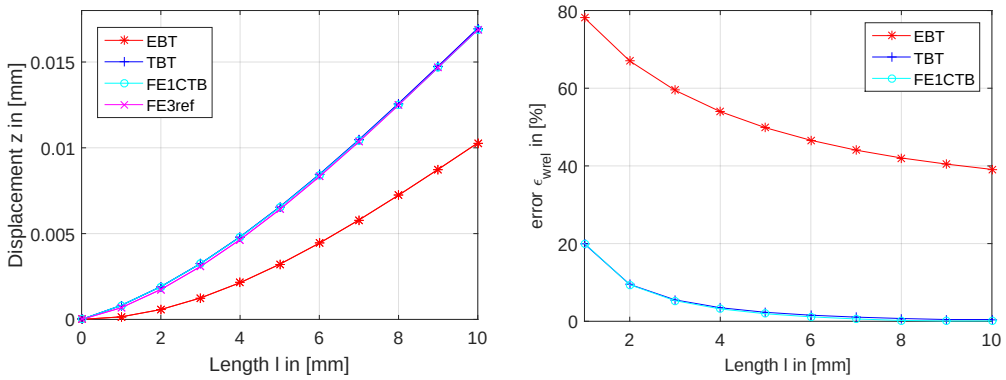

(a) Displacements of the cantilevered composite beam

(b) Relative errors of different beam models

Figure 5.4: Bending of the cantilevered composite beam using Timoshenko beam elements in comparison to different beam models

5.3.2 Shear stresses and cross section parameters of the cantilevered composite beam

The cross section of a cantilevered composite beam is given as depicted in Figure 5.3b is given. The two material layers consist of different material properties, which are summarized in Table 5.3. The shear stresses of the cantilevered composite beam with orthotropic material properties are solved. This computation is based on the Neumann boundary value problem for the Saint-Venant torsion and the torsionless bending, derived in Section 5.2. Therefore, the finite element method is used. The results of these computations are compared to the solutions of a general three-dimensional problem, compare the subsection above.

5.3.2.1 Saint-Venant torsion

The multilayered composite beam is clamped on one end. On the other free end a torque of $M_x = 100\,\mathrm{N/mm^2}$ is imposed. The warping function of multi-layered cross sections with orthotropic material behavior is determined by solving the Neumann problem (5.28). Hence, the torsion-torque constant α, the warping constant $C_{\bar{\psi}\bar{\psi}}$ and the center of twist y_T and z_T are computed for the given problem. The numerical values of these parameters are calculated with different mesh sizes and summarized in Table 5.5. The element number of the different mesh sizes varies from 128 up to 4040 elements. Increasing the number of elements the numerical values converge to the correct value and the numerical error decreases .

Table 5.5: Torsion-torque constant α, warping constant $C_{\bar{\psi}\bar{\psi}}$ and center of twist y_T and z_T of the multilayered cross section in relation to the center of area for different mesh sizes computed with an element number el

el	α	$C_{\bar{\psi}\bar{\psi}}$ in mm^4	y_T in mm	z_T in mm
128	0.1962276	158.593183	1.858810	1.955377
244	0.1962467	161.750689	1.876884	1.975055
304	0.1962481	162.203715	1.879229	1.978010
524	0.1962495	162.764025	1.882441	1.981449
759	0.1962505	162.896627	1.883190	1.982268
1539	0.1962509	163.225903	1.885064	1.984291
4040	0.1962510	163.367759	1.885869	1.985162

Figures 5.5a and 5.5b show the shear stress distributions τ_{xy} and τ_{xz} in the multi-layered cross section with orthotropic material properties. Due to different material

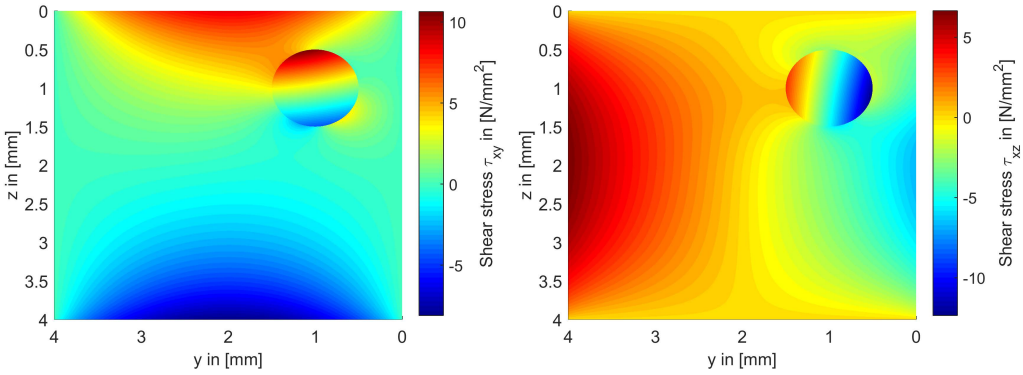

(a) Shear stress τ_{xy} **(b)** Shear stress τ_{xz}

Figure 5.5: Shear stresses τ_{xy} and τ_{xz} of the cantilevered composite beam, loaded with a torque $M_x = 100\,\mathrm{N/mm^2}$ on the free end

properties in each coordinate direction the stress distribution τ_{xy} and τ_{xz} is not symmetrical about any axis. The maximum stresses occur at the boundary region of the inner material layer. The stress values are between a stress range of $-12\,\mathrm{N/mm^2}$ to $10\,\mathrm{N/mm^2}$. At the coordinate position of the center of twist, the shear stresses are zero.

Tables 5.6 and 5.7 summarize the absolute error values of the shear stress distributions τ_{xy} and τ_{xz}. The stresses are compared to the solution of a full three-dimensional finite element model of this cantilevered beam. Therefore, 20-node brick elements are used. The model has an element number of 21573 elements. This model is the same as the reference model of the beam bending. In this case, the three-dimensional solution is used as the reference solution. The absolute error is calculated using Equation (4.95). The mean absolute error is defined in Equation (4.96).

Table 5.6: Mean absolute error $\bar{\varepsilon}_{\tau_{xy}}$, maximum error $\varepsilon_{max,\tau_{xy}}$ and minimum error $\varepsilon_{min,\tau_{xy}}$ in $\mathrm{N/mm^2}$ of the stress distribution τ_{xy} of the cantilevered composite beam for different mesh sizes computed with an element number el, loaded on the free end with a torque $M_x = 100\,\mathrm{Nmm}$

el	$\bar{\varepsilon}_{\tau_{xy}}$ in $\mathrm{N/mm^2}$	$\varepsilon_{max,\tau_{xy}}$ in $\mathrm{N/mm^2}$	$\varepsilon_{min,\tau_{xy}}$ in $\mathrm{N/mm^2}$
128	0.156966	1.005632	0.005820×10^{-4}
244	0.170408	0.995310	0.101530×10^{-4}
304	0.175179	0.995278	0.016970×10^{-4}
524	0.179588	1.002050	0.070118×10^{-4}
759	0.178558	0.741039	0.086782×10^{-4}
1539	0.180995	0.742513	0.029654×10^{-4}
4040	0.181778	0.551129	0.024836×10^{-4}

Table 5.7: Mean absolute error $\bar{\varepsilon}_{\tau_{xz}}$, maximum error $\varepsilon_{max,\tau_{xz}}$ and minimum error $\varepsilon_{min,\tau_{xz}}$ in $\mathrm{N/mm^2}$ of the stress distribution τ_{xz} of the cantilevered composite beam for different mesh sizes computed with an element number el, loaded on the free end with a torque $M_x = 100\,\mathrm{Nmm}$

el	$\bar{\varepsilon}_{\tau_{xz}}$ in $\mathrm{N/mm^2}$	$\varepsilon_{max,\tau_{xz}}$ in $\mathrm{N/mm^2}$	$\varepsilon_{min,\tau_{xz}}$ in $\mathrm{N/mm^2}$
128	0.147872	0.885946	0.115262×10^{-4}
244	0.138387	0.902583	0.010183×10^{-4}
304	0.136400	0.902608	0.082625×10^{-4}
524	0.134005	0.863654	0.141264×10^{-4}
759	0.133971	0.632886	0.166093×10^{-4}
1539	0.133159	0.634026	0.140108×10^{-4}
4040	0.132997	0.518204	0.035242×10^{-4}

Figures 5.6a and 5.6b depict the absolute error distribution of the shear stresses τ_{xy}

and τ_{xz} in the cross section of the multilayered beam loaded with a constant torque. The maximum error values are about $1/20$ of the maximum shear stress values. The largest errors occur at the boundary between the two material layers.

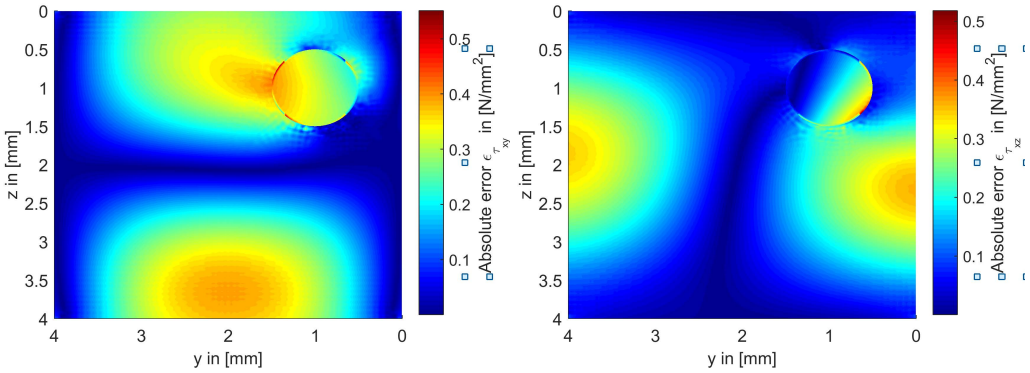

(a) Absolute error of the shear stress τ_{xy} **(b)** Absolute error of the shear stress τ_{xz}

Figure 5.6: Absolute errors $\varepsilon_{\tau_{xy}}$ and $\varepsilon_{\tau_{xz}}$ of the shear stresses of the cantilevered composite beam, loaded on the free end with a torque $M_x = 100\,\mathrm{N/mm^2}$

5.3.2.2 Torsionless bending

The cantilevered composite beam is loaded on the free end with constant shear forces $Q_y = 100\,\mathrm{N}$ and $Q_z = 100\,\mathrm{N}$. The shear forces are imposed as surface forces on the free end. Solving the Neumann boundary value problem in Equation (5.59) using the finite element method, the stress function acting in the cross section is determined. Hence, the shear correction factor and shear center are determined using equations (5.102), (5.103) and (5.90). Table 5.8 summarizes the numerical

Table 5.8: Shear center y_M and z_M and shear correction factors κ_y and κ_z of the multilayered cross section in relation to the center of area for different mesh sizes computed with an element number el

el	y_M in mm	z_M in mm	κ_y	κ_z
128	1.858810	1.955377	0.829414	0.704561
244	1.876884	1.975055	0.829413	0.704508
304	1.879229	1.978010	0.829417	0.704503
524	1.882441	1.981449	0.829423	0.704494
759	1.883190	1.982268	0.829420	0.704482
1539	1.885064	1.984291	0.829424	0.704478
4040	1.885869	1.985162	0.829425	0.704477

values of the shear center y_M and z_M and the shear correction factors κ_y and κ_z for

different mesh sizes. It should be noted that the twist center is equal to the shear center, compare Table 5.5.

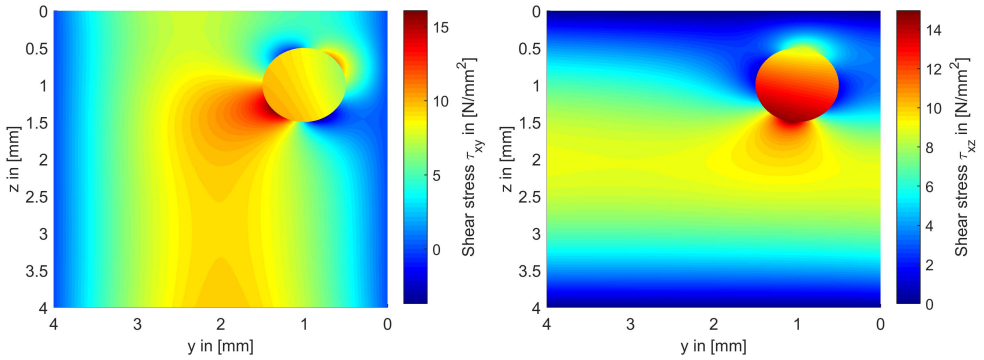

(a) Shear stress τ_{xy} **(b)** Shear stress τ_{xz}

Figure 5.7: Shear stresses τ_{xy} and τ_{xz} of the cantilevered composite beam, loaded on the free end with transversal forces $F_y = 100\,\mathrm{N}$ and $F_z = 100\,\mathrm{N}$

Figures 5.7a and 5.7b depict the shear stress distributions τ_{xy} and τ_{xz} due to imposed shear forces. The material properties are orthotropic in the outer material layer and isotropic in the inner material layer which leads to non-symmetrical stress distributions τ_{xy} and τ_{xz}. The maximum stresses occur at the boundary between the two material layers. The stress values are between a stress range of about $-3\,\mathrm{N/mm^2}$ to $16\,\mathrm{N/mm^2}$.

Tables 5.9 and 5.10 contain absolute error values of the shear stress distributions τ_{xy} and τ_{xz}. Equal to the torsional problem, the shear stresses are compared to the solution of a full three-dimensional finite element model. This model is the same as for the torsional problem and the three-dimensional solution is also used as the reference solution. The absolute errors are given by Equation (4.95). The mean absolute errors are obtained from Equation (4.96).

Figures 5.8a and 5.8b show the absolute error distribution of the shear stresses τ_{xy} and τ_{xz} in the cross section of the multilayered beam loaded with a constant shear force. The maximum numerical values of the absolute error distribution are about $1/10$ of the maximum shear stress values. The largest errors in case of torsionless bending occur at the same location as for the torsional problem. This location is found at the boundary between the to material layers again.

Table 5.9: Mean absolute error $\bar{\varepsilon}_{\tau_{xy}}$, maximum error $\varepsilon_{max,\tau_{xy}}$ and minimum error $\varepsilon_{min,\tau_{xy}}$ in $^{\mathrm{N}}/_{\mathrm{mm}^2}$ of the stress distribution τ_{xy} of the cantilevered composite beam for different mesh sizes computed with an element number el, loaded on the free end with $F_y = 100\,\mathrm{N}$ and $F_z = 100\,\mathrm{N}$

el	$\bar{\varepsilon}_{\tau_{xy}}$ in $^{\mathrm{N}}/_{\mathrm{mm}^2}$	$\varepsilon_{max,\tau_{xy}}$ in $^{\mathrm{N}}/_{\mathrm{mm}^2}$	$\varepsilon_{min,\tau_{xy}}$ in $^{\mathrm{N}}/_{\mathrm{mm}^2}$
128	0.339570	2.244728	0.158706×10^{-4}
244	0.326664	2.281103	0.099922×10^{-4}
304	0.325549	2.281237	0.565838×10^{-4}
524	0.324432	2.149507	0.198720×10^{-4}
759	0.318043	1.912713	0.159470×10^{-4}
1539	0.317079	1.914131	0.318080×10^{-4}
4040	0.316949	1.909448	0.249555×10^{-4}

Table 5.10: Mean absolute error $\bar{\varepsilon}_{\tau_{xz}}$, maximum error $\varepsilon_{max,\tau_{xz}}$ and minimum error $\varepsilon_{min,\tau_{xz}}$ in $^{\mathrm{N}}/_{\mathrm{mm}^2}$ of the stress distribution τ_{xz} of the cantilevered composite beam for different mesh sizes computed with an element number el, loaded on the free end with $F_y = 100\,\mathrm{N}$ and $F_z = 100\,\mathrm{N}$

el	$\bar{\varepsilon}_{\tau_{xz}}$ in $^{\mathrm{N}}/_{\mathrm{mm}^2}$	$\varepsilon_{max,\tau_{xz}}$ in $^{\mathrm{N}}/_{\mathrm{mm}^2}$	$\varepsilon_{min,\tau_{xz}}$ in $^{\mathrm{N}}/_{\mathrm{mm}^2}$
128	0.203406	2.625724	0.262057×10^{-5}
244	0.189963	1.976678	0.318348×10^{-5}
304	0.189263	1.976997	0.281860×10^{-7}
524	0.190016	2.371406	0.411170×10^{-5}
759	0.184895	1.582416	0.310578×10^{-6}
1539	0.183780	1.453867	0.235130×10^{-5}
4040	0.183068	1.294565	0.273431×10^{-5}

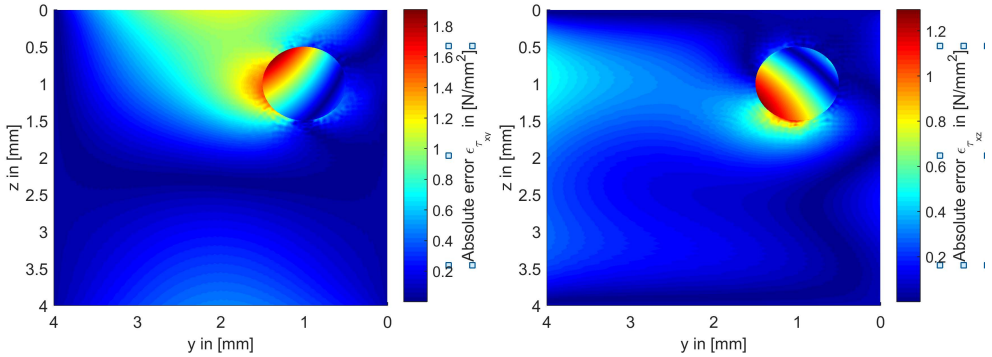

(a) Absolute error of the shear stress τ_{xy} **(b)** Absolute error of the shear stress τ_{xz}

Figure 5.8: Absolute errors $\varepsilon_{\tau_{xy}}$ and $\varepsilon_{\tau_{xz}}$ of the shear stresses of the cantilevered composite beam, loaded on the free end with transversal forces $F_y = 100\,\mathrm{N}$ and $F_z = 100\,\mathrm{N}$

CHAPTER 6

Modeling the rotor of electrical machines using beam elements

The simplest model of a flexible rotor is the Jeffcott rotor. The Jeffcott rotor consists of a flexible and massless shaft and a point mass. The dynamic behavior was studied by Jeffcott [80]. This model shows some basic characteristics of the dynamic behavior of a rotor. However, this model does not consider typical machine designs and geometric influences. In order to consider the flexible continuum of the rotor, the transfer matrices approach is used. This method was very common in the past [176], [54]. Nowadays, the finite element method is the widely used method for a mechanical simulation of rotor-dynamical systems. Three-dimensional finite element models for rotor-dynamical problems require an enormous numerical effort, especially when computing transient effects. One-dimensional finite element models are sufficient for many cases and computationally much more efficient.

In this chapter, the mechanical model of a rotor of an induction machine is modeled. The investigated machine is used in wind power plants. The heterogeneous structure of the rotor is taken into account using composite Timoshenko beam elements. The cross section parameters are computed in an additional simulation apriori. The material behavior is assumed to be linear. Further, an experimental modal analysis is performed in order to test the vibrational behavior. The obtained modal parameters are compared to the results of a numerical modal analysis in order to validate the finite element model of the rotor. Finally, a run up simulation of the rotor is performed in frequency domain , where the gyroscopic effect and the spin softening effect are taken into account.

6.1 General design of the rotor

Figure 6.1 shows a schematic drawing of the design of a rotor of an induction machine. The rotor is a slip ring rotor and consists of different components. Each component is composed of different materials with corresponding mechanical properties. The

main parts are named in Figure 6.1. The general mechanical characteristics of the rotor are summarized in Table 6.1.

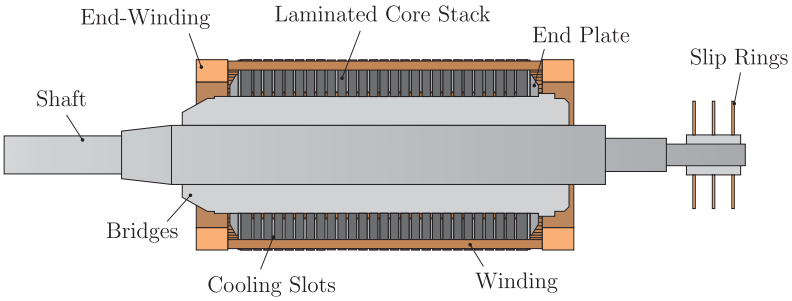

Figure 6.1: Design of an rotor of an induction machine

Table 6.1: General rotor parameters

parameter	value
length l_r	3760 mm
diameter d_r	905 mm
mass m_r	6840 kg
mass moment of inertia J_r	761 kgm^2

The shaft is the core part of the rotor. All other parts are mounted on the shaft. The shaft is made of steel and material properties are assumed to be linear elastic. Six bridges are welded onto the shaft, which provide a fixed connection between shaft and bridges. These are evenly spaced around the shaft axis. The bridges are made of the same material as the shaft. Laminated core stacks are pressed and locked against twisting on the bridges. For the laminated core stacks, the material model is homogenized and assumed to be transversal isotropically [111]. It is assumed that the prestress in the laminated core stack is constant and the change of the material properties for the transversally isotropic material model during vibration is neglectable. The core stack, which denotes the assembly of all laminated core stacks, is prestressed by the two end plates. These are welded on the bridges on both ends. The end plates are also made of steel and have the same linear elastic material properties as the shaft. Cooling slots are provided between the laminated core stacks. These slots allow for an air stream through the laminated core stack, which guarantees that the rotor operates in an adequate temperature range. The windings are mounted in slots through the laminated core stack. These copper rods are coated with isolation material and modeled as linear elastic material. The material parameters are a linear combination of the parameters of copper and the parameters of the isolation material depending on their volume. The end windings are mounted on both ends of the windings. They also consist of a combination of copper and isolation material. Slip rings are fixed at the rotor end. In the following numerical and experimental investigations, the slip rings are neglected.

As mentioned above, the material models of all rotor parts are linear elastic. Table 6.2 lists the material properties of each part. These parameters are used to create the one-dimensional beam model of the rotor.

Table 6.2: Material properties of all considered rotor assembly parts

Assembly parts	shaft	bridges	laminated core stack	windings	end-windings
density ρ	7850 $\frac{\text{kg}}{\text{m}^3}$	7850 $\frac{\text{kg}}{\text{m}^3}$	7525.7 $\frac{\text{kg}}{\text{m}^3}$	6123.2 $\frac{\text{kg}}{\text{m}^3}$	6123.2 $\frac{\text{kg}}{\text{m}^3}$
Young's modulus E_x	200×10^9 $\frac{\text{N}}{\text{m}^2}$	200×10^9 $\frac{\text{N}}{\text{m}^2}$	191.8×10^9 $\frac{\text{N}}{\text{m}^2}$	70.9×10^9 $\frac{\text{N}}{\text{m}^2}$	70.9×10^9 $\frac{\text{N}}{\text{m}^2}$
Young's modulus E_y	-	-	24×10^9 $\frac{\text{N}}{\text{m}^2}$	-	-
Young's modulus E_z	-	-	24×10^9 $\frac{\text{N}}{\text{m}^2}$	-	-
Shear modulus G_{xy}	-	-	73.8×10^9 $\frac{\text{N}}{\text{m}^2}$	-	-
Shear modulus G_{yz}	-	-	11×10^9 $\frac{\text{N}}{\text{m}^2}$	-	-
Shear modulus G_{xz}	-	-	11×10^9 $\frac{\text{N}}{\text{m}^2}$	-	-
Poisson ratio ν_{xy}	0.3	0.3	0.3	0.2996	0.2996
Poisson ratio ν_{yz}	-	-	0.3	-	-
Poisson ratio ν_{xz}	-	-	0.3	-	-

6.2 Finite element model of the rotor

A one-dimensional finite element model of the rotor is created. The structural damping is imposed on the model using the Rayleigh damping model. In a first stage, the bearings are considered as linear springs.

6.2.1 Mechanical description of rotor sections

The rotor of the electrical machine is modeled using one-dimensional finite elements. Timoshenko beam elements and composite Timoshenko beam elements are used, derived in Chapter 3 and Chapter 5. The nodal displacements of an element e are stored in the vector

$$\boldsymbol{u}^{(e)} = \begin{bmatrix} \hat{u}_k & \hat{v}_k & \hat{w}_k & \hat{\theta}_{xk} & \hat{\theta}_{yk} & \hat{\theta}_{zk} & \hat{u}_l & \hat{v}_l & \hat{w}_l & \hat{\theta}_{xl} & \hat{\theta}_{yl} & \hat{\theta}_{zl} \end{bmatrix}^T . \tag{6.1}$$

The indices k and l denote the corresponding nodes of the element e. Each element has different geometrical cross section properties and material properties.

The rotor consists of 170 one-dimensional elements with 31 different cross sections. The geometrical properties of each cross section are determined in an a priori computation of each cross section. Therefore, a two-dimensional mesh of each cross section type is created, see Chapter 4 and Section 5.2. Figure 6.2 shows a two-dimensional mesh of a typical cross section of a rotor. The blue colored mesh defines the shape of the shaft and the bridges, the green mesh defines the shape of

the laminated sheets and the multicolored rectangular meshes define the shape of the winding rods.

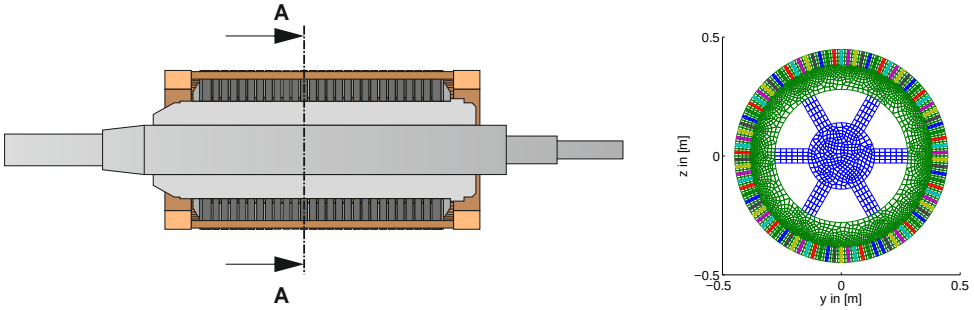

(a) Location of the rotor cross section

(b) Two-dimensional mesh of the rotor cross section $A - A$

Figure 6.2: Cross section of the rotor consisting of different material regions for shaft, laminated core stack and windings

In a numerical evaluation the geometrical parameters of the area, the center of area and the first and second moments of area are determined. Further, the shear center and the shear correction factors are determined. These parameters depend on the geometrical shape of the cross section and the material properties. They are determined for the Timoshenko beam elements and the composite beam elements, compare chapters 4 and 5. The material properties are summarized in Table 6.2.

6.2.2 Structural damping

The structural damping is considered using the Rayleigh damping model. The Rayleigh damping model is a proportional damping and noted by

$$D_s = \alpha \boldsymbol{M_s} + \beta \boldsymbol{K_s} \ . \tag{6.2}$$

The damping matrix $\boldsymbol{D}_s$ is proportional to the stiffness matrix $\boldsymbol{K}_s$ and the mass matrix $\boldsymbol{M}_s$. The proportional factors α and β weight the damping matrix. The advantage of the Rayleigh damping model lies in the handling of the damping in the equation of motion.

The eigenfrequencies of the proportional damped system are defined as

$$\omega_{di} = \omega_i \sqrt{1 - \zeta_i} \qquad \text{with} \quad \{i \in \mathbb{Z} | 1 \leq i \leq n\} \ , \tag{6.3}$$

where ζ_i is the modal damping of the i-th mode. The modal damping is defined as

$$\zeta_i = \beta \frac{\omega_i}{2} + \alpha \frac{1}{2\omega_i} \qquad \text{with} \quad \{i \in \mathbb{Z} | 1 \leq i \leq n\} \ . \tag{6.4}$$

The eigenvectors of the proportional damped system are identical with the eigen-

vectors of the undamped system. The proportional factors α and β are defined in the point of conformity of the damping coefficients of the first two measured and computed modes.

6.2.3 Assembling the global system

The dynamic behavior of the rotor is described by the equations of motion of a multi degree-of-freedom system

$$\boldsymbol{M}\ \ddot{\boldsymbol{u}} + [\boldsymbol{D} + \boldsymbol{G}(\Omega)]\ \dot{\boldsymbol{u}} + [\boldsymbol{K} + \boldsymbol{N}(\Omega)]\ \boldsymbol{u} = \boldsymbol{F}(t). \tag{6.5}$$

The stiffness matrix $\boldsymbol{K}$ is obtained from the the structural stiffness matrix $\boldsymbol{K}_s$ and the bearing stiffness $\boldsymbol{K}_b$. The mass matrix $\boldsymbol{M}$ consists of the structural mass matrix $\boldsymbol{M}_s$ and additional point masses $\boldsymbol{M}_p$. The structural stiffness and mass matrices are derived from assembling the local element stiffness and mass matrices:

$$\boldsymbol{K}_s = \bigcup_{e=1}^{n_e} = \boldsymbol{K}_s^{(e)} \qquad \text{and} \qquad \boldsymbol{M}_s = \bigcup_{e=1}^{n_e} = \boldsymbol{M}_s^{(e)}. \tag{6.6}$$

All components of the rotor are modeled with beam elements, except for the end windings. They have no contribution to the stiffness of the rotor and are considered as point masses $\boldsymbol{M}_p$ with translational and rotational inertia.

For modal tests the rotor is horizontally mounted on two steel racks. The bearings are included as linear springs in the three coordinate directions and summarized in the bearing stiffness matrix $\boldsymbol{K}_b$. The numerical values of the bearing stiffness are known parameters.

The damping matrix $\boldsymbol{D}$ is governed from the structural damping $\boldsymbol{D}_s$ and the damping of the bearings $\boldsymbol{D}_b$. The bearing model does not include a damping and the damping matrix of the bearing $\boldsymbol{D}_b$ is thus neglected. The Rayleigh damping model is chosen for the structural damping, compare Section 6.2.2. The parameters α and β are chosen to fit measurement results.

For the rotating system, the gyroscopic effects and the spin softening effects are included. These effects are taken into account by the gyroscopic matrix $\boldsymbol{G}$ and the spin softening matrix $\boldsymbol{N}$. The mass matrix $\boldsymbol{M}$ of a rotating structure consists of two parts, one is related to the translational inertia $\boldsymbol{M}_T$ and the other to the rotational inertia $\boldsymbol{M}_R$. The gyroscopic matrix is defined as

$$\boldsymbol{G} = 2\ \Omega\ \boldsymbol{M}_R\ . \tag{6.7}$$

Figure 6.3 depicts the unbalance of a beam element. The vector $\boldsymbol{x}$ marks the position of the center of area M with respect to the coordinate origin. The unbalance vector $\boldsymbol{\epsilon}$ defines the position of the center of gravity C with respect to M. The force vector

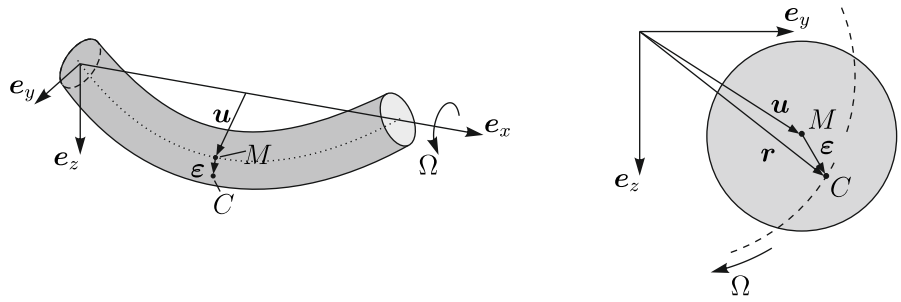

Figure 6.3: Unbalance of a beam element

$\boldsymbol{F}^e_{unb}$ considers the linear distribution of the rotor unbalance in an element e. The unbalance force is given by

$$\boldsymbol{F}^e_{unb} = \boldsymbol{H}^T \, \boldsymbol{f}_{unb} = \boldsymbol{H}^T \, \varrho \, \boldsymbol{H} \, \left(\boldsymbol{u} + \boldsymbol{\epsilon}\right) \Omega^2 \, , \tag{6.8}$$

where $\boldsymbol{H}$ is a matrix which contains the element shape functions and the density ϱ. The expression $\boldsymbol{H}^T \varrho \boldsymbol{H}$ yields the element mass matrix $\boldsymbol{M}^e$. The unbalance force is split into two parts

$$\boldsymbol{F}^e_{unb} = \Omega^2 \boldsymbol{M}^e \boldsymbol{u} + \Omega^2 \boldsymbol{M}^e \boldsymbol{\epsilon}. \tag{6.9}$$

The first part $\Omega^2 \boldsymbol{M}^e \boldsymbol{x}$ is shifted on the left side of the equation of motion (6.5) and delivers the spin softening matrix

$$\boldsymbol{N}^e = -\Omega^2 \boldsymbol{M}^e \, . \tag{6.10}$$

The unbalance force is reduced to

$$\boldsymbol{F}^e_{unb} = \Omega^2 \boldsymbol{M}^e \boldsymbol{\epsilon}. \tag{6.11}$$

6.3 Experimental investigations on the rotor

An experimental modal analysis is carried out on the rotor. Using an impact hammer and three-dimensional acceleration sensors, the frequency response functions (FRFs) are determined. Based on the FRFs the mode shapes are computed.

6.3.1 Test set up for vibrational measurements

Figure 6.4 shows a schematic drawing of the rotor. The slip rings are unmounted from the rotor for experimental investigations. The rotor is supported horizontally on two steel racks. Acceleration sensors, which record the movements in three directions, are used. They are mounted on the outer surface of the laminated core stack. There are 5 measurement points defined in axial direction. In azimuthal direction 18 rows of measurement points are given. This results in 90 evenly spaced

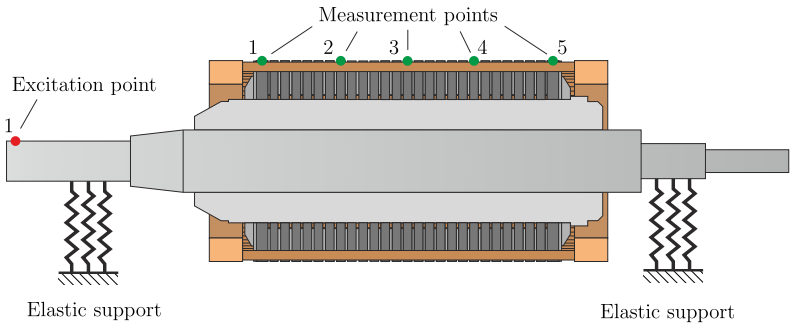

Figure 6.4: Measurement set up for modal testing

measurement points on the laminated core stack. Figure 6.5 depicts a photo of the acceleration sensors mounted on the rotor. The excitation signal is measured by a

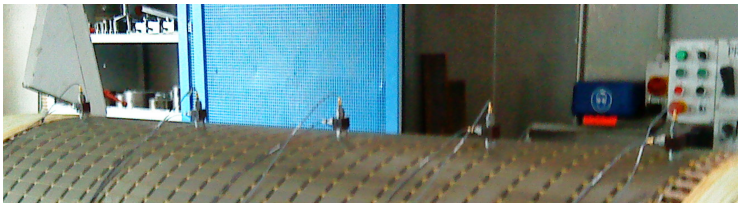

Figure 6.5: Acceleration sensors on the laminated core stack surface

force sensor mounted on the impact hammer. A tip with the impact hammer causes the rotor to vibrate. The excitation signal (force) and response signals (accelerations) are transformed into the frequency domain by a dynamic analyzer and the frequency response functions are determined.

6.3.2 Measurement results

Figure 6.6 plots the measured frequency response functions of all measurement points in a frequency range of 0 Hz to 500 Hz and the corresponding phase information. The most prominent eigenfrequency occurs at a frequency of 150 Hz. Further eigenfrequencies are seen in the plot. The eigenfrequencies at a frequency of approximately 100 Hz and 250 Hz shows a strong damping. The same is true for the eigenfrequencies between 450 Hz and 500 Hz. In the frequency range up to 50 Hz noise occurs in the measurement signals. This effect is mainly caused by the test setup. The rotor lies on two steel racks and gaping between steel rack and shaft is possible during vibration.

Using the singular value decomposition method, the numerical values of the eigenfrequencies are computed. The detected eigenfrequencies up to a frequency of 500 Hz are summarized in Table 6.3. The peaks between 450 Hz and 500 Hz could not be detected as eigenfrequencies by the singular value decomposition.

The mode shapes of some bending modes are depicted in Figure 6.7. Due to the

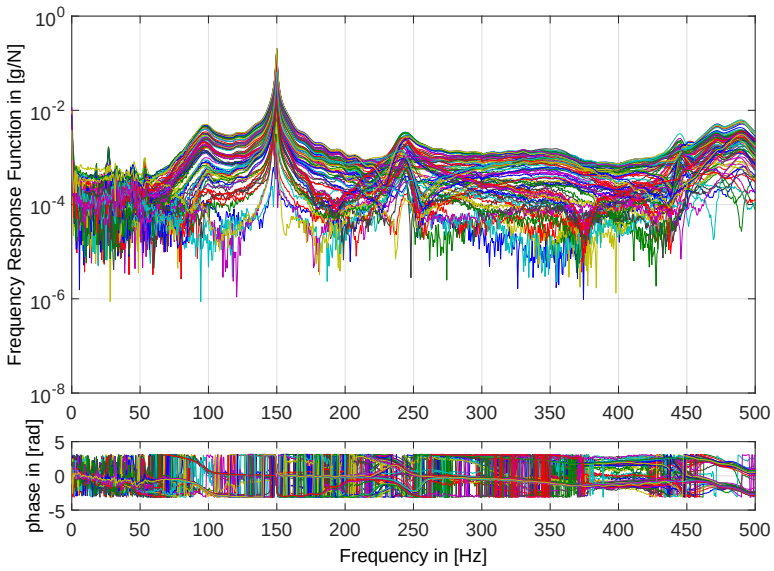

Figure 6.6: All measured frequency response functions

Table 6.3: Identified eigenfrequencies and characteristic mode shape

Mode no.	Eigenfrequency	Mode Shape
1	11.25 Hz	Bearing mode
2	53.13 Hz	Bearing mode
3	98.75 Hz	Bearing mode
4	147.50 Hz	Bending mode
5	150.00 Hz	Bending mode
6	243.75 Hz	Bending mode
7	445.00 Hz	Bending mode

fact that the acceleration sensors are only placed on the laminated core stack and not on the shaft, a clearer description of the bending mode shapes is not possible.

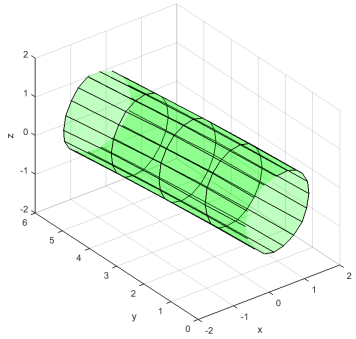

(a) Mode shape of measurement at 98.75 Hz

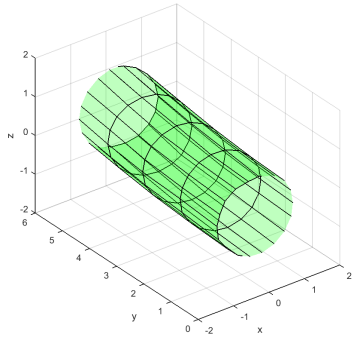

(b) Mode shape of measurement at 150.00 Hz

Figure 6.7: Mode shapes of several modes of the test rotor

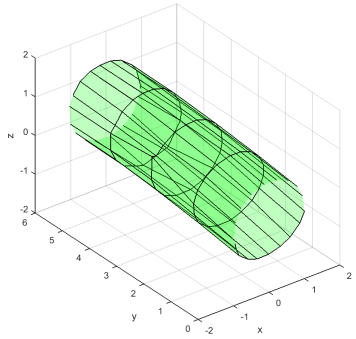

(c) Mode shape of measurement at 243.75 Hz

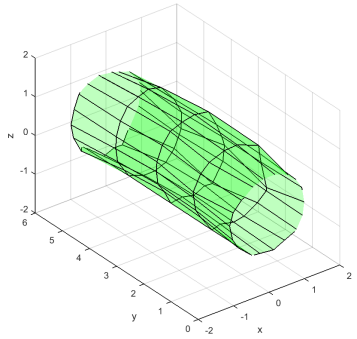

(d) Mode shape of measurement at 445.00 Hz

Figure 6.7: Mode shapes of several modes of the test rotor

6.4 Simulation results of the rotor

Numerical simulations are carried out with the assembled system, see subsection 6.2.3. Modal parameters are obtained from a numerical modal analysis. The frequency response functions are compared with the measurement results. Further, a run up simulation is performed and the results are presented.

6.4.1 Modal results and model validation

The finite element model is introduced in subsection 6.2.3. The resulting eigenfrequencies and corresponding modal damping coefficients are listed in Table 6.4.

The first three eigenfrequencies are mainly dominated by the spring stiffness of the bearings. The further eigenfrequencies are influenced by the structural stiffness and the mass distribution. The modal damping parameters are defined by the Rayleigh damping model.

Table 6.4: Modal results of the test rotor

Mode	Eigenfrequency	Modal damping
1	12.09 Hz	17.8549 %
2	65.52 Hz	2.6786 %
3	96.16 Hz	1.3245 %
4	145.17 Hz	0.0852 %
5	152.21 Hz	0.0526 %
6	153.78 Hz	0.0823 %
7	229.11 Hz	1.2793 %
8	322.30 Hz	2.4594 %
9	460.77 Hz	4.0083 %

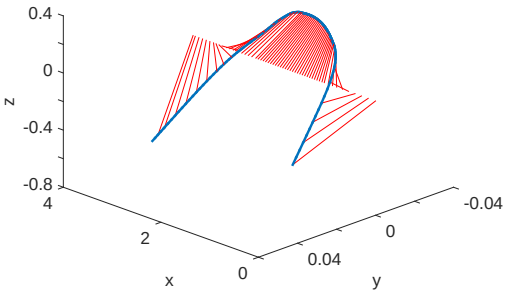

(a) Mode shape of mode no. 3

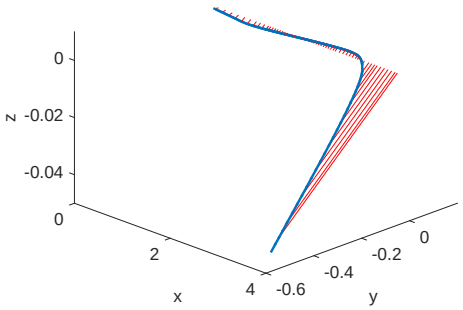

(b) Mode shape of mode no.5

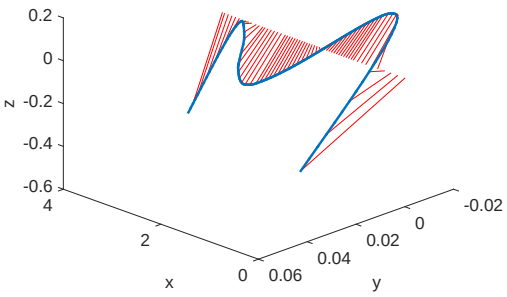

(c) Mode shape of mode no.7

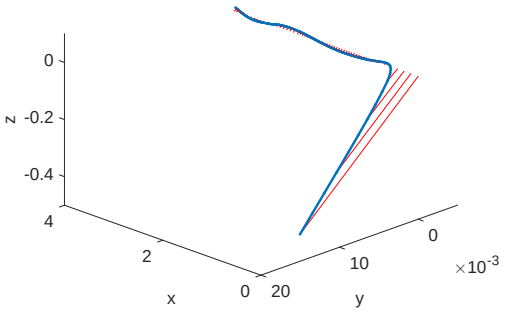

(d) Mode shape of mode no.9

Figure 6.8: Mode shapes of several modes of the test rotor

Figure 6.8 depicts various mode shapes of simulation results. The blue line marks the rotor axis and the red lines shows the distance from the rotor axis of the deformed mode shape to the rotor axis of the undeformed body. The mode shape of the mode 3 is, as already mentioned, a bearing mode and mainly influenced by the bearings. However, the mode shape shows the bending of the rotor. The mode shapes of the modes 5 and 9 are similar. In both cases a significant bending of the shaft is visible. For the mode 5 the shaft end of the drive-end has a high deflection. The shaft diameter of the drive-end is smaller than the diameter of the non-drive-end. Thus, the mode 5 occurs at a lower frequency than mode 9.

Figure 6.9 shows a comparison of measured and calculated frequency response functions. The blue line marks the measured frequency response function and the red line the simulated one. The three comparisons show different curves. Furthermore,

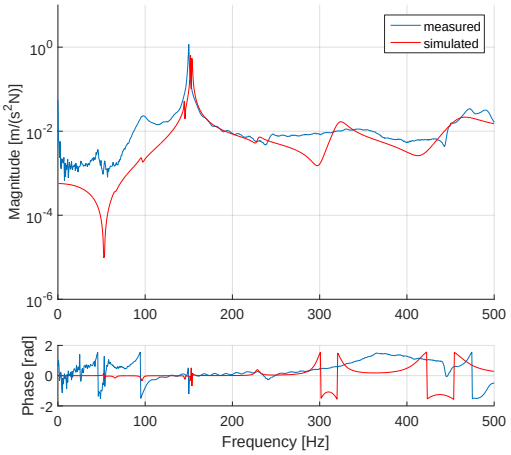

(a) Measured and simulated FRF 32 - 1

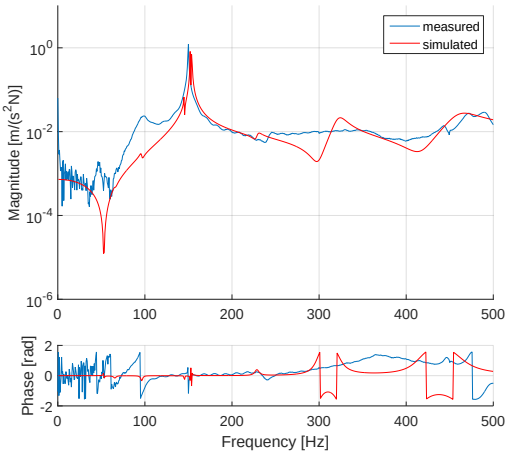

(b) Measured and simulated FRF 71 - 1

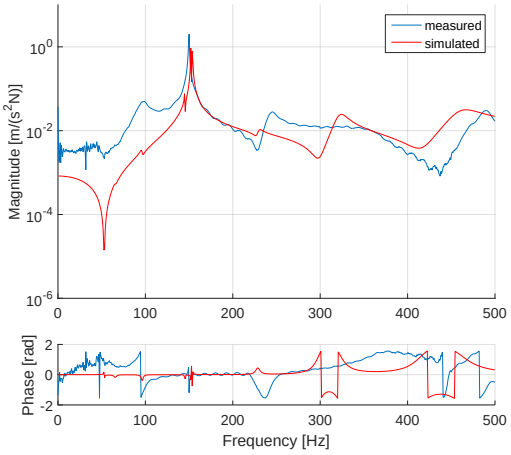

(c) Measured and simulated FRF 109 - 1

Figure 6.9: Comparison of measured and simulated frequency response functions

it has to be mentioned that the measured signal is recorded on the outer surface of the laminated core stack and the nodes of the finite element model are on the rotor axis. The compared frequency response functions of measured and simulated data do not have the exact same reference points. Nevertheless, these points are on the same axial position of the rotor and no in-plane modes occur in the low frequency range up to 500 Hz.

The measured and simulated frequency response functions have a similar behavior for all points. The eigenfrequencies at about 150 Hz fit rather well and the dynamic behavior over the investigated frequency range is conformable. The simulated eigenfrequency at 322 Hz is not visible in the measurement results. Further, the peak of the eigenfrequency at about 100 Hz is not as significant in the simulated curve as in the measured. Measurement inaccuracies can be seen up to a frequency of 50 Hz. This is mainly due to the test setup: The rotor is not clamped on the steel rack and a lift off during oscillation is possible. This contributes to the inaccurate determination of the rotor vibration for the low frequency range. The steel rack is a geometrically complex body, which is considered as a linear spring in the simulation. This also leads to a divergence in comparison, compulsorily.

6.4.2 Transient simulation of rotor vibrations considering nonlinear bearing stiffnesses

A transient run up simulation of the rotor is carried out. It is assumed that the rotor is mounted in the housing of the electrical machine supported by roller bearings. The normalized stiffness properties of the two roller bearings are depicted in Figure 6.10. The normalized stiffness coefficients of the roller bearing at the drive end are shown in Figures 6.10a and 6.10c. The main coefficients along and about the y- and z-axis dominate the bearing stiffnesses. The roller bearing at the non-drive-end shows nearly equal stiffness properties, depicted in Figures 6.10b and 6.10d. An exception of a lesser translational stiffness coefficient in y-direction is seen. Nonlinear stiffness properties are clearly visible for both bearings. The stiffness of the bearing shields is assumed to be isotropic for both ends. Further couplings between the housing and the rotor are neglected.

The balance quality of the rotor is 1×10^{-2} m/s at a rotational speed of 1500 rpm. For the numerical model, it is assumed that the rotor eccentricity only exists in elements of the rotor core stack. All other elements do no have unbalances.

The Newton-Raphson approach is used to achieve the transient solution of the rotor vibrations. Two different simulations are carried out: a run up simulation without gravity and a run up simulation with gravity. In both simulations the rotor runs up to 3 Hz and holds this rotational speed to come in a steady state. This takes 8 seconds. Afterwards, the rotor accelerates constantly to a rotational speed of 25 Hz in 17 seconds. This run up is investigated with two numerical models. The first model neglects and the second model considers gravity.

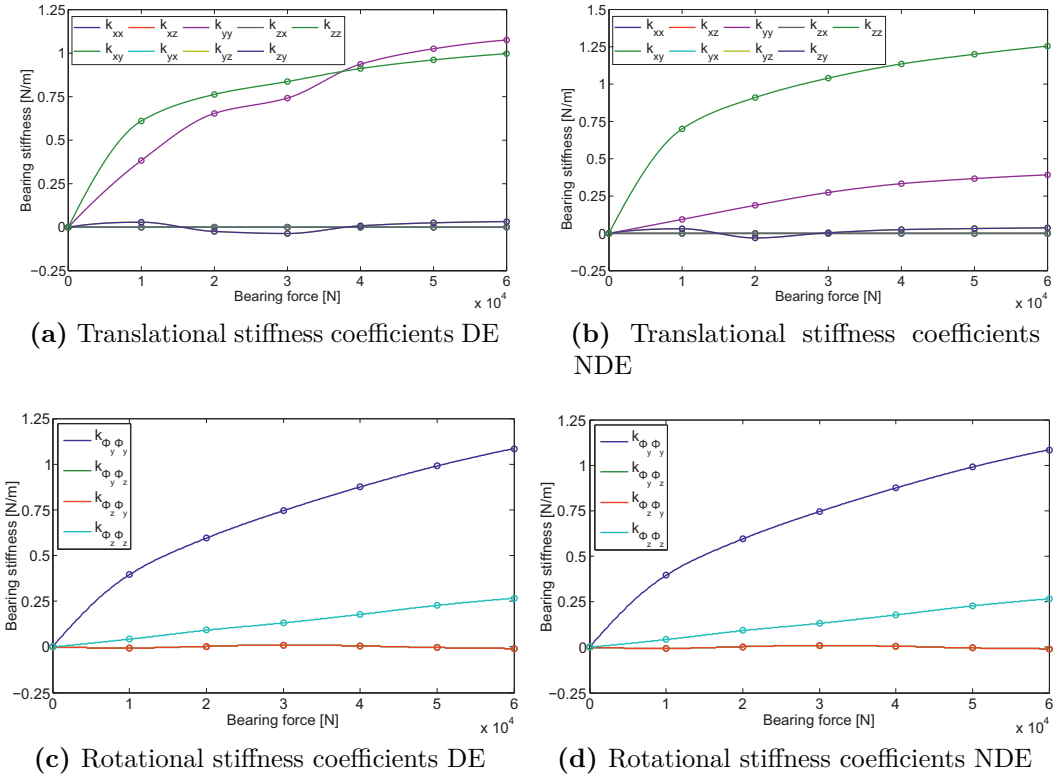

(a) Translational stiffness coefficients DE

(b) Translational stiffness coefficients NDE

(c) Rotational stiffness coefficients DE

(d) Rotational stiffness coefficients NDE

Figure 6.10: Normalized bearing stiffnesses of roller bearings located at drive-end and non-drive-end

Figure 6.11a depicts the spectrogram of the resulting acceleration of the node no. 56 in z-direction related to the rotational speed. This node is located in the middle of the rotor core stack. The acceleration is expressed in decibel with a reference value of $a_0 = 1\,\mathrm{m/s^2}$. The run up simulation, which does not take the gravity into account, shows higher harmonics related the rotational speed. However, the accelerations are small for the rotor which is only excited by the unbalance forces. The maximum amplitudes are about $-20\,\mathrm{dB}$. These amplitudes vanish when increasing rotational speed. This nonlinear effect is explained by the nonlinear bearing stiffnesses. The frequencies of the higher harmonics have no linear relation to the rotational speed. The amplitude of the first order arising from the rotor unbalance increases.

Figure 6.11b shows the orbit of the rotor motion at the node no. 56 and the rotational speed of 25 Hz. The orbit has a circle shape which is typical for linear vibrations. An almost linear vibration results, even though nonlinear bearing stiffnesses are adopted. This means that the motion is mainly dominated by the first order at a rotational speed of 25 Hz. The acting bearing forces are depicted in Figure 6.12. The absolute value of the forces of both bearings (drive-end and non-drive-end) oscillates approximately between $-1500\,\mathrm{N}$ and $1500\,\mathrm{N}$. Figure 6.10 shows, that the

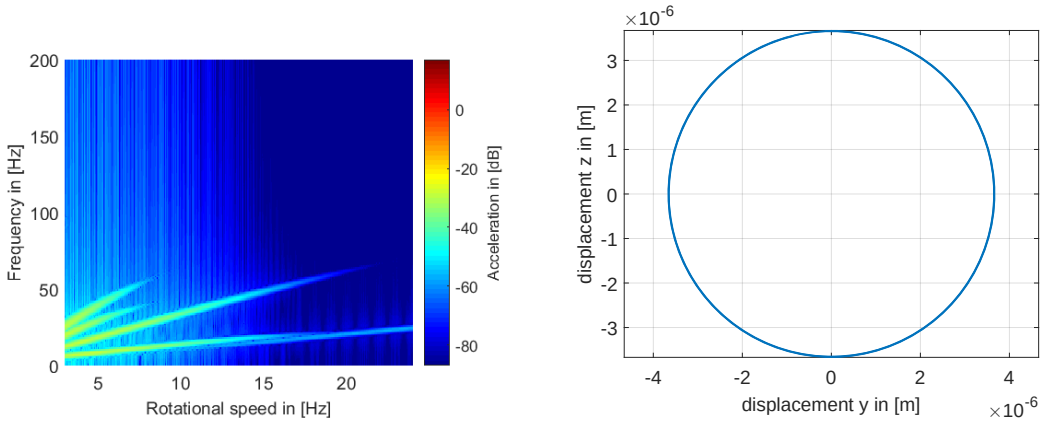

(a) Spectrogram **(b)** Orbit at 25 Hz

Figure 6.11: Results of run up simulation without gravity at node no. 56

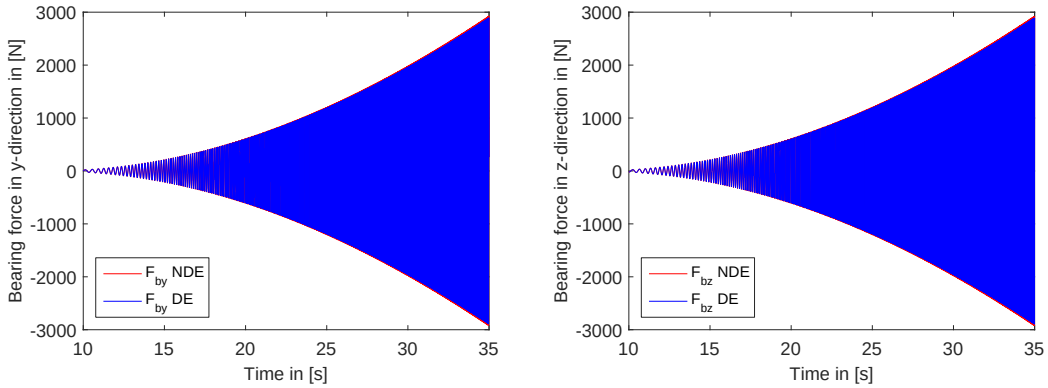

(a) Bearing forces in y-direction **(b)** Bearing forces in z-direction

Figure 6.12: Bearing forces of run up simulation without gravity

operation point is very low in the force range of the bearing stiffness. The difference of the amplitude between the bearing of the drive-end (DE) and the non-drive-end (NDE) is marginal, it is about 50 N.

The second transient simulation considers the effect of gravity. Figure 6.13 shows the bending of the rotor supported on the two nonlinear bearings. The blue line marks the rotor axis. The red marked points show the nodes on which the support is located. Further, this static deflection defines the rotational axis. This deflection is not taken into account for the computation of the unbalance forces.

Figure 6.14 shows the spectrogram of the node no. 56 in z-direction of the run up solution including the effect of gravity. The figure shows the first, second and third order response to a forcing. These three orders in the response differ significantly: In general, the higher the amplitude the lower the contribution to the response. At

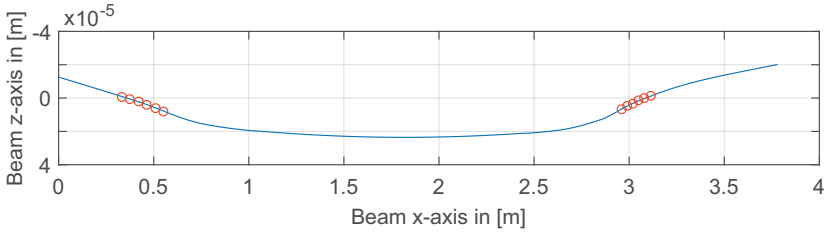

Figure 6.13: Static rotor bending due to gravitiy

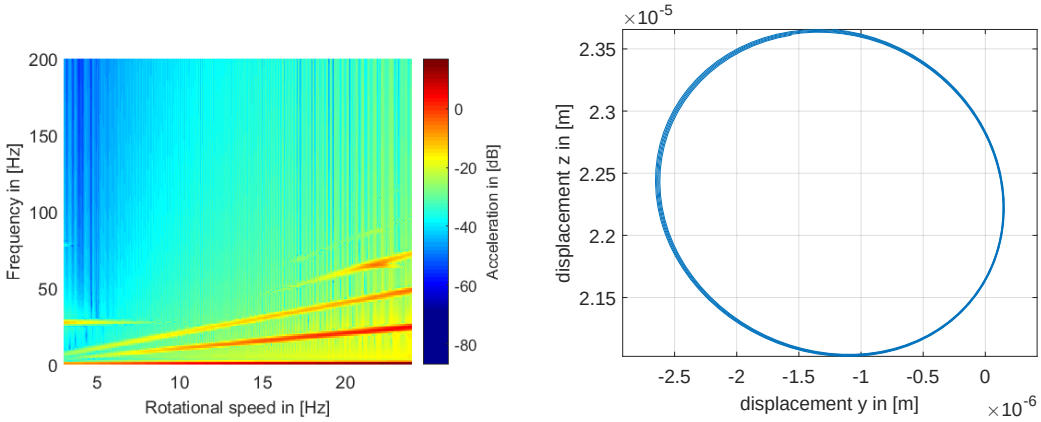

(a) Spectrogram **(b)** Orbit at 25 Hz

Figure 6.14: Results of run up simulation with gravity at node no. 56

approximately 21 Hz, the third order response reaches the first eigenfrequency of the rotor. The amplitude increases to approximately 10 dB. Another effect is seen at a frequency of 30 Hz for low rotational speeds. This rise in a the amplitudes is caused by bearing stiffnesses. The orbit of the investigated node is drawn in Figure 6.14b. It is influenced by the first, second and third order and the orbital path changes slightly during motion. The acting bearing forces are plotted in Figure 6.15. The difference between the bearing forces at the drive-end and the non-drive-end in both subfigures is about 50 N. The bearing force components in z-direction are dominated by the gravitational force. The bearing forces change between approximately 24 250 N and 27 500 N. Comparing these values to the characteristic curve in Figure 6.10, the nonlinearity in the stiffness is very significant.

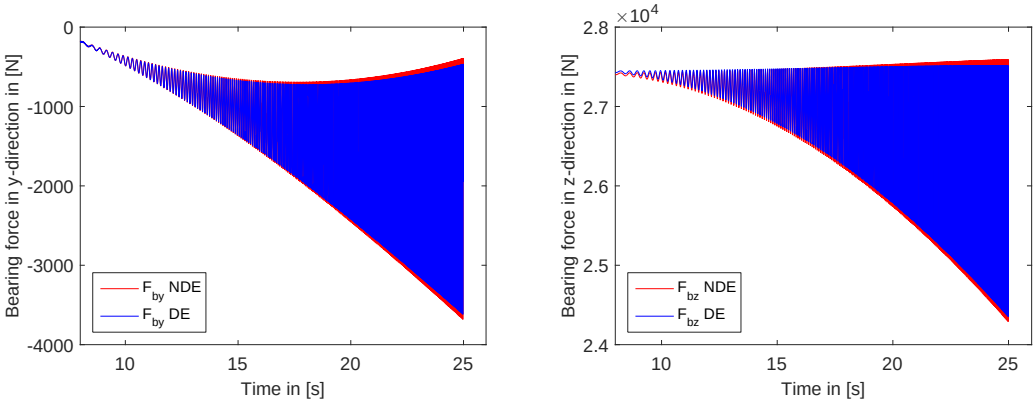

(a) Bearing forces in y-direction **(b)** Bearing forces in z-direction

Figure 6.15: Bearing forces of run up simulation with gravity

CHAPTER 7

Nonlinear rotor vibrations

Roller bearings used in the rotor model Section 6.4.2 show nonlinear stiffness characteristics. The Hertzian contact theory [73] imposed to the contact between the rollers and the bearing shell causes nonlinear bearing stiffnesses. Specially, the relation between the radial contact force and the radial displacement is nonlinear.

In this chapter, further investigations are carried out in order to understand the vibrational behavior regarding to the bearing nonlinearities. Therefore, a simple linear beam model of a rotor is used and side effects are neglected. The roller bearing model is equal to the model used in the chapter above. Run up and run down simulations are carried out and the resulting spectral contents are compared to each other. Further, the run up and down orbits are compared. Detailed investigations of the nonlinear rotor vibrations are done for different rotational speeds. Finally, the influence of the bearing parameters are presented.

7.1 Simple rotor model with bearing nonlinearities

For the investigation of the roller bearing nonlinearities, a simple elastic rotor model with few degrees of freedom is set up. The model's mass is chosen equal to the mass of the rotor investigated in Chapter 6.

7.1.1 Structural model

The rotor model consists of a circular shaft with two different cross sections C_1 and C_2, depicted in 7.1a. The rotor's geometrical measures are drawn in Figure 7.1b.

The geometric cross section properties of the two different cross sections are summarized in Table 7.1. Both cross sections show the shape of a full circle. Further, each cylindrical section of the shaft C_1 and C_2 consists of a different material, which are noted in Table 7.2. The material model of the shaft sections C_1 and C_2 are linear

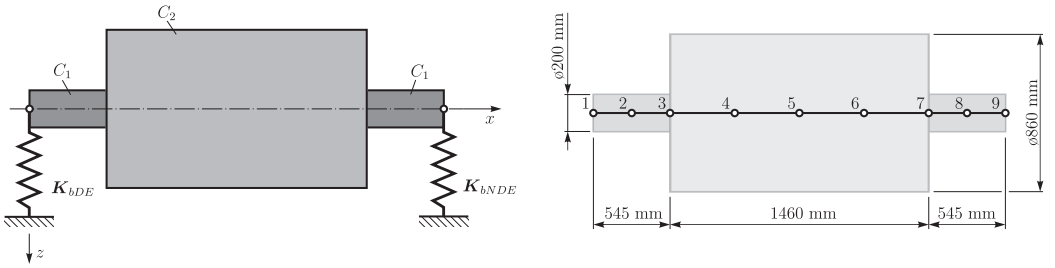

(a) Sketch of simple rotor model **(b)** Node of disctretized rotor

Figure 7.1: Rotor model with nonlinear bearing stiffnesses

elastic. The shaft section C_1 has isotropic material properties and the shaft section C_2 has transversal isotropic material properties. The geometrical parameters and material properties are equal to the rotor investigated in the section above.

Table 7.1: Cross section parameters of rotor model

Cross section	C_1	C_2
Shape	full circle	full circle
Area A	$3.14 \times 10^{-2}\,\mathrm{m}^2$	$4.30 \times 10^{-1}\,\mathrm{m}^2$
Second moment of area I_{yy}	$7.85 \times 10^{-5}\,\mathrm{m}^4$	$2.69 \times 10^{-2}\,\mathrm{m}^4$
Second moment of area I_{zz}	$7.85 \times 10^{-5}\,\mathrm{m}^4$	$2.69 \times 10^{-2}\,\mathrm{m}^4$
Second moment of area I_{yz}	$0\,\mathrm{m}^4$	$0\,\mathrm{m}^4$
Shear correction factor κ_y	0.8507	0.9229
Shear correction factor κ_z	0.8507	0.9229

The rotor vibrations are investigated using the finite element method. Therefore, a discrete finite element model, which consists of eight elements, is formulated. The applied element types are based on the Timoshenko beam theory introduced in Chapter 3. Each node has six degrees of freedom, three translational and three rotational. The entire rotor system consists of 54 degrees of freedom.

The rotor model includes structural damping. For a suitable handling of the damping properties, a linear damping model is advantageous. Thus, the Rayleigh damping model is used, see Subsection 6.2.2.

7.1.2 Nonlinear bearing stiffnesses of the roller bearing

Nonlinear bearing stiffnesses of a roller bearing are imposed on the nodes number 1 and number 2. The stiffnesses values are the same as regarded in Section 6.4.2, shown in Figure 6.10. The bearing of the drive-end (DE) which is located at the node 9 is softer as the bearing of the non-drive-end (NDE). The damping effects of the roller bearing are neglected in further simulations of the investigated model.

Table 7.2: Material parameters of the rotor model

Cross section	C_1	C_2
Properties	Isotropic	Transversal isotropic
Density ϱ	$7850\,\mathrm{kg/m^3}$	$7600\,\mathrm{kg/m^3}$
Young's modulus E_x	$200 \times 10^9\,\mathrm{N/m^2}$	$200 \times 10^9\,\mathrm{N/m^2}$
Young's modulus E_y	-	$50 \times 10^9\,\mathrm{N/m^2}$
Young's modulus E_z	-	$50 \times 10^9\,\mathrm{N/m^2}$
Shear modulus G_{xy}	$\frac{E}{2(1+\nu)}$	$20 \times 10^9\,\mathrm{N/m^2}$
Shear modulus G_{yz}	-	$\frac{E_x}{2(1+\nu_{xy})}$
Shear modulus G_{xz}	-	$20 \times 10^9\,\mathrm{N/m^2}$
Poisson ratio ν_{xy}	0.3	0.3
Poisson ratio ν_{yz}	-	0.3
Poisson ratio ν_{xz}	-	0.3

7.1.3 Acting forces on the rotor model

The rotor model is subjected to gravity. The gravity constant is $g = 9.81\,\mathrm{m/s^2}$. A nonlinear static simulation of the rotor bending gives the rotor deflection due to gravity using the Newton-Raphson procedure is applied. Figure 7.2 depicts the static bending. The blue line shows the rotor bending and the red circles mark the nodes where the bearings are located. The resulting deflection gives the initial state for all further transient simulations in which the gravity forces are considered.

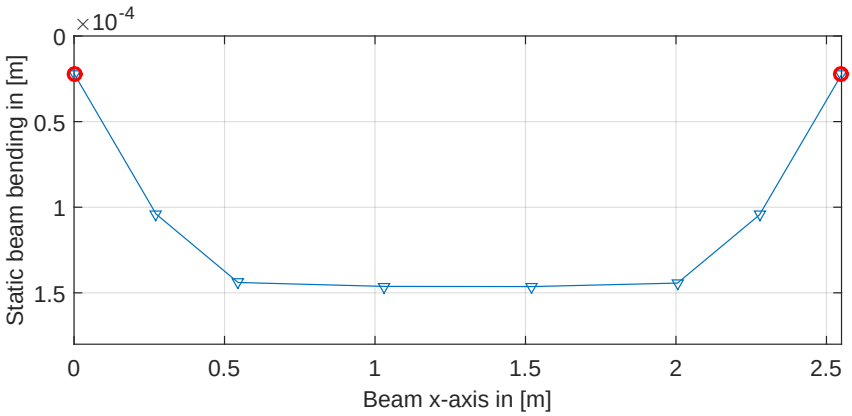

Figure 7.2: Static rotor bending due to gravity

The unbalance forces are considered by defining a constant mass eccentricity. This eccentricity is determined by the unbalance quality of 0.01 m/s at a rotational speed

of 1500 rpm. The eccentricity is located at the nodes of the cylindrical shaft section C_2.

7.2 Transient investigations of vibrations due to bearing nonlinearities

In order to determine the influence of the bearing nonlinearities on the rotor vibrations, transient simulations are done. A run up and a run down simulation are presented and compared to each other. In this rotor vibrations nonlinear effects are investigated in detail at different rotational speeds.

7.2.1 Run up/down simulations

The rotor model introduced Section 7.1 is investigated in detail. In advance, two transient simulations are carried out, a run up simulation and a run down simulation. The rotor accelerates from 0 Hz up to a speed of 35 Hz at the run up simulation and decelerates again to 0 Hz at the run down simulation. The acceleration and the deceleration phase take 30 s for each simulation. The run up from 0 Hz to 2 Hz takes 5 s in order to reduce transient phenomena.

Figures 7.3a and 7.3b show the spectral content of resulting vibrations for the run up and run down. The acceleration of node no. 5 in z-direction is used for the evaluation of these spectrograms. The acceleration is plotted in decibel with a reference acceleration of $a_0 = 1 \times 10^3\,\mathrm{m/s^2}$.

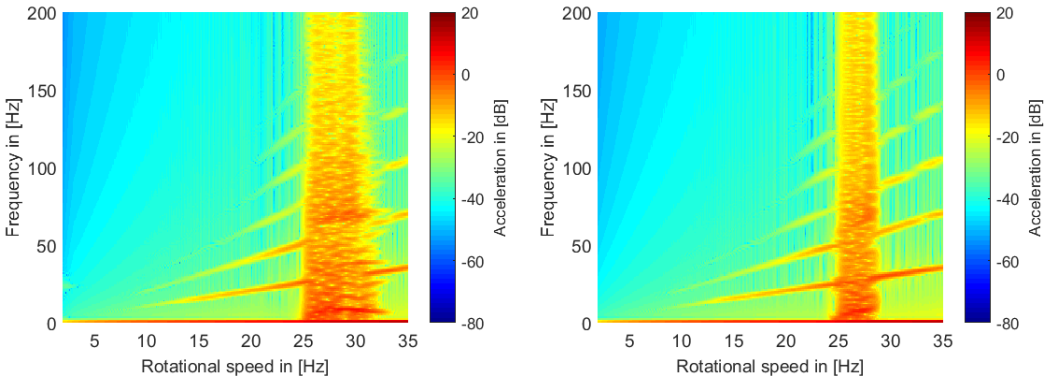

(a) Spectrogram of run up simulation **(b)** Spectrogram of run down simulation

Figure 7.3: Spectrograms of run up/down simulations for rotational speeds between 2 Hz and 35 Hz

Both spectrograms show a similar behavior of the rotor vibrations. Effects of higher orders are seen in both figures. The higher order arise at a rotational speed of

about 15 Hz. Higher orders are only visible in the spectrogram for higher rotational speeds. Furthermore, in both spectrograms a rotational speed range exists with a high acceleration level for all frequencies. This speed range is larger in the run up than in the run down results. In case of a run up this special nonlinear effect occurs for rotational speeds between about 25 Hz and 33 Hz. A run down delivers this effect between rotational speeds of about 25 Hz and 28 Hz. The static part in the spectrum is seen at a frequency of 0 Hz for rotational speeds. The amplitudes of the static part are about −20 dB at a low rotational speed and increase up to 10 dB. The other orders show a higher amplitude level near the speed range with non harmonic vibrations.

Figure 7.4 depicts the forced response of the nonlinear system. In this plot the displacements of node no. 5 for the run up and the run down are shown. The red and blue dots denote results of the run up simulation and the yellow and green dots those of the run down simulation. In case of the run up, blue dots with higher values mark the orbit's maximum displacement and blue dots with lower values the minimum displacement. The motion orbit lies between these values for one rotation. The red points are mean values of the nodal displacement. The same principle is used for the run down results. However, the motion orbit is located between the green dots and the yellow dots mark the mean displacement values.

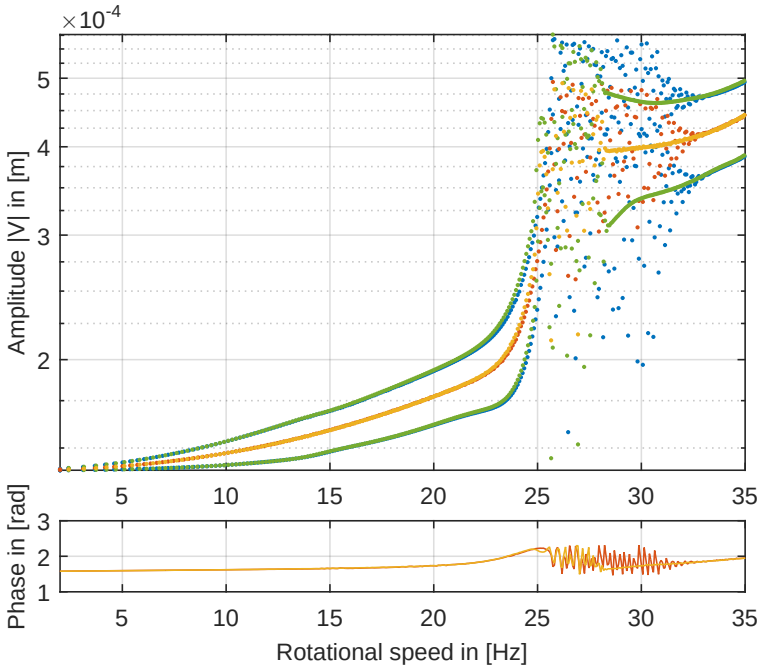

Figure 7.4: Forced response of the center node for rotational speeds between 2 Hz and 35 Hz

In Figure 7.4 a comparison between displacement results of the run up and the run down is given. The rotor vibrations of the run up are nearly the same as the rotor

vibrations of the run down. At a rotational speed of 23 Hz the amplitude increases significantly and results in a non harmonic motion at 25 Hz. This non harmonic motion occurs until a rotational speed of 33 Hz in case of run up. The orbits of the rotor motion are larger for rotational speeds higher than those 23 Hz mentioned above. For deceleration the displacement amplitude is on the same attractor down to 28 Hz. Starting from this point the rotor oscillates non harmonically again until a rotational speed of 25 Hz is reached.

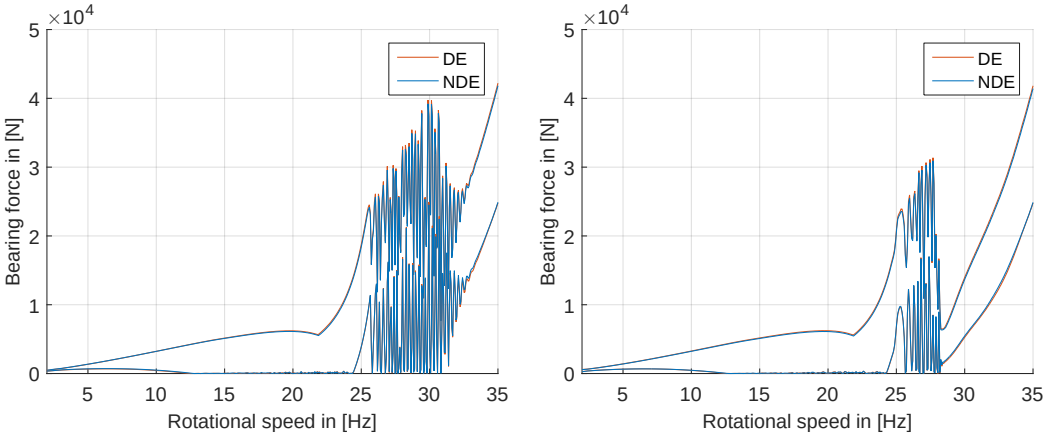

(a) Radial bearing forces in the run up simulation

(b) Radial bearing forces in the run down simulation

Figure 7.5: Radial bearing forces in the run up/down simulations for rotational speeds between 2 Hz and 35 Hz

Figure 7.5 shows the bearing forces acting at drive-end and non-drive-end bearings during run up and run down. The lines with the high amplitude mark the maximum force amplitudes during one rotation whereas the lines with the lower amplitude mark the minimum force amplitude. The bearing forces also show a non-harmonic behavior in the highly oscillating speed range. This behavior is related to the non harmonic rotor vibrations in this frequency range.

7.2.2 Rotor vibrations at constant rotational speeds

Rotor vibrations are investigated in detail for constant rotational speeds of 15 Hz, 27.5 Hz and 35 Hz. All investigations are evaluated for node no. 5 which is located in the middle of the core stack. As a result of Figure 7.4, one expects different vibrational behavior for these chosen values. Small vibrations are expected for a rotational speed of 15 Hz. By increasing the speed the amplitudes of the rotor vibrations amplify. The detected non harmonic vibrations are classified at a rotational speed of 27.5 Hz. A further increase of the rotational speed persuades the rotor to oscillate harmonically. The harmonic vibrations at 35 Hz are elaborated.

Figure 7.6a depicts the transient solution of the rotor vibrations for a rotational

speed of 15 Hz. It resembles a sine wave and nonlinear vibrations are not immediately obvious. The corresponding orbit of this vibration is depicted in Figure 7.6b. The

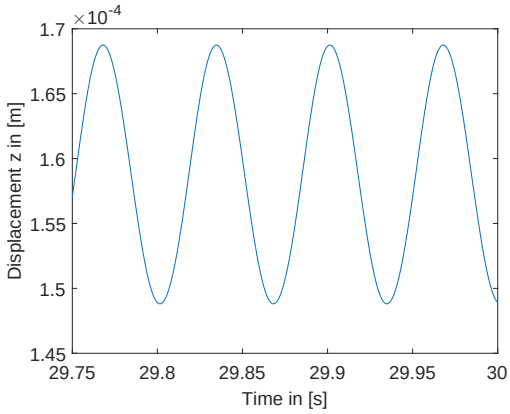

(a) Displacement in z-direction of node no. 5 at 15 Hz rotational speed

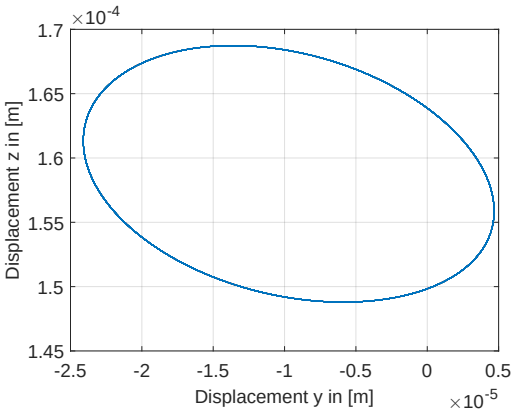

(b) Orbit of node no. 5 at 15 Hz at a rotational speed

Figure 7.6: Displacement of node no. 5 at a rotational speed of 15 Hz

orbit's shape is nearly elliptical. However, the spectral content of the acceleration in z-direction shows a small influence of the higher orders on the rotor vibrations. The higher orders are whole numbered and the amplitudes of these arising orders constantly decrease in the spectrum. The amplitudes of the fourth and fifth order are significantly lower than those of the other orders and barely provide a contribution to the vibration. The resulting spectral content shows the small nonlinearity of the rotor vibration at a speed of 25 Hz. The phase portrait and Poincaré diagram in Figure 7.7b shows a preferred region in the phase space. The Poincaré points are close together and a single accumulation point can be identified.

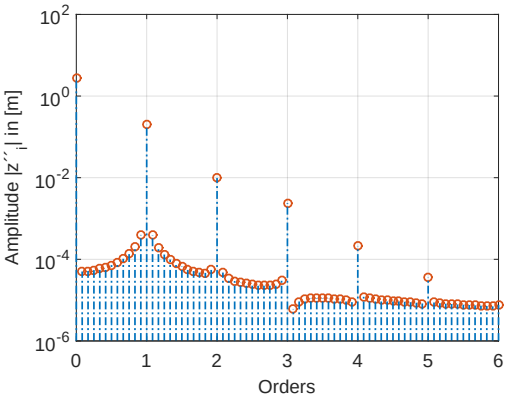

(a) Orders of the acceleration in z-direction of node no. 5 at 15 Hz rotational speed

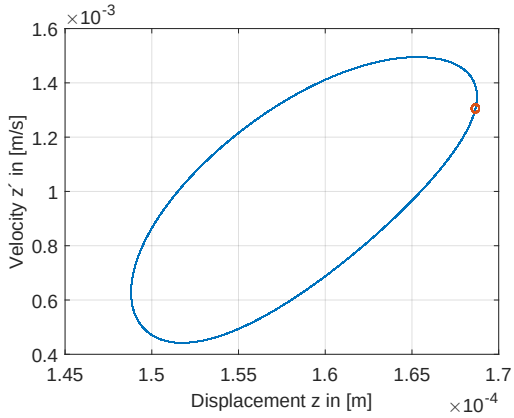

(b) Poincaré diagram of node no. 5 at 15 Hz rotational speed

Figure 7.7: Nonlinear results of node no. 5 at a rotational speed of 15 Hz

The vibrations at a rotational speed of 27.5 Hz are depicted in Figure 7.8a. A non harmonic oscillation of the rotor in the time domain is seen. For this rotational speed, the vibrational behavior is not assignable on a first look. The same non

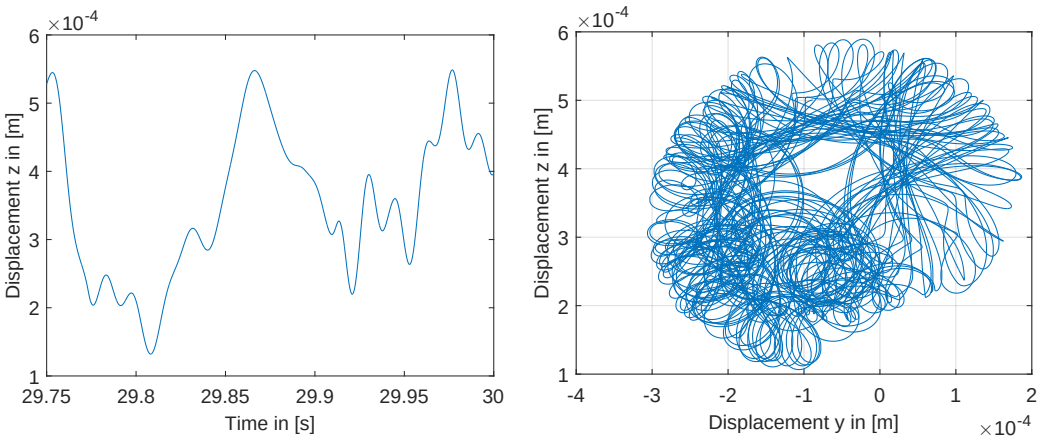

(a) Displacement in z-direction of node no. 5 at 27.5 Hz rotational speed

(b) Orbit of node no. 27.5 Hz at a rotational speed

Figure 7.8: Displacement of node no. 5 at a rotational speed of 27.5 Hz

harmonic behavior is seen in the orbit plot, see Figure 7.8b. With regard to the displacement amplitude at a rotational speed of 15 Hz, see Figure 7.6, the amplitudes are significantly increasing at a rotational speed of 27.5 Hz.

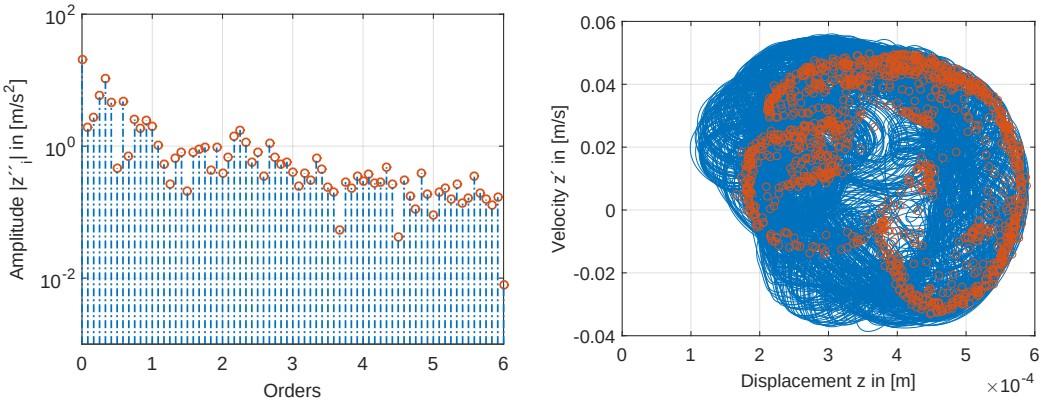

(a) Orders of the acceleration in z-direction of node no. 5 at 27.5 Hz rotational speed

(b) Poincaré diagram of node no. 5 at 27.5 Hz rotational speed

Figure 7.9: Nonlinear results of node no. 5 at a rotational speed of 27.5 Hz

The spectral content of the acceleration in z-direction, depicted in Figure 7.9a, shows a high amplitude level for all orders. It is not possible to identify special orders which have an influence on the vibrations. The Poincaré diagram shows arbitrary distributed points in the phase diagram.

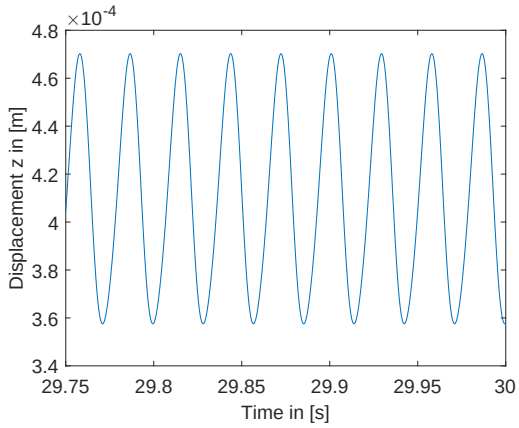

(a) Displacement in z-direction of node no. 5 at 35 Hz rotational speed

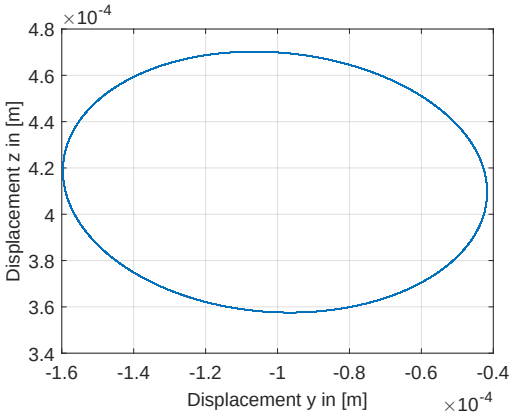

(b) Orbit of node no. 35 Hz at a rotational speed

Figure 7.10: Displacement of node no. 5 at a rotational speed of 35 Hz

The z-displacement in time domain as well as the orbit are plotted in Figure 7.10 for a rotational speed of 35 Hz. A similar behavior, which is nearly linear, is seen for a rotational speed 15 Hz. Compared to Figure 7.6b the elliptic orbit is twisted and the amplitudes are larger.

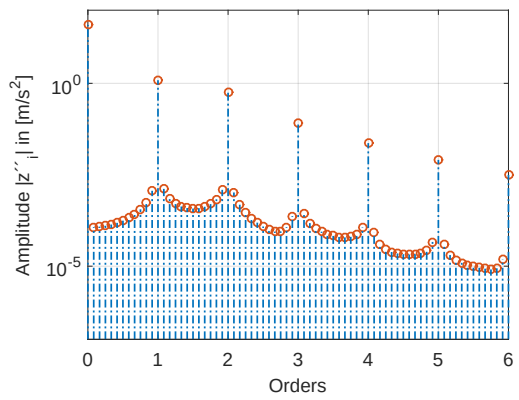

(a) Orders of the acceleration in z-direction of node no. 5 at 35 Hz rotational speed

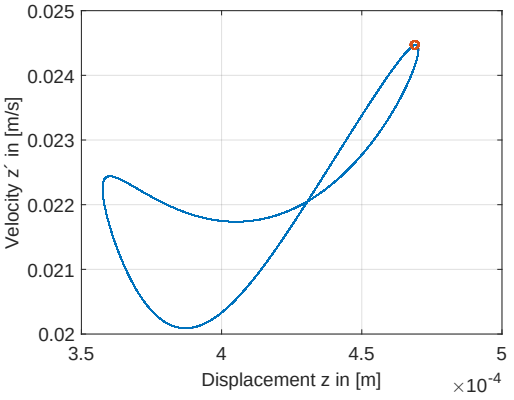

(b) Poincaré diagram of node no. 5 at 35 Hz rotational speed

Figure 7.11: Nonlinear results of node no. 5 at a rotational speed of 35 Hz

However, the spectrum of the z-accelerations shows more contribution of the higher orders to the rotor vibrations than for a rotational speed of 15 Hz, see Figure 7.11a. The phase portrait and Poincaré diagram are plotted in Figure 7.11b. The trajectories shows the nonlinearity of the rotor motion an the Poincaré points are forced to a single accumulation point.

7.3 Influence of roller bearings on rotor vibrations

In order to investigate the influence of different bearing models on the forced response, the rotor model introduced in Section 7.1 is used. However, the bearing models will be changed in the following simulations. In these investigations five different bearing models are used:

1. fixed bearings,
2. isotropic stiffness coefficients,
3. orthotropic stiffness coefficients,
4. linearly changing orthotropic stiffness coefficients,
5. nonlinearly changing orthotropic stiffness coefficients.

The simulation results are evaluated for node no. 5 which is located in the middle of the core stack.

First, the forced response of the rotor model with fixed bearings is investigated. The bearings are considered using Dirichlet boundary conditions in the equation of motion which is given by

$$\boldsymbol{M}\,\ddot{\boldsymbol{u}} + [\boldsymbol{D} + \boldsymbol{G}(\Omega)]\;\dot{\boldsymbol{u}} + \boldsymbol{K}\,\boldsymbol{u} = \boldsymbol{F}(t)\;. \tag{7.1}$$

The force vector $\boldsymbol{F}(t)$ contains the rotor unbalance and the gravity effects. The equation of motion is solved in a rotation body-fixed coordinate system and the solution is transformed in an inertal system.

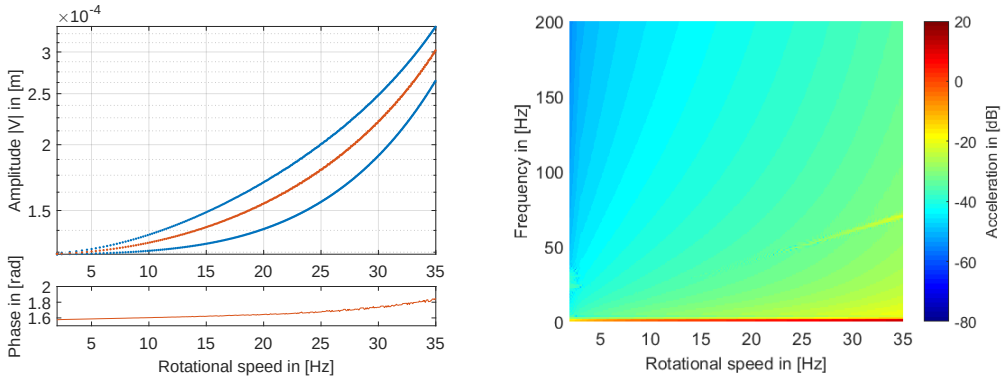

(a) Forced response **(b)** Spectrogram

Figure 7.12: Run up of rotor with fixed bearings from 2 Hz to 35 Hz

As expected, the solution of this linear equation of motion delivers linear rotor vibrations. Figure 7.12 shows the results of a rotor run up between 2 Hz and 35 Hz. The nodal displacement of the rotation is plotted in Figure 7.12a. The blue dots mark the maximum and the minimum rotor deflection in one rotation. The red dots

show the mean rotor deflection. Figure 7.12b depicts the spectral content of run up results, where the amplitude of the first order response is seen.

For the simulation with isotropic bearings, the stiffness coefficients have to imposed on the equation of motion. The bearing stiffness coefficients have to be transformed in the rotor's body-fixed coordinate system. The bearing stiffness coefficients are related to a coordinate system where the x-axis is identically to the rotor axis and the z-axis points in the direction of the radial bearing force. This transformation is carried out by the transformation matrix $\boldsymbol{A}(u)$ and the equation of motion takes the form

$$\boldsymbol{M}\,\ddot{\boldsymbol{u}}+[\boldsymbol{D}+\boldsymbol{G}(\Omega)]\;\dot{\boldsymbol{u}}+\boldsymbol{A}(u)\boldsymbol{D}_b\boldsymbol{A}(u)^T\;\dot{\boldsymbol{u}}+\boldsymbol{K}\;\boldsymbol{u}+\boldsymbol{A}(u)\boldsymbol{K}_b\boldsymbol{A}(u)^T\;\boldsymbol{u}=\boldsymbol{F}(t)\;. \quad (7.2)$$

The transformed bearing stiffness matrix $\boldsymbol{A}(u)\boldsymbol{K}_b\boldsymbol{A}(u)^T$ is equal to the untransformed bearing stiffness matrix $\boldsymbol{K}_b$ in the special case of isotropic bearings. The bearing stiffness coefficients k_{yy} and k_{zz} have the same numerical values and all other stiffness coefficients in the bearing stiffness matrix are zero for the isotropic support. Hence, the equation of motion (7.2) results in a linear system of equations.

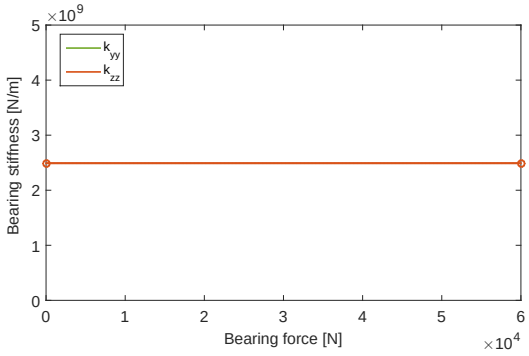

(a) Isotropic bearing stiffnesses

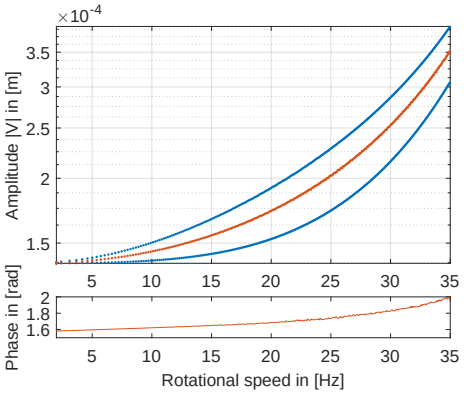

(b) Forced response

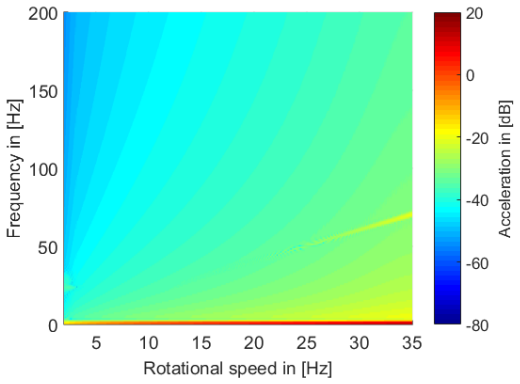

(c) Spectrogram

Figure 7.13: Run up of rotor with isotropic bearing coefficients from 2 Hz to 35 Hz

The used stiffness coefficients for the isotropic bearing model are plotted in Figure 7.13a. The damping in this bearing model is realized by a stiffness proportional model $\boldsymbol{D}_b = \beta \boldsymbol{K}_b$. The simulations in this subsection use always the same coefficient $\beta = 0.001$. The results of the rotor supported by isotropic bearings show a linear behavior similar to the results of the rotor with fixed bearings. However, a larger rotor deflection can be seen in Figure 7.13b. The spectrogram in Figure 7.13c also provides a similar linear vibrational behavior.

Using constant orthotropic bearing coefficients, the transformation of the bearing stiffness coefficients in the body-fixed coordinate system $\boldsymbol{A}(u)\boldsymbol{K}_b\boldsymbol{A}(u)^T$ introduces a geometric nonlinearity to the equation of motion (7.2). The transformation matrix influences the rotor motion and due to orthotropic coefficients geometric, nonlinear functions are taken into account for the equation of motion. These geometric functions determine the nonlinearity for the rotor system. The orthotropic bearing coefficients are depicted in the Figures 7.14a and 7.14b.

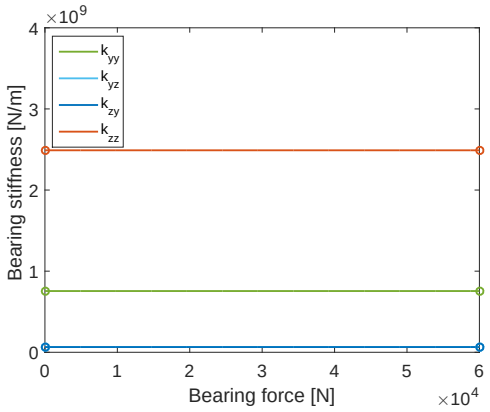

(a) Translational coefficients of orthotropic bearing stiffnesses

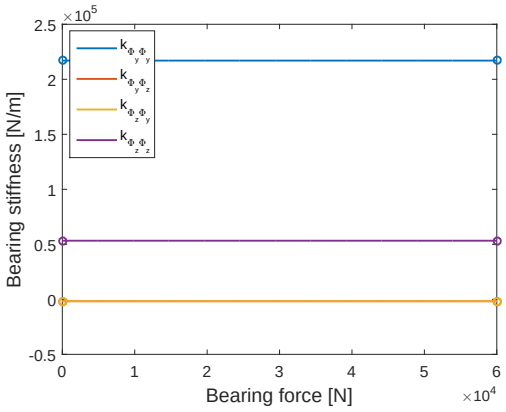

(b) Rotational coefficients of orthotropic bearing stiffnesses

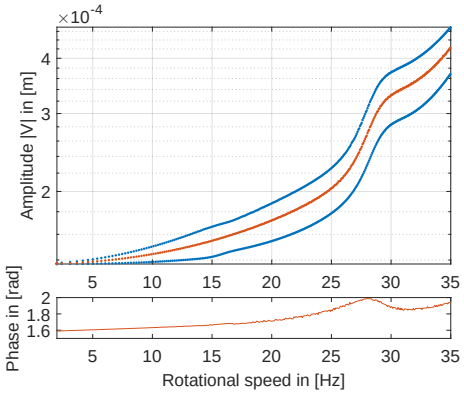

(c) Forced response

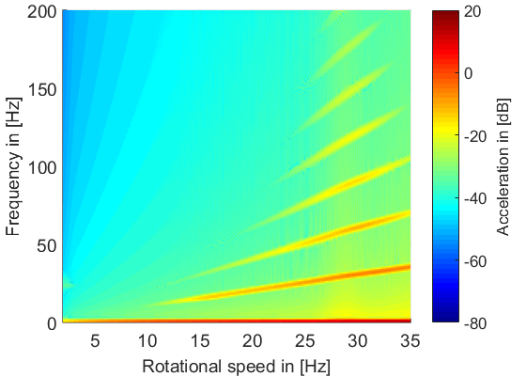

(d) Spectrogram

Figure 7.14: Run up of rotor with orthotropic bearing coefficients from 2 Hz to 35 Hz

The rotor model, which includes orthotropic bearing coefficients, causes a resonance at about 30 Hz, compare Figure 7.14c. This effect is not seen in the solution with fixed or isotropic bearings. Furthermore, the level of rotor deflection is larger compared to the deflections of the rotor with isotropic bearings. The resonance is also seen in the spectrogram plotted in Figure 7.14d. The geometrically nonlinear terms in the equation of motion excite higher order in the spectrum. They occur at the rotational speed of about 30 Hz, the speed of the existing resonance.

In the fourth simulation case, the rotor model is supported on orthotropic bearings with linearly varying coefficients. Figures 7.15a and 7.15b show the used coefficients of the bearing model. This bearing model shifts the occurring resonance down. The rotor is not any longer on a stable orbit in a speed range between about 25 Hz and 33 Hz, see Figure 7.15c. Additionally to the higher order amplitudes, frequencies arises in this speed range and a non-harmonic vibration results, which can be seen in the spectrogram in Figure 7.15d.

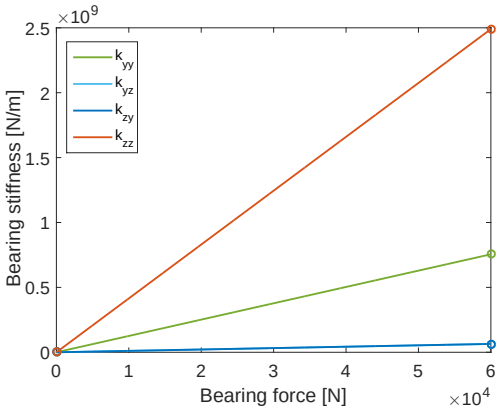

(a) Translational coefficients of nonlinear bearing stiffnesses

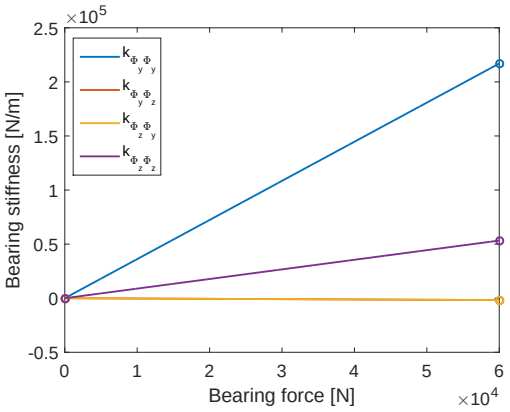

(b) Rotational coefficients of nonlinear bearing stiffnesses

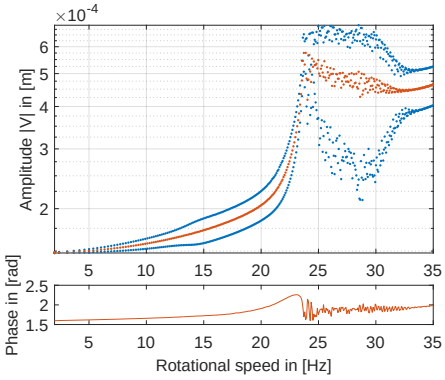

(c) Forced response

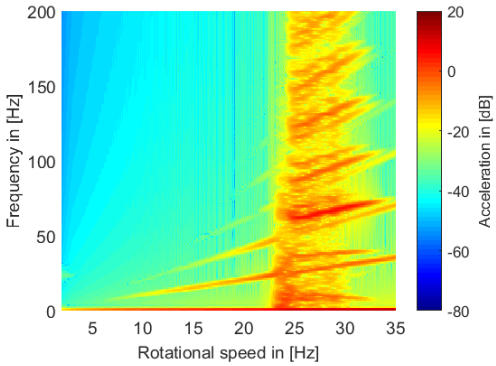

(d) Spectrogram

Figure 7.15: Run up of rotor with linear bearing coefficients from 2 Hz to 35 Hz

In the fifth and final simulation of this investigation, the rotor model is supported on orthotropic bearings with nonlinear stiffness coefficients. The orthotropic bearing coefficients are plotted in Figures 7.16a and 7.16b. The bearing coefficients depend on the bearing forces piecewise quadratically. Thus, the resonance arises at a higher rotational speed of about 26 Hz, see Figure 7.16c. At this speed the rotor vibration leaves the stable attractor and results in a non harmonic motion. This non harmonic motion is acting until the a harmonic attractor is reached at about 32 Hz. A band of frequencies is seen seen at this speed range in the spectrogram, see Figure 7.16d. This band contains amplitudes with a high level in the whole frequency range for rotational speeds between about 26 Hz and 32 Hz.

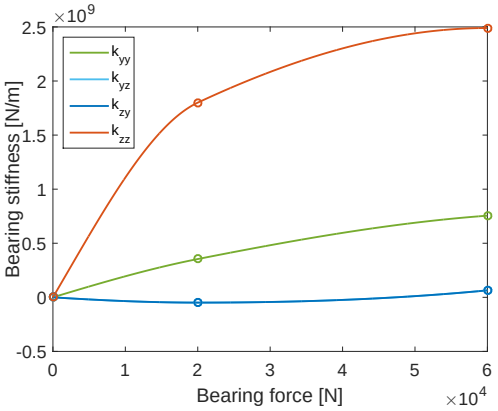

(a) Translational coefficients of nonlinear bearing stiffnesses

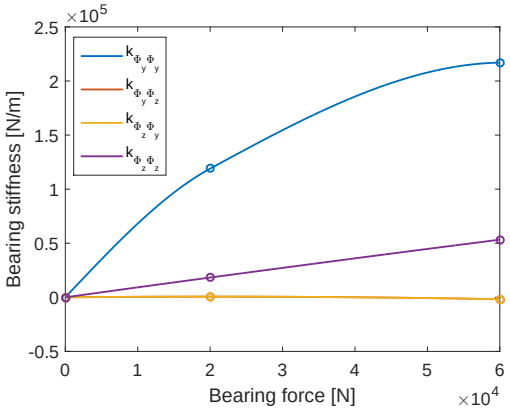

(b) Rotational coefficients of nonlinear bearing stiffnesses

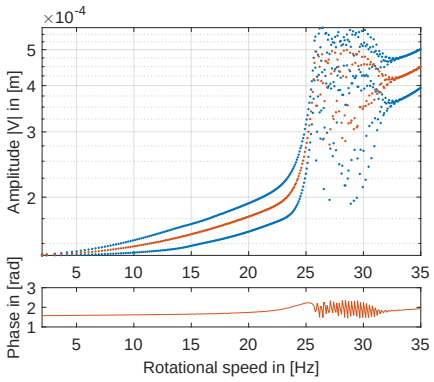

(c) Forced response

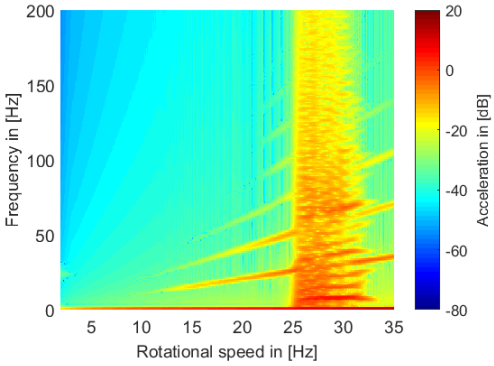

(d) Spectrogram

Figure 7.16: Run up of rotor with nonlinear bearing coefficients from 2 Hz to 35 Hz

CHAPTER 8

Rotor vibrations in electromagnetic field regarding static and dynamic eccentricities

In this chapter rotor vibrations due to unbalanced magnetic pull are investigated. Therefore, a model of a two-pole induction machine is set up. The machine is supported on two journal bearings. The rotor is exposed to an electromagnetical field and electromagnetical forces are acting on the rotor core stack. For the formulation of these forces an analytical approach is chosen. Finally, the rotor vibrations are computed in the time domain.

8.1 Model of a two pole induction machine

For the rotor model the same approach as in Chapter 6 is used. The rotor is modeled with beam elements and the corresponding cross section parameters are achieved in an a priori simulation of each cross section.

In Figure 8.1 a schematic rotor drawing of an induction machine is depicted. The rotor has a similar assembly as the rotor investigated in Chapter 6. A laminated core stack is pressed onto the shaft and between two end plates. The windings are

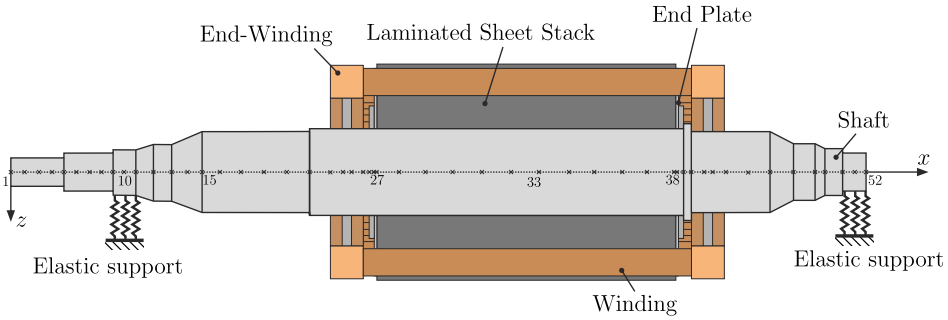

Figure 8.1: Design of an rotor of an two-pole induction machine

mounted through the laminated core stack. End-windings are on both sides of the

windings. General machine properties of the investigated rotor are summarized in Table 8.1.

Table 8.1: General rotor parameters of the two-pole induction machine

parameter	value
Rated power P_N	1.25 MW
Rated voltage U_N	5.55 kV
Rated frequency f_N	50 Hz
Rated speed n_N	2991.1 rpm
Rotor mass m_R	1239.6 kg

All rotor parts consist of the same material properties as in Chapter 6. The shaft is made of steel and it is linear elastic with isotropic properties. The laminated core stack is modeled as a homogeneous and linear elastic part with transversal properties. The windings and end-windings are made of a mix of different materials, such as are copper, resign and isolation material. It is assumed that the windings and end-windings are linear elastic with isotropic properties. The used material parameters are listed in Table 6.2.

The rotor is modeled using Timoshenko beam elements and composite beam elements. The model consists of 51 two-node elements and 19 different cross sections. The finite element model includes 52 nodes where each node has six degrees of freedom. The cross section parameters are computed a priori by a two-dimensional finite element simulation, see Chapter 4 and Section 5.2. The rotor damping is included using the Rayleigh damping model [53]. The rotor unbalance is given by a balance quality of $G = 1\,\mathrm{mm/s}$. The rotor is exposed to a gravitational field, the gravitational constant is $9.81\,\mathrm{m/s^2}$. Figure 8.2 shows the static bending line of the rotor due to gravity. The red markers are placed on the bearing positions.

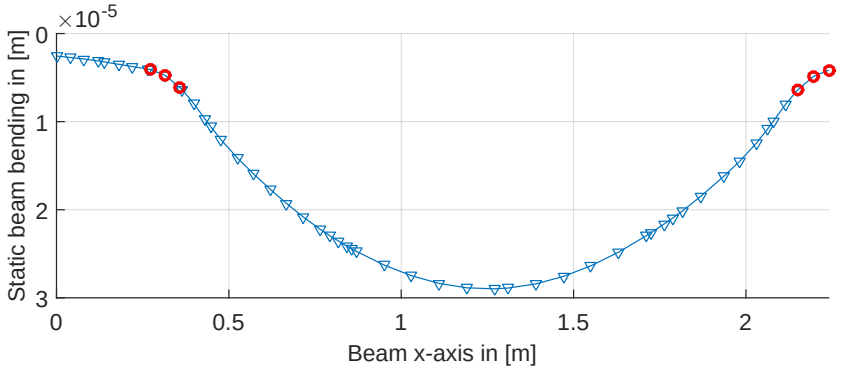

Figure 8.2: Static rotor bending due to gravity

The bearings of the rotor are assumed to be linear and isotropic. The bearing stiffness coefficient is $2.5 \times 10^9\,\mathrm{N/m}$. In further simulations this simple bearing model is

used. A more complex model would influence the rotor vibrations significantly and it would not be possible to distinguish bearing effects and electromagnetic effects.

8.2 Forces acting on a two pole induction machine

Generally, the eccentricity is decomposed into a static and a dynamic deflection, e_s and e_d, which are depicted in Figure 8.3 along with a inertial coordinate system I and a body-fixed coordinate system R. The two planar coordinate systems have the origins O and W and the barycenter of the shaft is marked by C. The whirling axis is located at the origin W. The vector $\boldsymbol{e}_s$, which is defined by the two points O and W, describes the static deflection of the shaft. The dynamic deflection is given by the vector $\boldsymbol{e}_d$, which marks the barycenter C in relation to the origin W. The dynamical deflection is the sum of the vector $\boldsymbol{r}'$, which is defined by the center of area M and the origin W, and the vector $\boldsymbol{e}_0$, given by the center of area M and the barycenter C.

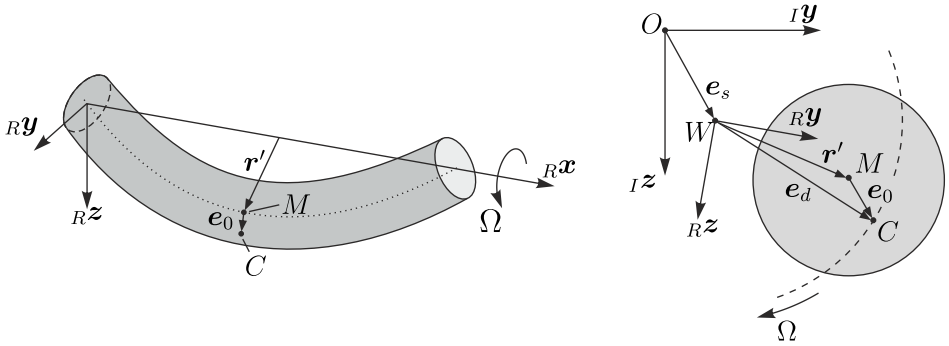

Figure 8.3: Eccentricity split into static and dynamic component

In this model of a two-pole induction machine unbalance forces, gravity forces and the unbalanced magnetic pull are regarded. The effect of unbalanced magnetic pull is caused by electromagnetical forces. Gravity and unbalance forces are nodal forces which are caused by the body force density. They are considered by

$$\boldsymbol{F}^e = \int_V \boldsymbol{H}^T \, \boldsymbol{f}_b^e(x,y,z,t) \, dV \tag{8.1}$$

in the finite element model, where $\boldsymbol{f}_b^e(x,y,z,t)$ is a body force density of element e and $\boldsymbol{H}^T$ is a shape function matrix. The electromagnetical forces acting on the surface of the rotor core stack. The nodal force due to surface forces are computed by

$$\boldsymbol{F}^e = \int_A \boldsymbol{H}^T \, \boldsymbol{f}_s^e(x,y,z,t) \, dA \ , \tag{8.2}$$

with $\boldsymbol{f}_s^e(x,y,z,t)$ as surface force density.

8.2.1 Unbalance and gravity force

The unbalance force depends on the dynamic eccentricity $\boldsymbol{e}_d$ of the shaft. The body force density of the rotor unbalance is given by

$$\boldsymbol{f}_u = \varrho\, \Omega^2\, \boldsymbol{e}_d \ , \tag{8.3}$$

where Ω is the rotational speed, ϱ is the density and $\boldsymbol{e}_d$ is the dynamic eccentricity, compare Figure 8.3. The rotor is acting in a gravity field. The body force density of the gravity is defined by

$$\boldsymbol{f}_g = \varrho\, \boldsymbol{g} \ , \tag{8.4}$$

where $\boldsymbol{g}$ is the gravity. Nodal forces due to gravity and rotor unbalance are computed by

$$\boldsymbol{F}^e = \int_V \boldsymbol{H}^T\ \varrho\ \left(\boldsymbol{g} + \Omega^2\ \boldsymbol{e}_d\right)\ dV \ . \tag{8.5}$$

8.2.2 Unbalanced magnetic pull

The slotting of the stator and the rotor, the saturation and the eccentric positioning of the rotor due to manufacturing reasons cause permeance variations $\Lambda(\varphi,t)$ which, together with the magnetomotive force $V_\delta(\varphi,t)$, cause a magnetic field $B(\varphi,t)$

$$B(\varphi,t) = \Lambda(\varphi,t) V_\delta(\varphi,t) \tag{8.6}$$

varying with the azimuthal coordinate φ and time t [152].

A common approach, especially in analytical methods, is the decomposition of the magnetic field into single wave components by applying a two-dimensional Fourier transformation and the computation of surface force wave components σ_ν

$$\sigma_\nu = \hat{\sigma}_\nu cos(\nu\varphi - \omega_\nu t - \psi_\nu) \tag{8.7}$$

by evaluating the Maxwell stress tensor [152]. Whereas, on the stator, surface force components with large spatial ordinal numbers ν have to be taken into account for vibration analyses. Only surface forces with $\nu = \pm 1$ are relevant for the computation of the rotor vibrations, since the resulting force F

$$\boldsymbol{F} = \int_0^{2\pi} \sigma_\nu\, \boldsymbol{R}\, l\, \mathrm{d}\varphi \tag{8.8}$$

is zero for higher order force waves. This force is called the unbalanced magnetic pull. It is well known that the leading cause for unbalanced pull is the eccentric positioning of the rotor [48]. The eccentricity of a rotor is caused by manufacturing tolerances. The centre axis of the bearing shell, the whirling axis and the barycentre (and thus the main axis of inertia) are not concentric. Further, the static and

dynamic rotor deformation, caused by gravity, unbalance forces and unbalanced magnetic pull influence the rotor eccentricity. The influences of the homopolar flux, parallel windings and the saturation are neglected. Only the magnetic field components due to the permeance variation caused by the off-centered movement of the shaft are determined.

8.2.3 Air gap definition

The eccentricity ${}_I\boldsymbol{e}$ (the index I or R on the left denotes the basis of the coordinate system) is then given in the inertial coordinate system I as

$$ {}_I\boldsymbol{e}(t) = {}_I\boldsymbol{e}_s + {}_I\boldsymbol{e}_d = e_s \begin{bmatrix} 0 \\ \cos\varphi_s \\ \sin\varphi_s \end{bmatrix} + e_d \begin{bmatrix} 0 \\ \cos(\varphi_d + \Omega t) \\ \sin(\varphi_d + \Omega t) \end{bmatrix} . \tag{8.9} $$

For the derivation of the permeance function $\Lambda_e(t)$, the variation of the air gap δ due to the eccentricity along the circumference with the coordinate η has to be defined:

$$ {}_I\boldsymbol{\delta}(\eta,t) = (R_S - R_R) \begin{bmatrix} 0 \\ \cos\eta \\ \sin\eta \end{bmatrix} - e_s \begin{bmatrix} 0 \\ \cos\varphi_s \\ \sin\varphi_s \end{bmatrix} - e_d \begin{bmatrix} 0 \\ \cos(\varphi_d + \Omega t) \\ \sin(\varphi_d + \Omega t) \end{bmatrix} . \tag{8.10} $$

Thus, the radial component of the air gap $\delta_r(\eta,t)$ is described as a function of η by

$$ {}_I\delta_r(\eta,t) = \delta'' - e_s\cos(\eta - \varphi_s) - e_d\cos(\eta - \varphi_d - \Omega t) . \tag{8.11} $$

Introducing the azimuthal relative coordinate φ of the rotor angle, the relation

$$ \eta = \varphi + \Omega t \tag{8.12} $$

is given which allows for the transformation of $\delta_r(\varphi,t)$ into the rotating coordinate system R. This transformation is necessary since the computation with the mechanical rotor model is carried out in the body-fixed coordinate system. The transformation of the air gap results in

$$ {}_R\delta_r(\varphi,t) = \delta'' - e_s\cos(\varphi - \varphi_s + \Omega t) - e_d\cos(\varphi - \varphi_d) . \tag{8.13} $$

In the rotating coordinate system, the static eccentricity now varies with time t. The dynamic eccentricity is time independent.

8.2.4 Permeance waves

The permeance function Λ_e due to eccentricity is given as a function of φ noted as

$$ \Lambda_e(\varphi,t) = \frac{\mu_0}{{}_R\delta_r(\varphi,t)} = \frac{\mu_0}{\delta'' - e(\varphi,t)} , \tag{8.14} $$

where $e(\varphi,t)$ is the sum of the static and dynamic eccentricity components. Afterwards, a binomial series of the permeance function is set up

$$\Lambda_e(\varphi,t) = \frac{\mu_0}{\delta''}\left(1 - \begin{pmatrix} -1 \\ 1 \end{pmatrix}\frac{e(\varphi,t)}{\delta''} + \begin{pmatrix} -1 \\ 2 \end{pmatrix}\left(\frac{e(\varphi,t)}{\delta''}\right)^2 - \dots\right) \tag{8.15}$$

which results in

$$\Lambda(\varphi,t) = \frac{\mu_0}{\delta''}\left(1 + \frac{e(\varphi,t)}{\delta''} + \left(\frac{e(\varphi,t)}{\delta''}\right)^2 + \dots\right) . \tag{8.16}$$

Assuming the eccentricities e_s and e_d are small compared to the air gap length δ'', the permeance function is obtained

$$\Lambda_e(\varphi,t) = \Lambda_0\left(1 + \epsilon_s\cos(\varphi - \varphi_s + \Omega t) + \epsilon_s\cos(\varphi - \varphi_d)\right) , \tag{8.17}$$

with relations of the relative static ϵ_s and dynamic ϵ_d eccentricity and the fundamental permeance amplitude Λ_0 :

$$\epsilon_s = \frac{e_s}{\delta''} , \qquad \epsilon_d = \frac{e_d}{\delta''} \qquad \text{and} \qquad \Lambda_0 = \frac{\mu_0}{\delta''} . \tag{8.18}$$

8.2.5 Magnetic flux density

The relation for the magnetic flux density $B(\varphi,t)$ is given in Equation (8.6). It is a product of the permeance function with the magnetomotive force. The magnetomotive force $V(\eta,t)$ resulting from the surface current density is also expressed as a series of rotating wave components, see [152]. This investigation is limited to the magnetomotive force due to the fundamental surface current density which is defined as

$$V(\eta,t) = V_p\cos(p\,\eta - \omega_p t - \varphi_p) \tag{8.19}$$

with

$$\omega_p = 2\pi f_p . \tag{8.20}$$

The machine's pole pair number is denoted as p and the line frequency is f_p. In the rotor coordinate system the magnetomotive force is written as

$$V(\varphi,t) = V_p\cos(p\,\varphi - (\omega_p - \Omega)t - \varphi_p) . \tag{8.21}$$

Together with the permeance function in Equation (8.17), the radial component of the magnetic flux density $B(\varphi,t)$ is obtained by

$$\begin{aligned} B(\varphi,t) = \Lambda_0 V_p\cos(p\,\varphi - (\omega_p - \Omega)t - \varphi_p)\,(1 + \dots \\ +\epsilon_s\cos(\varphi - \varphi_s + \Omega t) + \epsilon_d\cos(\varphi - \varphi_d)) \end{aligned} \tag{8.22}$$

which results in

$$\begin{aligned} B(\varphi,t) =& B_p \cos(p\,\varphi - (\omega_p - \Omega)t - \varphi_p) \\ &- \frac{1}{2}\Lambda_0 \epsilon_s V_p \cos\left((p \pm 1)\varphi - ((\omega_p - \Omega) \pm \Omega)\, t - (\varphi_p \pm \varphi_s)\right) \\ &- \frac{1}{2}\Lambda_0 \epsilon_d V_p \cos\left((p \pm 1)\varphi - (\omega_p - \Omega)t - (\varphi_p \pm \varphi_d)\right) \ . \end{aligned} \tag{8.23}$$

Additionally, four eccentricity field components B_e with spatial ordinal numbers of $p \pm 1$ arise in the definition of the fundamental magnetic field.

8.2.6 Force components of unbalanced magnetic pull

Using Maxwell's stress tensor the radial component of the surface force density is defined as

$$\sigma_r(\varphi,t) = \frac{B(\varphi,t)^2}{2\mu_0} \ . \tag{8.24}$$

The square of the magnetic flux density function leads to six terms. Only two of these six surface force terms are regarded in this work: The term $\sigma_{es}(\varphi,t)$ is resulting from the fundamental magnetic field and the static eccentricity with

$$\begin{aligned} \sigma_{es}(\varphi,t) = \frac{1}{2} B_p B_{es} \big(&\cos(-\varphi - \Omega t + \varphi_s) + \cos(\varphi + \Omega t - \varphi_s) \\ &\cos\left((2p+1)\varphi - (2(\omega_p - \Omega) + \Omega)\, t - (2\varphi_p + \varphi_s)\right) \\ &\cos\left((2p-1)\varphi - (2(\omega_p - \Omega) - \Omega)\, t - (2\varphi_p - \varphi_s)\right)\big) \ . \end{aligned} \tag{8.25}$$

The term $\sigma_{ed}(\varphi,t)$ is derived from the fundamental magnetic field and the dynamic eccentricity by

$$\begin{aligned} \sigma_{ed}(\varphi,t) = \frac{1}{2} B_p B_{ed} \big(&\cos(-\varphi + \varphi_d) + \cos(\varphi - \varphi_d) + \\ &\cos\left((2p+1)\varphi - 2(\omega_p - \Omega)t - (2\varphi_p + \varphi_d)\right) \\ &\cos\left((2p-1)\varphi - 2(\omega_p - \Omega)t - (2\varphi_p - \varphi_d)\right)\big) \ . \end{aligned} \tag{8.26}$$

An integration of the surface force along the azimuthal direction leads to the force components,

$${}_R F_y(t) = l \int_0^{2\pi} \sigma_e(\varphi,t)\ \sin\varphi\ R\ d\varphi \quad \text{and} \quad {}_R F_z(t) = l \int_0^{2\pi} \sigma_e(\varphi,t)\ \cos\varphi\ R\ d\varphi \ . \tag{8.27}$$

8.3 Transient investigations of rotor vibrations in the electromagnetical field

The equations of motion consider gyroscopic effects, rotor unbalance and gravity, compare Equation (6.5). Additionally, electromagnetical forces are included in the rotating system. These nonlinear forces have to be redetermined in each time step. The Newton-Raphson procedure is used for transient simulations. The energy momentum algorithm is imposed on the equations of motion. All transient simulations are carried out at a rotational speed of 49.85 Hz. The rotor runs up in 0.5 s to the final speed and holds it for 1.5 s. A time step of 5×10^{-4} s is chosen.

Simulations with different air gaps are carried out. Figure 8.4 plots the transient vibrations of node no. 33 in z direction. This node is chosen as it is in the middle of the laminated core stack. In the figure two periods are depicted. The blue line marks the result of the rotor vibration neglecting the unbalanced magnetic pull. A linear rotor vibration is seen. The other colored lines show rotor vibrations including the unbalanced magnetic pull for different air gap lengths. Rotor vibrations are nonlinear and smaller air gap lengths result in higher amplitudes.

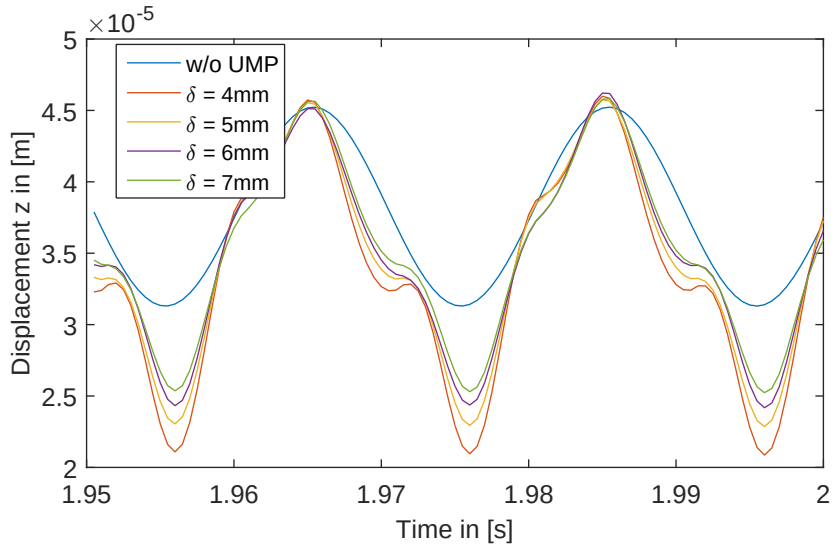

Figure 8.4: Displacements of node no. 33

Figure 8.5 shows the orbit of node no. 33 at a rotational speed of 49.85 Hz. The orbits of different air gap lengths are compared to the orbits without unbalanced magnetic pull. The blue lines mark the orbit without the unbalanced magnetic pull and the red lines show the orbits of the electromechanical system. The center of the linear orbit is not on the z-axis as the position of the orbit center is influenced by the gravity force which acts only in z-direction and by the structural damping. The structural damping causes force components in the rotating system which deflect the

rotor in y-direction additionally. The red lines show the orbits with air gap lengths of 4 mm, 5 mm, 6 mm and 7 mm. The fact that small air gap lengths cause higher amplitudes is also seen in orbits. Further the orbit's shapes show an attractor where the rotor is moving. This attractor nearly shows the shape of two circles. Hence, this is an indication for two equilibrium positions. The behaviour is seen for all air gap lengths.

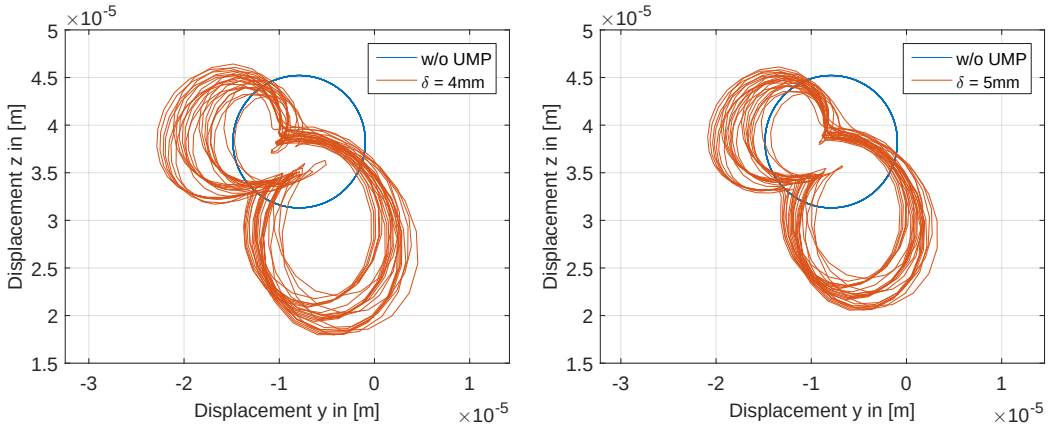

(a) Air gap 4 mm

(b) Air gap 5 mm

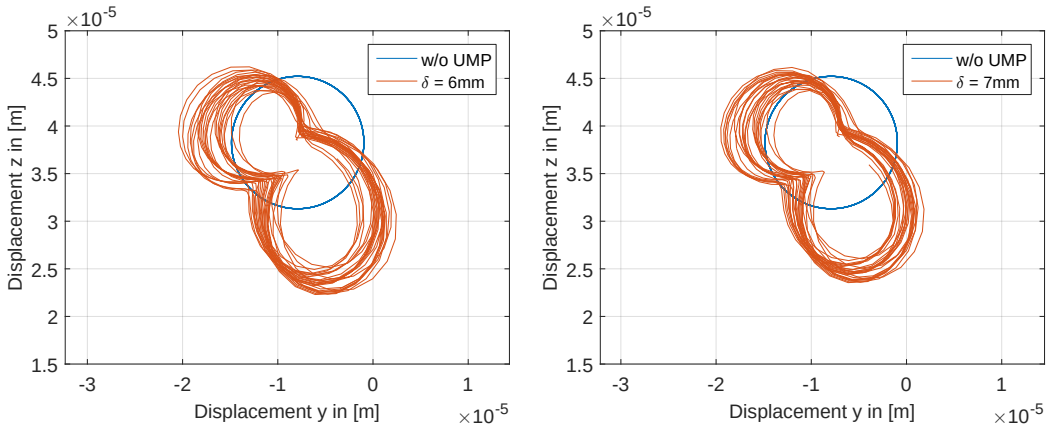

(c) Air gap 6 mm

(d) Air gap 7 mm

Figure 8.5: Displacement orbits of node no. 33

Figure 8.6 shows the unbalanced magnetic pull in z-direction of node no. 33. The force is plotted in a frequency range of 0 Hz to 1000 Hz. Due to the derivation of the unbalanced magnetic pull peaks are arising at $f = 0$, $f = 2f_p$, $f = 2f_p \pm f_R$ and further multiples of these frequencies. The line frequency f_p is given with 50 Hz. The rotational speed is 49.85 Hz. The force amplitudes at the frequencies $f = 0$ and $f = 2f_p \pm f_R$ are significantly higher than the other amplitudes. These frequencies have the strongest influence on the rotor motion.

The unbalanced magnetic pull is plotted for all investigated air gaps in Figure 8.6. All simulations deliver a similar behavior of the unbalanced magnetic pull. The smaller air gap lengths result in higher electromagnetical forces which is consistent with higher amplitudes of the rotor vibrations. The highest forces reach a level of about 200 N. The unbalance force and gravity force are depicted in Figure 8.7. The

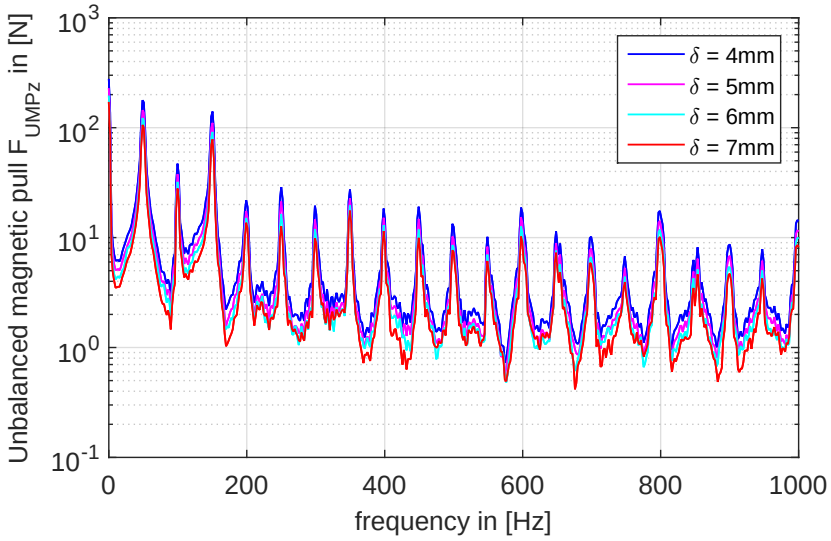

Figure 8.6: Unbalanced magnetic pull of node no. 33 in z-direction

proportion of the gravity force can be seen at the frequency $f = 0$ Hz. The amplitude is about 700 N. All other amplitudes are determined by the rotor unbalance. Due to

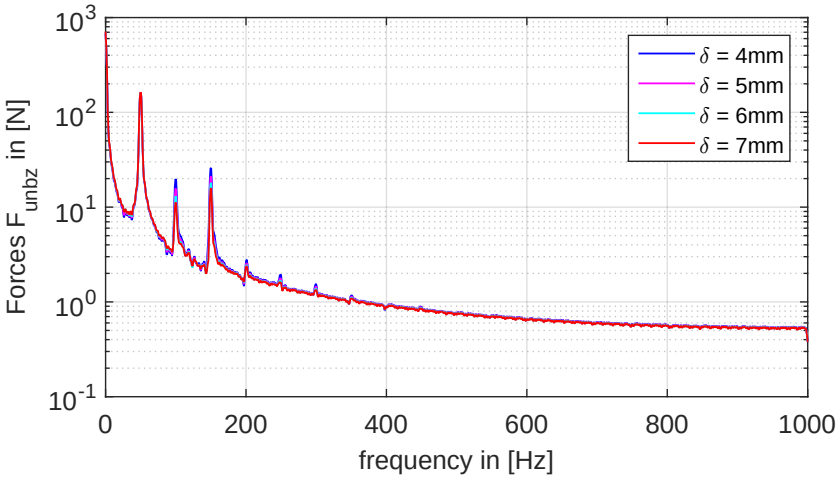

Figure 8.7: Unbalanced force of node no. 33 in z-direction

the nonlinear rotor vibration the unbalance force is not only influenced by the first order of the rotational speed. Higher multiples of the rotational speed are included in the unbalance force. The first order at 49.85 Hz gives the highest contribution

to the unbalance force. The amplitude of this peak is about 200 N. The peak level of the first order is independent from the air gap lengths, whereas the peak level of the second and third order is about a decimal power lower than the first order. The air gap lengths influences these amplitudes. Higher orders make hardly any contribution to the unbalance force.

The displacement's spectral content measured at node no. 33 is depicted in Figure 8.8. Whole-numbered orders are detected in the displacement response. It shows a similar behavior for all air gap lengths. Only the amplitudes decrease slightly by higher air gap lengths, compare Figure 8.5.

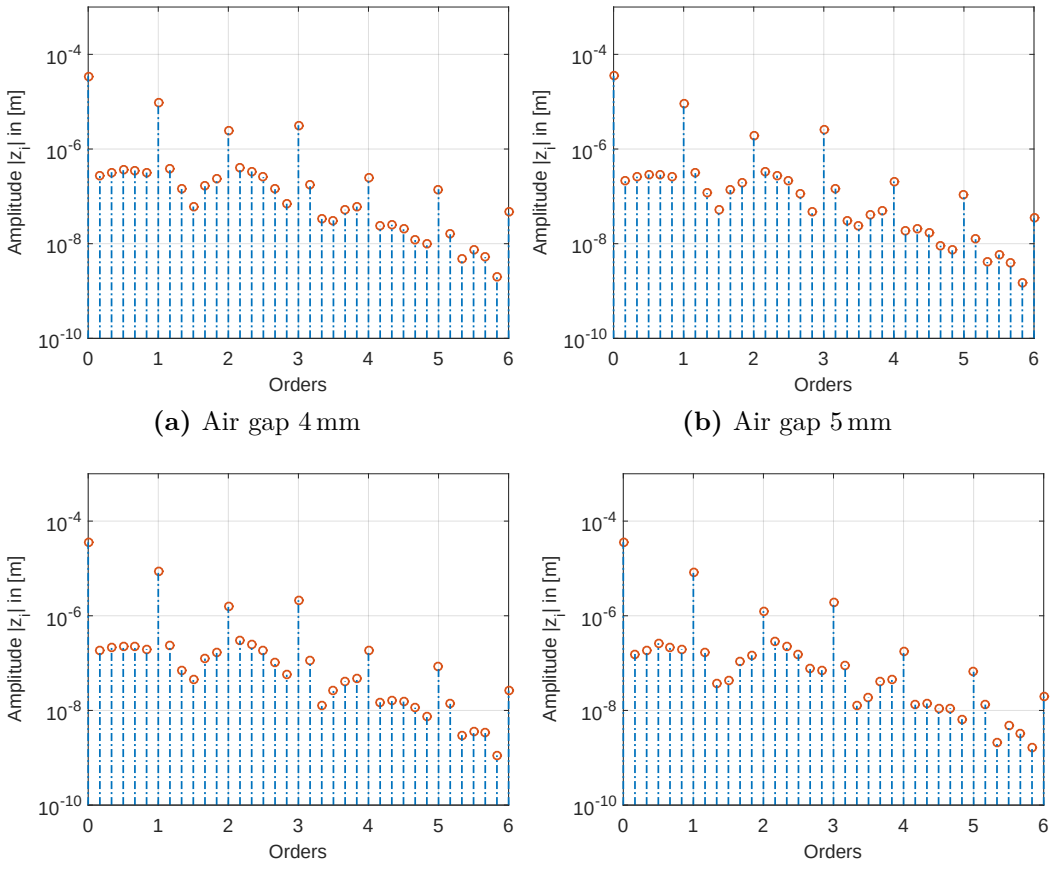

(a) Air gap 4 mm **(b)** Air gap 5 mm

(c) Air gap 6 mm **(d)** Air gap 7 mm

Figure 8.8: Orders of displacement in z direction (node no. 33)

Figure 8.9 depicts the phase diagrams and Poincaré sections for different air gap lengths at node no. 33. The blue lines depicts the trajectories and the red points are the Poincaré points. All simulation results have a similar behavior with different amplitudes. The trajectories show a nonlinear rotor motion for all air gap lengths and several forced accumulation points are visible in the Poincaré sections.

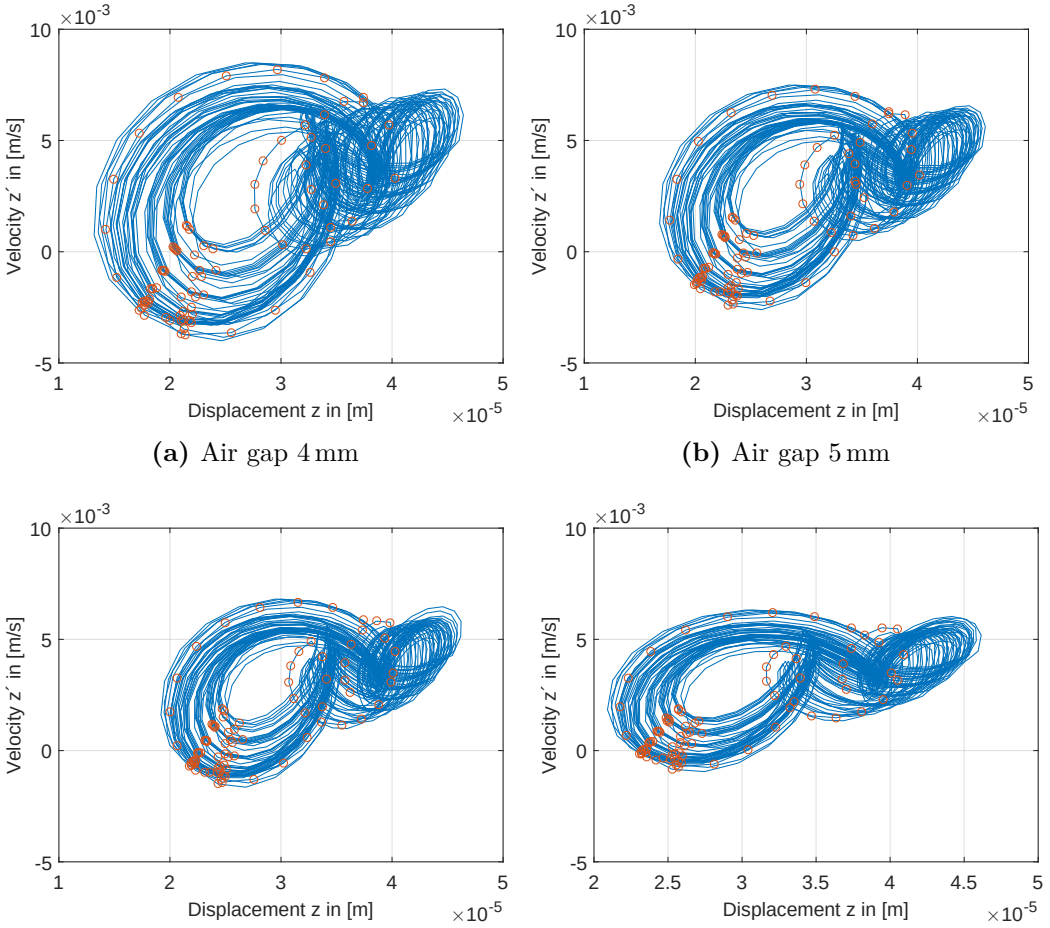

(a) Air gap 4 mm **(b)** Air gap 5 mm

(c) Air gap 6 mm **(d)** Air gap 7 mm

Figure 8.9: Poincaré diagram of vibrations in z direction (node no. 33)

CHAPTER 9

Conclusion

This dissertation treats the modelling and analysis of the rotor of an electrical machine. Taking the heterogeneous structure of the rotor assembly into account, a one-dimensional finite element model is derived. This model has the advantage of a significant smaller model size than a full three-dimensional model. The approach is based on the Timoshenko theory and is applicable for orthotropic materials. It is demonstrated that the proposed one-dimensional model achieve a sufficient accuracy for the application of electrical machine's rotors. The model allows for an efficient analysis of the rotor's dynamical behavior in frequency and time domain. The main contribution of the presented work can be summarized as follows:

- Development of composite beam elements which include *shear coefficients for orthotropic materials* computed with a two-dimensional finite element model of arbitrary cross sections,
- Application and implementation of the composite beam elements in a computer code,
- Analysis of the *rotor vibrations in frequency and time domain* with special regard for the heterogeneous assembly of components,
- Computation and *coupling of electromagnetical forces* with the one-dimensional rotor model including static and dynamic eccentricities using an analytical approach.

The torsion of a shaft with arbitrary cross section is formulated as a Neumann boundary value problem. The derivation considers homogeneous as well as composite beams. The procedure leads to warping functions which include the effects of isotropic or orthotropic material properties. Key parameters describing the shear such as the shear center and the shear correction factor, are obtained from torsionless beam bending. The associated Dirichlet boundary value problem is solved using a two-dimensional finite element method. The results have been validated numerically by comparing a test example with the solution of a full three-dimensional finite element

model. The error in the beam deflection is below 0.5 %. The comparison between the shear stresses showed that the highest errors are located in boundary regions. The error level at these positions depends on the mesh size and is reasonable.

Based on these numerical formulations, a rotor of an electrical machine is modeled. The advantage of the beam elements results from the reduced number of degrees of freedom in comparison to a full three-dimensional model. The beam model of the rotor includes structural damping using the Rayleigh model. Further, gyroscopic effects are considered. The rotor unbalance is included in unbalance forces and the gravity field is imposed on the rotor model. In order to validate the numerical model, an experimental modal analysis is carried out on a real rotor model. A very good match is achieved for the first bending frequencies. The accuracy decreases for higher modes depending on the bearing model of the steel racks where the rotor is supported. Additionally, run up simulations are carried out. In these simulations, a roller bearing model with nonlinear stiffness coefficients is imposed on the simulation model. The transient run up shows higher order vibrations in the response of rotor. The influence of the bearings on a simplified rotor mode is investigated. Also, ranges of non-harmonic response are found. Different simulations with constant speed allow for a classification of the resulting vibrations The bearing stiffness has a dominant effect.

Furthermore, the effect of the unbalanced magnetic pull on the rotor vibrations is analyzed. An analytical approach is used to compute the electromagnetical forces for steady state vibrations. Maxwell's stress tensor gives the radial components of the resulting surface forces. The formulation is based on the magnetic flux density which includes the actual geometric rotor position in the stator bore. This value is updated in each step of the time integration, allowing for the computation of the electromagnetical forces in each time step. The method is used for a two-pole induction machine. The nonlinear rotor vibrations are investigated for different air gap lengths. Effects due to the unbalanced magnetic pull are presented in detail.

In conclusion, the present thesis provides a methodology for the modeling of electrical machine's rotors and the computation of mechanical rotor vibrations. The introduced model allows for coupling with multi-physical forces and is usable for extending it with electrical machine's housing or other machine components.

Bibliography

1. Abbas, B.A.H. and J. Thomas: 'The second frequency spectrum of timoshenko beams'. *Journal of Sound and Vibration* (1977), vol. 51(1): pp. 123–137.
2. Adiletta, G., A.R. Guido, and C. Rossi: 'Nonlinear Dynamics of a Rigid Unbalanced Rotor in Journal Bearings. Part I: Theoretical Analysis'. English. *Nonlinear Dynamics* (1997), vol. 14(1): pp. 57–87.
3. Adiletta, G., A.R. Guido, and C. Rossi: 'Nonlinear Dynamics of a Rigid Unbalanced Rotor in Journal Bearings. Part II: Experimental Analysis'. English. *Nonlinear Dynamics* (1997), vol. 14(2): pp. 157–189.
4. Alfares, Mohammed A and Abdallah A Elsharkawy: 'Effects of axial preloading of angular contact ball bearings on the dynamics of a grinding machine spindle system'. *Journal of Materials Processing Technology* (2003), vol. 136(1-3): pp. 48–59.
5. Anderson, G.L.: 'Free vibrations of a laminated beam by a microstructure theory'. *Journal of Sound and Vibration* (1973), vol. 27(2): pp. 137–155.
6. Anderson, R.A.: 'Flexural vibrations in uniform beams according to the Timoshenko theory'. *Journal of Applied Mechanics* (1953), vol. 20(4): pp. 504–510.
7. Auricchio, Ferdinando, Giuseppe Balduzzi, and Carlo Lovadina: 'A new modeling approach for planar beams: finite-element solutions based on mixed variational derivations'. *Journal of Mechanics of Materials and Structures* (2010), vol. 5(5): pp. 771–794.
8. Auricchio, Ferdinando, Giuseppe Balduzzi, and Carlo Lovadina: 'The dimensional reduction modelling approach for 3D beams: Differential equations and finite-element solutions based on Hellinger-Reissner principle'. *International Journal of Solids and Structures* (2013), vol. 50(25-26): pp. 4184–4196.
9. Bach, Carl v.: 'Versuche über die tatsächliche Widerstandsfähigkeit von Balken mit C-förmigen Querschnitt'. *Zeitschrift des VDI* (1909), vol. 53: pp. 1790–1795.

10. Bathe, K.-J.: *Finite-Elemente-Methoden*. Springer-Verlag, 2002.

11. Batra, RC, S Vidoli, and F Vestroni: 'Plane wave solutions and modal analysis in higher order shear and normal deformable plate theories'. *Journal of Sound and Vibration* (2002), vol. 257(1): pp. 63–88.

12. BAZOUNE, A., Y.A. KHULIEF, and N.G. STEPHEN: 'Shape functions of three-dimensional Timoshenko beam element'. *Journal of Sound and Vibration* (2003), vol. 259(2): pp. 473 –480.

13. Belahcen, A.: 'Vibrations of rotating electrical machines due to magnetomechanical coupling and magnetostriction'. *Magnetics, IEEE Transactions on* (2006), vol. 42(4): pp. 971–974.

14. Belmans, R., A. Vandenput, and W. Geysen: 'Influence of unbalanced magnetic pull on the radial stability of flexible-shaft induction machines'. *Electric Power Applications, IEE Proceedings B* (1987), vol. 134(2): pp. 101–109.

15. Bishop, R. E. D.: 'The vibration of rotating shafts'. *Journal of Mechanical Engineering Science* (1959), vol. 1(1): pp. 50–65.

16. Bishop, R. E. D. and G. M. L. Gladwell: 'The vibration and balancing of an unbalanced flexible rotor'. *Journal of Mechanical Engineering Science* (1959), vol. 1(1): pp. 66–77.

17. Bishop, Richard Evelyn Donohue and Amie Gladys Parkinson: 'Second order vibration of flexible shafts'. *Philosophical Transactions of the Royal Society of London. Series A, Mathematical and Physical Sciences* (1965), vol. 259(1095): pp. 1–31.

18. Bonet, Javier and Richard D. Wood: *Nonlinear Continuum Mechanics for Finite Element Analysis*. Cambridge: Cambridge University Press, 2008.

19. Bossavit, Alain: 'Virtual power principle and Maxwell's tensor: which comes first?' *COMPEL - The international journal for computation and mathematics in electrical and electronic engineering* (2011), vol. 30(6): pp. 1804–1814.

20. Brosens, Pierre J. and S. H. Crandall: 'Whirling of unsymmetrical rotors'. *Journal of Applied Mechanics* (1961), vol. 28(3): pp. 355–362.

21. Budó, A.: *Theoretische Mechanik*. Berlin: VEB Deutscher Verlag der Wissenschaften, 1987.

22. Campbell, Wilfred: *Protection of steam turbine disk wheels from axial vibration*. General electric Company, 1924.

23. Carpenter, Nicholas, Ted Belytschko, and Henryk Stolarski: 'Locking and shear scaling factors in C^0 bending elements'. *Computers & Structures* (1986), vol. 22(1): pp. 39–52.

24. Cho, K.: *Reconstruction of Macroscopic Maxwell Equations*. Berlin: Springer-Verlag, 2010.

25. Chou, S.I.: 'Determination of centers of flexure using the boundary element method'. *Engineering Analysis with Boundary Elements* (1993), vol. 12(4): pp. 321–324.

26. Choy, F. K., M. J. Braun, and Y. Hu: 'Nonlinear Transient and Frequency Response Analysis of a Hydrodynamic Journal Bearing'. *Journal of Tribology* (July 1992), vol. 114(3): pp. 448–454.

27. Chree, C.: 'LX. The whirling and transverse vibrations of rotating shafts'. *Philosophical Magazine Series 6* (1904), vol. 7(41): pp. 504–542.

28. Chree, C.: 'The Equations of an Isotropic Elastic Solid in Polar and Cylindrical Coordinates, Their Solution and Application'. *Transactions of the Cambridge Philosophical Society* (1889), vol. 14: p. 250.

29. Cowper, G. R.: 'The Shear Coefficient in Timoshenko's Beam Theory'. *Journal of Applied Mechanics* (1966), vol. 33(2): pp. 335–340.

30. Davies, R.M.: 'The frequency of transverse vibration of a loaded fixed-free bar III. The effect of the rotatory inertia of the bar'. *Philosophical Magazine Series 7* (1937), vol. 23(155): pp. 563–573.

31. Davis, R., R.D. Henshell, and G.B. Warburton: 'A Timoshenko beam element'. *Journal of Sound and Vibration* (1972), vol. 22(4): pp. 475–487.

32. Dawe, D.J.: 'A finite element for the vibration analysis of Timoshenko beams'. *Journal of Sound and Vibration* (1978), vol. 60(1): pp. 11–20.

33. DeBortoli, M.J., S.J. Salon, D.W. Burow, and C. J. Slavik: 'Effects of rotor eccentricity and parallel windings on induction machine behavior: a study using finite element analysis'. *Magnetics, IEEE Transactions on* (1993), vol. 29(2): pp. 1676–1682.

34. Dimentberg, F. M.: 'Bending oscillations of rotating shaft'. *AS the USSR* (1959), vol.

35. Dolph, C.L.: 'On the Timoshenko Theory of Transverse Beam Vibrations'. *QUARTERLY OF APPLIED MATHEMATICS* (1954), vol. 12(2): pp. 175–187.

36. Dorrell, D.G., W.T. Thomson, and S. Roach: 'Analysis of airgap flux, current, and vibration signals as a function of the combination of static and dynamic airgap eccentricity in 3-phase induction motors'. *Industry Applications, IEEE Transactions on* (1997), vol. 33(1): pp. 24–34.

37. Dungen, F. H. van den: 'Über die Biegungsschwingungen einer Welle'. *Zeitschrift für Angewandte Mathematik und Mechanik* (1928), vol. 8(3): pp. 225–231.

38. Dunkerley, Stanley: 'On the Whirling and Vibration of Shafts'. *Philosophical Transactions of the Royal Society of London A: Mathematical, Physical and Engineering Sciences* (1894), vol. 185: pp. 279–360.

39. Ede, J.D., Z.Q. Zhu, and D. Howe: 'Rotor resonances of high-speed permanent-magnet brushless machines'. *Industry Applications, IEEE Transactions on* (2002), vol. 38(6): pp. 1542–1548.

40. Egle, D. M.: 'An approximate theory for transverse shear deformation and rotary inertia effects in vibrating beams'. *NASA contractor report*. CR-1317. National Aeronautics and Space Administration, 1969.

41. Eshleman, R. L. and R. A. Eubanks: 'On the critical speeds of a continuous rotor'. *Journal of Manufacturing Science and Engineering* (1969), vol. 91(4): pp. 1180–1188.

42. Ewins, D.J.: *Modal testing: theory and practice*. Mechanical engineering research studies: Engineering dynamics series. Research Studies Press, 1984.

43. Foote, W. R., H. Poritsky, and J. J. Slade: 'Critical speeds of a rotor with unequal shaft flexibilities, mounted in bearings of unequal flexibility—I'. *Trans. ASME* (1943), vol. 10: A77–A84.

44. Föppl, A.: 'Das Problem der Lavalschen Turbinenwelle'. *Civilingenieur* (1895), vol. 41: pp. 248–250.

45. Frahm, Hermann: *Neue Untersuchungen über die dynamischen Vorgänge in den Wellenleitungen von Schiffsmaschinen mit besonderer Berücksichtigung der Resonanzschwingungen*. Julius Springer, 1902.

46. Friedman, Z. and J.B. Kosmatka: 'An improved two-node timoshenko beam finite element'. *Computers & Structures* (1993), vol. 47(3): pp. 473–481.

47. Friedman, Z. and J.B. Kosmatka: 'Torsion and flexure of a prismatic isotropic beam using the boundary element method'. *Computers & Structures* (2000), vol. 74(4): pp. 479–494.

48. Früchtenicht, J., H. Jordan, and H.O. Seinsch: 'Exzentrizitätsfelder als Ursache von Laufinstabilitäten bei Asynchronmaschinen - Teil 1: Elektromagnetische Felderzahl und elektromagnetische Dämpfungskonstante'. German. *Archiv für Elektrotechnik* (1982), vol. 65(4-5): pp. 271–281.

49. Früchtenicht, J., H. Jordan, and H.O. Seinsch: 'Exzentrizitätsfelder als Ursache von Laufinstabilitäten bei Asynchronmaschinen - Teil 2: Selbsterregte Biegeeigenschwingungen des Läufers'. German. *Archiv für Elektrotechnik* (1982), vol. 65(4-5): pp. 283–292.

50. Garvey, S.D.: 'The vibrational behaviour of laminated components in electrical machines'. *Electrical Machines and Drives, 1989. Fourth International Conference on*. 13-15 Sep 1989: pp. 226–231.

51. Garvey, SD, JET Penny, MI Friswell, and AW Lees: 'The Stiffening Effect of Laminated Rotor Cores on Flexible-Rotor Electrical Machines'. *8th International Conference on Vibrations in Rotating Machinery, Swansea, UK*. 2004: pp. 193–202.

52. Gasch, R., R. Nordmann, and H. Pfützner: *Rotordynamik*. Vol. 2., vollständig neu bearbeitete und erweiterte Auflage. Berlin: Springer-Verlag, 2002.

53. Gasch, Robert, Klaus Knothe, and Robert Liebich: *Strukturdynamik: Diskrete Systeme und Kontinua*. Berlin: Springer-Verlag, 2012.

54. Genta, Giancarlo: *Dynamics of rotating systems*. New York: Springer Science & Business Media, 2007.

55. Gerstner, Robert W.: 'Stresses in a Composite Cantilever'. *Journal of Composite Materials* (1968), vol. 2(4): pp. 498–501.

56. Giavotto, V., M. Borri, P. Mantegazza, G. Ghiringhelli, V. Carmaschi, G.C. Maffioli, and F. Mussi: 'Anisotropic beam theory and applications'. *Computers & Structures* (1983), vol. 16(1-4): pp. 403–413.

57. Giet, M. van der, K. Kasper, R.W. De Doncker, and K. Hameyer: 'Material parameters for the structural dynamic simulation of electrical machines'. *Electrical Machines (ICEM), 2012 XXth International Conference on*. 2-5 Sept. 2012: pp. 2994–3000.

58. Goens, E.: 'Determination of Young's Modulus from Flexural Vibrations'. *Ann. Phys.* (1931), vol. 11(6): pp. 649–678.

59. Goodier, J. N.: 'A Theorem on the Shearing Stress in Beams with Applications to Multicellular Sections'. *Journal of the Aeronautical Sciences* (1944), vol. 11(3): pp. 272–280.

60. Greenhill, A. G.: 'On the Strength of Shafting When Exposed Both to Torsion and to End Thrust'. *Proceedings of the Institution of Mechanical Engineers* (1883), vol. 34(1): pp. 182–225.

61. Gruttmann, F. and W. Wagner: 'Shear correction factors in Timoshenko's beam theory for arbitrary shaped cross-sections'. English. *Computational Mechanics* (2001), vol. 27(3): pp. 199–207.

62. Gruttmann, F., R. Sauer, and W. Wagner: 'Shear stresses in prismatic beams with arbitrary cross-sections'. *International Journal for Numerical Methods in Engineering* (1999), vol. 45(7): pp. 865–889.

63. Gümbel, E: 'Verdrehschwingungen eines Stabes mit fester Drehachse und beliebiger zur Drehachse symmetrischer Massenverteilung unter dem Einfluß beliebiger harmonischer Kräfte'. *Z. VDI* (1912), vol. 56: p. 1025.

64. Gunduz, Aydin, Jason T. Dreyer, and Rajendra Singh: 'Effect of bearing preloads on the modal characteristics of a shaft-bearing assembly: Experiments on double row angular contact ball bearings'. *Mechanical Systems and Signal Processing* (2012), vol. 31: pp. 176–195.

65. Guo, D., F.Chu, and D. Chen: 'The unbalanced magnetic pull and its effects on vibration in a three-phase generator with eccentric rotor'. *Journal of Sound and Vibration* (2002), vol. 254(2): pp. 297–312.

66. Guo, Yi and Robert G. Parker: 'Stiffness matrix calculation of rolling element bearings using a finite element/contact mechanics model'. *Mechanism and Machine Theory* (2012), vol. 51: pp. 32–45.

67. Ha, K.H. and J.P. Hong: 'Dynamic rotor eccentricity analysis by coupling electromagnetic and structural time stepping FEM'. *Magnetics, IEEE Transactions on* (2001), vol. 37(5): pp. 3452–3455.

68. Haag, A. C. and G. O. Sankey: 'Elastic and damping properties of oil-film journal bearings'. *Journal of Applied Mechanics* (1956), vol. 23: pp. 101–108.

69. Haberl, G. and F. Och: 'Eine Finite-Element-Lösung für die Torsionssteifigkeit und den Schubmittelpunkt beliebiger Querschnitte'. *Z. f. Flugwiss.* (1974), vol. 22(4): pp. 115–119.

70. Hearmon, R. F. S.: 'The influence of shear and rotatory inertia on the free flexural vibration of wooden beams'. *British Journal of Applied Physics* (1958), vol. 9(10): pp. 381–388.

71. Herrmann, G.: 'Forced motions of Timoshenko beams'. *J. of Appl. Mech. ASME* (1955), vol. 22: pp. 53–56.

72. Herrmann, L. R.: 'Elastic Torsional Analysis of Irregular Shapes'. *Journal of the Engineering Mechanics Division* (1965), vol. 91(6): pp. 11–20.

73. Hertz, H.: 'Über die Berührung fester elastischer Körper'. *Journal für die reine und angewandte Mathematik* (1881), vol. 92: pp. 156–171.

74. Hohenemser, K. and W. Prager: *Dynamik der Stabwerke*. Springer-Verlag Berlin Heidelberg, 1933.

75. Holmes, R.: 'The Vibration of a Rigid Shaft on Short Sleeve Bearings'. *Journal of Mechanical Engineering Science* (1960), vol. 2(4): pp. 337–341.

76. Holopainen, T. P., A. Tenhunen, and A. Arkkio: 'Electromagnetic circulatory forces and rotordyrotor instability in electric machines'. *Proceedings if the 6th International Conference on Rotor Dynamics*. Vol. 1. Sydney, 2002: pp. 446–463.

77. Holzer, H.: 'Torsionsschwingungen von Wellen mit beliebig vielen Massen'. *Schiffbau* (1907), vol. Bd. 8: p. 823.

78. Huang, T. C.: 'The Effect of Rotatory Inertia and of Shear Deformation on the Frequency and Normal Mode Equations of Uniform Beams With Simple End Conditions'. *Journal of Applied Mechanics* (Dec. 1961), vol. 28(4): pp. 579–584.

79. Hutchinson, J. R.: 'Shear Coefficients for Timoshenko Beam Theory'. *Journal of Applied Mechanics* (2001), vol. 68(1): pp. 87–92.

80. Jeffcott, H.H.: 'XXVII. The lateral vibration of loaded shafts in the neighbourhood of a whirling speed. - The effect of want of balance'. *Philosophical Magazine Series 6* (1919), vol. 37(219): pp. 304–314.

81. Jordan, H, R.-D. Schroeder, and H. O. Seinsch: 'Zur Berechnung einseitig magnetischer Zugkräfte in Drehfeldmaschinen'. *Archiv für Elektrotechnik* (1981), vol. 63: pp. 117–124.

82. Jr., Nelson R. Bauld and Tzeng Lih-Shyng: 'A Vlasov theory for fiber-reinforced beams with thin-walled open cross sections'. *International Journal of Solids and Structures* (1984), vol. 20(3): pp. 277–297.

83. Jun, Li, Hua Hongxing, and Shen Rongying: 'Dynamic finite element method for generally laminated composite beams'. *International Journal of Mechanical Sciences* (2008), vol. 50(3): pp. 466–480.

84. Kahya, Volkan: 'Dynamic analysis of laminated composite beams under moving loads using finite element method'. *Nuclear Engineering and Design* (2012), vol. 243(0): pp. 41–48.

85. Kaneko, T: 'On Timoshenko's correction for shear in vibrating beams'. *Journal of Physics D: Applied Physics* (1975), vol. 8(16): pp. 1927–1936.

86. Kantorovich, L. V. and V. I. Krylov: *Approximate Methods of Higher Analysis*. Translated by Curtis D. Benster. Interscience Publishers, 1958: p. 681.

87. Kapania, Rakesh K. and Stefano Raciti: 'Recent Advances in Analysis of Laminated Beams and Plates, Part I: Shearеffects and Buckling.' *AIAA Journal* (July 1989), vol. 27(7): pp. 923–935.

88. Kapania, Rakesh K. and Stefano Raciti: 'Recent Advances in Analysis of Laminated Beams and Plates, Part II: Vibrations and Wave Propagation'. *AIAA Journal* (July 1989), vol. 27(7): pp. 935–946.

89. Kapur, Kanwar K.: 'Vibrations of a Timoshenko Beam, Using Finite Element Approach'. *The Journal of the Acoustical Society of America* (1966), vol. 40(5): pp. 1058–1063.

90. Kienzler, Reinhold and Roland Schröder: *Einführung in die Höhere Festigkeitslehre*. Berlin Heidelberg: Springer-Verlag, 2009.

91. Kim, Cheol and Scott R. White: 'Thick-walled composite beam theory including 3-d elastic effects and torsional warping'. *International Journal of Solids and Structures* (1997), vol. 34(31-32): pp. 4237–4259.

92. Kim, Y.-C. and K.-W. Kim: 'Influence of Lamination Pressure upon the Stiffness of Laminated Rotor'. *JSME international journal* (2006), vol. 49: pp. 426–431.

93. Kimball, A. L.: 'Internal friction as a cause of shaft whirling'. *Phil. Mag* (1925), vol. 49: pp. 724–727.

94. Kimball, A. L.: 'Internal friction theory of shaft whirling'. *General Electric Review* (1924), vol. 27(4): pp. 244–251.

95. Klinkel, S. and S. Govindjee: 'Anisotropic bending-torsion coupling for warping in a non-linear beam'. English. *Computational Mechanics* (2003), vol. 31(1-2): pp. 78–87.

96. Kourtis, Lampros C., Haneesh Kesari, Dennis R. Carter, and Gary S. Beaupré: 'Transverse and torsional shear stresses in prismatic bodies having inhomogeneous material properties using a new 2d stress function'. *Journal of Mechanics of Materials and Structures* (2009), vol. 4(4): pp. 659–673.

97. Krahula, J. L. and G. F. Lauterbach: 'A finite element solution for Saint-Venant torsion'. *AIAA Journal* (1969), vol. 7(12): pp. 2200–2203.

98. Kruszewski Edwin T., United States. National Advisory Committee for Aeronautics.: *Effect of transverse shear and rotary inertia on the natural frequency of a uniform beam.* Washington, D.C.: National Advisory Committee for Aeronautics, 1949.

99. Leckie, F. and G. Lindberg: 'The effect of lumped parameters on beam frequencies'. *The Aeronautical Quarterly* (1963), vol. 14: pp. 224–240.

100. Lee, Y.-S. and C.-W. Lee: 'Modelling and Vibration Analysis of Misaligned Rotor-Ball Bearing Systems'. *Journal of Sound and Vibration* (1999), vol. 224(1): pp. 17–32.

101. Lim, T.C. and R. Singh: 'Vibration transmission through rolling element bearings, part I: Bearing stiffness formulation'. *Journal of Sound and Vibration* (1990), vol. 139(2): pp. 179–199.

102. Lim, T.C. and R. Singh: 'Vibration transmission through rolling element bearings, part II: System studies'. *Journal of Sound and Vibration* (1990), vol. 139(2): pp. 201 –225.

103. Lo, K. H., R. M. Christensen, and E. M. Wu: 'A High-Order Theory of Plate Deformation - Part 1: Homogeneous Plates'. *Journal of Applied Mechanics* (Dec. 1977), vol. 44(4): pp. 663–668.

104. Lo, K. H., R. M. Christensen, and E. M. Wu: 'A High-Order Theory of Plate Deformation - Part 2: Laminated Plates'. *Journal of Applied Mechanics* (Dec. 1977), vol. 44(4): pp. 669–676.

105. Love, A.E.H.: *A Treatise on the Mathematical Theory of Elasticity.* A Treatise on the Mathematical Theory of Elasticity. at the University Press, 1906.

106. Lund, J. W.: 'Calculation of Stiffness and Damping Properties of Gas Bearings'. *Journal of Lubrication Technology* (Oct. 1968), vol. 90(4): pp. 793–803.

107. Lund, J. W.: 'Review of the Concept of Dynamic Coefficients for Fluid Film Journal Bearings'. *Journal of Tribology* (Jan. 1987), vol. 109(1): pp. 37–41.

108. Lund, J. W.: 'Stability and Damped Critical Speeds of a Flexible Rotor in Fluid-Film Bearings'. *Journal of Engineering for Industry* (May 1974), vol. 96(2): pp. 509–517.

109. Lund, J. W. and E. Saibel: 'Oil Whip Whirl Orbits of a Rotor in Sleeve Bearings'. *Journal of Engineering for Industry* (1967), vol. 89(4): pp. 813–823.

110. Luo, Y.: 'An efficient 3D Timoshenko beam element with consistent shape functions'. *Advances in Theoretical and Applied Mechanics* (2008), vol. 1: pp. 95–106.

111. Mair, Mathias, Bernhard Weilharter, Siegfried Rainer, Katrin Ellermann, and Oszkár Bíró: 'Numerical and experimental investigation of the structural characteristics of stator core stacks'. *COMPEL: The International Journal for Computation and Mathematics in Electrical and Electronic Engineering* (2013), vol. 32(5): pp. 1643–1664.

112. Mair, Mathias, Bernhard Weilharter, and Katrin Ellermann: 'Rotor Vibrations in Electrical Machines Due to Electromagnetic Forces'. English. *Proceedings of the 9th IFToMM International Conference on Rotor Dynamics*. Ed. by Pennacchi, Paolo. Vol. 21. Mechanisms and Machine Science. Springer International Publishing, 2015: pp. 601–611.

113. Mang, Herbert A., Günter Hofstetter, and J. Eberhardsteiner: *Festigkeitslehre*. Vol. 3. Auflage. Springer, 2008.

114. Mason, W. E. and L. R. Herrmann: 'Elastic Shear Analysis of General Prismatic Beams'. *Journal of the Engineering Mechanics Division* (1968), vol. 94(4): pp. 965–986.

115. Meirovitch, Leonard: 'A new method of solution of the eigenvalue problem for gyroscopic systems'. *AiAA Journal* (1974), vol. 12(10): pp. 1337–1342.

116. Mindlin, R.D. and L.E. Goodman: 'Beam vibrations with time-dependent boundary conditions'. *Journal of Applied Mechanics* (1950), vol. 14(4): pp. 377–380.

117. Mindlin, R.D. and H. Deresiewicz: 'Timoshenko's shear coefficient for flexural vibrations of beams'. *Proceedings of the Second U.S. National Congress of Applied Mechanics*. 1954: pp. 175–178.

118. Mogenier, G., N.-B. Thouraya, R. Dufour, L. Durantay, and N. Barras: 'Identification of constitutive properties of a laminated rotor at rest through a condensed modal functional'. *Mécanique & Industries* (2010), vol. 11: pp. 309–326.

119. Mogenier, G., N.-B. Thouraya, R. Dufour, L. Durantay, and N. Barras: 'Identification of Lamination Stack Properties: Application to High-Speed Induction Motors'. *IEEE Trans. on Industrial Electronics* (2010), vol. 57(1): pp. 281–287.

120. Mogenier, G., T. Baranger, R. Dufour, Ferraris Besso, and L. Durantay: 'Nonlinear centrifugal effects on a prestressed laminated rotor'. *Mechanism and Machine Theory* (2011), vol. 46(10): pp. 1466–1491.

121. Mokos, V.G. and E.J. Sapountzakis: 'A {BEM} solution to transverse shear loading of composite beams'. *International Journal of Solids and Structures* (2005), vol. 42(11-12): pp. 3261–3287.

122. Morley, A.: 'The Calculation of Vibration and Whirling Speeds'. *Engineering* (1909), vol. 88: p. 135.

123. Müller, Peter C.: *Stabilität und Matrizen: Matrizenverfahren in der Stabilitätstheorie linearer dynamischer Systeme*. Berlin: Springer-Verlag, 1977.

124. Myklestad, N. O.: 'A New Method of Calculating Natural Modes of Uncoupled Bending Vibration of Airplane Wings and Other Types of Beams'. *Journal of the Aeronautical Sciences* (1944), vol. 11(2): pp. 153–162.

125. Newkirk, B. L.: 'Shaft whipping'. *General Electric Review* (1924), vol. 27(3): pp. 169–178.

126. Newkirk, B. L. and H. D. Taylor: 'Shaft whipping due to oil action in journal bearings'. *General Electric Review* (1925), vol. 28(8): pp. 559–568.

127. Nickel, R. E. and G. A. Secor: 'Convergence of consistently derived Timoshenko beam finite elements'. *International Journal for Numerical Methods in Engineering* (1972), vol. 5(2): pp. 243–252.

128. Nouri, T. and D. Gay: 'Shear stresses in orthotropic composite beams'. *International Journal of Engineering Science* (1994), vol. 32(10): pp. 1647–1667.

129. Olsson, R.G.: 'Die tatsächliche Durchbiegung des gebogenen Balken'. *Der Stahlbau* (1934), vol. 7(2): pp. 13–14.

130. Pacoste, Costin and Anders Eriksson: 'Beam elements in instability problems'. *Computer Methods in Applied Mechanics and Engineering* (1997), vol. 144(1-2): pp. 163–197.

131. Parkus, Heinz: *Mechanik der festen Körper*. Vol. 2. Auflage. Wien: Springer-Verlag, 2005.

132. Parsell, J. K., P. E. Allaire, and L. E. Barrett: 'Frequency Effects in Tilting-Pad Journal Bearing Dynamic Coefficients'. *A S L E Transactions* (1983), vol. 26(2): pp. 222–227.

133. Pennacchi, Paolo: 'Nonlinear effects due to electromechanical interaction inÂ generators with smooth poles'. English. *Nonlinear Dynamics* (2009), vol. 57(4): pp. 607–622.

134. Pickett, Gerald: 'Flexural Vibration of Unrestrained Cylinders and Disks'. *Journal of Applied Physics* (1945), vol. 16(12): pp. 820–831.

135. Pirnat, Miha, Gregor Čepon, and Miha Boltežar: 'Introduction of the linear contact model in the dynamic model of laminated structure dynamics: An experimental and numerical identification'. *Mechanism and Machine Theory* (2013), vol. 64: pp. 144–154.

136. Pochhammer, L.: 'Über die Fortpflanzungsgeschwindigkeiten kleiner Schwingungen in einem isotropen Kreiscylinder'. *Journal für die Reine und Angewandte Mathematik* (1876), vol. 81: pp. 324–336.

137. Prandtl, L.: 'Beiträge zur Frage der kritischen Drehzahlen.' *Polytechnisches Journal* (1918), vol. 333. Ed. by Dingler, Johann Gottfried: pp. 179–182.

138. Prathap, G. and G. R. Bhashyam: 'Reduced integration and the shear-flexible beam element'. *International Journal for Numerical Methods in Engineering* (1982), vol. 18(2): pp. 195–210.

139. Prohl, M. A.: 'A general method for calculating critical speeds of flexible rotors'. *Journal of Applied Mechanics-Transactions of the ASME* (1945), vol. 12(3): A142–A148.

140. Rand, Omri: 'Interlaminar shear stresses in solid composite beams using a complete out-of-plane shear deformation model'. *Computers & Structures* (1998), vol. 66(6): pp. 713–723.

141. Rankine, W.: 'On the centrifugal force on rotating shafts'. *The Engineer* (1869), vol. Apr. 9: p. 249.

142. Rao, K.M. and B.G. Ghosh: 'Exact analysis of unsymmetric laminated beam'. *ASCE J Struct Div* (1979), vol. 105(11): pp. 2313–2325.

143. Rao, S. Ramalingeswara and N. Ganesan: 'Dynamic responce of non-uniform composite beams'. *Journal of Sound and Vibration* (1997), vol. 200(5): pp. 563–577.

144. Robertson, David: 'XII. Whirling of a journal in a sleeve bearing'. *The London, Edinburgh, and Dublin Philosophical Magazine and Journal of Science* (1933), vol. 15(96): pp. 113–130.

145. Royston, T.J. and I. Basdogan: 'Vibration Transmission Through Self-Aligning Spherical Rolling Element Bearings: Theory and Experiment'. *Journal of Sound and Vibration* (1998), vol. 215(5): pp. 997–1014.

146. Ruhl, Roland L. and J. F. Booker: 'A finite element model for distributed parameter turborotor systems'. *Journal of Manufacturing Science and Engineering* (1972), vol. 94(1): pp. 126–132.

147. Saada, A. S.: *Elasticity*. Pergamon Press Inc., 1974: p. 644.

148. Sankar, Bhavani V.: 'A Beam Theory for Laminated Composites and Application to Torsion Problems'. *Journal of Applied Mechanics* (Mar. 1993), vol. 60(1): pp. 246–249.

149. Santoro, Roberta: 'Solution of De Saint Venant flexure-torsion problem for orthotropic beam via {LEM} (Line Element-less Method)'. *European Journal of Mechanics - A/Solids* (2011), vol. 30(6): pp. 924–939.

150. Sapountzakis, E.J. and V.M. Protonotariou: 'A displacement solution for transverse shear loading of beams using the boundary element method'. *Computers & Structures* (2008), vol. 86(7-8): pp. 771–779.

151. Schwalbe, W. L.: 'Über den Schubmittelpunkt in einem durch eine Einzellast gebogenen Balken'. *ZAMM - Zeitschrift für Angewandte Mathematik und Mechanik* (1935), vol. 15(3): pp. 138–143.

152. Seinsch, H. O.: *Oberfelderscheinungen in Drehfeldmaschinen - Grundlagen zur analytischen und numerischen Berechnung*. B. G. Teubner, Stuttgart, 1992.

153. Sheinman, Izhak: 'On the analytical closed-form solution of high-order kinematic models in laminated beam theory'. *International Journal for Numerical Methods in Engineering* (2001), vol. 50(4): pp. 919–936.

154. Silverman, I.K.: 'Flexure of laminated beams'. *ASCE J Struct Div* (1980), vol. 106(3). cited By 13: pp. 711–725.

155. Simeon, Bernd: *Computational Flexible Multibody Dynamics: A Differential-Algebraic Approach*. Springer-Verlag, 2013: p. 249.

156. Singhal, S., K.V. Singh, and A. Hyder: 'Effect of laminated core on rotor mode shape of large high speed induction motor'. *Electric Machines Drives Conference (IEMDC), 2011 IEEE International*. 2011: pp. 1557–1562.

157. Soderberg, C Richard: 'On the subcritical speeds of the rotating shaft'. *Trans. ASME* (1932), vol. 54: pp. 45–52.

158. Song, S.J. and A.M. Waas: 'Effects of shear deformation on buckling and free vibration of laminated composite beams'. *Composite Structures* (1997), vol. 37(1): pp. 33–43.

159. Spence, G. B. and E. J. Seldin: 'Sonic Resonances of a Bar and Compound Torsion Oscillator'. *Journal of Applied Physics* (1970), vol. 41(8): pp. 3383–3389.

160. Spinner, S, Reichard W., and Tefft W. E.: 'A Comparison of Experimental and Theoretical Relations Between Young's Modulus and the Flexural and Longitudinal Resonance Frequencies of Uniform Bars'. *Journal of Research of the National Bureau of Standards—A. Physics and Chemistry* (1960), vol. 64A(2): pp. 147–155.

161. Stemple, Alan D. and Sung W. Lee: 'Finite-Element Model for Composite Beams with Arbitrary Cross-Sectional Warping'. *AIAA Journal* (Dec. 1988), vol. 26(12): pp. 1512–1520.

162. Stephen, N. G.: 'Discussion: "Shear Coefficients for Timoshenko Beam Theory" (Hutchinson, J. R., 2001, ASME J. Appl. Mech., 68, pp. 87-92)'. *Journal of Applied Mechanics* (Nov. 2001), vol. 68(6): pp. 959–960.

163. Stephen, N. G.: 'Timoshenko's Shear Coefficient From a Beam Subjected to Gravity Loading'. *Journal of Applied Mechanics* (1980), vol. 47(1): pp. 121–127.

164. Sternlicht, B.: 'Elastic and damping properties of cylindrical journal bearings'. *Journal of Basic Engineering* (1959), vol. 81: pp. 101–108.

165. Stodola, A.: *Die Dampfturbinen: Mit einem Anhang über die Aussichten der Wärmekraftmaschinen und über die Gasturbine*. Springer Berlin Heidelberg, 1910.

166. Stodola, A.: 'Neuere Beobachtungen über die kritischen Umlaufzahlen von Wellen'. *Schweizer Bauzeitung* (1916), vol. 68: pp. 210–214.

167. Stodola, A.: 'Steam and Gas Turbines'. *IIMcGraw-Hill, New York* (1927), vol. Vol. I: pp. 1039–1073.

168. Stojek, Dieter: 'Zur Schubverformung im Biegebalken'. *ZAMM - Zeitschrift für Angewandte Mathematik und Mechanik* (1964), vol. 44(8-9): pp. 393–396.

169. Stolarski, Henryk and Ted Belytschko: 'Shear and membrane locking in curved {C0} elements'. *Computer Methods in Applied Mechanics and Engineering* (1983), vol. 41(3): pp. 279–296.

170. Strutt, John William: *Theory of Sound*. London: Macmaillian Publications Co., Inc., 1877: p. 326.

171. Szabó, István: *Höhere Technische Mechanik*. Vol. 6.Auflage. Berlin: Springer-Verlag, 2001.

172. Taylor, H. D.: 'Critical-speed behavior of unsymmetrical shafts'. *Journal of Applied Mechanics* (1940), vol. 7(2): pp. 71–79.

173. Tessler, A. and S.B. Dong: 'On a hierarchy of conforming timoshenko beam elements'. *Computers & Structures* (1981), vol. 14(3-4): pp. 335–344.

174. Thomas, D.L., J.M. Wilson, and R.R. Wilson: 'Timoshenko beam finite elements'. *Journal of Sound and Vibration* (1973), vol. 31(3): pp. 315–330.

175. Thomas, J. and B.A.H. Abbas: 'Finite element model for dynamic analysis of Timoshenko beam'. *Journal of Sound and Vibration* (1975), vol. 41(3): pp. 291–299.

176. Thomson, W. T.: 'Matrix solution for the vibration of nonuniform beams'. *Journal of Applied Mechanics-Transactions of the ASME* (1950), vol. 17(3): pp. 337–339.

177. Timoshenko, S.: *Strength of Materials*. Vol. Second Edition. D. Van Nostrand Co., Inc., 1940: p. 359.

178. Timoshenko, S. and J. N. Goodier: *Theory of Elasticity*. Vol. Second Edition. McGraw-Hill Book Co., Inc., 1951: p. 506.

179. Timoshenko, S.P.: 'On the correction for shear of the differential equation for transverse vibrations of prismatic bars'. *Philosophical Magazine Series 6* (1921), vol. 41(245): pp. 744–746.

180. Timoshenko, S.P.: 'X. On the transverse vibrations of bars of uniform cross-section'. *Philosophical Magazine Series 6* (1922), vol. 43(253): pp. 125–131.

181. TIWARI, R., A.W. LEES, and M.I. FRISWELL: 'Identification of Speed-Dependent Bearing Parameters'. *Journal of Sound and Vibration* (2002), vol. 254(5): pp. 967 –986.

182. Tolle, M.: *Regelung von Kraftmaschinen*. Vol. 3. Auflage. Julius Springer, 1921.

183. Traill-Nash, R. W. and A. R. Collar: 'The effect of shear flexibility and rotatory inertia on the bending vibrations of beams'. *The Quarterly Journal of Mechanics and Applied Mathematics* (1953), vol. 6(2): pp. 186–222.

184. Trefftz, E.: 'Über den Schubmittelpunkt in einem durch eine Einzellast gebogenen Balken'. *ZAMM - Zeitschrift für Angewandte Mathematik und Mechanik* (1935), vol. 15(4): pp. 220–225.

185. Tsai, C.-L., I. M. Daniel, and G. Yaniv: 'Torsional Response of Rectangular Composite Laminates'. *Journal of Applied Mechanics* (June 1990), vol. 57(2): pp. 383–387.

186. Čermelj and M Boltežar: 'An indirect approach to investigating the dynamics of a structure containing ball bearings'. *Journal of Sound and Vibration* (2004), vol. 276(1-2): pp. 401–417.

187. Vogelius, M and I Babuška: 'On a dimensional reduction method. III. A posteriori error estimation and an adaptive approach'. *Mathematics of computation* (1981), vol. 37(156): pp. 361–384.

188. Vogelius, Michael and Ivo Babuška: 'On a dimensional reduction method. I. The optimal selection of basis functions'. *Mathematics of computation* (1981), vol. 37(155): pp. 31–46.

189. Vogelius, Michael and Ivo Babuška: 'On a dimensional reduction method. II. Some approximation-theoretic results'. *Mathematics of computation* (1981), vol. 37(155): pp. 47–68.

190. Walker, J.H., G.J. Rogers, and R.L. Jackson: 'Pressing and clamping laminated cores'. *Electrical Engineers, Proceedings of the Institution of* (1964), vol. 111(3): pp. 565–577.

191. Weber, Constantin: 'Übertragung des Drehmomentes in Balken mit doppelflanschigem Querschnitt'. *ZAMM - Zeitschrift für Angewandte Mathematik und Mechanik* (1926), vol. 6(2): pp. 85–97.

192. Weber, Constantin: 'Biegung und Schub in geraden Balken.' *ZAMM - Zeitschrift für Angewandte Mathematik und Mechanik* (1924), vol. 4(4): pp. 334–348.

193. Weilharter, Bernhard: 'Noise Computation of Induction Machines'. PhD thesis. Graz University of Technology, 2012.

194. Weinstein, A.: 'The center of shear and the center of twist'. *Quarterly of Applied Mathematics* (1947), vol. 5: pp. 97–99.

195. Werner, U.: 'Optimized rotor design for rigid balancing of large flexible induction rotors'. *Electric Drives Production Conference (EDPC), 2011 1st International*. 2011: pp. 249–254.

196. Werner, U.: 'Theoretical analysis of shaft vibrations in two-pole induction machines considering static rotor eccentricity'. *Power Electronics Electrical Drives Automation and Motion (SPEEDAM), 2010 International Symposium on*. 2010: pp. 853–860.

197. Wriggers, Peter: *Nonlinear finite element methods*. Springer Science & Business Media, 2008.

198. W.R.Osgood: 'The center of shear again'. *Journal of Applied Mechanics* (1943), vol. 10(2): A62–A64.

List of Figures

List of Tables